Optimisation problems at the air/water interface : From ship hulls to rowing propulsion

Jean-Philippe Boucher

▶ **To cite this version:**

université
PARIS-SACLAY

Thèse de doctorat

ÉCOLE
POLYTECHNIQUE
UNIVERSITÉ PARIS-SACLAY

Problèmes d'optimisation à la surface de l'eau

Des coques de bateaux à la propulsion par rame

Thèse de doctorat de l'Université Paris-Saclay
préparée à l'Ecole polytechnique

École doctorale n°579 : Sciences Mécaniques et Energétiques,
Matériaux et Géosciences (SMEMAG)
Spécialité de doctorat: Mécanique des Fluides

Thèse présentée et soutenue à Palaiseau, le 11 décembre 2018, par

Jean-Philippe Boucher

Composition du Jury :

Christophe ELOY
Professeur, Ecole Centrale Marseille   Président
Thierry DAUXOIS
Directeur de Recherche, ENS de Lyon   Rapporteur
François GALLAIRE
Professeur Associé, Ecole Polytechnique Fédérale de Lausanne   Rapporteur
Frédéric MOISY
Professeur, Université Paris-Sud   Examinateur
Christophe CLANET
Directeur de Recherche, Ecole polytechnique   Directeur de thèse
Michael BENZAQUEN
Chargé de Recherche, Ecole polytechnique   Directeur de thèse
Frédéric CHEVY
Professeur, ENS de Paris   Invité

Remerciements

Avant tout, j'aimerais souligner que j'ai vraiment passé trois années exceptionnelles au LadHyX. Trois années évidemment riches au niveau scientifique, mais aussi rythmées par un grand nombre d'activités "extrascolaires": la réparation d'une jeep, les soirées pizza, les barbecues, les excursions à la ferme, quelques très bons restos ou encore une fameuse sortie en bateau qui m'a fait découvrir en même temps la voile et le mal de mer. Je voudrais donc largement remercier toutes les personnes avec lesquelles j'ai eu la chance et le plaisir d'interagir pendant ces trois années de thèse.

Je voudrais remercier plus particulièrement les membres de mon jury, Frédéric Chevy, Thierry Dauxois, Christophe Eloy, François Gallaire et Frédéric Moisy, pour avoir accepté d'être dans mon jury de thèse, pour leur relecture minutieuse de mon manuscrit ainsi que pour toutes les questions très pertinentes posées à l'issue de ma présentation. En particulier, les remarques de mes rapporteurs ont contribué à l'amélioration du manuscrit.

Je veux maintenant remercier Christophe, d'abord pour m'avoir proposé ce projet de recherche en laboratoire sur la propulsion par palme et pour m'avoir ensuite invité à continuer à travailler sur ce projet en thèse. Je te remercie pour ta disponibilité et ta confiance dont on a eu à plusieurs reprises la démonstration, notamment lorsque tu as accepté que Romain et moi construisions une piscine pour nos expériences dans le laboratoire. Tu n'es jamais à court de nouvelles idées et de nouveaux sujets très intéressants, comme celui de l'aviron, qui font qu'on en abandonne presque son sujet de thèse initial. Merci aussi pour les nombreux conseils que tu m'as donnés lors de la préparation de ma soutenance.

Je remercie Michael d'avoir co-encadré ma thèse. Tu es arrivé au milieu de ma deuxième année de thèse et, avec l'étude de l'optimisation des formes de coques de bateau, tu as redonné un nouvel élan à ma thèse. J'ai apprécié de faire un peu de théorie, ainsi que la façon dont on a travaillé ensemble avec Romain. La rédaction des articles m'a beaucoup appris et a rendu la rédaction de ma thèse plus facile. Je te remercie pour tous les conseils que tu m'as donnés, en particulier pour la rédaction de ce manuscrit et la préparation de ma soutenance.

Je veux remercier Romain pour tout le travail que nous avons accompli ensemble, mais aussi (et surtout) pour toute l'animation que tu as apportée au labo (sans toi, point de barbecues, de four à pizza, de jeep remise en état, et j'en passe ...). Merci pour tout ce que tu m'as appris, en particulier sur le bricolage, la mécanique et la mesure d'effort ! Je suis très heureux que notre collaboration, commencée il y a près de 3 ans, continue aujourd'hui avec *Phyling*.

Je remercie toute l'équipe du préfa, les anciens: Caro, Tim, Manu, Eline et les petits jeunes: Ambre, Thibault, Pierre, Tom et Juliette. J'ai passé de très bons moments à vos côtés ! Je veux remercier plus spécialement Pierre pour avoir partager avec nous son code de trainée de vague et son rapport de master d'une excellente qualité, et Tim, pour nous avoir ouvert les portes du monde de l'aviron, pour m'avoir aidé à partir quelques mois au Japon, pour toutes les références "culturelles" que tu m'as apprises (Kaamelott en particulier) et les nombreux sushis à volonté.

Je remercie les stagiaires Kozeta, Alexis, Mathieu, Louis, Varvara et Vedant, avec qui j'ai travaillé et qui ont tous contribué au travail qui est présenté ici. Je veux remercier aussi Vinh avec qui j'ai travaillé pendant 2 mois à l'Université de Tokyo. Ce fut une superbe expérience même si malheureusement les résultats n'ont pas tout à fait été au rendez-vous. Je remercie Thomas Baroukh de nous avoir invité à assister à l'un de ses entrainements à Versailles ainsi que Augustin Mouterde et Hugo Maciejewski pour les discussions très intéressantes que nous avons eues autour de l'aviron.

Résumé de la thèse

Plusieurs problèmes d'optimisation – dans l'eau ou à l'interface avec l'air – sont abordés dans cette thèse, allant de l'optimisation de la forme des coques de bateaux à celle de la propulsion en aviron et dans la nage avec palmes. Des approches théorique, expérimentale et numérique sont ainsi combinées.

Dans le **chapitre 1**, nous identifions d'abord les paramètres sans dimension qui influencent la traînée sur un objet se déplaçant dans l'eau ou à son interface. Les valeurs typiques de ces paramètres pour les bateaux et quelques animaux sont données. Ensuite, nous décomposons la force de traînée en trois termes principaux qui sont chacun détaillés: la traînée de peau, la traînée de pression (ou de forme) et la traînée de vague. Enfin, la composante de masse ajoutée, pertinente pour les mouvements instationnaires, est présentée.

Dans le **chapitre 2**, nous introduisons d'abord les bases de l'aviron. Ce sport mêle physiologie, mécanique et dynamique des fluides, ce qui le rend beaucoup plus complexe qu'il n'y parait. A partir d'expériences et de données de terrain, nous analysons ensuite la cinématique du bateau, d'une rame et d'un rameur. Enfin, un modèle de traînée sur la coque d'un bateau d'aviron est proposé et validé par des expériences et des études antérieures.

Dans une première partie, nous nous intéressons à la question de l'optimisation des formes de coque de bateaux.

Les données empiriques révèlent une grande variété de formes de coque parmi les différentes catégories de bateaux. Dans le **chapitre 3**, nous présentons une approche théorique minimale pour traiter de l'optimisation de la forme de la coque d'un navire. Nous montrons que les rapports d'aspect de coque optimaux résultent – pour une charge et une puissance de propulsion données – d'un équilibre subtil entre la traînée de vague, la traînée de pression et la trainée de peau. Les coques élancées sont plus favorables en terme de réduction de la résistance de vague et de la trainée de pression, tandis que les coques plus larges ont une surface mouillée plus petite pour un volume immergé donné, ce qui réduit la trainée de peau. Nous comparons nos résultats théoriques aux données réelles et expliquons les différences observées en considérant les autres contraintes de conception des coques, telles que les contraintes de stabilité ou de manoeuvrabilité.

Le **chapitre 4** a pour but d'évaluer l'effet de l'asymétrie avant-arrière d'une coque sur sa traînée totale et en particulier sur sa traînée de vague. Nous considérons un ensemble de coques d'asymétrie croissante et déterminons à la fois expérimentalement et numériquement leur traînée pour trouver l'asymétrie optimale. La comparaison entre les deux approches fournit de nouveaux éléments particulièrement intéressants dans le contexte de l'optimisation des formes de coque.

Dans une deuxième partie, nous étudions la propulsion en aviron et dans la nage avec palmes.

Dans le **chapitre 5**, nous revenons ainsi sur la question de la dépendance de la vitesse d'un bateau à rames avec le nombre de rameurs. On constate en effet avec les records du monde dans les différentes catégories d'aviron que la vitesse augmente lentement avec le nombre de rameurs. McMahon a montré que la relation entre les deux est une loi de puissance (avec une puissance $1/9$) qui correspond assez bien aux observations. Nous retirons deux des hypothèses du modèle de McMahon et constatons que cela affecte peu la loi de puissance. Enfin, nous considérons une limitation du modèle de McMahon pour un grand nombre de rameurs, qui découle de la nécessité d'un espacement suffisant entre rameurs consécutifs.

Le **chapitre 6** s'intéresse à la question de la synchronisation des rameurs sur un bateau

d'aviron. En effet, la synchronisation en aviron apparaît comme une condition cruciale pour remporter les courses de haut niveau. Cependant, dans la nature, on peut observer des animaux avec plusieurs pattes, comme le krill, nageant de manière désynchronisée. Du point de vue du physicien, l'aviron désynchronisé semble une bonne idée car il réduit les fluctuations de vitesse et donc la traînée sur le bateau. Dans cette étude, nous avons construit une maquette de bateau d'aviron à l'échelle 1/10 pour étudier l'effet de la synchronisation des rameurs sur les performances du bateau. Les résultats expérimentaux sont comparés aux prévisions d'un modèle théorique.

La propulsion dans l'eau ou à sa surface peut également être réalisée avec des plaques flexibles, appelées nageoires, inspirées de la nage des poissons; c'est l'objet du **chapitre 7**. Dans cette étude expérimentale et théorique, nous examinons l'effet de la géométrie et de l'élasticité sur les performances propulsives de plaques flexibles rectangulaires soumises à un mouvement vertical forcé. La géométrie optimale d'une plaque rectangulaire est principalement dictée par sa fréquence de résonance.

Contents

Foreword

Once during my thesis, as I was briefly presenting the research that we were conducting with Romain Labbé on rowing, a member of the audience made the remark that it had been two thousand years that people were rowing in synchrony, so why consider another way of rowing? To be exact, it has been more than two thousand years that people are using oars to propel boats: the first representation of a rowing boat dates back to 5800 BC in Finland [1]. But still, rowing greatly evolved over the centuries from the Phoenician boats or Greek triremes (boats with three rows of oars), as represented on reliefs from antiquity (see Fig. 1), to modern rowing boats and there is still a room for improvement in today's rowing technique and equipments. The first record of a rowing race is found in the *Aeneid* written between 29 and 19 BC by Virgil (70 – 19 BC).
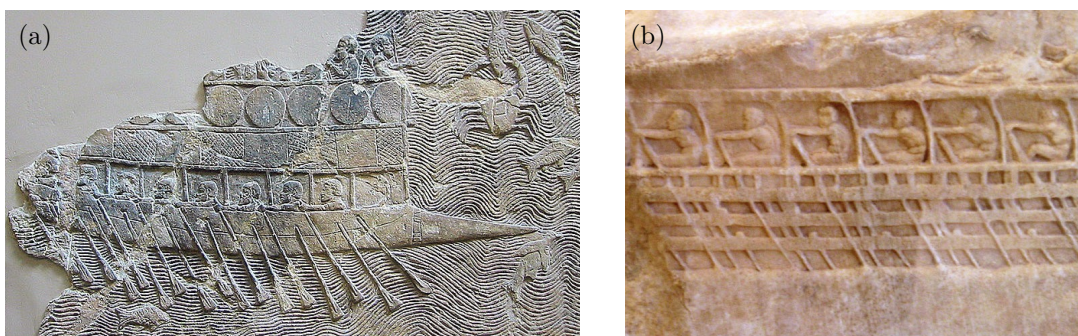
Figure 1: (a) Phoenician warship with two rows of oars found on a relief from Nineveh, around 700 BC [2]. (b) Lenormant relief from the Athenian Acropolis, depicting the rowers of an Athenian trireme (with three rows of oars), around 410 BC. Pictures taken from [3].

Race rowing, as the modern sport known today, appeared in England during the reign of Henry VII (1509 – 1547) [1]. With the competitions and the worldwide development of rowing, important progresses in the equipment and the technique were made. For instance, in the 1860s, slides with wheels were invented as, until that time, rowers were greasing their seat and wearing leather bottom trousers to increase the stroke length [1]. In the meantime, the boats became narrower and narrower, leading to the development of riggers[1] to increase or at least keep the same leverage as before.

The observed evolution of the aspect ratio of rowing boats over the years is related to the aim of minimising the total drag on the hull. This objective is actually common among all ship categories as they seek to expend the minimum energy to move at a given speed with a given load under some constraints, such as stability, manoeuvrability or seakindliness. The experimental study of the flow past a ship hull and of the corresponding drag force exerted on the hull dates back to Leonardo da Vinci (1452 – 1519), who tested three ship models of different fore-aft distribution of volumes [4]. Samuel Fortrey (1622 – 1681) carried out experiments with different models towed in a tank by falling weights [5]. Around 1757, Pieter van Zwijndregt (1711 – 1790) also used this technique in his towing experiments as shown in Fig. 2(a). Towing three different hulls (represented in Fig. 2(b)), he concluded that the largest width of the hull should be as far towards the stern as practically possible. The English engineer William Froude (1810 – 1879) built the first modern towing tank (85 m long, 10 m wide and 3 m deep, see Fig. 3) and found a scaling law, which is still used today, to extrapolate the results from towing tests at small scale to real ship hulls.

---

[1]A rigger is a bracket on a racing shell to support the rowlock (see Fig. 2.2).
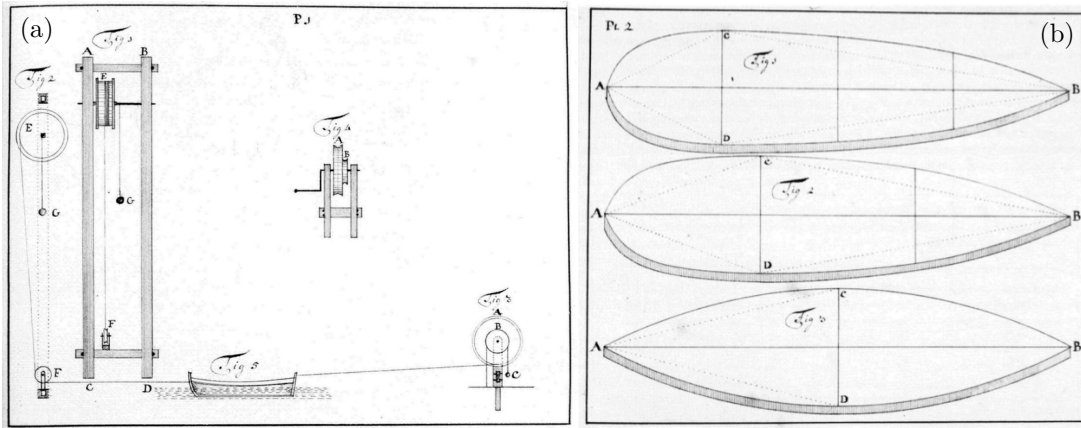
Figure 2: (a) Apparatus and (b) hull shapes used by Pieter van Zwijndregt in his towing experiments around 1757. The model hulls were towed over a 50 m distance. Reprinted from [6].

The development of the corresponding theoretical framework started with the work of the Australian mathematician Michell (1863 – 1940) [7], which was then pursued by Havelock (1877 – 1968) [8]. Various numerical methods to model the flow past a ship were used from the 1960s following the introduction of computers [5]. However, towing experiments are still used today to precisely predict the resistance of ship hulls and, because of the complexity of the problem, the optimisation of ship hulls is still an active field of research.

In this thesis, we first distinguish the different drag components acting on an object moving at the air-water interface (Chap. 1). In Chap. 2, we introduce the basics of rowing and present kinematic analyses of rowing. As mentioned above, the length-to-width aspect ratio of rowing boats has increased over the years. Chap. 3 on the optimal aspect ratios of ship hulls can help understand this evolution. Then, following the observations of Pieter van Zwijndregt, we seek the optimal asymmetry of ship hulls (Chap. 4). In Chap. 5, the effect of the number of rowers on the mean boat speed is discussed. This is followed by the study of the effect of the synchronisation between rowers (Chap. 6). Finally, we identify and discuss the propulsive mechanism at stake in fin-swimming (Chap. 7).
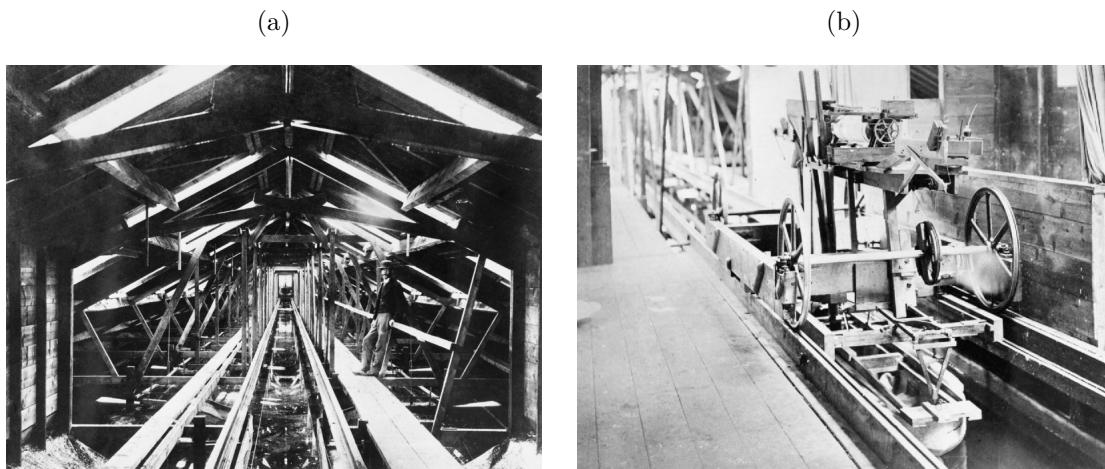
Figure 3: (a) View of the first naval test tank constructed in Torquay (England) by the civil engineer and naval architect William Froude in 1872. (b) View of the trolley used to tow ship models across the test tank. Images taken from [9].

PART I

INTRODUCTION

1

GENERAL INTRODUCTION

In this chapter, we first identify the dimensionless parameters that influence the drag on an object moving in water or at its interface. The typical values of these parameters for ships and animals are given. Then we decompose the drag force into three main components: skin drag, pressure drag and wave drag. Finally, the two force components, arising for an unsteady motion, are detailed.
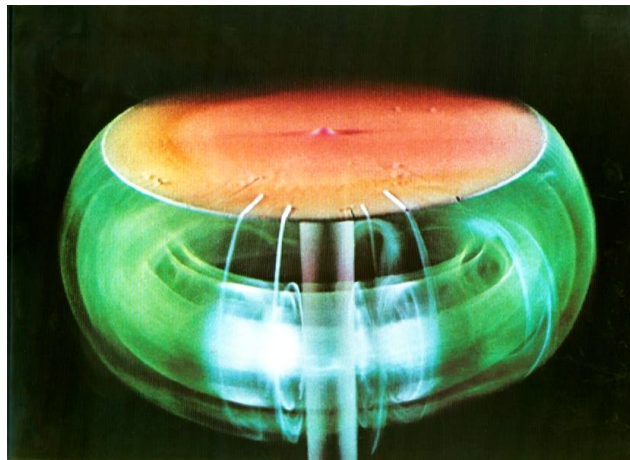
Starting vortex behind a disk normal to the flow. Photo credits: Henri Werlé, ONERA.

Contents

1.1   Dimensional analysis

We shall start this chapter with a simple dimensional analysis of the drag on an object at the water surface. Let us consider a duck of typical length ℓ, width w and mass M (equivalently immersed volume Ω, related to M through Archimedes principle), paddling at speed U in a pond of depth h (see Fig. 1.1), and let us seek a relation between the drag R experienced by the duck and the relevant parameters of the problem.

Figure 1.1: Duck moving at the water surface and creating a nice wake.

The drag should depend on the following parameters: ℓ, w, Ω, a dimensionless parameter $\bar{G}$ accounting for the precise geometry of the duck, h, U, the water density ρ, the viscosity of water μ and the acceleration of gravity g. Under such assumptions, there exists a function $\mathcal{F}_1$ such that:

$$\mathcal{F}_1(R, \ell, w, \Omega, \bar{G}, h, U, \rho, \mu, g) = 0 \ . \tag{1.1}$$

Eq. (1.1) contains 10 parameters involving 3 dimensions. Then, following Buckingham's Π theorem, this equation can be reduced with $10 - 3 = 7$ dimensionless parameters using a dimensionless function $\mathcal{F}_2$:

$$\mathcal{F}_2(C, w/\ell, \Omega/\ell^3, \bar{G}, h/\ell, \mathrm{Re}, \mathrm{Fr}) = 0 \ , \tag{1.2}$$

where we introduced the drag coefficient $C = R/(\rho\ell^2 U^2)$, the Reynolds number $\mathrm{Re} = \rho U \ell/\mu$ (which compares inertia and viscosity) and the Froude number $\mathrm{Fr} = U/\sqrt{g\ell}$ (which compares inertia and gravity).

Finally, the total drag on the duck is written: $C = R/(\rho\ell^2 U^2) = \mathcal{F}_3(w/\ell, \Omega/\ell^3, \bar{G}, h/\ell, \mathrm{Re}, \mathrm{Fr})$ which, in the case of an infinitely deep fluid ($h \gg \ell$), reduces to :

$$\frac{R}{\rho\ell^2 U^2} = \mathcal{F}_4(w/\ell, \Omega/\ell^3, \bar{G}, \mathrm{Re}, \mathrm{Fr}) \ . \tag{1.3}$$

In Chap. 3 and Chap. 4, the expression of the total drag on an object will be detailed in the case of an infinitely deep fluid. When the object is immersed in a homogeneous fluid, the total drag can be decomposed into *pressure drag* and *skin drag* [10]. When the body moves at the water surface, it experiences an additional component of drag called the *wave drag* [10]. These three main components of the total drag are described below.

1.2 Orders of magnitude

In Table 1.1, a few orders of magnitude are given for various bodies moving at the water surface such as liners, rowing boats, sprint kayaks, sailing boats and animals. The Froude number is typically between 0.1 and 1 and the Reynolds number ranges from $2 \cdot 10^5$ to $5 \cdot 10^9$ (typically $\mathrm{Re} \in [10^7, 5 \cdot 10^9]$, for ships).

(a)	(b)	(c)
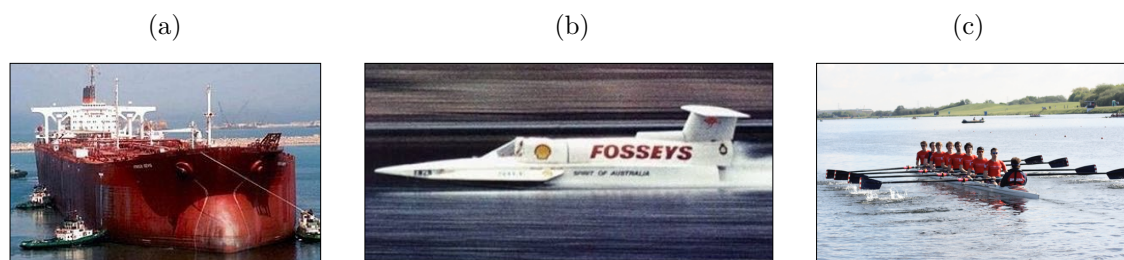
Figure 1.2: Pictures of (a) the *Seawise Giant*, the longest ship ever built ($\ell = 458$ m) (source: [11]), (b) the *Spirit of Australia*, the fastest ship ($U = 142$ m/s) (source: [12]), and (c) an *eight* rowing boat (source: [13]), one of the fastest man-powered boat ($U \simeq 6.3$ m/s). See Table 1.1 for their complete characteristics.

In particular, the *Seawise Giant* (see Fig. 1.2(a)) is the longest ship ever built. It was 458-meter long, 69-meter wide and 30-meter high (25-meter draft), weighed 650 000 tons and had a cruising speed of about 30 km/h. This corresponds to a Froude number of 0.13 and a Reynolds number of $4 \cdot 10^9$. The world fastest ship is the jet-powered hydroplane *Spirit of Australia* (see Fig. 1.2(b)). It reached a speed of 511.11 km/h on Blowering Dam Lake (Australia), on 8 Oct. 1978. For man-powered boats such as rowing boats (see Fig. 1.2(c)), sprint canoes or sprint kayaks, in competitions the typical values for the Froude number are comprised between 0.5 and 0.7, while the Reynolds number ranges from 10^7 to 10^8. For animals and human swimmers, the values of these dimensionless numbers are smaller (see Table 1.1).

Boat Name	Length ℓ (m)	Width w (m)	Mass M (kg)	Speed U (m/s)	Power (*) $\mathcal{P}$ (kW)	Froude number Fr	Reynolds number Re
Seawise Giant	458	68.9	$6.5 \cdot 10^8$	8.3	$3.7 \cdot 10^4$	0.13	$4 \cdot 10^9$
Spirit of Australia	8.22	2.5	1 500	142	4 500	15	$1 \cdot 10^9$
Eight rowing boat	17.7	0.56	820	6.26	3.2	0.48	$1 \cdot 10^8$
Laser sailing boat	4.2	1.39	130	4.1	2.7	0.64	$2 \cdot 10^7$
Duck	0.3	0.2	5	0.66	N.A.	0.38	$2 \cdot 10^5$
César Cielo (swimmer)	1.95	0.6	88	2.1	N.A.	0.46	$4 \cdot 10^6$

Table 1.1: Characteristics of some bodies moving at the water surface. N.A. stands for *Not Available*. (*) The power is estimated through diverse methods depending on the category of the boat. See Table 3.1 for more boat characteristics and the details on the methods used for the estimation of the power.

1.3 General expression of the total drag

In continuum mechanics, to model the forces inside a given medium, one classically introduces the Cauchy stress tensor $\boldsymbol{\sigma}$. From this tensor, one can express the stress vector $\boldsymbol{T}$ exerted by one part of a medium on another through an interface of normal vector $\boldsymbol{n}$ through: $\boldsymbol{T} = \boldsymbol{\sigma} \cdot \boldsymbol{n}$. In a fluid, the Cauchy stress tensor is written:

$$\boldsymbol{\sigma} = -p \, \mathbb{1} + \boldsymbol{\tau} \, , \tag{1.4}$$

where p is the pressure in the fluid, $\mathbb{1}$ is the identity tensor and $\boldsymbol{\tau}$ is the shear stress tensor [14]. For a Newtonian fluid, the stresses depend linearly on the local strain rate, so that:

$$\boldsymbol{\tau} = \lambda \left(\boldsymbol{\nabla} \cdot \boldsymbol{u} \right) \mathbb{1} + \mu \left(\boldsymbol{\nabla} \boldsymbol{u} + \boldsymbol{\nabla} \boldsymbol{u}^T \right) \, , \tag{1.5}$$

where λ and μ are the viscous coefficients, $\boldsymbol{u}$ is the velocity vector and $\boldsymbol{\nabla} \boldsymbol{u}^T$ denotes the transpose of the velocity gradient $\boldsymbol{\nabla} \boldsymbol{u}$. The coefficient λ is associated with changes of volumes, while μ is the classical dynamic viscosity (associated with shear). Finally, assuming the fluid to be incompressible ($\boldsymbol{\nabla} \cdot \boldsymbol{u} = 0$), the Cauchy stress tensor takes the simpler form:

$$\boldsymbol{\sigma} = -p \, \mathbb{1} + \mu \left(\boldsymbol{\nabla} \boldsymbol{u} + \boldsymbol{\nabla} \boldsymbol{u}^T \right) \, . \tag{1.6}$$

The general expression for the total drag on an object immersed in a fluid is:

$$\boldsymbol{R} = \iint_{S_w} \boldsymbol{\sigma} \cdot \boldsymbol{n} \, \mathrm{d}S \, , \tag{1.7}$$

where S_w is the wetted surface of the object. Injecting the expression of $\boldsymbol{\sigma}$ from Eq. (1.6) in Eq. (1.7), one gets:

$$\boldsymbol{R} = - \iint_{S_w} p \, \boldsymbol{n} \, \mathrm{d}S + \mu \iint_{S_w} \left(\boldsymbol{\nabla} \boldsymbol{u} + \boldsymbol{\nabla} \boldsymbol{u}^T \right) \cdot \boldsymbol{n} \, \mathrm{d}S \, . \tag{1.8}$$

The total drag $\boldsymbol{R}$ is thus divided into two terms: the first term is related to the pressure and thus includes both the pressure drag and the wave drag, while the second term corresponds to the skin friction. These different components are detailed in the following sections.

1.4 Skin drag

The component of *skin drag*, denoted $\boldsymbol{R}_{\mathrm{s}}$, is due to the friction of the water particles along the surface of the object and thus depends on the total wetted surface of the object [10]. From Eq. (1.8), one has:

$$\boldsymbol{R}_{\mathrm{s}} = \mu \iint_{S_w} \left(\boldsymbol{\nabla} \boldsymbol{u} + \boldsymbol{\nabla} \boldsymbol{u}^T \right) \cdot \boldsymbol{n} \, \mathrm{d}S \, . \tag{1.9}$$

This component of drag is the dominant one for streamlined bodies such as airfoils (see Fig. 1.3). In the case of a flat plate, an approximate expression for $\boldsymbol{R}_{\mathrm{s}}$ was first derived by Blasius.

Blasius boundary layer. Let us consider a semi-infinite flat plate coinciding with the half plane ($y = 0$, $x > 0$) subjected to a parallel flow with a constant velocity U, at large Reynolds number $\mathrm{Re} = \rho U \ell / \mu \gg 1$ (see Fig. 1.4). The flow can be considered as inviscid
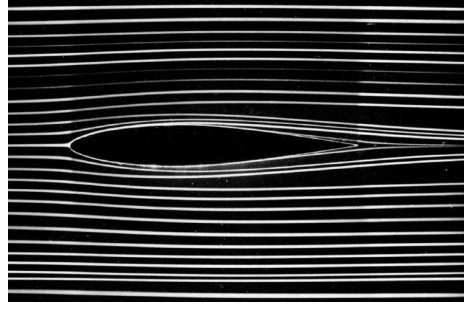
Figure 1.3: Picture of the flow past a NACA 64A015 airfoil profile at Re = 7 000. The profile is at zero incidence in a water tunnel. Colored fluid injected upstream is used to show the streamlines. Photo credits: Wale 1974, ONERA (taken from [15]).

except in the region close to the wall, called the *boundary layer*, which ensures the no-slip boundary condition and is the origin of the shear stress. Let $\boldsymbol{u} = (u_x, u_y)$ be the velocity of the fluid. One can show that, in the laminar region, the horizontal component of velocity u_x follows a similarity solution [14]: $u_x/U = f(\eta)$, where $\eta = y\sqrt{\mathrm{Re}_x}/x$ with $\mathrm{Re}_x = \rho U x/\mu$ the Reynolds number based on the coordinate x.
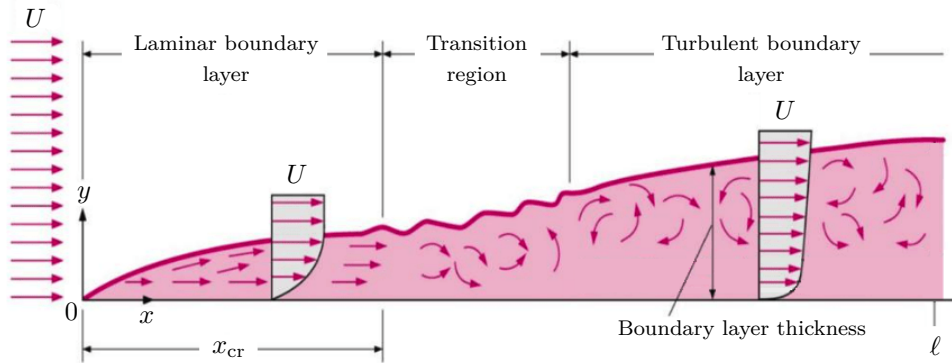
Figure 1.4: Schematics of the boundary layer which develops along a flat plate with the transition from laminar to turbulent from the critical position x_{cr}. Adapted from [16].

By definition, the local wall shear stress is:

$$\tau_0 = \mu \left(\frac{\partial u_x}{\partial y} \right)_0 , \tag{1.10}$$

where the subscript zero means at the wall ($y = 0$). Then, injecting the similarity solution for u_x inside this equation, one finds:

$$\tau_0 = \frac{\rho U^2 f'(0)}{\sqrt{\mathrm{Re}_x}} \simeq \frac{0.332 \, \rho U^2}{\sqrt{\mathrm{Re}_x}} . \tag{1.11}$$

The value $f'(0) \simeq 0.332$ is obtained by solving a differential equation for $f(\eta)$, which results from the Navier-Stokes equations approximated in the boundary layer. Using Eq. (1.9) to estimate the skin friction $R_{\mathrm{s}} = |\boldsymbol{R}_{\mathrm{s}}|$ on a portion of a plate of length ℓ and span w, one gets:

$$R_{\mathrm{s}} \simeq \frac{0.664 \, \rho w \ell U^2}{\sqrt{\mathrm{Re}}} , \tag{1.12}$$
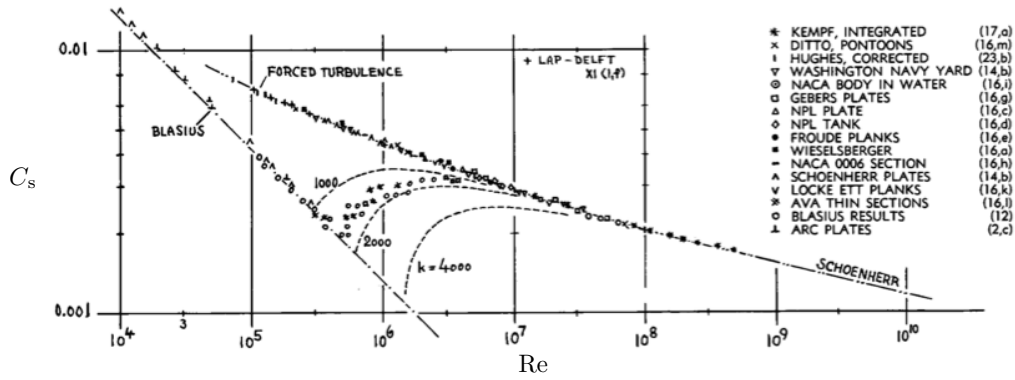
Figure 1.5: Skin friction coefficient C_s for various plates parallel to the flow from experiments in air and water. For $\mathrm{Re} \in [10^4, 10^6]$, the dash-dotted line shows the theoretical prediction from Blasius solution (laminar regime); while for $\mathrm{Re} \in [10^5, 10^{10}]$, the dash-dotted line shows the empirical law established by Schoenherr in the turbulent regime. Image reprinted from [10].

where $\mathrm{Re} = \rho U \ell / \mu$ is now the Reynolds number based on the length ℓ. It follows that the skin drag coefficient in the laminar regime reads:

$$C_s = \frac{R_s}{1/2 \rho w \ell U^2} \simeq \frac{1.33}{\sqrt{\mathrm{Re}}} \ . \tag{1.13}$$

This result from Blasius means that the skin friction depends on $U^{3/2}$, which is a different scaling than for the more classical pressure drag which scales as U^2 (as will be seen in the next section).

The evolution of the skin friction coefficient with the Reynolds number over the range $[10^4, 10^{10}]$ is represented in Fig. 1.5. The theoretical prediction from Blasius in the laminar regime shows a very good agreement with experimental data points in the range $10^4 < \mathrm{Re} < 10^6$. However, when the Reynolds number becomes bigger than a critical Reynolds number $\mathrm{Re}_{cr} \sim 5 \cdot 10^5 - 10^6$, the flow transitions from laminar to turbulent and the experimental points start to deviate from the Blasius law [17]. This transition is also illustrated in Fig. 1.4 for a flat plate and appears once a critical position $x_{cr} = \mathrm{Re}_{cr} \mu / (\rho U)$ is reached. In the turbulent regime, the skin friction coefficient C_s then shows a slower decrease with the Reynolds number $C_s \sim \mathrm{Re}^{-1/7}$. In this regime, many semi-empirical and empirical laws try to capture this evolution. In particular, Schoenherr established the following law [10]: $\log(\mathrm{Re}\ C_s) = 0.242/\sqrt{C_s}$, which is found in good agreement with the experimental data points in the regime of turbulence and of forced turbulence.

In ship design, the commonly accepted formula is the one from the International Towing Tank Conference (ITTC) of 1957 (see [18, 19, 20]):

$$C_s(\mathrm{Re}) \simeq \frac{0.075}{[\log(\mathrm{Re}) - 2]^2} \ . \tag{1.14}$$

As can be seen in Fig. 1.6, this formula deviates from the Schoenherr line for $\mathrm{Re} < 10^7$. For ships, the Reynolds number is in the range $10^7 < \mathrm{Re} < 5 \cdot 10^9$. Over this range, Eq. (1.14) and Schoenherr show good agreement and the skin drag coefficient varies between 10^{-3} and $3 \cdot 10^{-3}$.
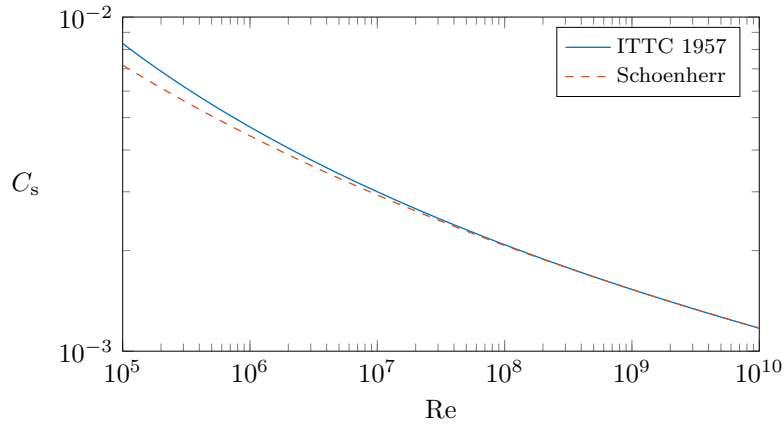
Figure 1.6: Comparison of the skin friction coefficient C_s as a function of the Reynolds number for the Schoenherr line and the ITTC 1957 line.

1.5 Pressure drag

The component of *pressure drag* (also called *form drag*), denoted $\boldsymbol{R}_\mathrm{f}$, results from the combination of all the pressure forces on the surface of the object and thus can be written (see Eq. (1.8)) as:

$$\boldsymbol{R}_\mathrm{f} = -\iint_{S_w} p\,\boldsymbol{n}\,\mathrm{d}S \ , \tag{1.15}$$

where p is the pressure at the surface of the object and the integration is performed over the whole wetted surface. This force arises when the boundary layer separates from the surface of the object, leading to the formation of vortices at the rear of the object. It scales with the cross-sectional area of the object, denoted S, and is particularly dominant for bluff bodies such as cylinders or spheres (see Fig. 1.7) [10].
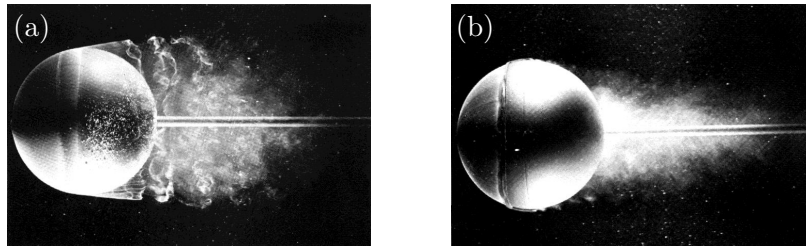
Figure 1.7: Picture of the instantaneous flow past a sphere (a) at $\mathrm{Re} = 15\,000$ (below the critical Reynolds number for the drag crisis Re_cr) and (b) at $\mathrm{Re} = 30\,000$ (above the critical Reynolds number). A wire is used to initiate the transition at a lower Reynolds number than the one for a sphere, which is $\mathrm{Re}_\mathrm{cr} \simeq 5 \cdot 10^5$. Photo credits: Henri Werlé, 1980 (ONERA).

We define the pressure drag coefficient as:

$$C_\mathrm{f} = \frac{R_\mathrm{f}}{\frac{1}{2}\rho S U^2} \ , \tag{1.16}$$

11

with $R_f = |\boldsymbol{R}_f|$, and the pressure coefficient c_p as:

$$c_p = \frac{p - p_\infty}{\frac{1}{2}\rho U^2} \; , \tag{1.17}$$

where p_∞ is the pressure far from the object. Thus, one has $C_f = (1/S)| \iint c_p \, \boldsymbol{n} \, dS|$.

Flow past a cylinder. Let us consider a cylinder of diameter D in a flow of constant velocity U. The Reynolds number is defined as Re $= \rho U D/\mu$. Different flow regimes are observed depending on the Reynolds number (see Fig. 1.8(a)) [14, 21].

- For Re < 4, the flow is laminar and attached to the cylinder.

- For 4 < Re < 40, a recirculation bubble forms behind the cylinder.

- For 80 < Re < 200, a Von Karman Vortex Street develops characterized by the alternative shedding of vortices from the two sides of the cylinder.

- For 200 < Re < Re$_{cr}$ = $3 \cdot 10^5$, the Vortex Street destabilises and the wake of the cylinder becomes turbulent.

- For Re > Re$_{cr}$ = $3 \cdot 10^5$, the laminar boundary layer upstream of the separation point also becomes turbulent. As the turbulent boundary layer has a higher energy than the laminar one and is able to withstand higher adverse pressure gradients, the separation point is moved downstream. The drag coefficient then decreases abruptly. This phenomenon is called the *drag crisis*. Re$_{cr}$ denotes the critical Reynolds number from which the boundary layer transitions from laminar to turbulent.

In Fig. 1.8(b), the pressure coefficient along the surface of a cylinder is plotted for Reynolds numbers below and above the critical Reynolds number Re$_{cr}$, together with the potential flow solution $c_p = 1 - 4\sin^2\theta$, with θ the angular distance to the stagnation point. It can
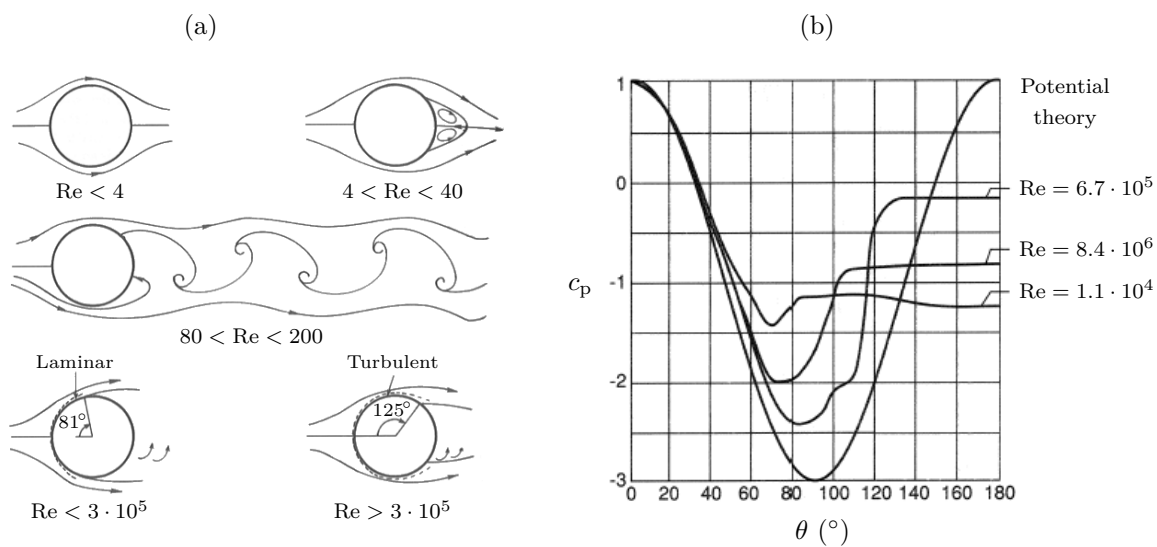
Figure 1.8: (a) Different flow regimes past a cylinder depending on the Reynolds number. Reprinted from [14]. (b) Distribution of the pressure coefficient c_p along a cylinder depending on the angular distance to the stagnation point θ, for different Reynolds numbers and in the potential flow limit. Reprinted from [21].

be noticed that the experimental pressure distributions follow the potential flow solution until $\theta \approx 40°$. Then, from a given angle θ_s (the angle at which the flow separates), the pressure coefficient reaches a plateau, the value of which depends on the Reynolds number. As explained above, the curves at $\mathrm{Re} = 1.1 \cdot 10^4 < \mathrm{Re_{cr}}$ and at $\mathrm{Re} = 6.7 \cdot 10^5 > \mathrm{Re_{cr}}$ highlight the shift of the separation angle θ_s from about 81° to about 125°, corresponding to a smaller wake and a reduced drag coefficient (see also Fig. 1.7 for an illustration of this phenomenon in the case of a sphere). The evolution of the drag coefficient C_f with the Reynolds number is shown in Fig. 1.9 (blue curve). Interestingly, the drag coefficient plateaus for $10^3 < \mathrm{Re} < \mathrm{Re_{cr}}$ at a value $C_\mathrm{f} \approx 1.2$ before decreasing drastically at the drag crisis ($\mathrm{Re} = \mathrm{Re_{cr}}$).
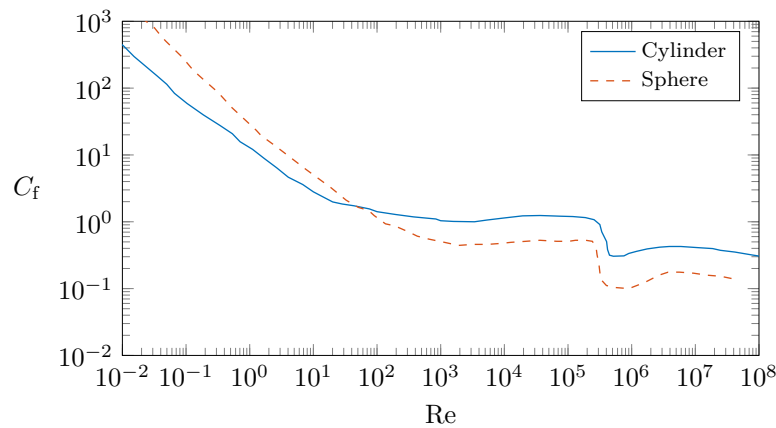
Figure 1.9: Pressure drag coefficient C_f of a cylinder and a sphere depending on the Reynolds number Re. Data gathered from [10].
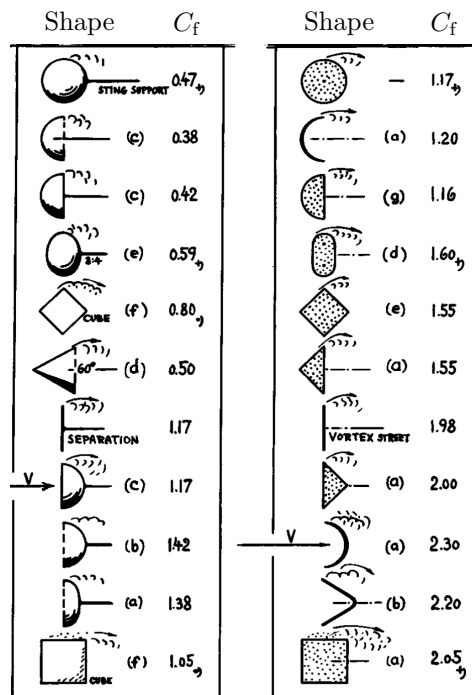
Figure 1.10: Drag coefficients of various 2D (right column) and 3D-axisymmetric (left column) bodies at Reynolds numbers between 10^4 and 10^6. Reprinted from [10].

Comparison with other 2D and 3D bodies. The case of a sphere is quite different from the one of a cylinder due to three-dimensional effects. The critical Reynolds number is a little bit different and the value of the drag coefficient on the plateau is now $C_f \approx 0.47$, as can be seen in Fig. 1.9 (red dashed curve). We thus see that the shape of the object plays a major role in its resulting pressure drag. Fig. 1.10 highlights this point by listing the drag coefficients of different 2D and 3D-axisymmetric bluff bodies (for $\text{Re} \in [10^4, 10^6]$).

Roughness effects. It should also be mentioned that the critical Reynolds number Re_{cr} at which the boundary layer transitions from laminar to turbulent is highly affected by the roughness of the solid surface. The values given for a cylinder and a sphere were obtained for smooth bodies. If the roughness is increased, then the value of Re_{cr} decreases and the drag crisis occurs at a smaller Reynolds number [22].

1.6 Wave drag

As mentioned in Sect. 1.1, when an object moves at the water surface, the flow around it is characterised by two dimensionless numbers: the Reynolds number Re and the Froude number Fr defined as:

$$\text{Fr} = \frac{U}{\sqrt{g\ell}} \ , \tag{1.18}$$

where U is the velocity of the object, g the acceleration of gravity and ℓ the length of the object along its direction of motion. As a body moves at the air-water interface (faster than $c_{\min} \simeq 23$ cm/s [23]), it generates dispersive surface waves with a characteristic V-shape wake (also called *Kelvin wake* [24], see Fig. 1.11(a)), which remove energy to infinity. Consequently, the object is subjected to an additional component of drag called the *wave drag* (or *wave resistance*), which is denoted R_w [7, 8, 25]. An evidence of wave drag is the fact that submarines move $20 - 40\%$ slower at the interface than when they are fully immersed (see Table 1.2). The same effect is observed for swimmers, especially when swimming with fins (see Chap. 7).

Submarine name	Speed when submerged (km/h)	Speed at the surface (km/h)
Daphné (FR)	28	22
Agosta (FR)	37	23
Franklin-class (US)	39	30
Ohio-class (US)	37	22
Typhoon (USSR)	50	40
Oscar II (USSR)	59	28

Table 1.2: Speed of different submarines when submerged and at the surface. Data gathered from [9].

The Froude number comes into play as it compares inertia and gravity, or equivalently, the wavelength λ of the waves produced and the length of the object (see Fig. 1.11(b)-(d)):

$$\text{Fr} = \frac{1}{\sqrt{2\pi}}\sqrt{\frac{\lambda}{\ell}} \ . \tag{1.19}$$

Equation (1.19) is valid in an infinitely deep fluid and is deduced from the dispersion relation $\omega = \sqrt{gk}$ with ω the angular frequency and $k = 2\pi/\lambda$ the wave number. The schematics in Fig. 1.11(b)-(d) illustrate the waves produced by a ship moving at three particular Froude numbers for which the waves produced at the front of the boat can interfere with those produced at the stern. For Fr $\simeq 0.33$ and Fr $\simeq 0.56$, they can interfere coherently, while for Fr $\simeq 0.4$ they interfere destructively. This strongly affects the value of the wave drag.
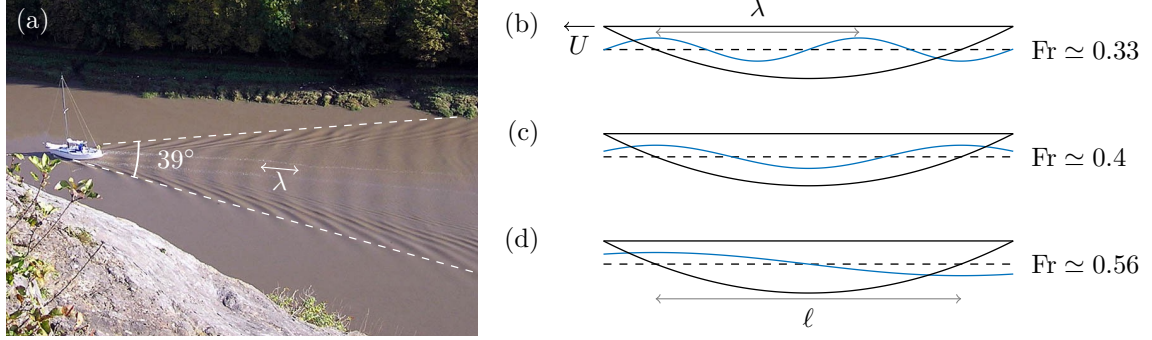
Figure 1.11: (a) Picture of the wake of a ship (source: [26]). The angle of the wake, delimited by the white dashed lines, is about 39° [24]. (b)-(d) Schematics of the wave elevation along the ship hull for different Froude numbers corresponding to different ratios of the wavelength λ to the ship length ℓ: (b) $\lambda/\ell = 2/3$, (c) $\lambda/\ell = 1$ and (d) $\lambda/\ell = 2$.

Froude's hypothesis. As it is not possible to build scale-model hulls with Reynolds and Froude numbers matching the ones for real boats, William Froude made the assumption that the total drag coefficient $C(\mathrm{Re}, \mathrm{Fr})$ can be written as:

$$C(\mathrm{Re}, \mathrm{Fr}) \simeq C_\mathrm{s}(\mathrm{Re}) + C_\mathrm{res}(\mathrm{Fr}) \ , \tag{1.20}$$

where C_s, the skin drag coefficient as defined in Sect. 1.4, only depends on the Reynolds number and C_res, the residual drag coefficient, only depends on the Froude number. Actually, C_res contains both the wave drag C_w and the pressure drag C_f but, in the range of Reynolds number operated for ship hulls, the pressure drag is fairly constant, so that $C_\mathrm{res}(\mathrm{Fr}, \mathrm{Re}) \simeq C_\mathrm{res}(\mathrm{Fr})$. This hypothesis was verified experimentally with different hull shapes [27] .

1.6.1   Problem statement

Let us consider a hull of length ℓ, width w and draft d moving at the water surface at velocity U which is first supposed to be constant. We define a cartesian coordinate system (x, y, z) with x opposite to the direction of motion of the hull. Consistent with usual parametrisation [7, 28, 29, 30], the hull shape is considered symmetric about the center-plane $y = 0$ and defined through the function f by: $y = \pm f(x, z)$ (see Fig. 1.12). The water surface is assumed to be infinite in x and y directions.

We can then introduce the dimensionless coordinates through $x = \tilde{x}\ell$, $y = \tilde{y}\ell$ and $z = \tilde{z}\ell$ as well as $f(x, z) = \tilde{f}(\tilde{x}, \tilde{z})w$. Note that w is used in the definition of $\tilde{f}$ as it simplifies the expression of the wave drag coefficient in Michell's model (see Subsect. 1.6.3). We further define the aspect ratios $\alpha = \ell/w$ and $\beta = \ell/d$. We take as a characteristic surface $\Omega^{2/3}$ with:

$$\Omega = \ell w d \ . \tag{1.21}$$

This volume scales as the immersed volume of the hull, denoted Ω_i.[1] This particular choice

---

[1]One has: $\Omega_\mathrm{i} = \Omega \iint \tilde{f} \, \mathrm{d}\tilde{x} \, \mathrm{d}\tilde{z}$.
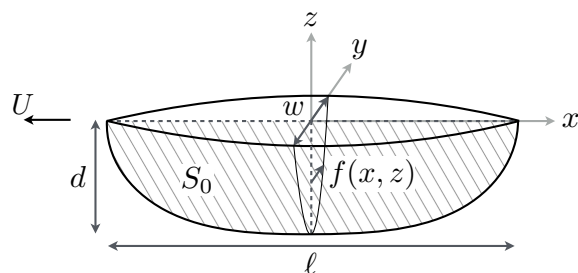
Figure 1.12: Schematics of a hull with illustration of its length ℓ, width w and draft d. The hull shape follows the parametrisation $y = f(x, z)$. The centerplane projection of the hull is denoted S_0. Note that only the part of the hull immersed in the water is represented.

of characteristic surface is motivated by the objective of comparing the drag on hulls that have the same immersed volume. The wave drag coefficient is thus defined through:

$$C_{\mathrm{w}} = \frac{R_{\mathrm{w}}}{\rho \Omega^{2/3} U^2} \ . \tag{1.22}$$

Fig. 1.13 shows the typical evolution of C_{w} with the Froude number for a parabolic hull from experiments [31] and theoretical predictions [32]. Interestingly, the wave drag coefficient is maximum for Fr $\simeq 0.5$.
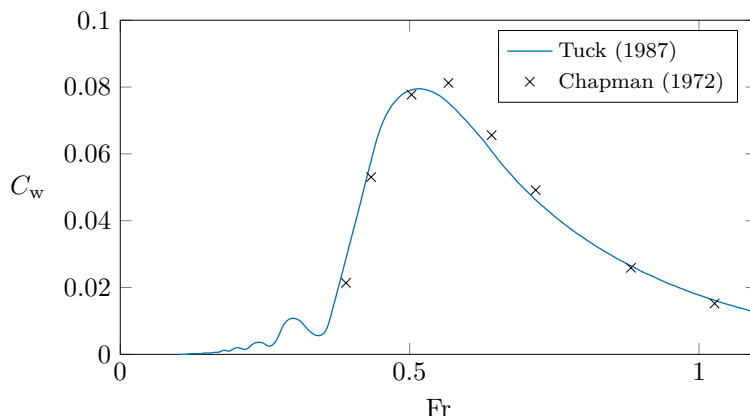
Figure 1.13: Wave-drag coefficient C_{w} as a function of the Froude number Fr predicted theoretically by [32] together with experimental data points from [31] (black crosses). The hull has a parabolic shape with $\alpha = 6.7$ and $\beta = 2.3$.

Here we present the two leading theoretical models to compute the wave drag. The first one, developed by Havelock, represents the ship hull as a moving pressure disturbance [8, 25]; while the second one, developed by Michell, solves, in the limit of slender hulls, the linearised potential flow problem with a distribution of sources along the centerplane of the ship [7, 28, 30, 33].

For both models, the frame of reference is attached to the hull, so that the flow is in the x direction. The fluid is assumed to be steady, inviscid, incompressible and irrotational. Such a flow can be described as a potential flow [14]. That is, there exists a potential Φ satisfying $\boldsymbol{u} = \boldsymbol{\nabla}\Phi$. Using incompressibility, $\boldsymbol{\nabla} \cdot \boldsymbol{u} = 0$, it follows that Φ solves the Laplace equation:

$$\boldsymbol{\nabla}^2 \Phi = 0 \ . \tag{1.23}$$

The velocity component along the x direction is written:

$$\Phi_x = U + \tilde{\Phi}_x \ , \tag{1.24}$$

with $\tilde{\Phi}_x \ll U$. Note that, f_x denotes the derivative of the function $f(x)$ with respect to the variable x, that is $f_x = \partial f / \partial x$. The water interface is described by the function $z = Z(x, y)$.

1.6.2 Havelock's model

As mentioned before, in Havelock's model the ship hull is replaced by a moving surface pressure disturbance $p(x, y)$ [8, 23, 25]. It is somewhat tantamount to considering that there is a cover applying the pressure p on the whole water surface (with p decaying far from the disturbance). This model allows to compute the far-field wave pattern as well as the wave resistance [23, 34, 35].

1.6.2.1 Model assumptions

Boundary conditions. Ensuring that water particles do not cross the air-water interface yields the kinematic condition:

$$\Phi_z = \Phi_x Z_x + \Phi_y Z_y \ . \tag{1.25}$$

The Bernoulli equation at the air-water interface is written:

$$p + \frac{1}{2}\rho[\Phi_x^2 + \Phi_y^2 + \Phi_z^2] + \rho g Z = p_0 + \frac{1}{2}\rho U^2 \ , \tag{1.26}$$

with p_0 the atmospheric pressure.

For an infinitely deep fluid, we further have:

$$\lim_{z \to -\infty} \Phi_z = 0 \ , \tag{1.27}$$

while, for a fluid of finite depth h, this condition would be replaced by $\Phi_z(z = -h) = 0$.

The last condition is the radiation condition:

$$\lim_{x \to -\infty} \sqrt{x^2 + y^2}[\Phi_x^2 + \Phi_y^2 + \Phi_z^2 - U^2] = 0 \ . \tag{1.28}$$

This condition ensures that the velocity potential vanishes in the far-field upstream of the boat.

Linearisation. The combination of the linearised kinematic and dynamic conditions at the water surface (1.25, 1.26) yields:

$$\Phi_z + \frac{U^2}{g}\Phi_{xx} + \frac{U}{\rho g}p_x = 0 \ , \tag{1.29}$$

while the linearisation of Eq. (1.25) alone gives $\Phi_z = U Z_x$.

1.6.2.2 Wave displacement

Taking the Fourier transform of Eq. (1.23), combining it with the boundary conditions and writing: $P(x, y, t) = e^{\varepsilon t} p(x, y)$ (with $\varepsilon \to 0$) to ensure the radiation condition, one finds [23]:

$$Z(x, y) = -\lim_{\varepsilon \to 0} \frac{1}{4\pi^2 \rho} \iint \frac{k\, \hat{p}(k_x, k_y) e^{-i(k_x x + k_y y)}}{gk - U^2 k_x^2 + 2i\, \varepsilon\, U\, k_x}\, \mathrm{d}k_x\, \mathrm{d}k_y \ , \tag{1.30}$$

where $\hat{p}(k_x, k_y)$ is the Fourier transform of the pressure field $p(x, y)$ and $k = [k_x^2 + k_y^2]^{1/2}$. Interestingly, one can notice that, in the expression of the wave displacement, appears the ratio between the pressure source term and the dispersion relation. The wave displacement is therefore maximum when the pressure source term resonates with the dispersion relation.

In dimensionless form, using $\hat{p} = \rho g \ell^3 \tilde{\hat{p}}$, $k_x = \tilde{k}_x/\ell$, $k_y = \tilde{k}_y/\ell$, $k = \tilde{k}/\ell$, $\varepsilon = \tilde{\varepsilon}\sqrt{g/\ell}$, and $Z = \tilde{Z}\ell$, one obtains:

$$\tilde{Z}(\tilde{x}, \tilde{y}) = -\lim_{\tilde{\varepsilon} \to 0} \frac{1}{4\pi^2} \iint \frac{\tilde{k}\, \tilde{\hat{p}}(\tilde{k}_x, \tilde{k}_y) e^{-i(\tilde{k}_x \tilde{x} + \tilde{k}_y \tilde{y})}}{\tilde{k} - \mathrm{Fr}^2 \tilde{k}_x^2 + 2i\, \tilde{\varepsilon}\, \mathrm{Fr}\, \tilde{k}_x}\, \mathrm{d}\tilde{k}_x\, \mathrm{d}\tilde{k}_y \ . \tag{1.31}$$

1.6.2.3 Wave resistance

According to [8, 25], the wave resistance is the sum of all the pressure contributions at the interface in the x direction, that is:

$$R_{\mathrm{w}} = -\iint p(x, y) Z_x(x, y)\, \mathrm{d}x\, \mathrm{d}y \ . \tag{1.32}$$

After injecting the wave displacement Z from Eq. (1.30) into Eq. (1.32), one finds:

$$R_{\mathrm{w}} = \lim_{\varepsilon \to 0} \frac{1}{4\pi^2 \rho} \iint \frac{i\, k_x\, k |\hat{p}(k_x, k_y)|^2}{gk - U^2 k_x^2 + 2i\, \varepsilon\, U\, k_x}\, \mathrm{d}k_x\, \mathrm{d}k_y \ . \tag{1.33}$$

Using the dimensionless parameters introduced before, the wave drag coefficient is written:

$$\frac{R_{\mathrm{w}}}{\rho g \ell^3} = \lim_{\tilde{\varepsilon} \to 0} \frac{1}{4\pi^2} \iint \frac{i\, \tilde{k}_x\, \tilde{k} |\tilde{\hat{p}}(\tilde{k}_x, \tilde{k}_y)|^2}{\tilde{k} - \mathrm{Fr}^2 \tilde{k}_x^2 + 2i\, \tilde{\varepsilon}\, \mathrm{Fr}\, \tilde{k}_x}\, \mathrm{d}\tilde{k}_x\, \mathrm{d}\tilde{k}_y \ . \tag{1.34}$$

1.6.2.4 Limitations of Havelock's model

Havelock provides a nice theory to model the wave pattern of ships. It is however too simple to account for the exact shape of the hull and especially to study the effect of the draft. In particular, it is quite difficult to predict theoretically the pressure field $p(x, y)$ to be injected in the formulas, which itself should depend on the hull shape and on its velocity U.

1.6.3 Michell's model

Michell developed a model to predict the wave resistance for slender ships [7, 28, 30, 33]. This model is based on solving the linearised potential flow problem with a distribution of sources on the centerplane of the hull.

1.6.3.1   Model assumptions

Following [7, 28, 36], we rewrite the boundary conditions and the assumptions made to derive Michell's model.

Boundary conditions. The condition that water particles do not cross the hull boundary is written:

$$\Phi_y = \Phi_x f_x + \Phi_z f_z \ . \tag{1.35}$$

Similarly, ensuring that water particles do not cross the air-water interface yields the kinematic condition given in Eq. (1.25). The Bernoulli equation at the air-water interface is written:

$$p_0 + \frac{1}{2}\rho \boldsymbol{u}^2 + \rho g Z = p_0 + \frac{1}{2}\rho U^2 \ , \tag{1.36}$$

with p_0 the atmospheric pressure. It is then straight-forward to obtain the dynamic condition:

$$2gZ + \Phi_x^2 + \Phi_y^2 + \Phi_z^2 = U^2 \ . \tag{1.37}$$

For an infinitely deep fluid, we further have the condition given in Eq. (1.27) (which is replaced by $\Phi_z(z = -h) = 0$ for a fluid of finite depth h). The last condition to ensure is the radiation condition given in Eq. (1.28).

Linearisation. The main assumption of Michell's model is to consider that the hull is thin ($w \ll \ell$, corresponding to small longitudinal slopes $f_x, \ f_z \ll 1$).

The linearisation of the kinematic condition on the hull boundary (1.35) leads to:

$$\Phi_y(x, \pm 0, z) = \pm U f_x \ . \tag{1.38}$$

The combination of the linearised kinematic and dynamic conditions (1.25, 1.37) gives on $z = 0$:

$$k_0 \Phi_z(x, y, 0) + \Phi_{xx}(x, y, 0) = 0 \ , \tag{1.39}$$

where $k_0 = g/U^2$.

Michell solves the Laplace equation (1.23) with the boundary conditions given in Eqs. (1.27, 1.28) and Eqs. (1.38, 1.39) using Fourier-transform methods.

1.6.3.2   Derivation of the wave resistance

Following [37] (p.579, see also [7, 30, 36]), the linearised potential flow problem is solved by distributing sources of strength $U f_x/(2\pi)$ on the centerplane projection of the hull, denoted S_0 (see Fig. 1.12). The velocity potential can then be obtained through:

$$\Phi(x, y, z) = \frac{U}{2\pi} \iint_{S_0} f_\xi(\xi, \zeta) \times G(x, y, z, \xi, 0, \zeta) \, \mathrm{d}\xi \mathrm{d}\zeta \ , \tag{1.40}$$

where $G(x, y, z, \xi, \eta, \zeta)$ is the Green function corresponding to the potential created by a source at point (ξ, η, ζ) satisfying all the boundary conditions except Eq. (1.38). The expression of G can be obtained by Fourier transform and is given in [37] (p.484) for an

infinitely deep fluid:

$$
\begin{aligned}
G(x, y, z, \xi, \eta, \zeta) = &\frac{1}{r_-} - \frac{1}{r_+} \\
&- \frac{4k_0}{\pi} \int_0^{\frac{\pi}{2}} \mathrm{d}\theta \, \sec^2\theta \!\!\!\!\fint_0^{+\infty} \mathrm{d}k \, \frac{e^{k(z+\zeta)}}{k - k_0 \sec^2\theta} \cos[k(x-\xi)\cos\theta] \cos[k(y-\eta)\sin\theta] \\
&+ 4k_0 \int_0^{\frac{\pi}{2}} \mathrm{d}\theta \, \sec^2\theta \, e^{k_0(z+\zeta)\sec^2\theta} \sin[k_0(x-\xi)\sec\theta] \cos[k_0(y-\eta)\sin\theta\sec^2\theta] \,, \quad (1.41)
\end{aligned}
$$

with $r_\pm = \sqrt{(x-\xi)^2 + (y-\eta)^2 + (z\pm\zeta)^2}$ and where the dashed integral in the third term of G is a Cauchy principal value integral.

In Eq. (1.41), the first term corresponds to the classic potential for a point source in an infinite fluid. The next three terms are added to ensure that the linearized free-surface conditions and the conditions at infinity are satisfied. In particular, the second term corresponds to the potential of a second point source being the mirror of the first one with respect to the plane $z = 0$.

The wave resistance $R_\mathrm{w}(f)$ is calculated from the velocity potential Φ given in Eq. (1.40) using:

$$
R_\mathrm{w}(f) = - \iint_{S_w} p n_x \, \mathrm{d}S \simeq -2 \iint_{S_0} p n_x \, \mathrm{d}S \,, \tag{1.42}
$$

where $n_x = -f_x$ and the pressure p is obtained from the linearised Bernoulli equation: $p = \rho U \Phi_x$. Thus, one has:

$$
R_\mathrm{w}(f) = \frac{\rho U^2}{\pi} \iint_{S_0} \mathrm{d}x \mathrm{d}z \, f_x(x, z) \iint_{S_0} \mathrm{d}\xi \mathrm{d}\zeta \, f_\xi(\xi, \zeta) G_x(x, 0, z, \xi, 0, \zeta) \,. \tag{1.43}
$$

One can notice that the first three terms of G_x are odd in $(x-\xi)$ and the fourth one is even in $(x-\xi)$. Consequently, thanks to the symmetry of $R_\mathrm{w}(f)$ with respect to (x, z) and (ξ, ζ) (see Eq. (1.43)), only the even term will give a non-zero contribution to $R_\mathrm{w}(f)$. One then obtains:

$$
\begin{aligned}
R_\mathrm{w}(f) = \frac{4k_0^2 \rho U^2}{\pi} \iint_{S_0} \mathrm{d}x \mathrm{d}z \, f_x(x, z) \iint_{S_0} \mathrm{d}\xi \mathrm{d}\zeta \, f_\xi(\xi, \zeta) \\
\times \int_0^{\frac{\pi}{2}} \mathrm{d}\theta \, \sec^3\theta \, e^{k_0(z+\zeta)\sec^2\theta} \cos[k_0(x-\xi)\sec\theta] \,. \quad (1.44)
\end{aligned}
$$

Finally, letting $\lambda = \sec\theta$, using Euler's formula and integrating by parts, one finds:

$$
R_\mathrm{w}(f) = \frac{4\rho U^2}{\pi \ell^4 \mathrm{Fr}^8} \int_1^{+\infty} |\mathcal{I}_f(\lambda, \mathrm{Fr})|^2 \frac{\lambda^4}{\sqrt{\lambda^2 - 1}} \, \mathrm{d}\lambda \,, \tag{1.45}
$$

where:

$$
\mathcal{I}_f(\lambda, \mathrm{Fr}) = \int_{-d}^0 \mathrm{d}z \int_{-\frac{\ell}{2}}^{\frac{\ell}{2}} f(x, z) e^{\lambda^2 z/(\ell \mathrm{Fr}^2)} e^{i\lambda x/(\ell \mathrm{Fr}^2)} \, \mathrm{d}x \,. \tag{1.46}
$$

The wave drag coefficient for infinite depth C_w in dimensionless form then reads:

$$
C_\mathrm{w}(\mathrm{Fr}, \alpha, \beta) = \frac{4\beta^{2/3}}{\pi \alpha^{4/3} \mathrm{Fr}^8} \int_1^{+\infty} |\tilde{\mathcal{I}}_{\tilde{f}}(\lambda, \mathrm{Fr}, \beta)|^2 \frac{\lambda^4}{\sqrt{\lambda^2 - 1}} \, \mathrm{d}\lambda \,, \tag{1.47}
$$

where:

$$\tilde{\mathcal{I}}_{\tilde{f}}(\lambda, \mathrm{Fr}, \beta) = \int_{-\frac{1}{\beta}}^{0} \mathrm{d}\tilde{z} \int_{-\frac{1}{2}}^{\frac{1}{2}} \tilde{f}(\tilde{x}, \tilde{z}) e^{\lambda^2 \tilde{z}/\mathrm{Fr}^2} e^{i\lambda \tilde{x}/\mathrm{Fr}^2} \, \mathrm{d}\tilde{x} \ . \tag{1.48}$$

Finite depth. In the case of a fluid of finite depth h, the Green function given in Eq. (1.41) must be replaced (see [30, 37]). The wave drag then has a more complicated expression that can be found in [37] (p.581):

$$\mathcal{R}_{\mathrm{w}}(f, h) = \frac{2\rho U^2}{\pi \ell^2 \mathrm{Fr}^4} \int_{k_h}^{+\infty} |\mathcal{J}_f(k, \mathrm{Fr}, h)|^2 \frac{k^{3/2} \tanh(kh)}{\sqrt{k - k_0 \tanh(kh)}} \, \mathrm{d}k \ , \tag{1.49}$$

where $k_0 = g/U^2$, k_h is the solution of the dispersion relation: $k_h = k_0 \tanh(k_h h)$ (with $k_h \geq 0$) and where:

$$\mathcal{J}_f(k, \mathrm{Fr}, h) = \int_{-d}^{0} \mathrm{d}z \int_{-\frac{\ell}{2}}^{\frac{\ell}{2}} f(x, z) \frac{\cosh[k(z+h)]}{\cosh(kh)} e^{ix\sqrt{k_0 k \tanh(kh)}} \, \mathrm{d}x \ . \tag{1.50}$$

Note that k can be considered as a wave number.

Introducing the ratio $\gamma = h/\ell$, the wave drag coefficient in finite depth, denoted $\mathcal{C}_{\mathrm{w}}$, reads:

$$\mathcal{C}_{\mathrm{w}}(\mathrm{Fr}, \alpha, \beta, \gamma) = \frac{2\beta^{2/3}}{\pi \alpha^{4/3} \mathrm{Fr}^4} \int_{\tilde{k}_h}^{+\infty} |\tilde{\mathcal{J}}_{\tilde{f}}(k, \mathrm{Fr}, \beta, \gamma)|^2 \frac{\tilde{k}^{3/2} \tanh(\tilde{k}\gamma)}{\sqrt{\tilde{k} - \tanh(\tilde{k}\gamma)/\mathrm{Fr}^2}} \, \mathrm{d}\tilde{k} \ , \tag{1.51}$$

where $\tilde{k}_h$ is the solution of the dispersion relation: $\tilde{k}_h = \tanh(\tilde{k}_h \gamma)/\mathrm{Fr}^2$ ($\tilde{k}_h \geq 0$) and where:

$$\tilde{\mathcal{J}}_{\tilde{f}}(k, \mathrm{Fr}, \beta, \gamma) = \int_{-\frac{1}{\beta}}^{0} \mathrm{d}\tilde{z} \int_{-\frac{1}{2}}^{\frac{1}{2}} \tilde{f}(\tilde{x}, \tilde{z}) \frac{\cosh[\tilde{k}(\tilde{z}+\gamma)]}{\cosh(\tilde{k}\gamma)} e^{i\tilde{x}\sqrt{\tilde{k}\tanh(\tilde{k}\gamma)}/\mathrm{Fr}} \, \mathrm{d}\tilde{x} \ . \tag{1.52}$$

The expression of the wave drag coefficient in infinitely deep fluid (corresponding to $\gamma \to \infty$) is recovered from these equations by the change of variable $\tilde{k} = \lambda^2/\mathrm{Fr}^2$.
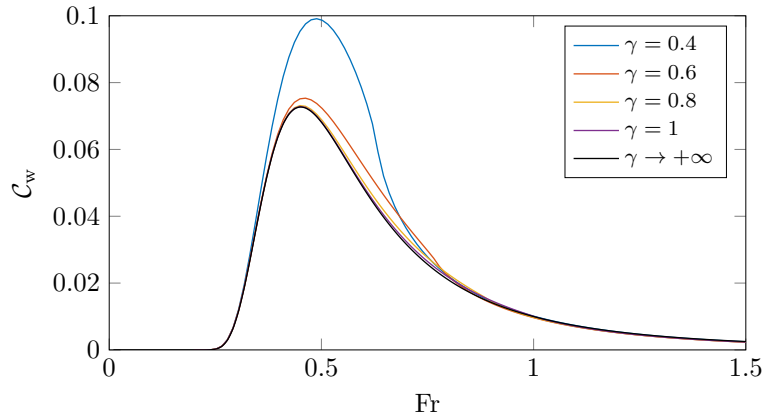
Figure 1.14: Wave drag coefficient $\mathcal{C}_{\mathrm{w}}$ as a function of the Froude number Fr predicted by Michell's model for increasing water depth $\gamma = h/\ell$ (for $\alpha = 6.7$, $\beta = 2.3$ and $\tilde{f} = 1/2 \exp(-16\tilde{x}^2)$). The black curve corresponds to the infinite depth case.

The wave drag coefficient $\mathcal{C}_{\mathrm{w}}$ can be computed numerically from Eqs. (1.51, 1.52). Fig. 1.14 shows the evolution of this coefficient with the Froude number for different values of the

ratio $\gamma = h/\ell$ and a gaussian hull profile (see Eq. (3.4) in Sect. 3.3). Differences with the curve for infinite depth (black curve) are observed in the range Fr $\in [0.4, 0.8]$ for $\gamma < 1$. As a result, the bottom of a water tank starts having an effect on the wave drag for $h \leq \ell$.

1.7   Unsteady forces

In the case of an unsteady motion, supplementary forces come into play: the added mass force, denoted R_{a}, and a history force, known as the Basset force, denoted R_{b}, which is usually neglected at high Reynolds number.

1.7.1   Added mass force

The added mass force is typically written:

$$R_{\mathrm{a}} = -m_{\mathrm{a}} \frac{\mathrm{d}U}{\mathrm{d}t} \ , \tag{1.53}$$

where $U(t)$ is now the instantaneous velocity of the object and m_{a} is the added mass of the object, which is defined as the mass of fluid that the object accelerates (or decelerates) during its motion. In the resulting dynamics of the object, it is as if the mass of the object was supplemented by the quantity m_{a}. In a more general way, an added mass matrix $\mathrm{M}_{\mathrm{a}} = (m_{ij})_{1 \leq i \leq 6, 1 \leq j \leq 6}$ can be defined [27]. The 6 dimensions correspond to the translations in the 3 spatial directions and the rotations about these 3 directions. Fig. 1.15 gives the added masses along the horizontal and vertical directions for a cylinder, an elliptical cylinder and a plate. It can be noticed that these three objects have the same added mass per unit length in the vertical direction – equal to ρ times the surface of the disk of radius a – but a different one in the horizontal direction. The added mass can thus generally be defined as the mass of fluid contained in the cylinder of diameter given by the extension of the object in the direction perpendicular to the flow.

m_{11}:	$\pi\rho a^2$	$\pi\rho b^2$	0
m_{22}:	$\pi\rho a^2$	$\pi\rho a^2$	$\pi\rho a^2$
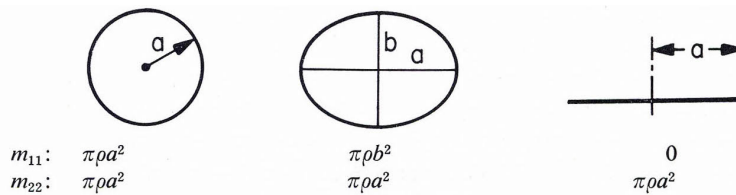
Figure 1.15: Added mass per unit length for various two-dimensional bodies. m_{11} is the added mass in the horizontal direction and m_{22} in the vertical direction. Reprinted from [27].

1.7.2   Basset force

The Basset force, which appears when an object is accelerating in a fluid, is related to the lagging boundary layer development with a varying flow velocity [38, 39].

In the viscous regime, this force has two components in phase quadrature: one, denoted R_{b}', is proportional to the fluid velocity and the other, denoted R_{b}'', is proportional to the fluid acceleration. One can show that these two components have the same dependence with the

parameters of the problem [40]. For a flat plate moving in a fluid, one can write:

$$R'_\mathrm{b} \sim R''_\mathrm{b} \sim \frac{\mu a \omega S}{\delta} \;, \tag{1.54}$$

with a the characteristic distance of oscillation of the plate, $\omega = 2\pi f$ the angular frequency of oscillation, S the wetted surface and $\delta \sim \sqrt{\mu/(\rho\omega)}$ the thickness of the boundary layer associated with the oscillations.

We further model the speed of the plate as: $U = \langle U \rangle (1 + \Delta U / \langle U \rangle \cos(\omega t))$ with $\langle U \rangle$ the mean speed and ΔU the amplitude of the fluctuations of speed. Then, one can compare the two components of the Basset force with in-phase drag terms: that is R'_b with R_s, the skin drag, and R''_b with R_a, the added mass force. One has:

$$\frac{R'_\mathrm{b}}{R_\mathrm{s}} \quad \sim \quad \frac{\mu a \omega S}{\delta} \times \frac{1}{\rho S \langle U \rangle^2} \sim \frac{\Delta U / \langle U \rangle}{\mathrm{Re}_\delta} \;, \tag{1.55a}$$

$$\frac{R''_\mathrm{b}}{R_\mathrm{a}} \quad \sim \quad \frac{\mu a \omega S}{\delta} \times \frac{1}{\rho \Omega_\mathrm{a} a \omega^2} \sim \frac{\delta}{d} \;, \tag{1.55b}$$

where $\mathrm{Re}_\delta = \rho \delta \langle U \rangle / \mu$ is the Reynolds number in the boundary layer and $\Omega_\mathrm{a} = m_\mathrm{a}/\rho \sim \Omega$ the volume corresponding to the added mass. For a rowing boat (see Chap. 2), one finds: $R'_\mathrm{b}/R_\mathrm{s} \simeq 10^{-4}$ and $R''_\mathrm{b}/R_\mathrm{a} \simeq 2 \cdot 10^{-2}$, so that the Basset force can be neglected.

1

Take home message of Chapter 1

When an object (such as a ship or a duck) moves **steadily** at the water surface at high Reynolds number, it experiences three main components of drag:

1. Skin friction is related to the friction of water particles along the surface of the object. It scales with the wetted surface and with the speed as $U^{3/2}$ in the laminar regime and U^2 in the turbulent regime.

2. Pressure drag (or form drag) is due to the separation of the boundary layer and the formation of vortices at the rear of the object. It is the resulting force of all the pressure forces exerted on the surface of the object in the absence of waves. It scales with the cross-sectional area of the object and with the speed as U^2.

3. Wave drag appears when the object moves at or close to the air-water interface because of the generation of surface waves. This drag component highly depends on the Froude number: $\mathrm{Fr} = U/\sqrt{g\ell}$ where ℓ is the length of the object in the direction of motion. The wave drag coefficient shows a non monotonic evolution with the Froude number, with a maximum around $\mathrm{Fr} \simeq 0.5$.

When an object accelerates in a fluid, it is subjected to (i) the **added mass force**, which is proportional to the acceleration of the object and the mass of the fluid accelerated and (ii) the **Basset force**, which is usually neglected at high Reynolds number.

2

ROWING BASICS AND KINEMATICS

Rowing is a challenging sport, not only for athletes but also for physicists. This sport mixes physiology, mechanics and fluid dynamics, making it much more complex than it seems. Thus, many scientists tried to figure out the details of rowing propulsion, in particular, with a view to improving the performance of rowing crews. In rowing, three main parts can be distinguished: the rowing boat, the oars and the rowers. Looking at the kinematics of these different elements gives very interesting information to understand the mechanics of rowing. In this chapter, we first introduce the basics of rowing. Then, the kinematics of the boat, the blades and the rowers are analysed with experiments and video analysis. Finally, a model for the drag on a rowing boat is suggested and validated by experiments and previous studies.

Picture of a water strider, a kind of "capillary rower". Source: [41].

Contents

2.1 The basics of rowing

In this section, we introduce the very basics of rowing with the definition of some vocabulary specific to rowing.

2.1.1 Rowing equipment

The two essential equipments in rowing are the rowing boat and the oars. As expected, these two equipments change from one rowing category to another (see Fig. 2.1). There are different rowing categories depending mostly on the number of rowers (typically 1, 2, 4 or 8) and on the number of oars per rower: the rowing boat is called a *sculling* boat when each rower has two oars and a *sweep* boat when each rower has one oar. Additional categories for sweep boats with 2 and 4 rowers depend on whether there is a coxswain[1] on the boat. Obviously, and as sketched in Fig. 2.1, the boat geometry depends on the rowing category: the boat length ranges from 8 m for a *single scull* (Fig. 2.1(a)) to 18 m for an *eight* (Fig. 2.1(f)).
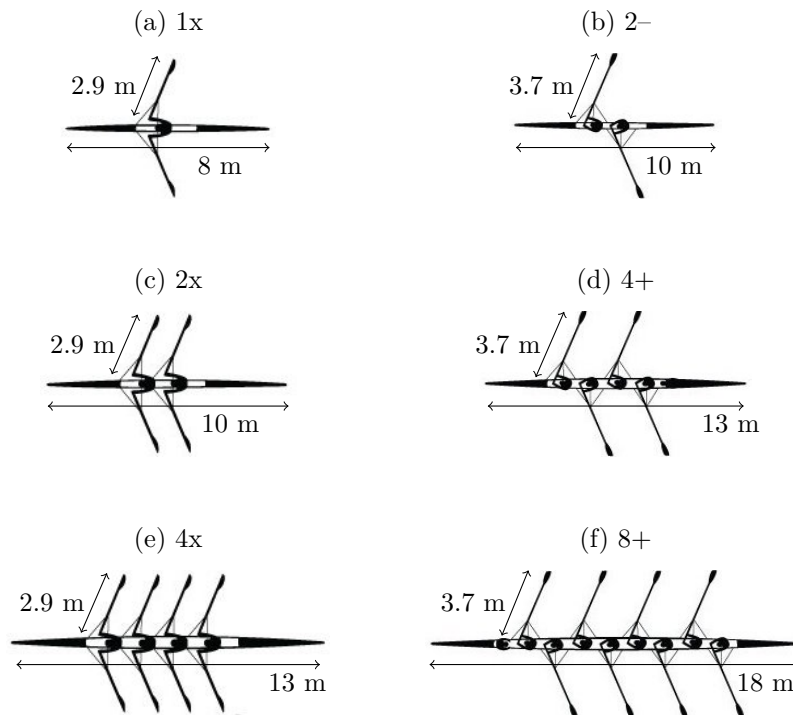
Figure 2.1: Schematics of the different rowing categories with indications of the typical lengths of the boats and the oars. The boats in the first column (a, c, e) are sculling boats (each rower has two oars), while the boats in the second column (b, d, f) are sweep boats (each rower has one oar). The categories in (b) and (d) exist with or without a coxswain. Note that, in the abbreviation of the boat category (*i.e.* 1x or 2–), the number indicates the number of rowers, the symbol x stands for sculling boats, the symbol – stands for a sweep boat without coxswain and the symbol + stands for a sweep boat with coxswain. See also Table 2.1 for details on the geometry of the different rowing boats.

The length, width and mass of rowing boats in the different rowing categories are given in Table 2.1. From these data, we can here point out one of the interesting particularities

---

[1]A coxswain is "a steersman of a racing shell who usually directs the rowers", according to Merriam-Webster dictionary.

of rowing boats: their length-to-width aspect ratio is very large (around 30 for all boat categories).

Boat Abbreviation	Boat Name	ℓ (m)	w (cm)	m_{boat} (kg)	M (kg)	$\langle U \rangle$ (m/s)
1x	Single Scull	8.1	28.2	14	104	5.08
2x	Double Scull	10	33.5	27	207	5.56
2–	Coxless Pair	10	33.5	27	207	5.43
4x	Quadruple Scull	12.8	41	52	412	6.02
4–	Coxless Four	12.7	42	50	410	5.92
8+	Coxed Eight	17.7	55.6	97	850	6.26

Table 2.1: Characteristics of current racing boats. The geometry characteristics and mass are for boats from *Filippi* supplier [42]. The mean boat speed $\langle U \rangle$ given in the table is the world record speed in each category.

Let us now give more details on the main parts of a rowing boat. Fig. 2.2(a) gives a detailed picture of a *coxless pair* rowing boat. In particular, one can see the sliding seat on which the rower sits with his feet attached to the boat through the foot stretcher system. The sliding seat allows the rower to use the strong muscles from the legs in addition to the muscles of the trunk and the arms to propel the boat. This feature together with the fact that rowers are facing the stern of the boat distinguish rowing from canoeing or kayaking.
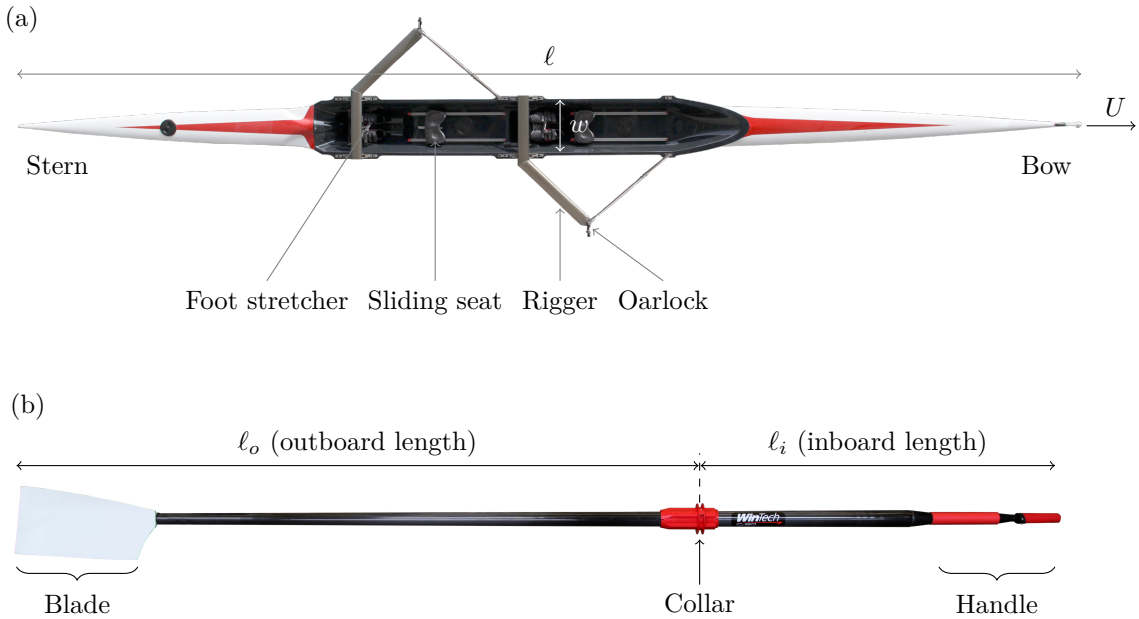
Figure 2.2: (a) Picture of a *coxless pair* rowing boat (category 2–) with the definition of some important parts of the boat. (b) Picture of a rowing oar with the definition of its main components. In particular, the oar rotates about the collar, which is attached to the oarlock of the boat (defined in (a)).

The oar is linked to the boat at the level of the collar (see Fig. 2.2(b)) via the oarlock, allowing the oar to rotate, while transmitting the force resulting from the action of the rower to the boat. The ratio between the outboard length ℓ_o and the inboard length ℓ_i, denoted η, is about 2.2 whatever the rowing category. However, Fig. 2.1 highlights that the total length of the oars depends on the rowing category: the ones used in sweep boats

are longer (total length of about 3.7 m) than the ones used in sculling boats (about 2.9 m). Fig. 2.3 illustrates different kinds of blades (from *Concept2* supplier [43]). The *Macon* blade (Fig. 2.3(a)) is the old blade model, while the *Big* blade (Fig. 2.3(b)) and the *Smoothie2 Plain Edge* blade (Fig. 2.3(c)) are models currently used in competitions.

(a)   (b)   (c)
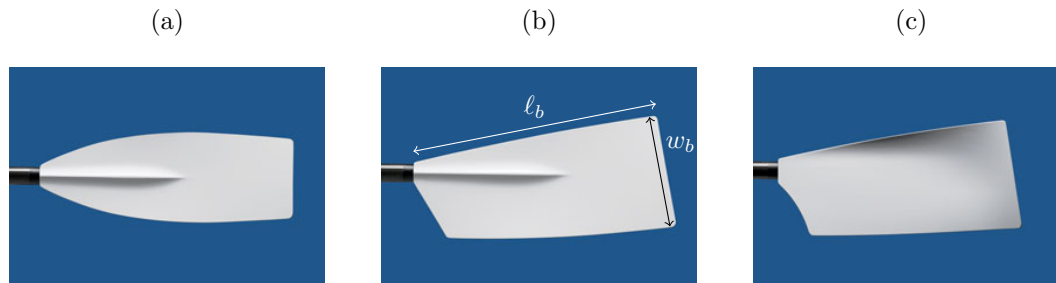
Figure 2.3: (a) Front view of a *Macon* blade, (b) a *Big* blade and (c) a *Smoothie2 Plain Edge* blade. We denote ℓ_b the length of the blade and w_b the width of the blade at the broadest point (see Table 2.2 for the values of ℓ_b and w_b for the different blades). Pictures taken from [43].

Denoting ℓ_b the length of the blade and w_b the width of the blade at the broadest point (see Fig. 2.3(b)), it appears that these two dimensions also depend on the boat category. The sculling blades are smaller – about 45 cm × 21 cm – than sweep blades – about 55 cm × 25 cm (see Table 2.2 for the details on the different blades geometry).

| Blade name	Boat category	ℓ_b (cm)	w_b (cm)	S_{bl} (m^2)
Macon blade	Sweep	58	21	0.12
Macon blade	Scull	50	18	0.09
Big blade	Sweep	55.5	25	0.14
Big blade	Scull	44	21.5	0.095
Smoothie2 Plain Edge blade	Sweep	54.5	25.5	0.14
Smoothie2 Plain Edge blade	Scull	46	21.5	0.10

Table 2.2: Characteristics of current blades from *Concept2* supplier [43]. w_b is the width of the blade at the broadest point and thus the blade surface $S_{bl} = \ell_b w_b$ is slightly overestimated.

2.1.2   The rowing technique

The rowing cycle is made of two phases: the power stroke during which the blades are inside water and propel the boat, and the recovery stroke during which the rower comes back to its initial position, with the blades out of the water, before starting again a new cycle. Fig. 2.4 illustrates the rowing cycle with time-lapse photographies from the training of the French athlete Thomas Baroukh. The first four pictures were taken during the power stroke and the last four pictures during the recovery stroke. From a technical point of view, there are two very important moments in this cycle: the beginning of the power stroke, called the *catch*, when the blades enter the water (see picture (1) in Fig. 2.4) and the end of the power stroke, called the *release*, when the blades go out of water (see picture (4) in Fig. 2.4).

This decomposition into a propulsive stroke and a recovery stroke is quite common in animal locomotion: for instance, it is observed at small scales for the biflagellate alga Chlamydomonas reinhardtii [44, 45] or, at larger scales, for water striders [46, 47] or fishing spiders
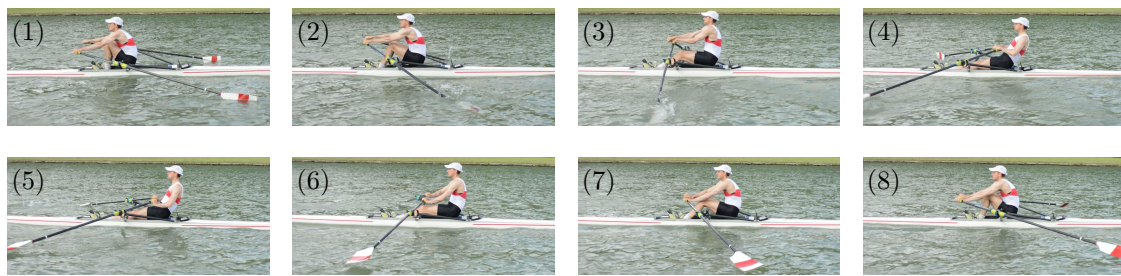
Figure 2.4: Time-lapse photographies of the rowing cycle for the French athlete Thomas Baroukh. Pictures (1) to (4) correspond to the power stroke, while pictures (5) to (8) correspond to the recovery stroke. The pictures were taken during a training on the *Grand canal* of Versailles. The time between two consecutive pictures is 0.3 s.

[48, 49], which could be seen as "capillary rowers". Fig. 2.5, reprinted from [48], shows that the fishing spider *Dolomedes triton* relies on two pairs of legs (out of four), activated synchronously, to propel itself at the surface of water. This stroke is somehow similar to the rowing stroke, even though the propulsive mechanism, involving capillary effects, is different.
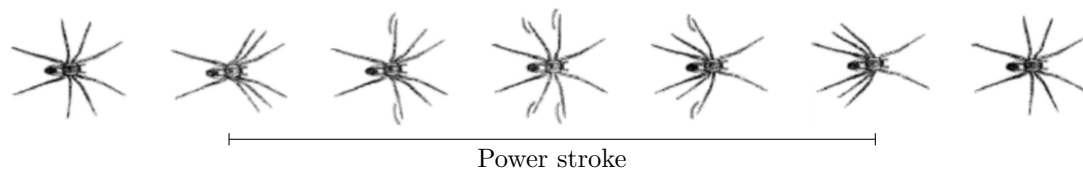
Power stroke

Figure 2.5: Time-lapse pictures of the propulsive stroke of the fishing spider *Dolomedes triton* including the power stroke and the recovery stroke. The drawings, adapted from [48], were obtained from video images. The time between two consecutive pictures is about 20 ms.

As mentioned before, during the rowing stroke, the rower uses the muscles of different segments: the legs, the trunk and the arms. A common rule among coaches is, for the power stroke, to use first the legs, then the trunk and finally the arms to move the blade in water, and to proceed in the reverse order for the recovery stroke. This is the general rule but there still exist different rowing styles – basically four (DDR, Rosenberg, Adam and Grinko styles) [50] – as illustrated in Fig. 2.6. These four different rowing styles are distinguished by looking, firstly, at the travel of the trunk compared to the travel of the legs, and secondly, at whether the motion of the trunk and the motion of the legs are simultaneous. This eventually shows the great complexity of the rowing technique.

2.1.3 Rowing in competition

Rowing competitions are typically run on a 2000 m distance. At a rowing frequency f of 30 to 40 strokes per minute depending on the rowing category, the fastest boats for men run this distance in 6 min 30 s for single sculls (M1x) and in 5 min 18 s for *eight* rowing boats (M8+), corresponding to mean velocities between 5.1 and 6.3 m/s. For women, the world record is 7 min 7 s for single sculls (W1x) and 5 min 54 s for *eight* rowing boats (W8+), corresponding to mean velocities between 4.7 and 5.6 m/s.
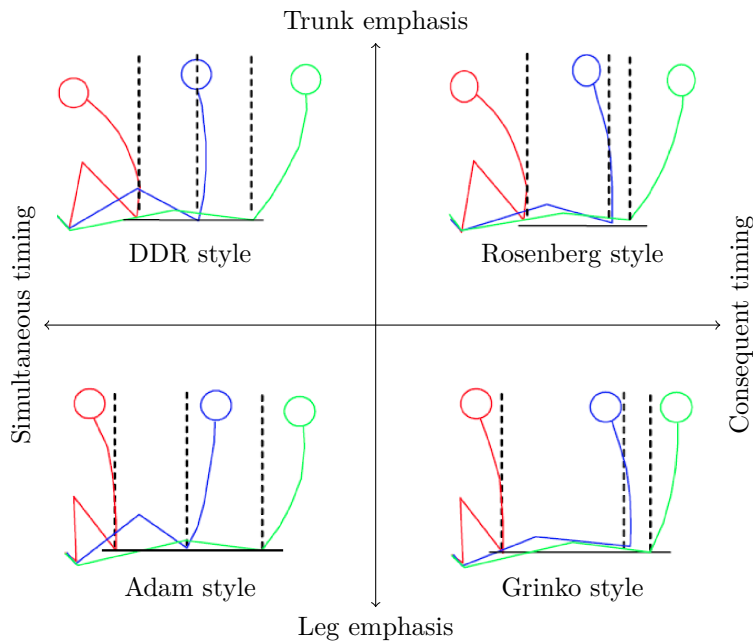
Figure 2.6: Schematics of the four main rowing styles. These styles depend on whether the emphasis is on the motion of the legs or of the trunk and whether the motion of the legs and the trunk are simultaneous or consequent. Schematics adapted from [50].

2.2 Analysis of the boat kinematics

Analysing videos from the rowing competitions at the Rio 2016 Olympics, we were able to estimate the instantaneous velocity of rowing boats of different categories (M1x, M4– and M8+) for a few rowing strokes. The evolution of the instantaneous velocity of a M4– rowing boat with time over about three strokes is represented in Fig. 2.7(a). We denote $\langle U \rangle$ the mean boat velocity over these three strokes, $f = 1/T$ the stroke frequency (with T the period of the stroke) and $2\Delta U$ the difference between the minimum and maximum velocities.[2]

Firstly, one can observe on the figure that the power stroke is shorter than the recovery stroke as it lasts about 40% of the total stroke. Secondly, as expected, the velocity increases during the power stroke (between the red and the green vertical dashed lines), but more surprisingly, it continues to increase during the first part of the recovery stroke before decreasing drastically. As will be seen in Chap. 6, this particular evolution of the hull velocity during the recovery phase is mostly related to the motion of the rowers on the boat. The whole dynamics of the rowing stroke thus leads to large fluctuations of the boat speed around the mean speed. For example, the velocity of the M4– rowing boat oscillates between 4.2 and 6.7 m/s for a mean velocity $\langle U \rangle = 5.6$ m/s. This corresponds to velocity fluctuations $\Delta U / \langle U \rangle \simeq 22\%$. Figs. 2.7(b) and (c) show that the mean velocity $\langle U \rangle$ as well as the stroke frequency f determined over a few strokes during the race, both tend to increase with the number of rowers. In Fig. 2.7(d), we compare the evolution of the boat velocity with time over one rowing stroke for the three rowing categories M1x, M4– and M8+, corresponding to an increasing number of rowers (1, 4 and 8). Very similar evolutions are observed provided that the time t and velocity U are rescaled by the period T and the mean speed $\langle U \rangle$ respectively.

---

[2]As will be discussed later, the mean velocity $\langle U \rangle$ and the stroke frequency f are changing during the race (see Fig. 2.8).
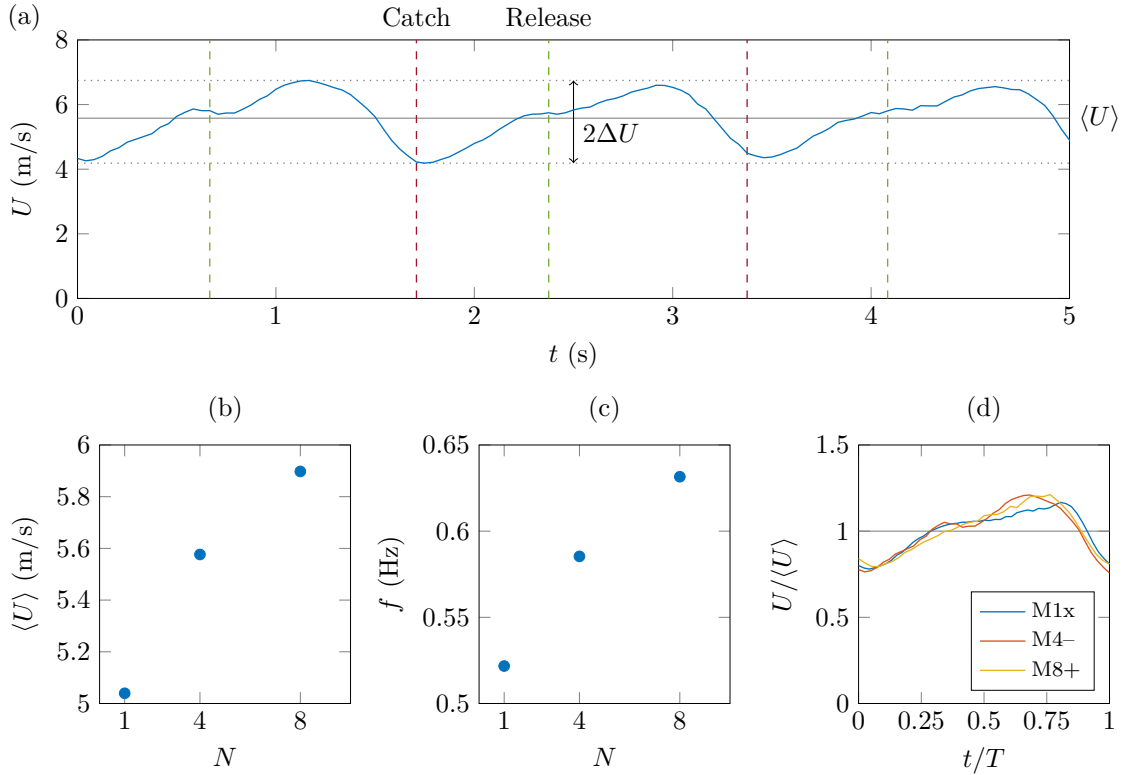
Figure 2.7: (a) Instantaneous velocity of a M4– rowing boat as a function of time for three strokes, obtained from image analysis of the video of the men coxless four Australian crew at the Rio 2016 Olympics. The vertical red dashed lines indicate the time of the catch (the blades enter the water) and the vertical green dashed lines indicate the time of the release (the blades go out of the water). The mean speed $\langle U \rangle$ is indicated with a gray horizontal line and the minimum and maximum speed values with dotted horizontal lines. (b) Mean boat velocity $\langle U \rangle$ over a few strokes depending on the number of rowers N. (c) Stroke rate f over a few strokes depending on the number of rowers N. (d) Dimensionless hull velocity $U/\langle U \rangle$ as a function of the dimensionless time t/T, where T is the period of the rowing cycle, for three different boats (M1x, M4– and M8+). The instantaneous velocity was obtained, in the same way as for (a), from image analysis of the videos of the different rowing competitions at the Rio 2016 Olympics.

Recently, the International Rowing Federation (also known as FISA, *Fédération Interna-tionale des Sociétés d'Aviron*) started collecting data during the world championships. The mean velocity $\langle U \rangle$ and stroke frequency f of each rowing boat every 50 m over the whole length of the race is available for each race [51]. We used the data available for the Lucerne 2016 world championship. In Fig. 2.8, the mean velocity and stroke frequency of the winner boat for four different rowing categories (M1x, M2–, M4– and M8+) is plotted as a function of the travelled distance (denoted X). For the M2–, M4– and M8+ categories, the trend is very similar: the mean velocity $\langle U \rangle$ increases very quickly during the first hundred meters of the race, it reaches a maximum around $X = 150$ m, then decreases to reach a fairly constant value and finally increases again during the last 500 m of the race. A similar evolution is observed for the stroke frequency f for the same categories: it is maximum at the beginning of the race, it then decreases to reach a plateau and eventually increases at the end of the race. The rowing strategy during the last 500 m of the race appears to be a little bit different for the winner boat of the *single scull* category as the mean boat speed and stroke rate decrease at the end of the race. This is probably related to the comfortable advance of
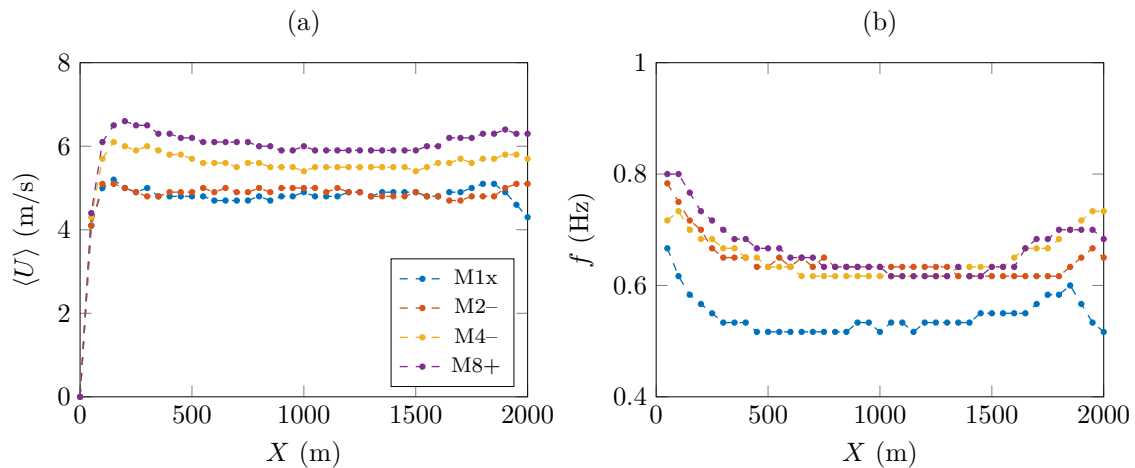
Figure 2.8: (a) Mean speed $\langle U \rangle$ over one cycle and (b) stroke rate f averaged over 50 m as a function of the distance X travelled during the race at the Lucerne 2016 world championship for the winner boat in four different rowing categories (M1x, M2–, M4– and M8+). Data extracted from [51].

the winner boat over the other boats in this particular race. The evolution of the velocity along the race, in particular with the existence of a maximum speed at the beginning of the race is fairly common among sports where a "long" distance has to be travelled in the least amount of time (*i.e.* swimming or running over long distances). It is in particular related to physiology and the change from anaerobic (short high intensity exercise) to aerobic (long low intensity exercise) metabolism [52, 53].

2.3 Analysis of the blade kinematics

This work was done with Alexis Goujon and Kozeta Tutulani (students from *Ecole polytechnique*).

Figure 2.9: (a) Experimental set-up used to characterise the kinematics of the blade in water. A GoPro camera is installed above one of the rowers on the *eight* rowing boat from the *Ecole polytechnique* rowing club. The videos of the rower's hands are coupled with the measurement of the speed of the boat from a sensor based on GPS and accelerometer sensors. (b) Picture taken by the GoPro camera during the measurements.

To characterise the blade kinematics, we performed an experiment on an *eight* rowing boat from the *Ecole polytechnique* rowing club. A GoPro camera was set-up above one of the rowers to record the motion of his hands (see Fig. 2.9) and this was coupled with a speed sensor (combining a GPS sensor and an accelerometer for better accuracy) to measure the instantaneous speed of the boat. The analysis of the videos recorded onboard during the training of the rowing team allowed us to extract the position and velocity of the rower's hands in the reference frame of the boat. Using $\eta = \ell_o/\ell_i$ the ratio between the outboard length and the inboard length of the oar (see Fig. 2.2(b)), we could get the position and velocity of the center of the blade in the reference frame of the hull. Finally, combining this with the synchronous measurement of the hull speed, we could get the position and velocity of the blade center in the reference frame of the water. In Fig. 2.10(a), the trajectory of the blade center in the reference frame of the water is plotted for three strokes. This trajectory is very similar from one stroke to the next. The blade travels a bit forward after the catch (entry of the blades inside water) and then backward until the release. Fig. 2.10(b) shows a zoom on one power stroke, with the position of the blade (represented as a segment) and the blade velocity vector $\boldsymbol{v}_{bl/w}$ (red vector).
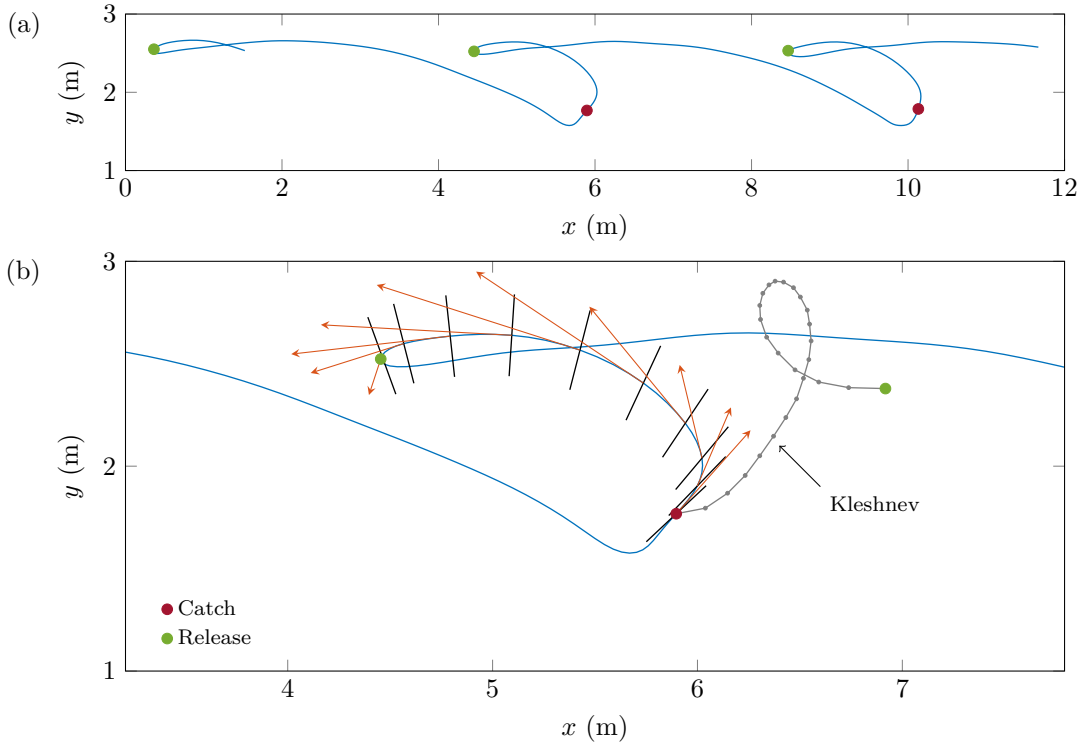
Figure 2.10: (a) Position of the center of the blade for three strokes in the reference frame of the water from in-situ measurements with the *Ecole polytechnique* rowing team. The red dot (resp. green dot) indicate the position at which the blade enters the water (resp. goes out of the water). (b) Zoom on the position of the center of the blade during one stroke with the plot of the blade position at different times (black lines) and the vectors of the blade velocity with respect to the water, during the power stroke (red arrows). The gray line is the blade path obtained from measurements for a single scull at a racing pace and is reprinted from [54]. Note that in both plots the origin of the y axis corresponds to the position of the oarlock and the boat is moving from the left to the right.

The blade path during the power stroke measured previously by Kleshnev and found in [54] is re-plotted on the same graph. The path is clearly very different from the one we obtained: after the catch, the blade moves much more forward in the direction of motion of the boat

before slightly moving backward and finally moves forward again until the release. Thus, the position of the release is found forward of the position of the catch, whereas we find the opposite with our measurements. The observation by Kleshnev is quite surprising as rowing propulsion is at first expected to be related to a drag force on the blade, which would require that the blade moves in the opposite direction to the direction of motion of the boat. This further implies that lift and added mass force provide important contributions to the total propulsive force. In particular, Caplan *et al.* distinguish four different phases depending on the respective contributions of drag and lift (see Fig. 2.11) [55]. They indicate that lift is important at the beginning and at the end of the power stroke, while drag contributes to the total force on the blade at the middle of the stroke (see also [50]). The significant difference between the results from the experiments with the *Ecole polytechnique* rowing team and the data found in literature [54] is surely related to the level of the rowers.
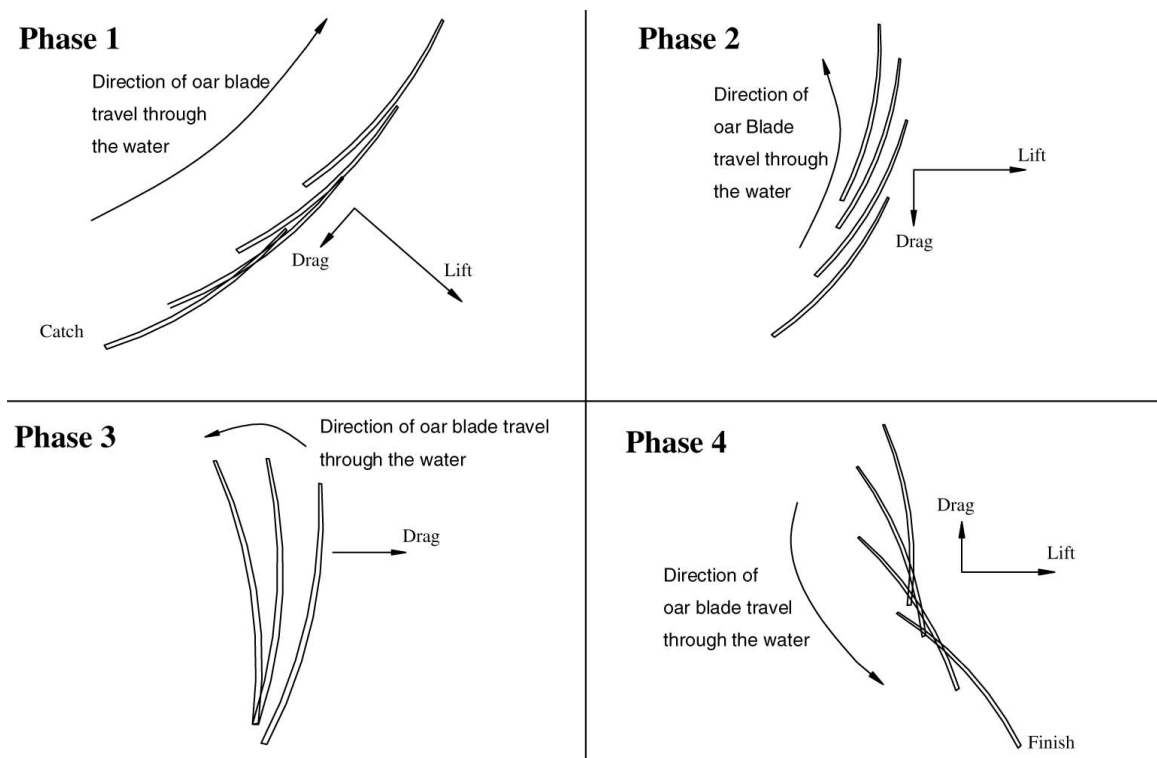
Figure 2.11: The four different phases of the blade trajectory during the power stroke. The lift and drag forces are qualitatively indicated for each phase. Reprinted from [55].

2.4   Analysis of the rower's kinematics

This study was conducted with the elite French rower Thomas Baroukh, bronze medal in lightweight *coxless four* at the Rio 2016 Olympics. The aim here was to look closer at the kinematics of the different segments of a rower (that is the legs, the trunk and the arms) to quantify their relative importance as mentioned in Subsect. 2.1.2, and also to roughly quantify the difference between the motion of the rower's hands and the motion of the center of mass of the rower.

Similarly to other studies [50, 56, 57, 58], we identify six segments to represent the rower's body: two segments for the legs, one for the trunk and two for the arms. We then define three angles: θ_1 the angle between the two segments of the legs, θ_2 the angle between the
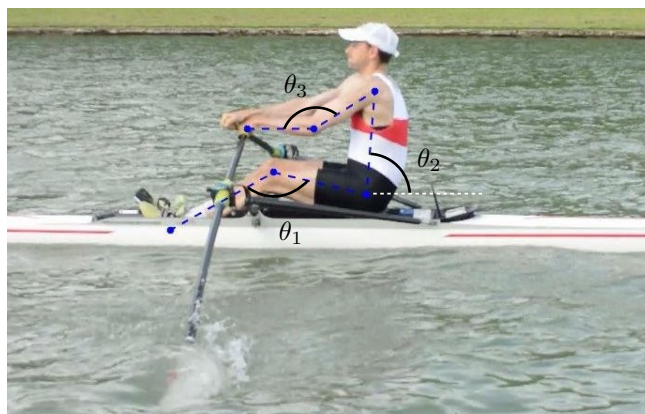
Figure 2.12: Picture from the experiment with the French athlete Thomas Baroukh on the *Grand canal* of Versailles. We define six segments (two for the legs, one for the trunk and two for the arms) and three angles θ_1, θ_2 and θ_3.

horizontal and the segment of the trunk and θ_3 the angle between the two segments of the arms (see Fig. 2.12). Note that to fully characterise the rower's position, one should introduce one more angle, which is the angle between the trunk and the upper arm. We filmed Thomas Baroukh from the side during his training. From the analysis of the videos, we could get the position of his segments during a few rowing cycles.
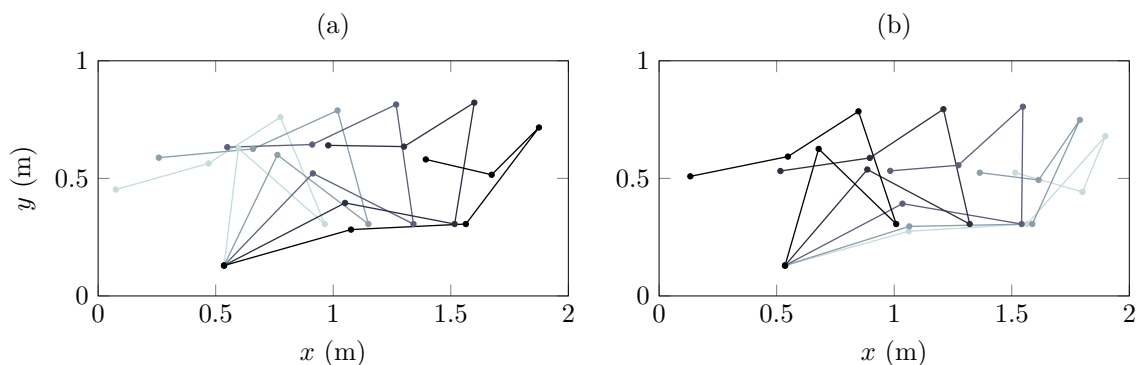
Figure 2.13: Position of the different segments of Thomas Baroukh's body extracted from the analysis of the video of his training at different instants during (a) the power stroke and (b) the recovery stroke. The color of the segments becomes darker with time.

Fig. 2.13 presents the results of this analysis for the higher stroke rate (27 strokes per minute) for one rowing cycle, with the position of the segments at different instants, distinguishing the power stroke and the recovery stroke. The two pictures qualitatively show when the different segments are activated: in particular, the trunk and the arms start to move at the end of the power stroke. The reverse dynamics is observed for the recovery stroke with the arms and trunk moving at the beginning of it. Note that one particularity of the recovery stroke is that the hands of the rower have a lower position than during the power stroke, which is needed to prevent the blade from touching the water during this phase.

The evolution of the corresponding angles θ_1, θ_2 and θ_3 is shown in Fig. 2.14(a). One can first observe that, θ_1 (angle between the two segments of the legs) increases quasi linearly with time during the power stroke (between $t = 0$ and the green vertical dashed line) – from about 50° to 170° –, then keeps a fairly constant value from the end of the power stroke to the end of the first quarter of the recovery stroke and finally decreases quasi linearly until

reaching about 50°. As for the angles θ_2 (angle between the horizontal and the trunk) and θ_3 (angle between the two segments of the arms), they show very similar evolutions with time. For both angles, two phases can be distinguished during the power stroke (and similarly during the recovery stroke): a first phase for which the angle slowly decreases and a second phase at the end of the power stroke with a fast decrease of the angle. This is in qualitative agreement with the decomposition of the motion of the different segments observed from Fig. 2.13.
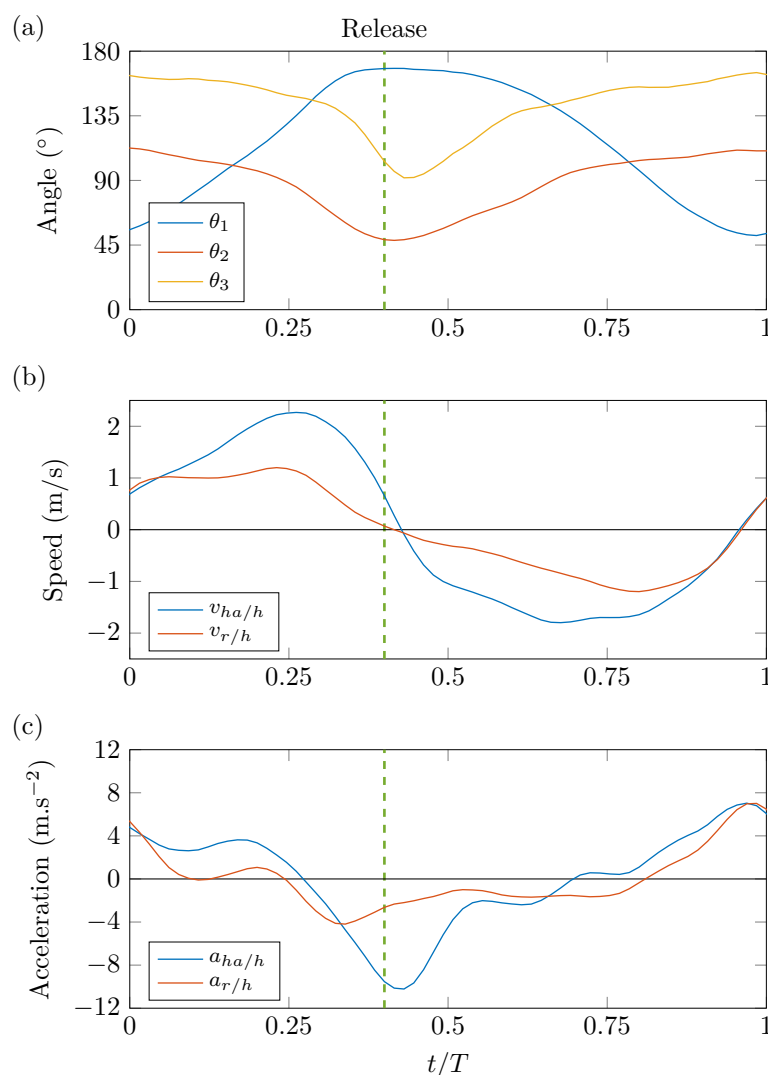
Figure 2.14: (a) Angles θ_1 (between the two segments of the legs), θ_2 (between the horizontal and the segment of the trunk) and θ_3 (between the two segments of the arms), (b) speed of the rower's hands $v_{ha/h}$ (blue curve) and of the center of mass of the rower $v_{r/h}$ (red curve) and (c) acceleration of the rower's hands $a_{ha/h}$ (blue curve) and of the center of mass of the rower $a_{r/h}$ (red curve) as a function of the dimensionless time t/T for one stroke. For the three plots, $t = 0$ is the time at which the blades enter the water and the vertical green dashed line indicates the time at which the blades go out of the water.

From this analysis, it is straight-forward to obtain the velocity $v_{ha/h}$ and acceleration $a_{ha/h}$ of the rower's hands. Computing the velocity $v_{r/h}$ and acceleration $a_{r/h}$ of the center of mass of the rower is a bit more tricky. We obtain them by estimating the position of the center of mass of the rower using the data of the location of the center of mass and the relative weight of the different segments of the body found in [59, 60]. The speed of the

rower's hands and of the center of mass of the rower are plotted in Fig. 2.14(b), while the corresponding accelerations are represented in Fig. 2.14(c). One can see that the velocity of the center of mass of the rower is always smaller than the velocity of the rower's hands. Its maximum is about 1 m/s, while the maximum of the rower's hands speed is about 2 m/s. It can also be noticed that the velocity of the rower's hands is still slightly positive at the end of the power stroke (*i.e.* at the release) to prevent from slowing down the boat when lifting up the blades. Looking now at the acceleration curves, it can be observed that the accelerations are of the order of magnitude of 1 *g*. As can be expected, the maximum of acceleration for both the rower's hands and the center of mass of the rower happens at the end of the recovery stroke, as the direction of motion of the rower changes. The minimum of acceleration for the rower's hands is situated at the beginning of the recovery stroke as the blade goes out of water before changing direction. On the contrary, the minimum of acceleration for the center of mass of the rower happens before the end of the power stroke. This is related to the dominant use of the arms in this phase of the stroke which do not affect much the position of the rower's center of mass.

2.5   Model for the drag on a rowing boat

Given the high length-to-width aspect ratio (typically about 30) of rowing boats, skin drag is their dominant drag component, as seen in Chap. 1. Wellicome *et al.* confirm this hypothesis as they specify that, in rowing, the wave drag accounts only for less than 8% of the total drag [61, 62]. Furthermore, the Reynolds number for a rowing boat in competition is typically about 10^8. This implies, as seen in Sect. 1.4, that the boundary layer along the hull is turbulent. The total drag on the hull can then be written as:

$$R = -\frac{1}{2}\rho S_\mathrm{h} C_\mathrm{h} U^2 \ , \tag{2.1}$$

where R is the projection of the total drag force on the hull over the direction of motion, S_h is the wetted surface of the hull and C_h is the drag coefficient of the hull.
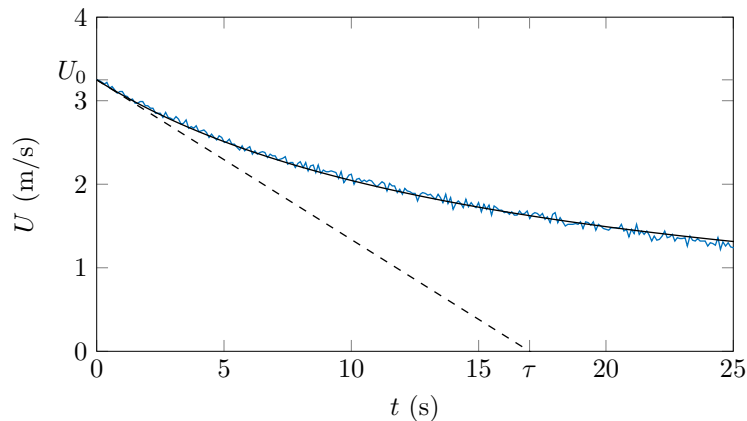
Figure 2.15: Instantaneous speed of an *eight* rowing boat as a function of time during a deceleration phase (blue curve). The black line is a fit of the experimental curve using Eq. (2.3) with $U_0 \simeq 3.25$ m/s and $\tau \simeq 17$ s. The dashed line is the tangent of the fitting curve in $t = 0$.

To estimate the hull drag coefficient C_h for a real rowing boat, we performed measurements

of the speed of an *eight* rowing boat (from the *Ecole polytechnique* rowing club) during a phase of deceleration with no rower's motion (see Fig. 2.15). This corresponds to a phase where the rowers stop rowing. In this case, the dynamical equation for the boat simply reads:

$$M\frac{\mathrm{d}U}{\mathrm{d}t} = -\frac{1}{2}\rho S_\mathrm{h} C_\mathrm{h} U^2 \; , \tag{2.2}$$

and, assuming C_h to be independent of U, its solution reads:

$$U = \frac{U_0}{1 + t/\tau} \; , \tag{2.3}$$

where U_0 is the initial speed of the boat at the beginning of the deceleration phase and $\tau = 2M/(\rho S_\mathrm{h} C_\mathrm{h} U_0)$ is the characteristic deceleration time. Fitting the experimental curve in Fig. 2.15(a) with Eq. (2.3) yields $U_0 \simeq 3.25$ m/s and $\tau \simeq 17$ s. Considering that $M \simeq 720$ kg and $S_\mathrm{h} = 10$ m^2, one gets $C_\mathrm{h} \simeq 2.6 \cdot 10^{-3}$.

This value of the hull drag coefficient is comparable to the one found in the literature. Previous studies where the fluid friction force on a rowing hull is modelled [57, 63, 64] indeed found $C_\mathrm{h} \simeq 2.5 \cdot 10^{-3}$. Other studies [65, 66] use the empirical relation: $R = -13.05 \, U^2 + 11.22 \, U - 24.93$, which was obtained by Wellicome for an *eight* rowing boat [61].

Let us now mention that Eq. (2.1) is supposed to hold in the case of a motion at constant speed U. However, as seen in Sect. 2.2, one particularity of rowing is the unsteadiness of the flow around the hull. Indeed, because of the motion of the rowers on the boat and the decomposition of the rowing cycle into a propulsive phase and a recovery phase, the boat moves with large fluctuations of speed, which are up to 30% of the mean speed. This special feature (which also appears for sprint canoes) might drastically affect the expression of the total drag R given in Eq. (2.1).
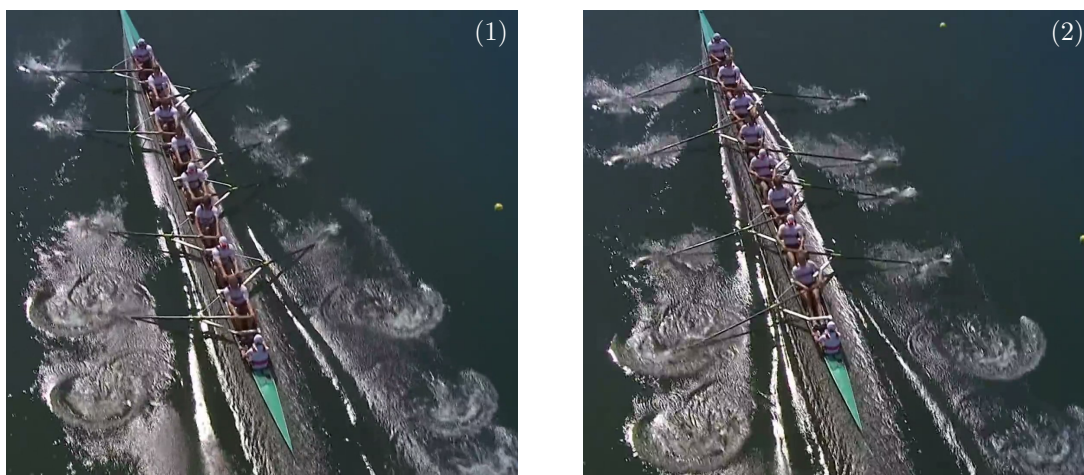
Figure 2.16: Pictures of an *Eight* rowing boat and its wake at the London 2012 Olympics (source: [67]).

In particular, if the distance travelled by the boat during one rowing cycle is smaller than the boat length, then the flow fluctuations with time are averaged out when computing the total resistance R because it is a spatial average. The drag coefficient C_h is then independent of time. On the contrary, if the distance travelled is larger than the boat length, C_h becomes a function of time. The case of rowing typically lies in between these two limit cases as the

distance travelled over one stroke is about the boat length. Furthermore, the fluctuations of speed of the hull are also expected to change the wave resistance in comparison with the case of a motion at constant speed. Looking at the pictures in Fig. 2.16 taken at the London 2012 Olympics, in addition to observing a turbulent wake, one can notice that larger waves are sometimes emitted during the rowing cycle. References [68] and [69] show both experimentally and numerically that the wave resistance increases when the velocity fluctuates compared to a motion at constant speed. The unsteady motion of rowing boats also surely induces added mass forces (see Sect. 1.7.1), which could be taken into account by adding to the total mass of the boat its added mass (to be evaluated).

So far, we only considered the hydrodynamic drag on the boat assuming calm waters and a boat with always the same orientation with respect to the horizontal plane. However, in reality, many other parameters can contribute to increase the drag on the boat. For example, a pitch motion[3] (taken into account in [64]) or the presence of surface waves can affect the hydrodynamic drag of the hull. Furthermore, the aerodynamic drag notably from the oars and the emerging part of the hull also adds a non-negligible contribution to the total drag on the boat (especially in case of wind).

---

[3]The up/down rotation of a vessel about its transverse (side-to-side or port-starboard) axis.

2

Take home message of Chapter 2

1. Boat kinematics. During a rowing race, after a transitory regime, the mean hull velocity over one rowing cycle reaches a fairly constant value. Taking a closer look at the instantaneous hull velocity, we observe that the velocity fluctuates around 20 to 30% about the mean velocity and that the maximum hull velocity is reached during the recovery stroke.

2. Blade kinematics. We conducted an experiment to measure the blade path in water and obtained a quite different trajectory from the one found in literature. This result shows that, depending on the velocity of the boat, the blade trajectory can be very different, which directly impacts the contribution of lift and drag to the total drag on the blade.

3. Rower's kinematics. Analysing videos of the training of the French athlete Thomas Baroukh, we recovered that the different segments of a rower (legs, trunk and arms) are activated consecutively. We further observed a substantial difference between the velocity of the rower's hands and the velocity of the center of mass of the rower.

4. Drag on a rowing boat. With a simple experiment, we find that considering only skin friction gives a good approximate for the total drag on the hull. This is coherent with previous studies, which state that skin friction accounts for more than 90% of the total drag. The slenderness of rowing boats minimises their wave drag component.

PART II

OPTIMISATION OF SHIP HULLS

3

OPTIMAL HULL ASPECT RATIOS

Empirical data reveal a broad variety of hull shapes among the different ship categories. We present a minimal theoretical approach to address the problem of ship hull optimisation. We show that optimal hull aspect ratios result – at given load and propulsive power – from a subtle balance between wave drag, pressure drag and skin friction. Slender hulls are more favourable in terms of wave drag and pressure drag, while bulky hulls have a smaller wetted surface for a given immersed volume, by that reducing skin friction. We confront our theoretical results to real data and discuss discrepancies in the light of hull designer constraints, such as stability or manoeuvrability.
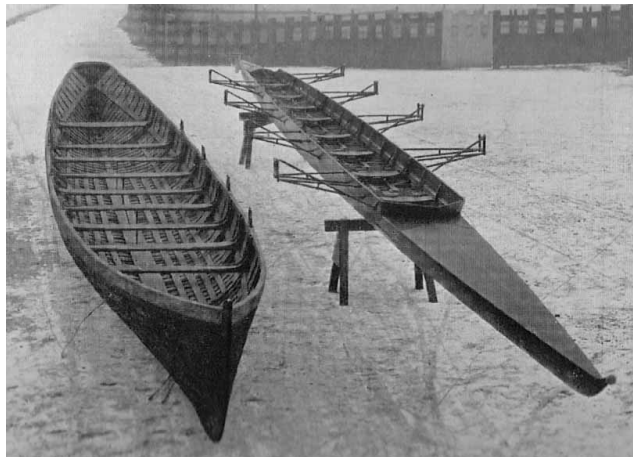
Picture of the 1829 (left) and 1929 (right) Oxford boats. Source: [70].

Contents

3.1 Position of the problem

The long-lived subject of ship hull design is with no doubt one of infinite complexity. Constraints may significantly vary from one ship class to another. When designing a sailing boat, stability and manoeuvrability are of paramount importance [5, 19, 20, 71]. Liners and warships must be able to carry a maximal charge and resist rough sea conditions. Ferrys and cruising ships must be sea-kindly such that passengers don't get sea-sick. All ship hulls share however one crucial constraint: they must suffer the weakest drag possible in order to minimise the required energy to propel themselves, or similarly maximise their velocity for a given propulsive power.

Figure 3.1: Bulbous bow of the passenger ship Zaandam in drydock (source: [72]). A bulbous bow is used to reduce its wave resistance.

As one can expect, a number of technological advances have been developed over the years, such as bulbous bows (see Fig. 3.1) intended to reduce wave drag through destructive interference [5, 73, 74]. There exists an extended literature of numerical and experimental studies dedicated to the optimisation of ship hulls. Quite surprisingly some of them only consider wave drag in the optimisation setup (see *e.g.* [34, 75, 76]). Others consider both the skin drag and the wave drag [74, 77, 78]. Very few consider the pressure drag [79] as most studies address slender streamlined bodies for which the boundary layer does not separate, leading to a negligible pressure drag. The complexity of addressing analytically this optimisation problem comes from the infiniteness of the search space. Indeed without any geometrical constraints, the functions defining the hull geometry can be anything, and computing the corresponding drag can become an impossible task. However, from this substantial literature, it is not self-evident to deduce how ship hulls should look like – notably in terms of aspect ratios – to minimise their drag.

In Fig. 3.2, the length to width aspect ratio $\alpha = \ell/w$ of different kinds of bodies moving at the water surface is plotted against their Froude number (see Table 3.1 for details). As one can see, different ship categories tend to gather into clusters. These groups display very different aspect ratios, from 2-3 to about 30, even in the same Froude number regime. The highest aspect ratios are reached for rowing boats ($\ell/w \approx 30$, Fr ≈ 0.5). The majority of ships stand on the left hand side of the plot (Fr $\lesssim 0.7$). For Fr $\gtrsim 0.7$, most hulls can no longer be considered as *displacement* hulls (weight balanced by buoyancy) but rather as *planing* hulls (weight balanced by hydrodynamic lift) and thus have a much smaller immersed volume [20]. Here we take a simple theoretical approach to determine the optimal aspect ratios for ship hulls depending on the required load and propulsive power. They are compared to the aspect ratios of real ship hulls to see how close existing hulls are from the optimal.
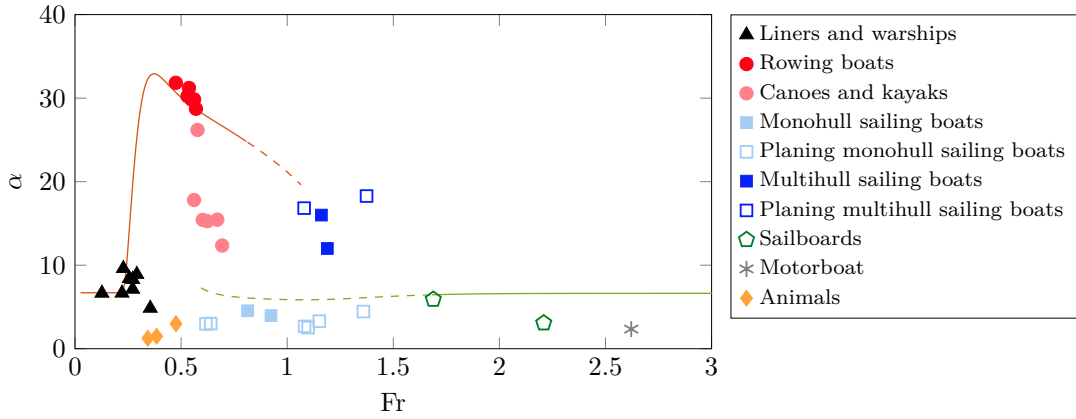
Figure 3.2: Aspect ratio $\alpha = \ell/w$ as a function of Froude number $U/\sqrt{g\ell}$ for different kinds of bodies moving at the water surface (see Table 3.1 for details). Solid symbols represent displacement hulls, whereas open symbols indicate planing hulls. The aspect ratio for multihulls is computed for each hull independently. The black line corresponds to the optimal aspect ratio, see Sect. 3.5. Solid lines indicate global optima, while dashed lines signify local optima.

Category	Boat Name	Length ℓ (m)	Width w (m)	Draft (*) d (m)	Mass M (kg)	Speed U (m/s)	Power (*) $\mathcal{P}$ (kW)
Liner	Titanic	269.0	28.00	13.89	$5.23 \cdot 10^7$	11.70	34000
Liner	Queen Mary 2	345.0	41.00	10.75	$7.6 \cdot 10^7$	14.90	115000
Liner	Seawise Giant	458.0	68.86	41.22	$6.5 \cdot 10^8$	8.50	37000
Liner	Emma Maersk	373.0	56.00	20.87	$2.18 \cdot 10^8$	13.40	88000
Liner	Abeille Bourbon	80.0	16.50	4.85	$3.2 \cdot 10^6$	9.94	16000
Liner	France	300.0	33.70	11.28	$5.7 \cdot 10^7$	15.80	118000
Warship	Charles de Gaulle	261.5	31.50	10.32	$4.25 \cdot 10^7$	13.77	61000
Warship	Yamato	263.0	36.90	15.04	$7.3 \cdot 10^7$	13.80	110000
Rowing boat	Single Scull	8.1	0.28	0.09	104	5.08	0.4
Rowing boat	Double Scull	10.0	0.34	0.12	207	5.56	0.8
Rowing boat	Coxless Pair	10.0	0.34	0.12	207	5.43	0.8
Rowing boat	Quadruple Scull	12.8	0.41	0.16	412	6.02	1.6
Rowing boat	Coxless Four	12.7	0.42	0.15	410	5.92	1.6
Rowing boat	Coxed Eight	17.7	0.56	0.18	867	6.26	3.2
Canoe	C1	5.2	0.34	0.12	104	4.45	0.4
Canoe	C2	6.5	0.42	0.15	200	4.80	0.8

Table 3.1 – *Continued from previous page*

Category	Boat Name	Length ℓ (m)	Width w (m)	Draft (*) d (m)	Mass M (kg)	Speed U (m/s)	Power (*) $\mathcal{P}$ (kW)
Canoe	C4	8.9	0.50	0.18	390	5.24	1.6
Kayak	K1	5.2	0.42	0.09	102	4.95	0.4
Kayak	K2	6.5	0.42	0.15	198	5.35	0.8
Kayak	K4	11.0	0.42	0.17	390	6.00	1.6
Sailing boat Monohull	Finn (p)	4.5	1.51	0.12	240	4.10	4.0
Sailing boat Monohull	505 (p)	5.0	1.88	0.15	300	7.60	18.9
Sailing boat Monohull	Laser (p)	4.2	1.39	0.10	130	4.10	2.7
Sailing boat Monohull	Dragon	8.9	1.96	0.50	1000	7.60	16.5
Sailing boat Monohull	Star	6.9	1.74	0.35	671	7.60	18.5
Sailing boat Monohull	IMOCA 60 (p)	18.0	5.46	0.50	9000	15.30	843.4
Sailing boat Monohull	18ft Skiff (p)	8.9	2.00	0.24	420	12.70	85.2
Sailing boat Monohull	49er (p)	4.9	1.93	0.20	275	7.60	25.9
Sailing boat Multihull	Nacra 450 (p)	4.6	0.25	0.12	330	9.20	20.7
Sailing boat Multihull	Hobie Cat 16 (p)	5.0	0.30	0.12	330	7.60	20
Sailing boat Multihull	Macif	30.0	2.50	0.50	14000	20.40	1218
Sailing boat Multihull	Banque populaire V	40.0	2.50	0.50	14000	23.00	1700
Sailboard	Mistral One Design (p)	3.7	0.63	0.07	85	10.20	6.9
Sailboard	RS:X (p)	2.9	0.93	0.06	85	11.70	10.2
Motorboat	Zodiac (p)	4.7	2.00	0.15	700	17.80	180.0
Animal	Swan	0.5	0.40	0.10	10	0.76	N.A.
Animal	Duck	0.3	0.20	0.17	5	0.66	N.A.
Animal	Human swimmer	1.8	0.60	0.17	90	2.00	0.3

Table 3.1: Characteristics of bodies moving at the water surface. The planing hulls are indicated with (p) in the column Boat Name. N.A. stands for *Not Available*. (*) For all hulls (including planing hulls for which this estimation might be too rough), the draft is estimated using the mass of the boat and the relation $M/\rho \simeq 2a_{\tilde{f}}\ell w d$ (with $a_{\tilde{f}} = 0.25$). The power is estimated through diverse methods depending on the category of the boat. For liners and warships, the propulsive power can easily be found in the specification documents. For rowing boats, canoes and kayaks, we consider that the power per oarsman is 400 W. For sailing boats and sailboards, we use the sail area of the boat to derive its propulsive power (with a typical wind of 10 m/s). Note that for multihull sailing boats, the indicated dimensions correspond to one of the hulls.

3.2 Model assumptions and simplifications

We consider here a much simpler hull geometry than in Chap. 1, that is hulls with a constant horizontal cross-section (see Fig. 3.3). The general parametrisation of the hull shape (see Subsect. 1.6.1) then becomes $y = f(x)\mathbb{1}_{z\in[-d,0]}$ where $\mathbb{1}_{z\in[-d,0]}$ denotes the indicator function ($\mathbb{1}_{z\in[-d,0]} = 1$ if $z \in [-d,0]$ and 0 otherwise).
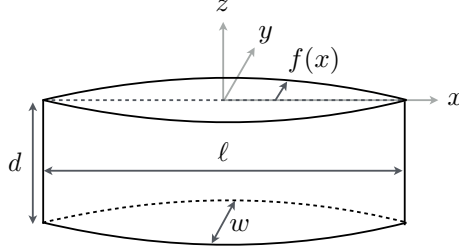

Figure 3.3: Schematics of the simplified hull geometry considered in this chapter. The hull shape follows the parametrisation $y = f(x)\mathbb{1}_{z\in[-d,0]}$. Note that only the part of the hull immersed in the water is represented.

In the same way as in Sect. 1.6, we define the length ℓ, width w and draft d (see Fig. 3.3) and introduce the dimensionless coordinates through $x = \tilde{x}\ell$, $y = \tilde{y}\ell$ and $z = \tilde{z}\ell$ as well as $f(x) = \tilde{f}(\tilde{x})w$. We remind the definition of the aspect ratios $\alpha = \ell/w$ and $\beta = \ell/d$.

Furthermore, the fluid is assumed to be infinitely deep and we use the theoretical model developed by Michell to predict the wave drag on this simple geometry (see Subsect. 1.6.3). Note that this model is only accurate in the limit of thin ships.

3.3 Wave drag expression

Applying Eqs. (1.47)-(1.48) for the simplified geometry defined above, the wave drag coefficient reads:

$$C_{\text{w}}(\text{Fr}, \alpha, \beta) = \frac{4\beta^{2/3}}{\pi\alpha^{4/3}\text{Fr}^4}\, G_{\tilde{f}}(\text{Fr}, \beta) \,, \tag{3.1}$$

where we have defined:

$$G_{\tilde{f}}(\text{Fr}, \beta) = \int_1^{+\infty} \frac{|I_{\tilde{f}}(\lambda, \text{Fr}, \beta)|^2}{\sqrt{\lambda^2 - 1}}\, \mathrm{d}\lambda \,, \tag{3.2}$$

$$I_{\tilde{f}}(\lambda, \text{Fr}, \beta) = \left(1 - e^{-\lambda^2/(\beta\text{Fr}^2)}\right)\int_{-\frac{1}{2}}^{\frac{1}{2}} \tilde{f}(\tilde{x})e^{i\lambda\tilde{x}/\text{Fr}^2}\, \mathrm{d}\tilde{x} \,. \tag{3.3}$$

Interestingly, one can notice here that the aspect ratio α only appears as $\alpha^{-4/3}$ in front of the function $G_{\tilde{f}}(\text{Fr}, \beta)$ in Eq. (3.1). Consequently, the higher α the lower the wave drag coefficient. The effect of the aspect ratio β is a bit more complex: for $\beta \ll 1$, C_{w} scales as $\beta^{2/3}$, while for $\beta \gg 1$, C_{w} scales as $\beta^{-4/3}$, which is notably the same power law as for α. From these scalings, we also see that there is a maximum of the wave drag coefficient for intermediate values of β.

To analytically compute the wave drag coefficient, we consider a gaussian hull profile:

$$\tilde{f}(\tilde{x}) \quad = \quad \frac{1}{2}\exp[-(4\tilde{x})^2]\ . \tag{3.4}$$

Indeed, with this particular hull profile, one can approximate analytically the integral in Eq. (3.3) by integrating $\tilde{x}$ over $\mathbb{R}$. One obtains:

$$G_{\text{gauss}}(\text{Fr},\beta) \quad = \quad \frac{\pi}{64}J\left(\frac{1}{32\text{Fr}^4}\right) - \frac{\pi}{32}J\left(\frac{1}{32\text{Fr}^4} + \frac{1}{\beta\text{Fr}^2}\right) + \frac{\pi}{64}J\left(\frac{1}{32\text{Fr}^4} + \frac{2}{\beta\text{Fr}^2}\right), \tag{3.5}$$

where:

$$J(u) = \int_1^{+\infty} \frac{e^{-u\lambda^2}}{\sqrt{\lambda^2-1}}\,\mathrm{d}\lambda = \frac{1}{2}e^{-u/2}\mathcal{K}_0(u/2)\ , \tag{3.6}$$

with $\mathcal{K}_0(u)$ the modified Bessel function of the second kind of order zero [80].
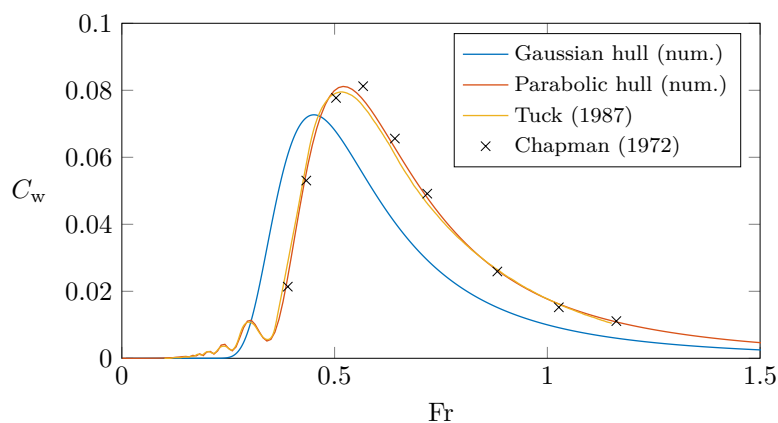
Figure 3.4: Wave-drag coefficient C_{w} as function of the Froude number Fr for a gaussian hull and a parabolic hull for $\alpha = 6.7$ and $\beta = 2.3$. These results are compared to the theoretical curve from [32] and experimental data points from [31] (black crosses).

In Fig. 3.4, the corresponding wave drag coefficient for an object of aspect ratios $\alpha = 6.7$ and $\beta = 2.3$ is represented as function of the Froude number. This is compared with the wave drag coefficient obtained numerically for a parabolic profile ($\tilde{f}(\tilde{x}) = 2\tilde{x}\,(1-\tilde{x})$), as well as numerical and experimental results from previous studies also obtained for parabolic objects with the same aspect ratios [31, 32]. The figure shows very good agreement between the two previous studies and our result for a parabolic profile, thus validating our numerical code. Compared to these results, the curve obtained for a gaussian profile has its maximum shifted to the left and do not display oscillations of the wave drag coefficient at low Froude numbers (Fr ≤ 0.3).[1] This comparison shows that the choice of a Gaussian profile rather than more realistic profiles, such as a parabolic profile, has no qualitative impact on our main results. We also recover from this plot that the wave drag coefficient is maximum for Fr ≈ 0.5.

Figure 3.5(a-c) displays the contour plots of C_{w} as function of (α,β) for Fr $\in \{0.3, 0.5, 1\}$. As expected from the previously derived scalings, the contour plots make it clear that the wave drag is minimum for large values of α and β, that is for thin and shallow hulls. The Froude number is also found to highly affect the values of C_{w}. Considering the three contour plots,

---

[1]The oscillations at Fr ≤ 0.3 appear to be related to the slopes of the hull profile in $\tilde{x} = -1/2$ and $\tilde{x} = 1/2$. We observed that the lower these slopes the lower the oscillations.
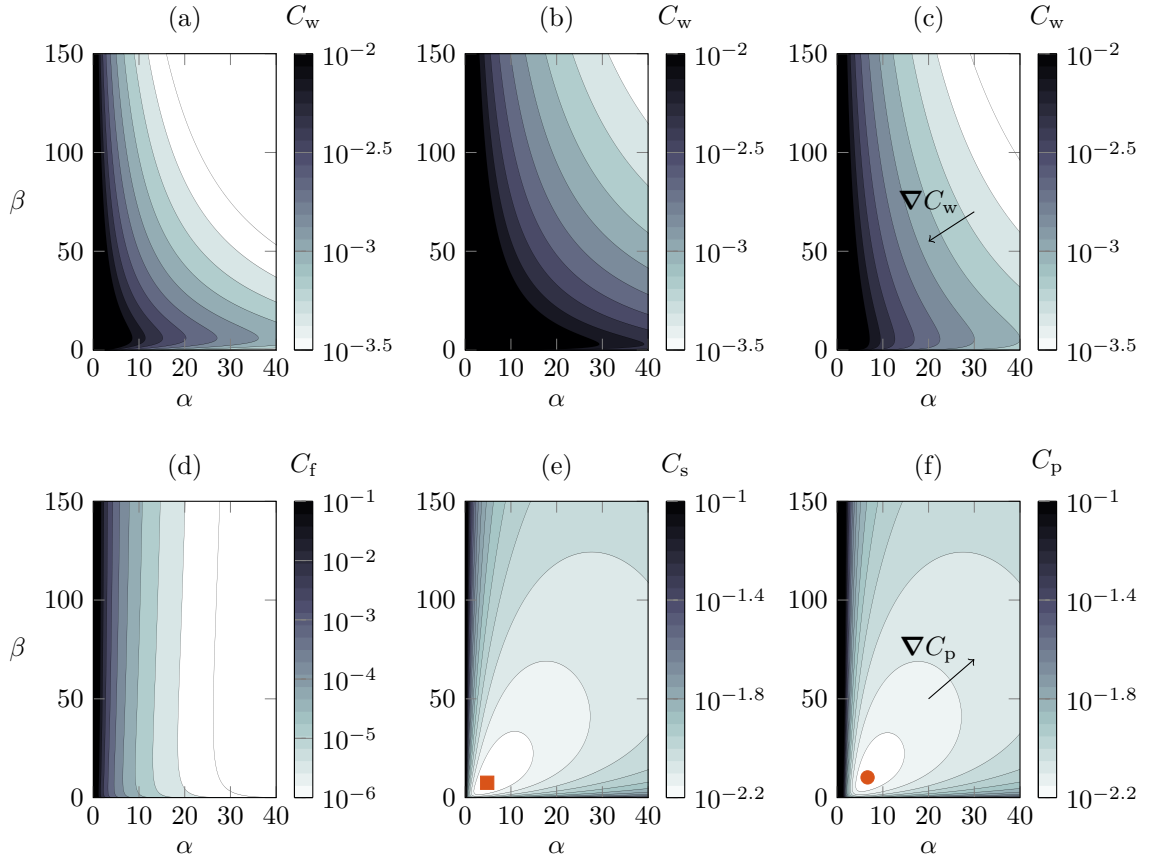
Figure 3.5: (a-c) Contour plots of the wave drag coefficient C_w as a function of the aspect ratios α and β, for (a) Fr = 0.3, (b) Fr = 0.5 and (c) Fr = 1. Black regions correspond to $C_\text{w} \geq 10^{-2}$. (d-f) Contour plots of (d) the pressure drag coefficient C_f, (e) the skin drag coefficient C_s and (f) the profile drag coefficient $C_\text{p} = C_\text{f} + C_\text{s}$ as a function of the aspect ratios α and β. Black regions correspond to $C_\text{f/s/p} \geq 10^{-1}$. In (e) the red dot indicates the position of the minimum of C_s ($\alpha_0 \simeq 5$, $\beta_0 \simeq 7.5$). In (f), it indicates the position of the minimum of C_p ($\alpha_0 \simeq 7$, $\beta_0 \simeq 10$). In (c) and (f) the gradients are indicated with black arrows.

the effect of the Froude number at given α and β seems to follow the evolution depicted in Fig. 3.4 with maximum values of the wave drag coefficient obtained for Fr $\simeq 0.5$.

3.4 Profile drag derivation

The *profile drag* R_p is defined as the sum of the skin drag and the pressure drag (or form drag) (see [10] and Chap. 1). It is also called *viscous resistance* (see [19] and [20]). In the typical range of Reynolds numbers for ships (Re $\in [10^7, 5 \times 10^9]$, see Sect. 1.2), both the skin and pressure components scale with U^2. Thus, the profile drag can be written as $R_\text{p} = (1/2)\rho S_h C_h U^2$ where S_h is the wetted surface of the hull and C_h its drag coefficient. The wetted surface can be decomposed in two contributions $S_h = S_\text{b} + \mathcal{L}d$ where $S_\text{b} = 2w\ell \int_{-1/2}^{1/2} \tilde{f}(\tilde{x}) \, \text{d}\tilde{x}$ is the surface of the bottom horizontal cross section of the hull and $\mathcal{L} =$

$2\ell \int_{-1/2}^{1/2}[1 + \tilde{f}'(\tilde{x})^2/\alpha^2]^{1/2}\,\mathrm{d}\tilde{x}$ is the perimeter of the hull. We define:

$$a_{\tilde{f}} = \int_{-\frac{1}{2}}^{\frac{1}{2}} \tilde{f}(\tilde{x})\,\mathrm{d}\tilde{x} \ , \tag{3.7a}$$

$$b_{\tilde{f}}(\alpha) = \int_{-\frac{1}{2}}^{\frac{1}{2}} [1 + \tilde{f}'(\tilde{x})^2/\alpha^2]^{1/2}\,\mathrm{d}\tilde{x} \ , \tag{3.7b}$$

so that $S_h = 2\ell[w\,a_{\tilde{f}} + d\,b_{\tilde{f}}(\alpha)]$. Finally, the profile drag can be written as $R_{\mathrm{p}} = \rho\Omega^{2/3}U^2 C_{\mathrm{p}}$ with:

$$C_{\mathrm{p}}(\alpha, \beta) = \frac{C_h(\alpha)\beta^{2/3}}{\alpha^{1/3}}\left[a_{\tilde{f}} + \frac{\alpha}{\beta}b_{\tilde{f}}(\alpha)\right] \ . \tag{3.8}$$

The evolution of the coefficient C_h with α was empirically derived for streamlined bodies [10]: $C_h(\alpha) = C_{\mathrm{s}}^{\infty}(1 + 2/\alpha + 60/\alpha^4)$ with C_{s}^{∞} the skin drag coefficient for a flat plate (see Sect. 1.4). The term $(1 + 2/\alpha)$ refers to the skin friction, while the term $60/\alpha^4$ corresponds to the pressure drag.[2] In the considered regimes, C_{s}^{∞} is only weakly dependent on the Reynolds number (see [10] and Sect. 1.4). In the following, we consider a constant skin drag coefficient $C_{\mathrm{s}}^{\infty} = 0.002$, corresponding to a Reynolds number $\mathrm{Re} \simeq 10^8$.

With this expression of the profile drag coefficient, it is straightforward to obtain the scalings at small and large aspect ratios. For $\alpha \ll 1$, $C_{\mathrm{p}} \sim \alpha^{-13/3}$, while for $\alpha \gg 1$, $C_{\mathrm{p}} \sim \alpha^{2/3}$. As for β, when $\beta \ll 1$, $C_{\mathrm{p}} \sim \beta^{-1/3}$ and when $\beta \gg 1$, $C_{\mathrm{p}} \sim \beta^{2/3}$. Very interestingly, in the same way as for the wave drag coefficient, α and β follow the same power law when they are large ($\alpha \gg 1$ and $\beta \gg 1$). Also, the scalings for both aspect ratios indicate the existence of a minimum for intermediate aspect ratios. This is shown with the contour plot of the profile drag coefficient C_{p} as a function of α and β (see Fig. 3.5(f)). The minimum is obtained for rather small aspect ratios: $\alpha_0 \simeq 7$, $\beta_0 \simeq 10$ (indicated by a red dot). If we only took into account the skin friction component C_{s} (see Fig. 3.5(e)), the optimal aspect ratios would be even smaller ($\alpha_0 \simeq 5$, $\beta_0 \simeq 7.5$) The contour plot of the pressure drag component C_{f} in Fig. 3.5(d) shows that C_{f} drastically increases for small aspect ratio α. This explains why, in comparison with C_{s}, the position of the minimum of C_{p} is shifted towards larger aspect ratios.

3.5 Optimisation

The total drag force on the hull reads $R = R_{\mathrm{w}} + R_{\mathrm{p}} = \rho\Omega^{2/3}U^2 C$ where:

$$C(\alpha, \beta, \mathrm{Fr}) = \frac{\beta^{2/3}}{\alpha^{4/3}}\left\{\frac{4}{\pi\mathrm{Fr}^4}G_{\tilde{f}}(\mathrm{Fr}, \beta) + C_h(\alpha)\alpha\left[a_{\tilde{f}} + \frac{\alpha}{\beta}b_{\tilde{f}}(\alpha)\right]\right\} \ . \tag{3.9}$$

Thus, within the present framework, the total drag coefficient is completely determined by the three dimensionless variables α, β and Fr, together with the function $\tilde{f}$.

We seek the optimal hull shapes, that is the choice of parameters that minimises the total drag for a given load (equivalently immersed volume through the Archimedes principle) and given propulsive power. This is consistent with operational conditions. Before engaging in any calculations, let us stress that the optimal aspect ratios will naturally result from a subtle balance between skin drag, pressure drag and wave drag. Indeed, on the one hand reducing skin drag amounts to minimising the wetted surface which corresponds to rather

---

[2]This empirical expansion is expected to hold for $\alpha \gtrsim 2$ (see [10]).
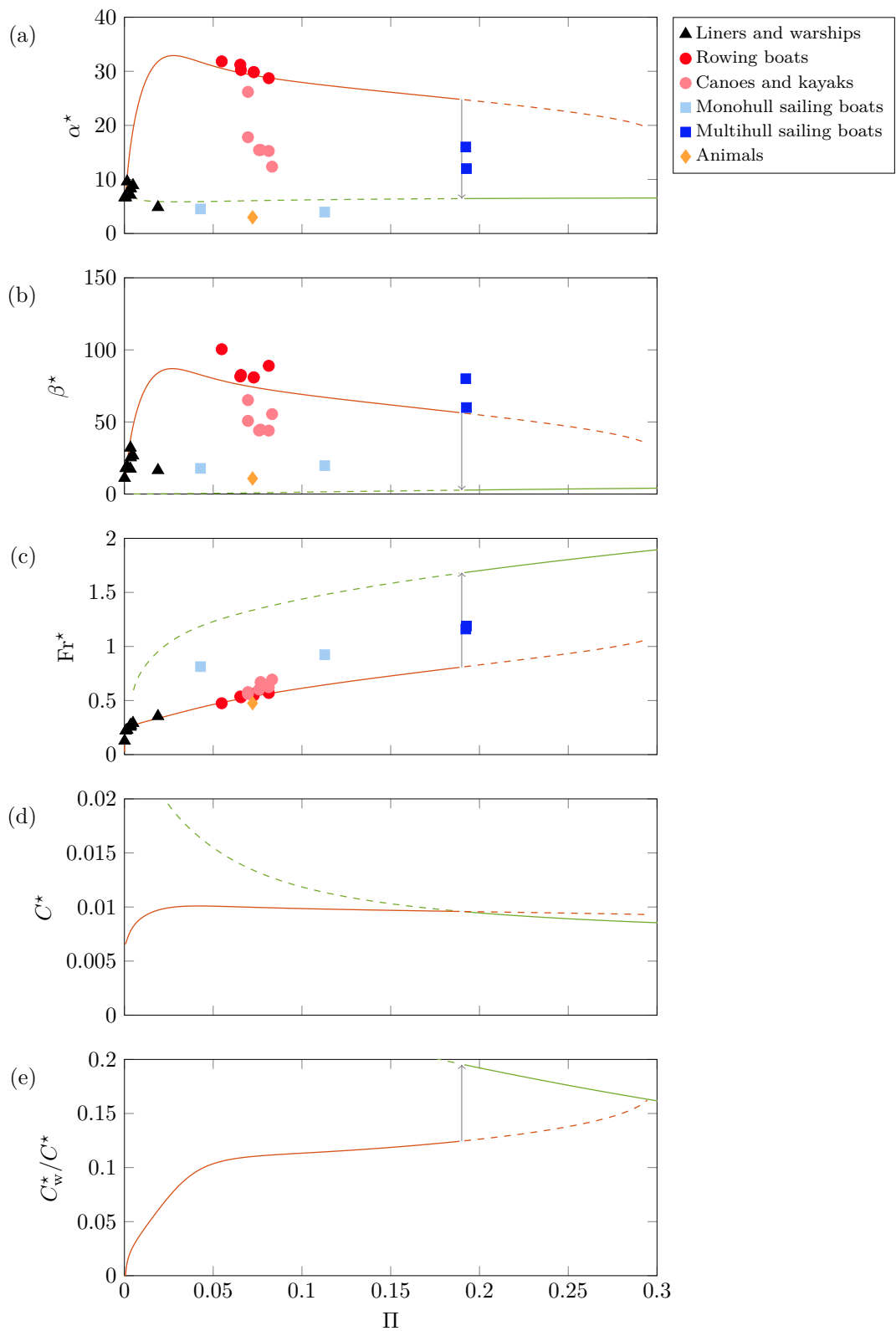
Figure 3.6: (a) Optimal aspect ratio $\alpha^\star$, (b) optimal aspect ratio $\beta^\star$, (c) optimal Froude number $\mathrm{Fr}^\star$, (d) corresponding value of the total drag coefficient $C^\star = C(\alpha^\star, \beta^\star, \mathrm{Fr}^\star)$, and (e) corresponding ratio between the wave drag coefficient and the total drag coefficient $C_{\mathrm{w}}^\star/C^\star$, as a function of the dimensionless power Π. The curves in orange and green represent the two optimal branches. Solid/dashed lines indicate global/local optima.

bulky hulls[3] (see Fig. 3.5(e)), while on the other hand reducing wave drag or pressure drag pushes towards rather slender hulls (see Figs. 3.5(a-c) and (d)). In Figs. 3.5(c) and (f) one can notice that for sufficiently large α and β the gradients $\boldsymbol{\nabla} C_{\mathrm{p}}$ and $\boldsymbol{\nabla} C_{\mathrm{w}}$ roughly point in opposite directions. This is totally coherent with the scalings derived in the previous sections for both the wave drag coefficient C_{w} and the profile drag coefficient C_{p}. Indeed, for large aspect ratios ($\alpha \gg 1$, $\beta \gg 1$), C_{w} scales as $(\alpha\beta)^{-4/3}$, promoting large aspect ratios, while C_{p} scales as $(\alpha\beta)^{2/3}$, in favor of rather small aspect ratios.

To close the problem, we define the imposed propulsive power $\mathcal{P} = RU$. Using $U = \mathrm{Fr}[\alpha\beta\Omega g^3]^{1/6}$ one obtains:

$$\mathrm{Fr}^3 \sqrt{\alpha\beta}\, C(\alpha, \beta, \mathrm{Fr}) = \Pi \;, \tag{3.10}$$

where $C(\alpha, \beta, \mathrm{Fr})$ is given by Eq. (3.9), and where we have defined the dimensionless power:

$$\Pi = \frac{\mathcal{P}}{\rho g^{3/2}\Omega^{7/6}} \;. \tag{3.11}$$

Minimising the total drag coefficient C as given by Eq. (3.9) with respect to α, β and Fr, under the constraint given by setting the dimensionless power Π in Eq. (3.10), yields the optimal set of parameters $(\alpha^\star, \beta^\star, \mathrm{Fr}^\star)$ for the optimal hull geometry at given load (equivalently Ω) and given propulsive power $\mathcal{P}$. This optimisation problem can be written:

$$\min_{(\alpha,\beta,\mathrm{Fr})\in K} C(\alpha, \beta, \mathrm{Fr}) \;, \tag{3.12}$$

where K is the set of triplets of real and positive parameters (α, β, Fr) satisfying Eq. (3.10).

It is solved numerically using an interior-point algorithm [81, 82]. The optimal parameters and the resulting total drag coefficient $C^\star = C(\alpha^\star, \beta^\star, \mathrm{Fr}^\star)$ as function of dimensionless power Π, are presented in Fig. 3.6, together with the empirical data points for comparison.

Interestingly the optimisation yields two separate solutions (see orange and green branches) corresponding to two local optima. For $\Pi \leq \Pi_{\mathrm{c}}$ (resp. $\Pi \geq \Pi_{\mathrm{c}}$) with $\Pi_{\mathrm{c}} \approx 0.2$, the orange (resp. green) branch constitutes the global optimum, consistent with a lower total drag coefficient $C^\star$ (see Fig. 3.6(d)). As previously mentioned, at large aspect ratios ($\alpha \gg 1$, $\beta \gg 1$), both the drag coefficients C_{w} and C_{p} have the same scalings in α and β. This explains why, on Figs. 3.6(a) and (b), the optimal aspect ratios $\alpha^\star$ and $\beta^\star$ show very similar evolutions with Π. On the one hand, both of them are maximal around $\Pi_{\mathrm{max}} \approx 0.03$ corresponding to $\mathrm{Fr}_{\mathrm{max}} \approx 0.4$, that is the maximum wave drag regime (see Fig. 3.4). This is consistent with the idea that thin and shallow hulls are favourable in terms of wave drag as illustrated in Fig. 3.5(a1-c1). On the other hand, for $\Pi \ll \Pi_{\mathrm{max}}$ or $\Pi \gg \Pi_{\mathrm{max}}$ the wave drag becomes negligible compared to the profile drag, and one recovers the optimal aspect ratios in the absence of wave drag: $\alpha^\star \simeq 7$ and $\beta^\star \simeq 10$. Figure 3.6(c) shows that the optimal Froude number $\mathrm{Fr}^\star$ increases with Π. Like for $\alpha^\star$ and $\beta^\star$, there is a shift of value from $\mathrm{Fr}^\star \approx 0.8$ to $\mathrm{Fr}^\star \approx 1.7$, for $\Pi = \Pi_{\mathrm{c}}$, which indicates that in this setting $0.8 < \mathrm{Fr} < 1.7$ is never a suitable choice. This shift is also made visible in Fig. 3.2 where the optimal aspect ratio $\alpha^\star$ is plotted against the Froude number together with the aspect ratio of existing hulls. The results of the optimisation obviously depend on the Reynolds number, through the value of the coefficient C_{s}^∞, but only weakly. Let us stress that, while for the optimal geometries ($\alpha^\star$, $\beta^\star$) the profile drag is always the dominant force regardless of the Froude number, our study shows that it is crucial to consider the wave drag in the optimisation. In

---

[3]With no constraint on the geometry of the hull, the shape minimising the wetted surface is a spherical cap.

particular, far from the optimal aspect ratios, the wave drag coefficient can surely become dominant. In Fig. 3.6(e), the ratio between the wave drag coefficient and the total drag coefficient on the optimal curve is represented as a function of the dimensionless power Π. We can see that, in the range $\Pi \in [0.05, 0.15]$, this ratio is about 0.1. This means that for rowing boats, which typically lie in this range, the wave drag is about 10 % of the total drag. This order of magnitude is comparable to the one found in literature (see [61] and Sect. 2.5).

3.6   Discussion

Our work provides a self-consistent framework to understand and discuss the design of existing boats.

3.6.1   Comparison with real data

Figure 3.6 confronts data from bodies moving at the water surface (*e.g.* liners, rowing boats, sailing boats or animals, see also Table 3.1) with the calculated optimal geometries. As one can see, while some ship categories are found in a rather good agreement with the theoretical predictions (such as liners and warships), others are very far from the computed optima (such as monohull sailing boats). Discrepancies with empirical data might primarily come from other constraints on the design of the boat which can prevail on the minimisation of the drag, such as stability, manoeuvrability, resistance to rough seas or seakindliness. They could also come from the assumptions of our model. In particular, a steady motion is considered here, while for rowing boats and sprint canoes, high fluctuations of speed are encountered (about 20% of the mean velocity) and are expected to affect the total drag, notably through added mass.

Back to racing shells. The case of rowing boats [83, 84], sprint canoes and sprint kayaks is of particular interest as they do not really have other constraints than the minimisation of the total drag. Indeed, manoeuvrability is not relevant as they usually only have to go along straight lines, stability is at its edge and they only need to carry the athletes, usually on very calm waters. The data for racing shells are found in good agreement with the optimal Froude number $\mathrm{Fr}^\star(\Pi)$. For rowing shells, while the aspect ratios α are found quite close to the optimal value, the aspect ratios β lie above the optimal curve. This indicates that rowing shells could be shorter or have a larger draft. This discrepancy might be related to the need for sufficient spacing between rowers (long shells) and/or for stability (small draft). For sprint canoes and sprint kayaks, the competition rules from the *International Canoe Federation* [85] impose maximal lengths for the boats[4] which could explain their relatively low aspect ratio α compared to the optimal one. Their aspect ratio β is also found slightly lower than the optimal results.

---

[4]The maximal lengths for sprint canoes and sprint kayaks are the same for the categories C1 and K1 (5.2 m), C2 and K2 (6.5 m) but not for C4 (9 m) and K4 (11 m) (see also Table 3.1). The letter C (resp. K) refers to sprint canoes (resp. sprint kayaks), and the following number indicates the number of rowers.

3.6.2 Discussion on stability

For the monohull sailing boats, the significant difference between real data and the computed optima surely comes from the need for stability. A simple criterion for static stability[5] can be derived for the model hull presented in Fig. 3.3, considering that it is a homogenous body of density $\rho_s < \rho$ (see Fig. 3.7).
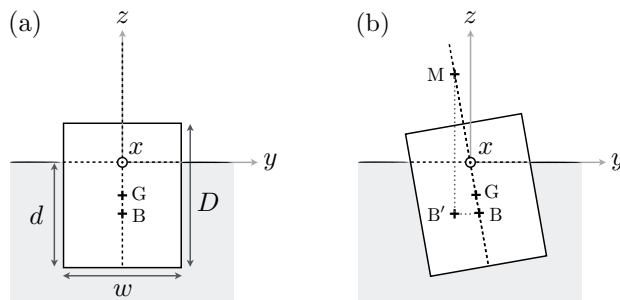

Figure 3.7: Cross-section of the model hull (see Fig. 3.3) in (a) vertical position and (b) slightly inclined position.

We define the center of gravity G, the center of buoyancy B, and the metacenter M [19, 20] as the point of intersection of the line passing through B and G and the vertical line through the new centre of buoyancy B′ created when the body is displaced (see Fig. 3.7(b)). Imposing that the metacenter be above the center of gravity reads $\overline{\text{GM}} > 0$, or equivalently $\overline{\text{BM}} > \overline{\text{BG}}$. On the one hand, the so-called metacentric height BM can be computed for small inclination angles through the longitudinal moment of inertia of the body $\mathscr{I} = (8c_{\tilde{f}})w^3\ell/12$ with $c_{\tilde{f}} = \int_{-1/2}^{1/2}[\tilde{f}(\tilde{x})]^3\,\mathrm{d}\tilde{x}$ and the immersed volume $\Omega_{\mathrm{i}} = 2a_{\tilde{f}}\Omega$ as:

$$\text{BM} = \frac{\mathscr{I}}{\Omega_{\mathrm{i}}} = \frac{c_{\tilde{f}}}{3a_{\tilde{f}}}\frac{w^2}{d}\ . \tag{3.13}$$

On the other hand, one has BG $= (D - d)/2$ where D is the total height of the hull. We then use the static equilibrium $\rho_s\Omega_{\mathrm{tot}} = \rho\Omega_{\mathrm{i}}$, where $\Omega_{\mathrm{tot}} = 2a_{\tilde{f}}w\ell D$ is the total volume of the body, to eliminate D. This finally yields the criterion $w/d > \psi(\rho_s/\rho)$ with:

$$\psi(u) = \sqrt{\frac{3a_{\tilde{f}}}{2c_{\tilde{f}}}\left(\frac{1}{u} - 1\right)}\ , \quad u \in [0,1]\ . \tag{3.14}$$

ψ is a decreasing function of u. For neutrally buoyant bodies, $\psi(1) = 0$, all configurations are stable as B and G coincide. While for bodies floating well above the level of water, $\lim_{u\to 0}\psi(u) = +\infty$, then wide and shallow hulls are required to ensure stability. In the specific model case of Fig. 3.3, one has $a_{\tilde{f}} \approx 0.33$, $c_{\tilde{f}} \approx 0.057$ and thus $\psi(u) \approx 3\sqrt{1/u - 1}$. Thus, the latter criterion reads: $w/d = \beta/\alpha > \psi(\rho_{\mathrm{s}}/\rho)$ where ψ is defined in Eq. (3.14). For real boats, the critical value of w/d depends on mass distribution and effective density of the hull and is highly affected by the presence of a keel, intended to lower the position of the center of gravity. This stability criterion constitutes an additional constraint that could be easily taken into account in the optimisation problem and that would reduce the search space. In short, stability favours wide and shallow ships. This explains why most real data points lie below the optimal curve $\alpha^\star(\Pi)$ in Fig. 3.6(a) but above the curve $\beta^\star(\Pi)$ in Fig. 3.6(b). Stability is all the more important for sailing boats where the action of

---

[5]Note that for real hull design one should also address dynamic stability [71], but the latter falls beyond the scope of our study.

the wind on the sail contributes with a significant destabilising torque. Interestingly, this matter is overcome for multihull sailing boats, in which both stability and optimal aspect ratios can be achieved by setting the appropriate effective beam, namely the distance between hulls [86]. This allows higher hull aspect ratios, closer to the optimal curves in Fig. 3.6.

3.6.3   Discussion on planing

As displayed in Fig. 3.6(c), we predict a shift in the Froude number for $\Pi \approx 0.2$ which indicates that boats should not operate in the range of Froude numbers $\mathrm{Fr} \in [0.8, 1.7]$. However, when the Froude number is above $\mathrm{Fr} \approx 0.7$, the hulls start riding their own bow wave: they are planing. Their weight is then mostly balanced by hydrodynamic lift rather than static buoyancy [10, 20]. As planing is highly dependent on the hull geometry and would require to consider tilted hulls, we do not expect our model to hold in this regime. Some changes though allow to understand the basic principles. Planing drastically reduces the immersed volume of the hull which in turn reduces both the wave drag and the profile drag. The effect on the immersed volume can be taken into account by adding the hydrodynamic lift in the momentum balance along the vertical direction. Thus, one has: $Mg \simeq \rho\Omega_{\mathrm{i}}g + 1/2\rho C_L \ell w \sin(2\theta)U^2$ where M is the mass of the boat, C_L is the lift coefficient, and $\theta(\mathrm{Fr})$ is the Froude-dependent angle of the hull with respect to the horizontal direction of motion [10, 20]. This leads to an immersed volume which depends on the Froude number through:

$$\Omega_{\mathrm{i}}(\mathrm{Fr}) \simeq \frac{\Omega_{\mathrm{i}}(0)}{1 + C_L \beta \sin(2\theta)\mathrm{Fr}^2/(4a_{\tilde{f}})} \ , \tag{3.15}$$

where $\Omega_{\mathrm{i}}(0) = M/\rho$. For low Froude number, $\theta(\mathrm{Fr}) \simeq 0$ and the volume is that imposed by static equilibrium, while for larger Fr number $\theta > 0$ and the volume $\Omega \sim \Omega_{\mathrm{i}}$ is decreased. Note that foil devices also contribute to decreasing the immersed volume by increasing the lift.

Eventually, our study provides the guidelines of a general method for hull-shape optimisation. It does not aim at presenting quantitative results on optimal aspect ratios, in particular due to the simplified geometry we consider and the limitations of Michell's theory for the wave drag estimation [28, 33, 87]. However, our method can be applied in a more quantitative way for each class of boat by considering more realistic hulls.

3

> ### Take home message of Chapter 3
>
> **1.** In ship hull design, the minimisation (under constraints) of the total drag on the hull is one of the main challenges. The different drag components have opposite effects: wave drag and pressure drag decrease with increasing aspect ratios and thus favour slender hulls, while skin drag is minimal for rather low aspect ratios and favours more bulky hulls.
>
> **2.** Using a simple theoretical approach (based on a simplified hull geometry), we derive the optimal aspect ratios for ship hulls regarding the minimisation of the total drag, at a given load and propulsive power.
>
> **3.** Optimal aspect ratios mostly depend on the imposed propulsive power. For low propulsive power (equivalently Froude number $Fr \ll 0.5$) and for high propulsive power (equivalently $Fr \gg 0.5$), the wave drag is negligible and the optimal hulls are rather bulky, while for intermediate propulsive power (corresponding to $Fr \simeq 0.5$), they are rather thin to minimise the wave drag.
>
> **4.** The aspect ratios of rowing boats are in good agreement with the optimal ones. The discrepancies observed for other boat categories, such as sailing boats, come from the importance of other constraints, such as stability or manoeuvrability.

4

A QUESTION OF ASYMMETRY

The purpose of this chapter is to assess the effect of the asymmetry of a hull on its total drag and in particular on its wave drag. We consider a set of hulls of increasing asymmetry and determine both experimentally and numerically their drag to find the optimal asymmetry. The comparison between the two approaches provides new insights in the context of the optimisation of hull shapes.
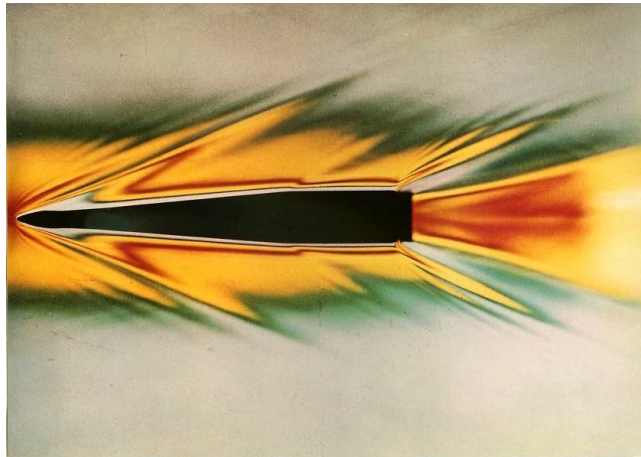
Supersonic flow around a wedge without incidence. Photo credits: Henri Werlé, ONERA.

Contents

4.1 Problem statement

After having analysed in the previous chapter the optimal aspect-ratios for ship hulls, we study the effect of the asymmetry between the front and the rear of a boat and pose the question of whether this asymmetry could decrease the total drag on the hull. On the one hand, when an object is moving in a homogeneous fluid, to avoid flow separation and thus minimise the pressure drag, it should be pointed at the rear and rather look like an airfoil profile (see Fig. 1.3). This is qualitatively what Huan *et al.* found when seeking numerically the two-dimensional shapes of minimum drag for different Reynolds numbers (see Fig. 4.1(a)-(c)) [88, 89]. For example, the *Dymaxion* car (see Fig. 4.1(d)), designed by the American inventor and architect Buckminster Fuller in 1933, has an aerodynamic bodywork to reduce its fuel consumption [90]. On the other hand, when the object is moving at the water surface, to create the least waves and thus reduce the wave drag, it should rather be narrow at the front. Consequently, for ship hulls, which are exposed to both pressure drag and wave drag, it is unknown whether asymmetry is optimal.
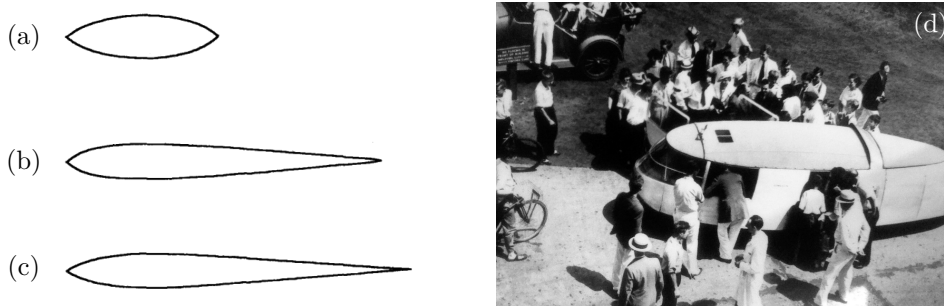
Figure 4.1: Two dimensional shapes of minimum drag found by [88] for (a) Re = 20, (b) Re = 5 000 and (c) Re = 20 000. (d) Picture of the *Dymaxion* car n°1, designed by the American inventor and architect Buckminster Fuller in 1933. This car had an aerodynamic bodywork to increase its fuel efficiency and reach top speed [90].

4.1.1 Asymmetry of existing hulls

As already mentioned, a large variety of shapes is found among ship hulls, in particular because of the number of constraints that hulls must satisfy depending on their function (stability, manoeuvrability, drag minimisation, sea-kindliness, ...).

Figure 4.2: Pictures of (a) a sprint canoe, (b) a sprint kayak, and (c) a single scull rowing boat. The three boats are moving from right to left. Pictures have been rescaled (see Table 2.1 for the characteristics of rowing boats and Table 5.1 for the characteristics of sprint canoes and sprint kayaks).

If one takes a closer look at sprint canoes (Fig. 4.2(a)), sprint kayaks (Fig. 4.2(b)), and rowing boats (Fig. 4.2(c)), hulls for which the main constraint is the drag minimisation, one can notice that, while rowing boats are nearly symmetric, sprint canoes and sprint kayaks are found narrower at the front than at the rear.

In this section, we focus on sprint canoes as it is easy to roughly estimate the asymmetry of these hulls from their top-view picture.[1] As defined in Sect. 1.6, we use the dimensionless coordinates $\tilde{x} = x/\ell$ and $\tilde{y} = y/\ell$ as well as the function $\tilde{f}(\tilde{x}) = f(x)/w$ that represents the edge of the hull (with $\tilde{x} \in [-1/2, 1/2]$). Fig. 4.3(a)-(c) shows three different canoes hulls $C1$.[2] The projected edge of each of these hulls $f(x)$ is obtained through image analysis and is plotted in dimensionless form $\alpha \tilde{y} = \tilde{f}(\tilde{x})$ (with $\alpha = \ell/w$) in Fig. 4.3(d). One can thus observe the differences between different hull models; in particular the *C1 Vanquish III* has a clearly more asymmetric shape than the two other hulls.
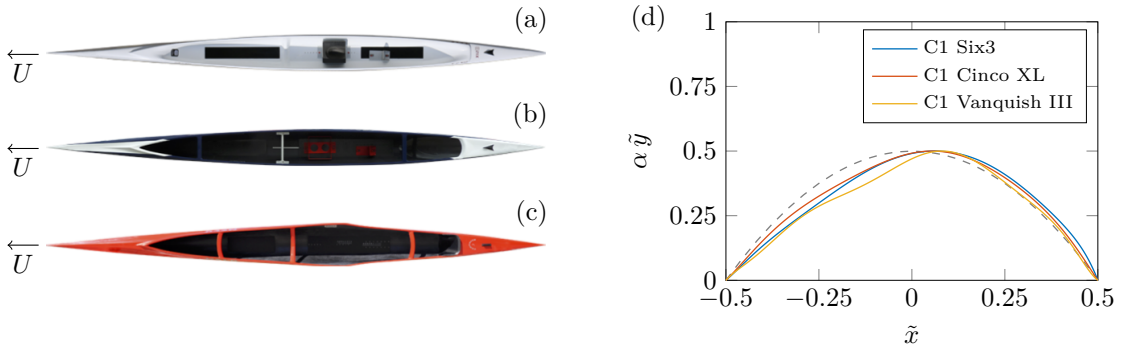

Figure 4.3: (a)-(c) Top view of three sprint canoes hulls (from *Nelo* manufacturer [91]), (a) *C1 Six3*, (b) *C1 Cinco XL* and (c) *C1 Vanquish III*. (d) Position of the edge of the hull $\alpha \tilde{y} = \tilde{f}(\tilde{x})$ for the three hulls (a), (b) and (c). The gray dashed line represents a parabolic hull profile.

In order to characterise the asymmetry of hulls, we define the asymmetry parameter ϵ as follows:

$$\epsilon = \kappa \left(\int_0^{1/2} \tilde{g}(\tilde{x})^2 \, \mathrm{d}\tilde{x} \right)^{1/2} , \tag{4.1}$$

where $\tilde{g}(\tilde{x}) = \tilde{f}(\tilde{x}) - \tilde{f}(-\tilde{x})$ and $\kappa = -\mathrm{sign}(\int_0^{1/2} \tilde{g}(\tilde{x}) \, \mathrm{d}\tilde{x})$. Except from the factor κ, this is the L^2 norm of the odd function $\tilde{g}(\tilde{x})$. The factor $\kappa = \mathrm{sign}(\epsilon)$ is introduced to distinguish between the two directions of motion of an asymmetric hull.
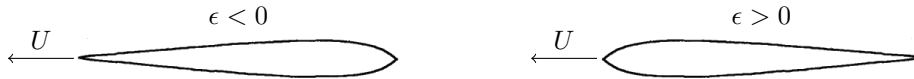
Figure 4.4: Schematics illustrating the two different configurations $\epsilon < 0$ and $\epsilon > 0$.

For example, a typical airfoil profile, such as a NACA profile (see Fig. 1.3), would have a positive asymmetry parameter ϵ when moving along its usual direction of motion (with the rounded part first), but a negative ϵ when moving in the reversed direction (with the

---

[1] A more accurate estimate would be obtained by considering their three-dimensional hull shape.
[2] *C1* refers to sprint canoes with only one rower, while *C2* and *C4* stand for sprint canoes with two and four rowers respectively.

pointed part first) (see Fig. 4.4).[3] The values of the asymmetry parameter for the three different hulls in Fig. 4.3 are given in Table 4.1. Consistent with what is observed in Fig. 4.3, the *C1 Vanquish III* hull is the most asymmetric one, then comes the *C1 Six3* and finally the *C1 Cinco XL*. Interestingly, it can be noticed that for these three hulls, the asymmetry parameter ϵ is negative, meaning that the front of the hull is more pointed than the rear.

Boat Name	ϵ
C1 Six3	-0.0588
C1 Cinco XL	-0.0386
C1 Vanquish III	-0.0597

Table 4.1: Asymmetry parameter ϵ for the three sprint canoes hulls shown in Fig. 4.3. As a means of comparison, for a triangular hull profile, one has $|\epsilon| \simeq 0.2$.

To sum up, we observe that sprint canoes are slightly asymmetric: they are narrower at the front than at the rear. The asymmetry is quantified with the parameter ϵ (see Eq. (4.1)). It is found to change from one boat to another within a given boat category and with the number of rowers.

4.1.2   Theoretical observations

This study started with the surprising observation that for the two theoretical models presented in Sect. 1.6, the prediction for the wave drag of an asymmetric hull is the same if the hull moves forward or backward, which contradicts experimental observations.

Havelock's model. In the expression of the wave drag given in Eq. (1.33), the pressure disturbance appears as $|\hat{p}(k_x, k_y)|^2$. To begin with, let us assume that the pressure disturbance $p(x, y)$ is changed into $p'(x, y) = p(-x, y)$ when the body moves in the opposite direction. As the pressure disturbance is symmetric about the center-plane $y = 0$ (left-right symmetry of the hull), then $p'(x, y) = p(-x, -y)$, so that when one takes the Fourier transform:

$$\hat{p}'(k_x, k_y) = \hat{p}(k_x, k_y)^\star \ , \tag{4.2}$$

where $\star$ denotes the complex conjugate. It can be deduced that the wave resistance R_w will be the same for both directions of motion. In fact, the assumption that the pressure disturbance is only reversed when changing the direction of motion of the body is obviously wrong. We conducted experiments to determine how the pressure distribution along an asymmetric hull changes depending on its direction of motion. The first results of this ongoing work are very promising (see Appendix B).

Michell's model. In this second model, changing the direction of motion is equivalent to replacing $f(x, z)$ by $f(-x, z)$ in Eq. (1.46). With a change of variable, one finds that $\mathcal{I}_f$ is then changed into $\mathcal{I}_f^\star$ and, as $\mathcal{I}_f$ appears as $|\mathcal{I}_f|^2$ in Eq. (1.45), one finds the same wave resistance in both directions of motion.

The identity of the wave resistance predicted by these two theoretical models when the body moves forward or backward comes from the use of the potential flow theory which leads to time-reversibility of the flow. As a first step to build a new theory that can include asymmetry in the wave drag, we study experimentally and numerically the effect of the hull asymmetry on the total drag and in particular on the wave drag component.

---

[3]Note that another asymmetry parameter could be the "infinity norm" $\epsilon_\infty = \kappa \max |\tilde{g}(\tilde{x})|$ or the "L^1 norm" $\epsilon_1 = \kappa \int_0^{1/2} |\tilde{g}(\tilde{x})| \, \mathrm{d}\tilde{x}$. The asymmetry parameters ϵ, ϵ_∞ and ϵ_1 can be generalised in 3d for hulls defined by $y = f(x, z)$.

4.2 Family of hull shapes

First, we aim at defining a family of hull shapes that continuously varies from perfectly symmetric to more and more asymmetric. To be able to compare the shapes, we should keep the cross-sectional area constant (so that, for a given draft, the immersed volume remains the same for all shapes) as well as the length-to-width aspect ratio, the effect of which was already analysed in Chap. 3. Thus, the function $\tilde{f}$ must satisfy the following constraints:

- $\tilde{f}(-1/2) = \tilde{f}(1/2) = 0$,

- $\int_{-1/2}^{1/2} \tilde{f}(\tilde{x})\,\mathrm{d}\tilde{x} = a_{\tilde{f}}$, where $a_{\tilde{f}}$ is a given dimensionless area (see Eq. (3.7a) in Sect. 3.4),

- $\max \tilde{f}(\tilde{x}) = \tilde{f}(\tilde{x}_0) = 0.5$, where $\tilde{x}_0$ is the position of the maximum of $\tilde{f}$.

A suitable function is:

$$\tilde{f}(\tilde{x}) = a \ln \left[\frac{1+b}{e^{\alpha(\tilde{x}-1/2)} + b e^{-\alpha\beta(\tilde{x}-1/2)}} \right] , \tag{4.3}$$

with the coefficients a, b, α and β that are numerically computed to satisfy the constraints. One of the advantages of this particular form of functions (compared with, for example, polynomial functions) is that it allows us to adjust the slope of the tangents in $\tilde{x} = -1/2$ and $\tilde{x} = 1/2$ by setting the values of α and β. Furthermore, it must be noted that the surface $a_{\tilde{f}}$ is set to $a_{\tilde{f}} = 0.312$ so that functions of the form given in Eq. (4.3) that satisfy the constraints can be found. Other functions could be defined, such as the Hügelschäffer egg [92], which we did not explore further.
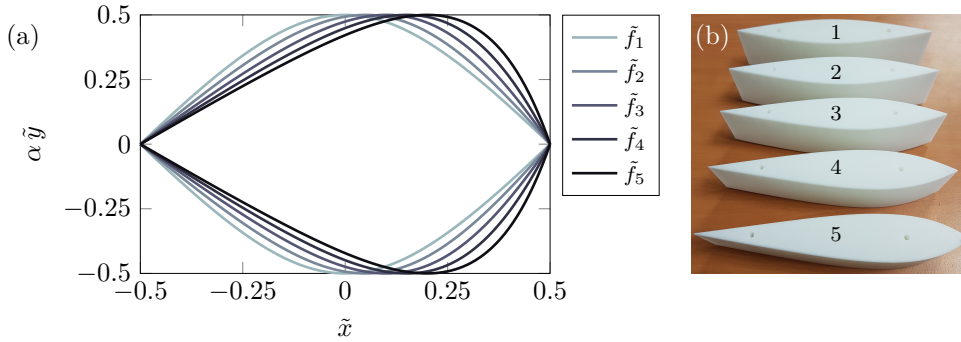

Figure 4.5: (a) Profile $\alpha\tilde{y} = \pm\tilde{f}(\tilde{x})$ for five different sets of the parameters (a, b, α, β) in Eq. (4.3), with increasing asymmetry. (b) Picture of the five 3d-printed model hulls defined by the functions $\tilde{f}_1$ to $\tilde{f}_5$. They are 18 cm-long, 3 cm-wide and 5 cm-high.

Figure 4.5(a) shows the profile of five particular functions, denoted $\tilde{f}_i$ (with $i \in \{1,2,3,4,5\}$), for $\tilde{x}_0$, the position of the maximum of $\tilde{f}$, ranging from 0 to 0.2 with uniform spacing. The coefficients a, b, α and β for these five functions are indicated in Table 4.2. The function $\tilde{f}_1$ is symmetric, then the functions $\tilde{f}_2$ to $\tilde{f}_5$ are more and more asymmetric (see the corresponding values of ϵ in Table 4.2).

In the following, the aim is to determine, both experimentally and numerically, the drag on these five particular hull shapes.

Function	a	b	α	β	ϵ
$\tilde{f}_1$	0.460	0.030	3.500	1	0
$\tilde{f}_2$	0.488	0.066	4.182	0.660	-0.040
$\tilde{f}_3$	0.592	0.163	4.864	0.402	-0.080
$\tilde{f}_4$	0.937	0.500	5.500	0.199	-0.114
$\tilde{f}_5$	9.007	9.195	6.091	0.017	-0.144

Table 4.2: Coefficients (a, b, α, β) defining the five functions $\tilde{f}_1$ to $\tilde{f}_5$, with the corresponding values of the asymmetry parameter ϵ.

4.3 Experimental study

Experiments were carried out with Varvara Zhukovskaya (student from Peter the Great St. Petersburg Polytechnic University, Russia).

4.3.1 Description of the experimental set-up

The five particular hull shapes defined in the previous section were 3d-printed (see Fig. 4.5(b)). They are 18 cm-long, 3 cm-wide and 5 cm-high, corresponding to the aspect ratios $\alpha = \ell/w = 6$ and $\ell/D = 3.6$ (with D the total height of the hull).

(a)   (b)
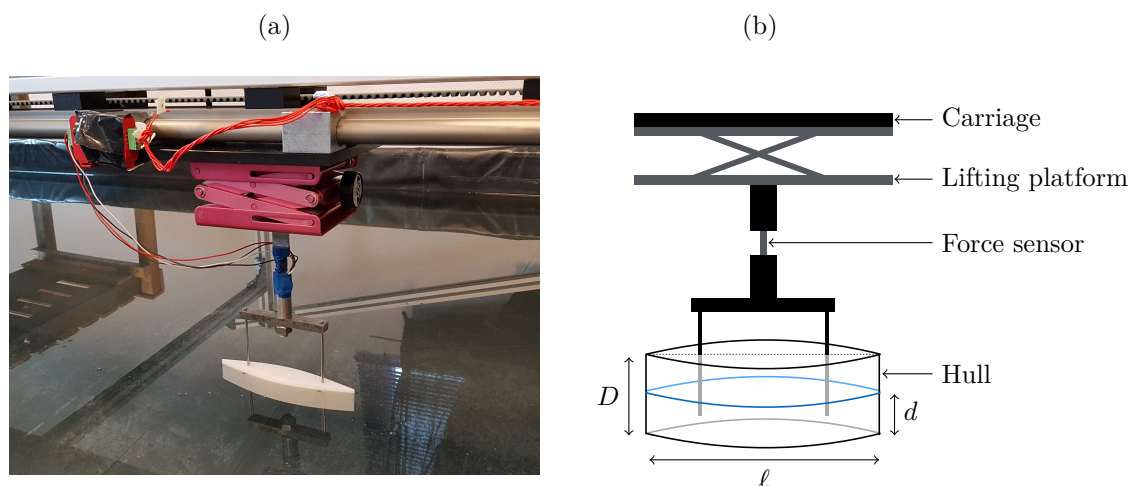
Figure 4.6: Picture (a) and schematics (b) of the experimental set-up. The hull is towed in a water tank via a carriage. A force sensor placed between the carriage and the hull measures the total drag force on the hull. A lifting platform allows us to change the immersion depth d (the distance from the bottom of the hull to the water surface). The total height of the hull is denoted D.

To measure their total drag, the different hulls were towed in a water tank (6 m long and 30 cm deep) with a force sensor placed between the carriage and the hull (see Fig. 4.6). The force sensor is composed of strain gauges stuck on a beam which links the hull and the carriage. The deformation measured by the strain gauges is related to the force exerted at the point of force application on the hull, a relation which is obtained through a calibration step. Three main parameters can be varied: the asymmetry of the hull (which depends on

the chosen hull and on its direction of motion), the speed U of the hull and its immersion d (*i.e.* the distance between the bottom of the hull and the free-surface). The corresponding dimensionless parameters are the asymmetry parameter ϵ (positive or negative depending on the direction of motion of the hull), the Froude number $\mathrm{Fr} = U/\sqrt{g\ell}$ and the ratio d/D, which compares the immersion d of the hull to its total height D (see Fig. 4.6). The drag force measured from the sensor is filtered and averaged on the time interval where the hull speed is constant. Each data point is the mean over three experiments. The measurements were carried out at a speed U ranging from 0.4 to 2 m/s, corresponding to a Froude number ranging from 0.3 to 1.5.

4.3.2 Experimental results

In the following, and similarly to the definitions of the drag coefficients in Chap. 1 and 3, the total drag coefficient C is defined by:

$$C = \frac{R}{\rho \Omega^{2/3} U^2} \; , \tag{4.4}$$

where R is the total drag force exerted on the hull and Ω scales as the immersed volume of the hull. One has: $\Omega = \ell w d$ when the hull is partly immersed, and $\Omega = \ell w D$ when the hull is fully immersed. The first measurements consisted in assessing the dependence of the total drag coefficient C with the Froude number and with the immersion depth d for a given hull.
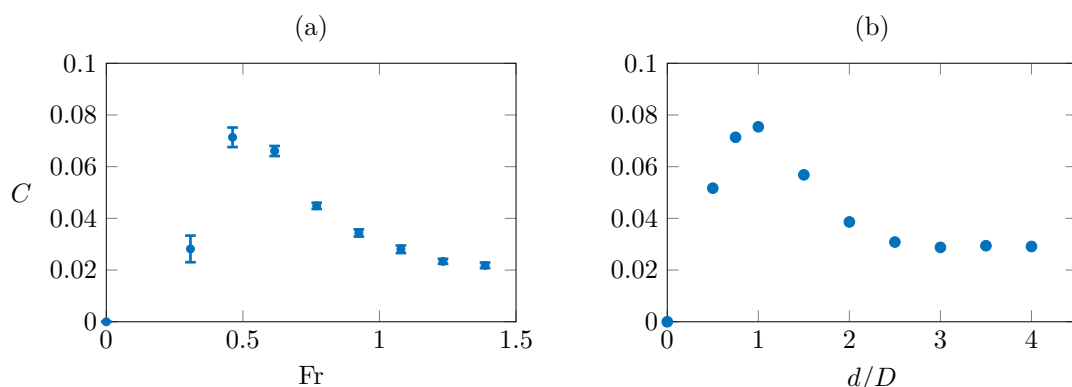

Figure 4.7: Total drag coefficient C for the symmetric hull (*i.e.* hull 1) as a function (a) of the Froude number for $d/D = 0.75$ and (b) of the ratio of immersion d/D for $\mathrm{Fr} = 0.46$. The data shown in (b) have been corrected for $d/D > 1$ to eliminate the contribution to the total drag of the two rods holding the hull (see Sect. 4.6).

Fig. 4.7(a) shows the evolution of the total drag coefficient C with the Froude number for the symmetric hull (*i.e.* hull 1, see Fig. 4.5) for the ratio of immersion $d/D = 0.75$. C reaches a maximum for $\mathrm{Fr} \simeq 0.5$, which is where the wave drag component is maximum (see Fig. 1.13 in Sect. 1.6). Fig. 4.7(b) displays the effect of the immersion depth on the total drag coefficient, for the symmetric hull and a given Froude number. The contribution to the total drag of the two rods holding the hull, when the hull is totally immersed (*i.e.* for $d/D > 1$) has been removed (see Sect. 4.6 for the details). One notices that C is maximum for $d/D = 1$. This can be explained by the additional contribution of the upper surface of the hull to the skin drag component when $d/D \geq 1$ and to the important contribution of the wave drag. One can also observe that the total drag coefficient reaches a plateau starting from $d/D \approx 2.5$. This corresponds to a regime where the hull is sufficiently far

from the water surface so that the wave drag component becomes negligible and does not contribute anymore to the total drag (see also Subsect. 7.3.3 in Chap. 7 for the same kind of discussion).
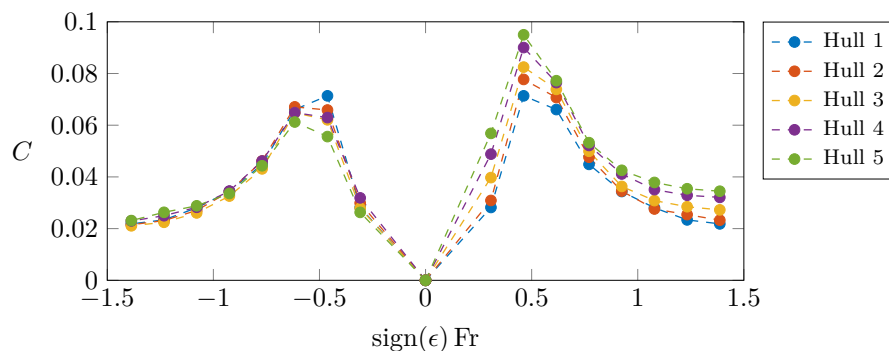

Figure 4.8: Total drag coefficient as a function of the signed Froude number $\text{sign}(\epsilon)\,\text{Fr}$ for the five hulls for $d/D = 0.75$. The use of the parameter $\text{sign}(\epsilon)\,\text{Fr}$ allows us to compare a given hull moving with the rounded part first ($\epsilon > 0$, right part of the plot) or with the pointed part first ($\epsilon < 0$, left part of the plot) (see Fig. 4.4).

The measurements of the total drag coefficient were then carried out for the five different hulls in both directions of motion. In Fig. 4.8, we plot C as a function of $\text{sign}(\epsilon)\,\text{Fr}$ for the five hulls at a given immersion. The parameter $\text{sign}(\epsilon)\,\text{Fr}$ is used to compare a given hull moving with the rounded part first ($\epsilon > 0$) or with the pointed part first ($\epsilon < 0$, see Fig. 4.4). The evolution of C with the Froude number for a given hull and a given direction of motion is similar to the one in Fig. 4.7(a). Comparing the different hulls, we find that, on the right part of the plot ($\epsilon > 0$), the maximum of drag is higher and higher as the hulls are more and more asymmetric (from hull 1 to hull 5). While, on the left part of the plot ($\epsilon < 0$), the maximum of drag is lower and lower as asymmetry is increased (from hull 1 to hull 5). Quantitatively, at $\text{Fr} = 0.46$, we observe, for $\epsilon > 0$, an increase in the total drag coefficient of about 33% between the symmetric hull and the most asymmetric one (hull 5), while, for $\epsilon < 0$, C is decreased by 22%.

Fig. 4.9 shows the contour plots of the total drag coefficient C for the five hulls depending on the parameter $\text{sign}(\epsilon)\,\text{Fr}$ and the immersion ratio d/D. Looking at a given contour plot,
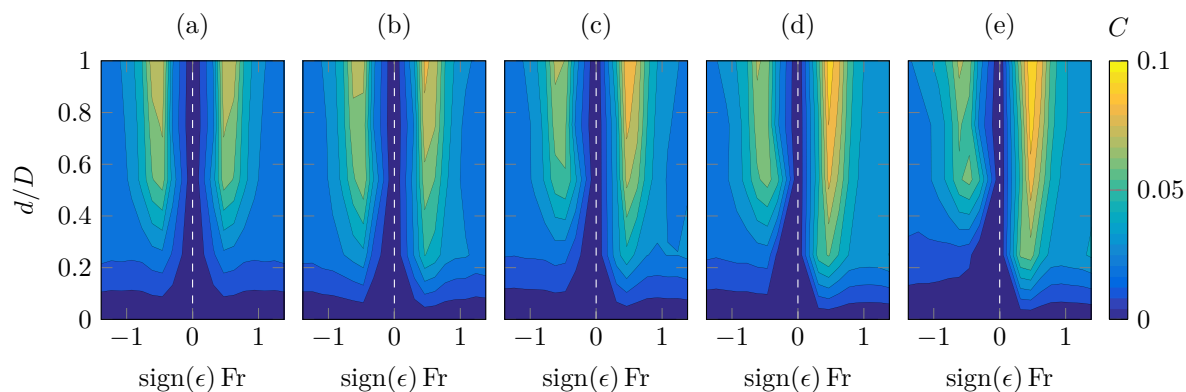

Figure 4.9: Contour plots of the total drag coefficient C depending on the signed Froude number $\text{sign}(\epsilon)\,\text{Fr}$ and the ratio of immersion d/D for hull 1 to 5 (a)-(e). The vertical dashed white line separates these two cases for each hull.

the same remarks as for Fig. 4.7(b) can be made, except that here the immersion ratio is restrained to $0 \leq d/D \leq 1$. When comparing the different hulls, it appears clearly that the contour plots become more and more asymmetric as the asymmetry is increased (from hull 1 to 5, see Fig. 4.9(a) to (e)).
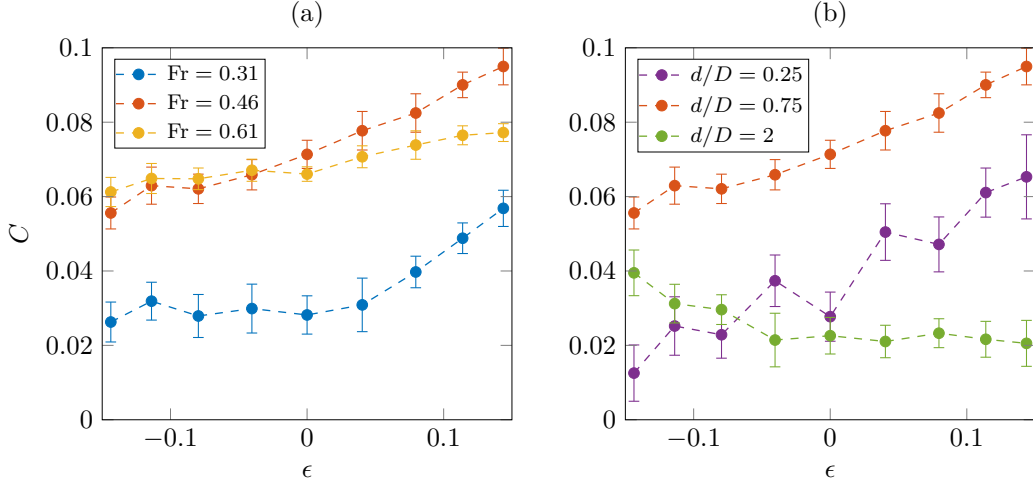

Figure 4.10: (a) Total drag coefficient C as a function of the asymmetry parameter ϵ (a) for three different values of the Froude number for $d/D = 0.75$, and (b) for three different values of the ratio of immersion d/D for Fr = 0.46.

The effect of the asymmetry is clearer in Fig. 4.10, where C is represented as a function of the asymmetry parameter ϵ depending on (a) the Froude number Fr or (b) the ratio of immersion d/D. For Fr = 0.46 and Fr = 0.61, the total drag coefficient is an increasing function of ϵ and the minimum drag coefficient is thus obtained for $\epsilon = -0.14$, that is for the most asymmetric hull (hull 5) moving with the pointed part first. For Fr = 0.31, C plateaus for $\epsilon \leq 0$, which could be related to the lower effect of the wave drag component. In Fig. 4.10(b), we observe that, while for $d/D = 0.25$ and $d/D = 0.75$, C is an increasing function of ϵ, for $d/D = 2$, it becomes a decreasing function of ϵ. This is due to the pressure drag component, which is larger for $\epsilon < 0$ and becomes dominant deep underwater. As a result, whilst at the water surface, optimal hulls are rather pointed at the front, deep under water optimal hulls are rather rounded at the front and pointed at the rear, similarly to the optimal shapes found in [88] (see Fig. 4.1(a-c)).

4.4 Numerical study

This numerical study was carried out by Louis Richard (student from ENS Cachan). The aim of this part is to compute the flow around the five hulls presented in Sect. 4.2 in order to compare the drag and wave pattern with the experiments.

4.4.1 Numerical set-up

To perform this study, we use the software *Gerris Flow Solver* (created by Stéphane Popinet and developed at *Institut Jean le Rond d'Alembert*, UPMC) which provides a framework to solve partial differential equations on quad/octree finite-volume meshes [93, 94]. Each hull is placed inside a three dimensional rectangular domain $\mathcal{D}$, composed of two fluids, air

and water, separated by a free-surface, initially at $\tilde{z} = \tilde{\xi}(\tilde{x}, \tilde{y}) = 0$. Using the left-right symmetry of the problem, it is solved only on one half of the fluid domain surrounding the hull, which considerably reduces the computation time. The computational domain approximately measures $9 \times 3 \times 3$ (in units of length of the hull).

The *Gerris* software solves the Navier-Stokes equations, that is:

$$\boldsymbol{\nabla} \cdot \boldsymbol{u} = 0 , \tag{4.5a}$$

$$\frac{\partial \boldsymbol{u}}{\partial t} + (\boldsymbol{u} \cdot \boldsymbol{\nabla})\boldsymbol{u} = -\frac{1}{\rho}\boldsymbol{\nabla}p + \nu\boldsymbol{\nabla}^2\boldsymbol{u} + \boldsymbol{g} , \tag{4.5b}$$

where $\nu = \mu/\rho$ is the kinematic viscosity. Using the dimensionless variables $\boldsymbol{u} = U\tilde{\boldsymbol{u}}$, $x = \ell\tilde{x}$, $y = \ell\tilde{y}$, $z = \ell\tilde{z}$, $p = \rho U^2\tilde{p}$, and $t = \ell/U\tilde{t}$, the dimensionless Navier-Stokes equations read:

$$\tilde{\boldsymbol{\nabla}} \cdot \tilde{\boldsymbol{u}} = 0 , \tag{4.6a}$$

$$\frac{\partial \tilde{\boldsymbol{u}}}{\partial \tilde{t}} + (\tilde{\boldsymbol{u}} \cdot \tilde{\boldsymbol{\nabla}})\tilde{\boldsymbol{u}} = -\tilde{\boldsymbol{\nabla}}\tilde{p} + \frac{1}{\mathrm{Re}}\tilde{\boldsymbol{\nabla}}^2\tilde{\boldsymbol{u}} - \frac{1}{\mathrm{Fr}^2}\boldsymbol{e}_z , \tag{4.6b}$$

where $\boldsymbol{e}_z$ is the unit vertical vector and, as defined before, $\mathrm{Re} = U\ell/\nu$ and $\mathrm{Fr} = U/\sqrt{g\ell}$. The flow is, as a first step, supposed to be inviscid ($\mathrm{Re} \to +\infty$) and is impulsively started from rest at $t = 0$ to reach the prescribed Froude number Fr.

Boundary conditions. Neumann or Dirichlet boundary conditions along the boundaries of the computational domain are imposed. The different boundaries are illustrated on Fig. 4.11.
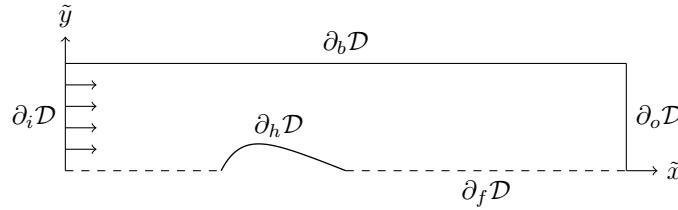

Figure 4.11: Schematics of a horizontal cross-section of the computational domain, with definition of the different boundaries. $\partial_i\mathcal{D}$ refers to the inlet boundary, while $\partial_o\mathcal{D}$ denotes the oulet boundary. $\partial_f\mathcal{D}$ and $\partial_b\mathcal{D}$ are the boundaries on the front and back sides of the domain and $\partial_h\mathcal{D}$ is the hull boundary. Two additional boundaries are not represented on this schematics: the top boundary $\partial_u\mathcal{D}$ and the bottom boundary $\partial_d\mathcal{D}$.

At the inlet $\partial_i\mathcal{D}$ and outlet $\partial_o\mathcal{D}$ boundaries, the velocity is considered unidirectional and thus we set:

$$\frac{\partial \tilde{u}_{\tilde{x}}}{\partial \tilde{x}} = 0, \ \tilde{u}_{\tilde{y}} = 0, \ \tilde{u}_{\tilde{z}} = 0, \ \text{and } \tilde{p} = 0 . \tag{4.7}$$

On the other sides of the domain, symmetry conditions are imposed, so that these boundaries are equivalent to free-slip, impermeable boundaries. Thus, for the sides $\partial_f\mathcal{D}$ and $\partial_b\mathcal{D}$, one has:

$$\frac{\partial \tilde{u}_{\tilde{x}}}{\partial \tilde{y}} = 0, \ \tilde{u}_{\tilde{y}} = 0, \ \frac{\partial \tilde{u}_{\tilde{z}}}{\partial \tilde{y}} = 0 \text{ and } \frac{\partial \tilde{p}}{\partial \tilde{y}} = 0 . \tag{4.8}$$

Similarly, for the top $\partial_u\mathcal{D}$ and bottom $\partial_d\mathcal{D}$ boundaries, one has:

$$\frac{\partial \tilde{u}_{\tilde{x}}}{\partial \tilde{z}} = 0, \ \frac{\partial \tilde{u}_{\tilde{y}}}{\partial \tilde{z}} = 0, \ \tilde{u}_{\tilde{z}} = 0, \ \text{and } \frac{\partial \tilde{p}}{\partial \tilde{z}} = 0 . \tag{4.9}$$

On the hull boundary $\partial_h \mathcal{D}$, an impermeability condition is imposed, that is $\tilde{\boldsymbol{u}} \cdot \boldsymbol{n} = 0$, with $\boldsymbol{n}$ the unit vector normal to the hull boundary. In the case of a viscous fluid, this condition would be replaced by a no-slip boundary condition ($\tilde{\boldsymbol{u}} = 0$). As *Gerris* software uses a Volume-of-Fluid advection scheme to resolve the position of the air-water interface, no boundary condition is imposed at the free-surface. An important feature of the code is the adaptive meshing refinement (using an octree finite volume discretisation). This has the advantages to increase the accuracy in the regions where the flow evolves with small scales and to reduce the computation time compared to algorithms with constant spatial resolution. Thus, in our case and as illustrated in Fig. 4.12, the mesh is refined at the hull boundary, at the air-water interface and in the regions of high vorticity. The computation time is however quite high (typically three days for Fr = 0.3).
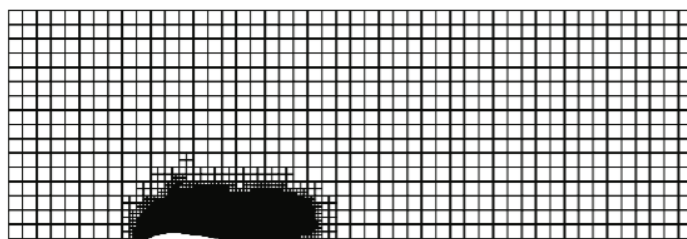

Figure 4.12: Mesh at the air-water interface for hull 4 soon after the beginning of the simulation. The mesh is refined in the region next to the hull.

The simulations are run until the computed flow converges to a steady flow. The outputs of the simulations are the resulting forces on the hull, the elevation of the free-surface and the pressure along the surface of the hull.

4.4.2 Numerical results

The simulations were carried for each hull moving forward and backward, with the Froude number Fr ranging from 0 to 0.3, and for an immersion ratio d/D ranging from 0 to 1. In Fig. 4.13, the resulting drag coefficient C', which is the total drag coefficient with no viscosity, is represented as a function of the two parameters Fr and d/D for each hull in the same way as for the experimental results (see Fig. 4.9). The right part (resp. left part) of each contour plot corresponds to the hull moving with the rounded part first (resp. with the pointed part first).
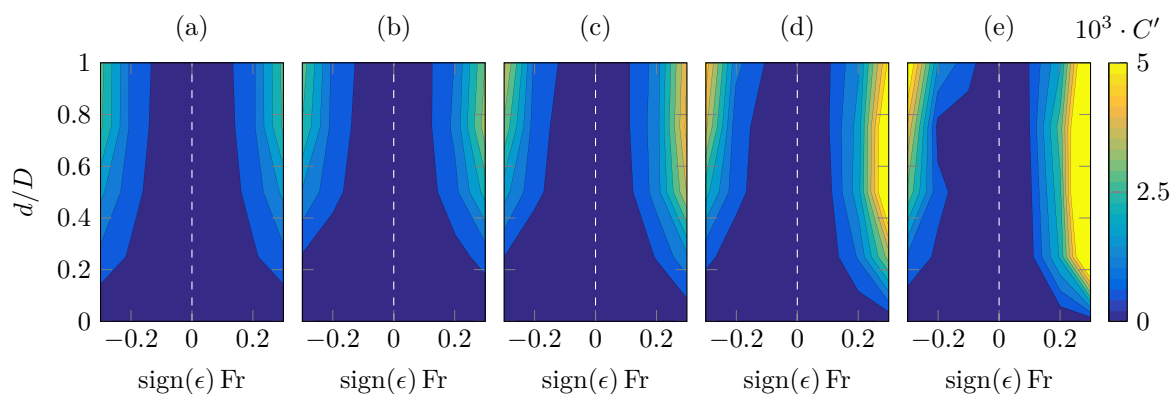
Figure 4.13: Contour plots of the total drag coefficient with no viscosity C' obtained numerically depending on the signed Froude number $\mathrm{sign}(\epsilon)\,\mathrm{Fr}$ and the ratio of immersion d/D for hull 1 to 5 (a)-(e). The vertical dashed white line separates these two cases for each hull.

As already observed with the experiments, we see that the drag coefficient increases with the Froude number in the range Fr $\in [0, 0.3]$ and with the immersion depth in the range $d/D \in [0, 1]$. When considering hulls of increasing asymmetry (from hull 1 to hull 5), the contour plots become more and more asymmetric (Fig. 4.13(a) to (e)). This effect is however not as strong as observed in the experiments. Also, one can observe that depending on the immersion ratio d/D, the hull with the lowest drag changes.
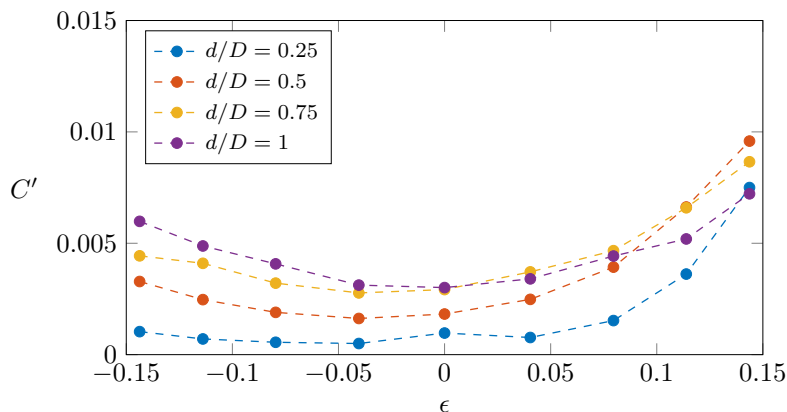

Figure 4.14: Drag coefficient C' as a function of the asymmetry parameter ϵ for four different immersion depths d/D at Fr $= 0.3$.

This is highlighted in Fig. 4.14 with the plot of the drag coefficient C' as a function of ϵ for different immersions d/D. For $d/D < 1$, the drag coefficient is minimum for $\epsilon \simeq -0.04$, corresponding to hull 2 moving with the pointed part first. On the contrary, for $d/D = 1$, the hull which has the lowest drag is the symmetric hull (*i.e.* hull 1). This result is different from the one obtained in the experiments (see Fig. 4.10(b)). The possible sources of discrepancies are discussed in the next section.
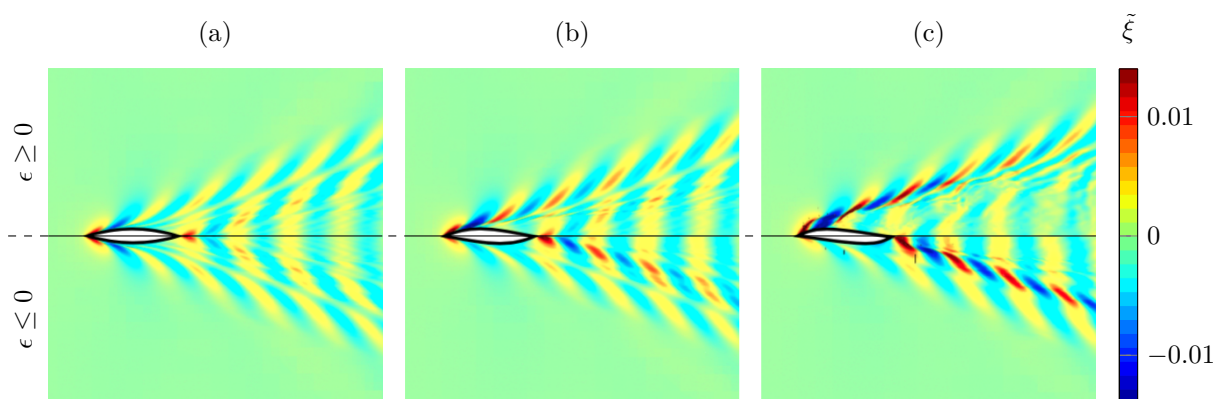
Figure 4.15: Dimensionless wave elevation $\tilde{\xi}$ obtained numerically for hulls 1, 3 and 5 (for Fr $= 0.3$ and $d/D = 0.5$). For each subplot, the upper half corresponds to the hull moving with the rounded part first ($\epsilon \geq 0$), while the lower half corresponds to the hull moving with the pointed part first ($\epsilon \leq 0$).

The fact that asymmetric hulls might not be optimal for all immersions can be understood when looking at the wave pattern generated by each hull (see Fig. 4.15). In general, there are two main sources of waves: the bow and stern of the hull (see Chap. 1, Sect. 1.6 and [5]). Fig. 4.15 shows the wave patterns for hull 1, 3 and 5. For hull 3 and 5, the upper half

of the plot corresponds to the hull moving with the rounded part first, while the lower half corresponds to the hull moving with the pointed part first. One can notice that, depending on the direction of motion of the hull, the highest waves are produced at the front ($\epsilon > 0$) or at the rear ($\epsilon < 0$) of the hull. This is particularly visible with the most asymmetric hull (hull 5, see Fig. 4.15(c)). Thus, even though the waves produced at the front of the hull are reduced when the hull is asymmetric and moves with the pointed part first, the waves generated at the rear become more and more important as the asymmetry of the hull increases. This can qualitatively explain why it is for a small asymmetry ($\epsilon \simeq -0.04$) that the drag coefficient is the smallest in the numerical simulations.

The results of these simulations and especially the computed pressure along each of the five hulls are further used in Appendix B.

4.5 Discussion

Using simple hull shapes of increasing asymmetry (with the same aspect ratio and immersed volume), we find both experimentally and numerically that slightly asymmetric hulls can have a lower drag than symmetric ones. The experiments show that the optimal hull, among the five which were tested, is the most asymmetric one with $\epsilon = -0.14$ (see Fig. 4.10). This promising result now requires to consider more asymmetric hulls to find the optimum of asymmetry. We indeed expect that for very asymmetric hulls the total drag coefficient should re-increase due to the pressure drag component. For the family of hull shapes that we defined, it is not possible to increase much the asymmetry because then the constraints of constant aspect ratio and cross-sectional area cannot be satisfied any more. A new family of hull shapes allowing for the design of very asymmetric hulls should be defined for future work.

Comparing quantitatively the experimental results with the numerical ones is not so easy. The numerical results were obtained for rather low values of the Froude number (up to Fr = 0.3), while, in the experiments, Fr $\geq$ 0.31. Computing the total drag numerically at larger Froude numbers is still an ongoing work. Also, we do not find exactly the same results with the numerics and the experiments, in particular for the optimal asymmetry: with the numerics, it is $\epsilon \simeq -0.04$ (see Fig. 4.14), while in the experiments, it is $\epsilon = -0.14$. An explanation for this discrepancy is most likely related to the fact that our numerical results were computed without viscosity. Taking into account viscosity will most likely affect the partition between the different drag components, thus shifting the optimal asymmetry.

Finally, let us come back to the initial problem of the asymmetry of racing shells. The experimental and numerical results of this study tend to point out the advantage of sprint canoes and sprint kayaks over rowing boats with regard to the optimal asymmetry. However, to get closer to the real problem, more complex geometries should be considered, which unfortunately goes together with the increasing difficulty of maintaining the aspect ratios and the immersed volume constant.

4.6 Appendix: Interaction between two cylinders

To account for the effect of the rods holding the hull and correct the drag measurements for fully immersed hulls ($d/D > 1$), we perform experiments with the rods only, changing their wetted length, denoted l_w. The total distance from the sensor to the tip of the rods is denoted $L = 26.5$ cm, the distance between the two rods $l_i = 10$ cm, and the diameter of a rod $d_t = 3$ mm (see Fig. 4.16(a)).
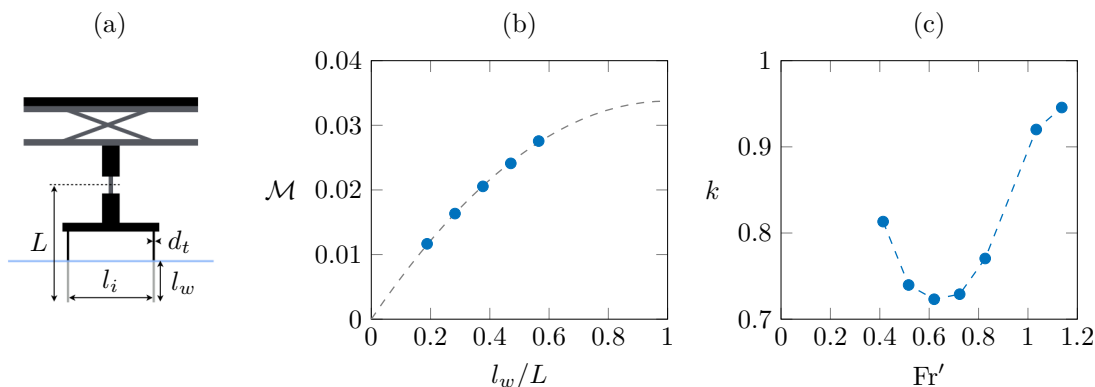

Figure 4.16: (a) Schematics of the experimental set-up to estimate the drag on the two rods holding the hull. The rods have a diameter $d_t = 3$ mm; the distance between them is $l_i = 10$ cm; the distance from the sensor to the tip of the rods is $L = 26.5$ cm; and the wetted length of the rods l_w ranges from 5 to 15 cm. (b) Measured torque $\mathcal{M}$ as a function of the ratio l_w/L for $U = 0.61$ m/s. The dotted line is a fit of the experimental data using Eq. (4.11). (c) Factor k defined in Eq. (4.12) as a function of the Froude number $\mathrm{Fr}' = U/\sqrt{gl_i}$ for two configurations $\theta = 0°$ and $\theta = 90°$.

The total torque $\mathcal{M}$ measured by the sensor results from the sum of all the contributions from the forces exerted by the water along the two rods. Thus, one has:

$$\mathcal{M} = 2 \int_{L-l_w}^{L} \delta f(z) z \, \mathrm{d}z \, , \tag{4.10}$$

where $\delta f(z)$ is the force per unit length in the vertical direction. We assume that $\delta f(z)$ is independent of z (which might be a crude assumption given the presence of the air-water interface) so that:

$$\mathcal{M} = \delta f L^2 (2\tilde{l}_w - \tilde{l}_w^2) \, , \tag{4.11}$$

where $\tilde{l}_w = l_w/L$. The measured torque $\mathcal{M}$ is plotted as a function of the dimensionless wetted length $\tilde{l}_w$ in Fig. 4.16(b). We further write:

$$\delta f = k \frac{1}{2} \rho d_t C_t U^2 \, , \tag{4.12}$$

where C_t is the drag coefficient of the rod (for a cylinder $C_t \simeq 1.2$) and k is a factor that can account for the presence of the free-surface and interactions between the two rods. The factor k is determined for a given velocity U by fitting the experimental curve $\mathcal{M}(\tilde{l}_w)$ with Eq. (4.11), as illustrated in Fig. 4.16(b). In Fig. 4.16(c), we plot this coefficient as a function of the Froude number based on the distance between the rods l_i, $\mathrm{Fr}' = U/\sqrt{gl_i}$. The configuration is the same as in the experiments with hulls (one rod lies behind the

other). We see that the factor k is minimum for Fr$' \simeq 0.6$, which can be a signature of an interaction between the wakes of the two rods. It could be interesting as a future study to look at the interaction between two rods depending on the angle between the horizontal line linking the two rods and the direction of motion.

These results are used in Subsect. 4.3.2 to correct the data for hulls when they are fully immersed in water. The corrected drag coefficient C_c is written:

$$C_c = C - \frac{\mathcal{M}}{\rho \Omega^{2/3} U^2 (L' + d/2)} \; , \tag{4.13}$$

where L' is the distance from the sensor to the upper surface of the hull and $\mathcal{M}$ is given by Eq. (4.11) in which L is replaced by L'.

4

Take home message of Chapter 4

1. When designing a ship, asymmetry can be an important parameter to play with. It is observed that typical sprint canoes and sprint kayaks are slightly asymmetric, while rowing boats are almost perfectly symmetric.

2. The existing theoretical models to estimate the wave drag predict the same value for an asymmetric boat moving forward or backward, which is in contradiction with observations.

3. After choosing a particular family of hull shapes of increasing asymmetry, we find with experiments and numerical simulations that asymmetry can decrease the overall drag. At the water surface, it appears that a slightly asymmetric hull, as drawn in Fig. 4.17, would be optimal.
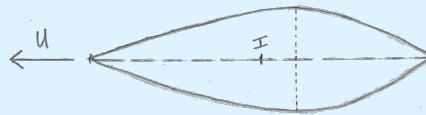
Figure 4.17: Schematics of a hull with optimal asymmetry.

4. This result shows the need for a theory that can include asymmetry in the wave drag.

PART III

PROPULSION IN ROWING AND FIN-SWIMMING

5

SCALING ANALYSIS OF ROWING

In this chapter, we reconsider the question of the dependence of the velocity of a rowing boat with the number of rowers. It is indeed observed with the world records in the different rowing categories that this velocity slowly increases with the number of rowers. McMahon showed that the relation between the two is a power law (power 1/9), which is in fairly good agreement with the observations. We relax two of the assumptions of McMahon's model and find that it does not change much the power law. Finally, we consider a limitation of McMahon's model for a large number of rowers, which comes from the need for sufficient spacing between consecutive rowers.
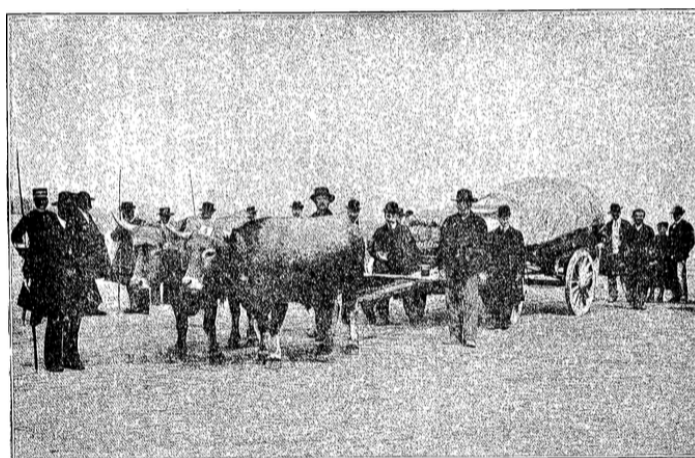
Picture of an Aubrac pair of steer yoked to a dynamometric cart for the experiments on force and power estimation by Ringelmann in 1907 (reprinted from [95]).

Contents

This work has been done with Romain Labbé, Michael Benzaquen and Christophe Clanet.

5.1 Introduction

In many sports, such as rowing, tug-of-war (see Fig. 5.1(a)) or rugby, individuals must rely on the power of the group to win. However, Ringelmann showed, with tug-of-war experiments, that the total power produced by a group of people (or animals such as oxen [95], see the picture on the previous page) was not equal to the sum of the power of each individual [96]. For instance, he measured that when eight men pull together on a rope the effort exerted by each individual is about half the effort developed by each individual when pulling alone (see Fig. 5.1(b)). Ringelmann explained this difference by a decrease in

(a)   (b)
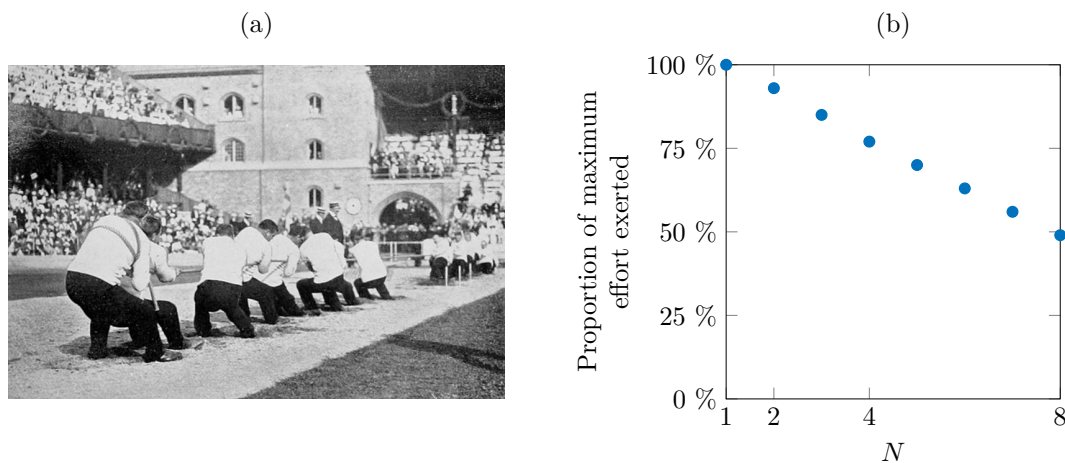
Figure 5.1: (a) Photograph of the only tug-of-war bout at the 1912 Olympics (source: [97]). (b) Proportion of maximum effort exerted on a rope during a pulling experiment depending on the number of people N [96].

motivation as well as coordination problems when pulling in a group compared to pulling alone [98]. More recent studies [99] show that this effect (also called Ringelmann effect) is mostly explained by social loafing. A similar effect has been recently observed by Phonekeo *et al.* for fire ants: they form aggregates and the contribution of each ant to their cohesion decreases with the number of ants [100]. Here we consider the problem of the effect of the number of rowers N on the speed of a rowing boat from a mechanical point of view with as a starting point the scaling analysis of McMahon [62]. Social loafing will thus be neglected in the following.

5.2 McMahon's model

To predict the velocity of racing shells depending on the number of rowers, McMahon makes four main assumptions.

(i) The racing shells have a geometric similarity regardless of the number of rowers on the boat. In other words, the aspect ratios $\alpha = \ell/w$ and $\beta = \ell/d$, introduced in Chap. 3, are constant for all racing shells.

(ii) The boat weight per oarsman is constant.

(iii) Each oarsman contributes equally to the total input power.

(iv) Lastly, the dissipation of the input power comes exclusively from skin friction.
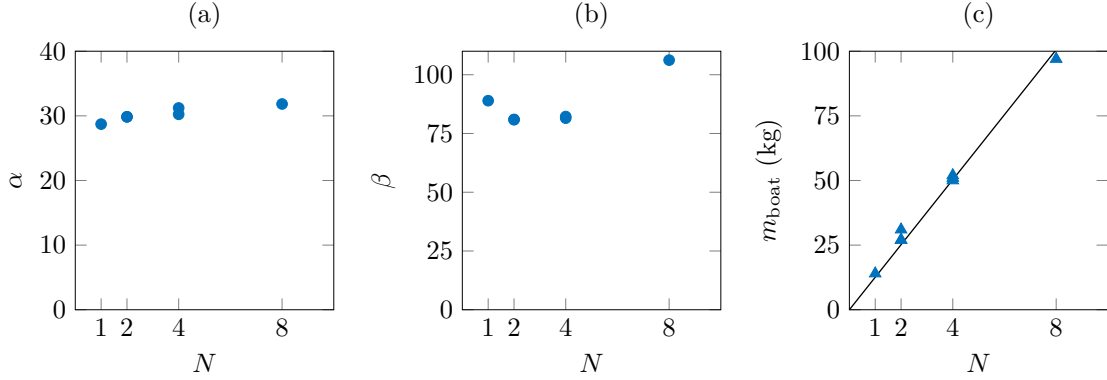
Figure 5.2: (a) Length-to-width aspect ratio α of racing rowing boats as a function of the number of rowers N (see Table 2.1). (b) Length-to-draft aspect ratio β of racing rowing boats as a function of the number of oarsmen N estimated from the mass of the boat with a momentum balance along the vertical. (c) Boat mass m_{boat} as a function of the number of oarsmen N. The black line is a linear fit of the data points ($m_{\text{boat}} \simeq 12.6 \times N$).

The first two assumptions can be tested for N ranging from 1 to 8 in the light of today's racing shells characteristics. In Fig. 5.2(a) and (b), the aspect ratios α and β of racing boats are plotted as a function of the number of rowers N. Although it can be noticed that α and β slightly increase with N, they can indeed be considered approximately constant: $\alpha \simeq 30$ and $\beta \simeq 91$ with 5% discrepancies for both. In the next section, the effect of relaxing this hypothesis will be assessed. Fig. 5.2(c) further shows that the evolution of the boat mass m_{boat} with N is very well approximated by a linear fit ($m_{\text{boat}} \simeq N m_1$ with $m_1 = 12.6$ kg), which validates the second assumption of the model. The third assumption is actually questionable if one accounts for social loafing as discussed in the introduction. But given the complexity of such effect, this assumption will not be put into question in the following. As for the last assumption, McMahon states (relying on measurements from [61]) that skin friction is the dominant component of drag and that wave drag accounts for less than 8% of the total drag (see also Sect. 2.5). Neglecting all the other components of drag is questionable, as well as considering that the dissipation of the input power from the rowers only comes from the dissipation by friction on the hull. In particular, a blade efficiency can be defined (see Appendix A) which probably depends on the number of rowers.

From the second hypothesis, the immersed volume of the hull for N rowers, denoted Ω_N, scales as $\Omega_N \sim N\Omega_1$ where $\Omega_1 \simeq (m_1 + m_r)/\rho$ is the volume displaced by one rower, with m_r the mass of each rower. And from the third assumption, the propulsive power for N rowers $\mathcal{P}_N$ reads $\mathcal{P}_N \sim N\mathcal{P}_1$ with $\mathcal{P}_1$ the power delivered by one rower. The total propulsive power is also written:

$$\mathcal{P}_N = RU \ , \tag{5.1}$$

with R the total resistance on the hull which is supposed to be dominated by skin friction, so that one has $R = 1/2\rho S_h C_h U^2$ (with S_h the hull wetted surface and C_h the hull drag coefficient, see also Eq. (2.1) in Sect. 2.5). The wetted surface can be approximated by $S_h \simeq \ell w = \ell^2/\alpha$ and the immersed volume by $\Omega_N \simeq \ell w d = \ell^3/(\alpha\beta)$, so that:

$$S_h \simeq \frac{\beta^{2/3}}{\alpha^{1/3}}\Omega_1^{2/3}N^{2/3} \ . \tag{5.2}$$

Combining this equation with Eq. (5.1), one finds:

$$U \simeq U_1(\alpha, \beta) N^{1/9} \, , \tag{5.3}$$

with $U_1(\alpha, \beta) = [2\mathcal{P}_1 \alpha^{1/3}/(\rho \beta^{2/3} \Omega_1^{2/3} C_h)]^{1/3}$, the hull velocity for $N = 1$. If we now use the first assumption, that is α and β are independent of N, then we directly get that $U \sim N^{1/9}$, as found by McMahon. This scaling can be checked by looking at the world record speeds in the different rowing categories (see Fig. 5.3(a)). We find a fairly good agreement with the scaling law for *coxless sweep* and *sculling* categories, but not for the *coxed sweep* category, which might be related to the larger effect of the presence of a coxswain on the boat for the *pair* and the *four* than for the *eight*, and also to the absence of the *coxed pair* and *coxed four* categories at the Olympics. Interestingly, taking $\mathcal{P}_1 = 400$ W, $\Omega_1 = 0.24$ m^3, $C_h = 2.5 \cdot 10^{-3}$, $\alpha = 30$ and $\beta = 91$, one has $U_1 \simeq 5.0$ m/s, which is very close to the world record speed for single sculls.
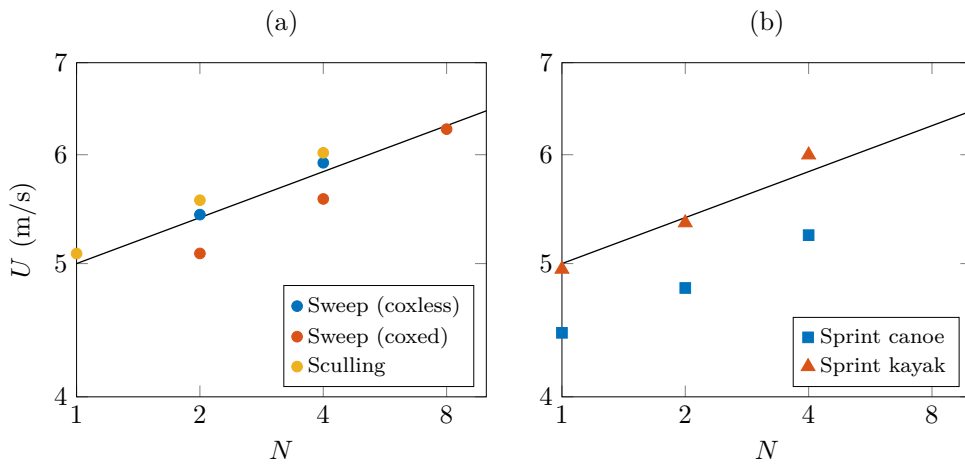
Figure 5.3: World record speed as a function of the number of oarsmen (a) for the different rowing categories and (b) for sprint canoes and sprint kayaks. Both plot have a logarithmic scale and the black line represents the scaling law $U \sim N^{1/9}$. Note that the race distance considered here is shorter for sprint canoes and sprint kayaks (1000 m) than for rowing boats (2000 m).

In Fig. 5.3(b), McMahon's scaling law ($U \sim N^{1/9}$) is tried for sprint canoes and sprint kayaks where the number of rowers this time ranges from 1 to 4. The third and fourth assumptions are also expected to hold for these kinds of boats. We refer to Fig. 5.7 in Sect. 5.5 for the verification of the first and second assumptions of the model. For sprint canoes, the two assumptions (α constant and $m_{boat} \sim N$) are quite well verified. For sprint kayaks, although the assumption for the mass of the boat seems to be respected, the assumption α independent of N is far from being valid. As U scales with $\alpha^{1/9}$ and $\beta^{-2/9}$, the scaling $U \sim N^{1/9}$ does not depend so much on this assumption, which explains the fairly good agreement between the scaling and the data points in Fig. 5.3(b). Let us mention that the record speeds for sprint kayaks are close to the record speeds in rowing. However, for sprint canoes and sprint kayaks, the distance of the race is 1000 m while, for rowing boats, the distance is 2000 m. Thus, rowing boats are the fastest man-powered boats, then come the sprint kayaks (for which the legs do not work) and finally the sprint canoes (for which the stroke frequency is lower than in kayak).

5.3   Extension of McMahon's model

In this section, we study the effect of removing the hypothesis of geometric similarity of boats and the hypothesis of negligible wave drag. Rowing boats do not really have other constraints than the minimisation of the total drag, so their aspect ratios α and β should result from the optimisation of the rowing shell at a given load, equivalently immersed volume Ω_N and given propulsive power $\mathcal{P}_N$. Letting $\Omega = \Omega_N$ and $\mathcal{P} = \mathcal{P}_N$ into Eq. (3.11) (see Sect. 3.5) yields:

$$\Pi = \Pi_1 N^{-1/6} \ , \tag{5.4}$$

where $\Pi_1 = \mathcal{P}_1/(\rho g^{3/2}\Omega_1^{7/6})$. Π is thus a decreasing function of N. Given the results of the optimisation presented in Sect. 3.5 (taking $\mathcal{P}_1 = 400$ W and $\Omega_1 = 0.24$ m^3), we can find the optimal aspect ratios $\alpha^\star$ and $\beta^\star$ and the optimal Froude number Fr* as a function of the number of rowers N. This is represented in Fig. 5.4 with the black line and compared to the empirical data points for rowing boats. We thus recover the increasing evolution of α with N and the decreasing evolution of Fr with N (see Fig. 5.4(a) and (c)).
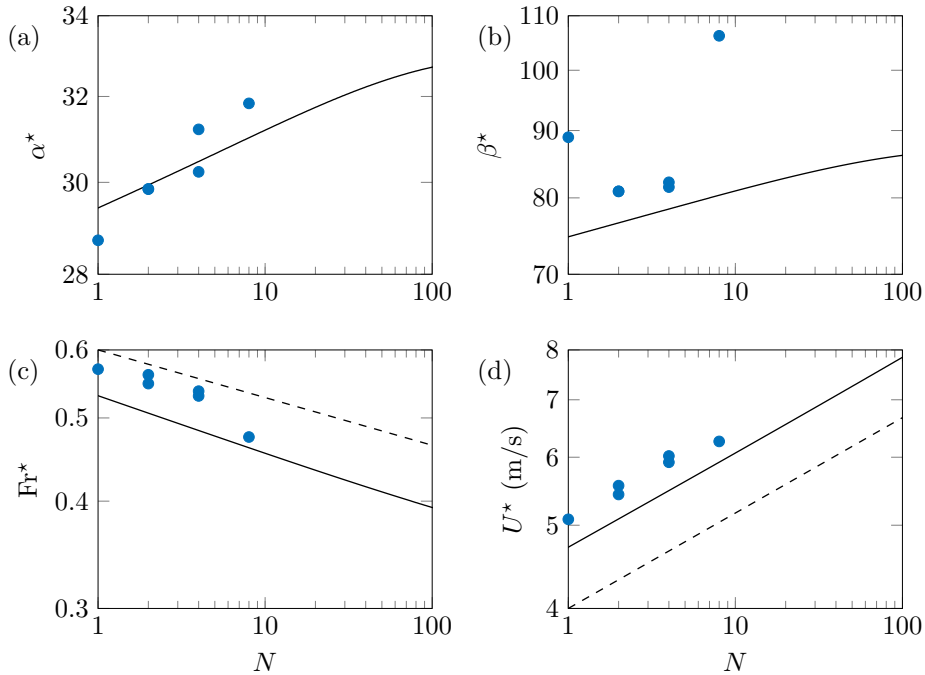
Figure 5.4: Log-log plot of (a) the optimal aspect ratio $\alpha^\star$, (b) the optimal aspect ratio $\beta^\star$, (c) the optimal Froude number Fr* and (d) the corresponding boat velocity $U^\star$, as a function of the number of rowers N from the optimisation presented in Sect. 3.5 (black line). The blue dots are the empirical data for real rowing boats (see Table 2.1). The Froude number is estimated from the world record speeds in the different rowing categories. In (c), the dashed line represents the scaling law Fr $\sim N^{-1/18}$ from McMahon's model. Similarly, in (d), the dashed line represents McMahon's scaling law $U \sim N^{1/9}$.

McMahon's model predicts the evolution of Fr with N: Fr $\sim N^{-1/18}$. But we see that McMahon's first assumption (α and β independent of N) is not exactly true, even though the evolution of α and β with N over two decades is very small. The increase of α and β with N is related to the decrease of the Froude number towards Fr $\simeq 0.5$, that is in the range where the wave drag is maximum, requiring larger aspect ratios.

In this framework, the hull velocity $U^\star$, which corresponds to the optimal hull geometry, is written:

$$U^\star \sim N^{1/9} \frac{\mathcal{P}_1^{1/3}}{\rho^{1/3}\Omega_1^{2/9}C(\alpha^\star(N),\beta^\star(N),\mathrm{Fr}^\star(N))^{1/3}} \ . \tag{5.5}$$

This velocity is plotted as a function of N in Fig. 5.4(d). We find an evolution with the number of rowers close to the observed evolution of the speed records. However, this evolution is also very close to the scaling law $U \sim N^{1/9}$ predicted by McMahon (see black dashed line). This is related to the fact that, in Eq. (5.5), the drag coefficient $C(\alpha^\star(N),\beta^\star(N),\mathrm{Fr}^\star(N))$ appears at the power $1/3$ and varies slowly with the number of oarsmen N ($\alpha^\star$ and $\beta^\star$ vary slowly with N).

This extension of McMahon's model, based on accounting for the optimisation of rowing shells, do not change the final scaling law $U \sim N^{1/9}$ of the model but allows us to understand the evolution of the aspect ratio α of current rowing boats.

5.4   A new approach

Using $\Omega_N \sim N\Omega_1$ and the first assumption of McMahon's model (aspect ratios α and β independent of the number of rowers N), one finds that the length of rowing boats scales as $\ell \sim N^{1/3}$. This is in quite good agreement with the available data for boats from one to eight rowers (see dashed line in Fig. 5.5(a)). However, in the specific case of rowing, a minimal spacing between consecutive rowers is needed so that they can perform their rowing stroke without hitting each other. This minimal spacing is slightly longer than the typical length of the legs of a rower. This dictates a new dependence of the length of a rowing boat with the number of rowers, this is:

$$\ell = \ell_c(N + a) \ . \tag{5.6}$$

To check this new relation, we are lucky that there exists a rowing boat, the *Stämpfli Express*, with 24 rowers measuring 44 m in length (see Fig. 5.6(a)). The corresponding data point appears in red in Fig. 5.5(a) and Eq. (5.6) gives a good fit of all the data with $\ell_c = 1.5$ m and $a = 4.1$ (solid black line in Fig. 5.5(a)). Interestingly, ℓ_c is of the order of the typical distance between two consecutive rowers (about 1.3 m for an *eight*). On the contrary, we see that the scaling law $\ell \sim N^{1/3}$ is not able to account for the data point of the *Stämpfli Express*. So we should now use Eq. (5.6) together with the assumption that the width w and the draft d are now independent of the number of rowers to respect the force balance along the vertical direction. The same steps as in Sect. 5.2 give:

$$U \simeq U_\infty \left(\frac{N}{N + a}\right)^{1/3} \ , \tag{5.7}$$

with $U_\infty = [2\mathcal{P}_1/(\rho w C_\mathrm{h}\ell_c)]^{1/3}$ the value reached when $N \to +\infty$. Taking $\mathcal{P}_1 = 400$ W, $w = 55$ cm and $C_\mathrm{h} = 2.5 \cdot 10^{-3}$, one has $U_\infty \simeq 7.2$ m/s. Looking at Fig. 5.5(b), we see that the speed attained by the *Stämpfli Express* is much lower than the one expected from McMahon's model and is actually smaller than the speed reached by an *Eight* rowing boat. This is surely related to the saturation of the speed when increasing the number of rowers expected from Eq. (5.7) but also to the absence of high level competitions with this boat and to the increasing difficulty for the rowers to remain synchronised when their number increases (see Chap. 6 for a discussion of the synchronisation problem). This study

eventually tends to indicate that, if rowing boats in competitions do not have more than eight rowers, it is for a good reason: boats with more rowers would hardly go faster!
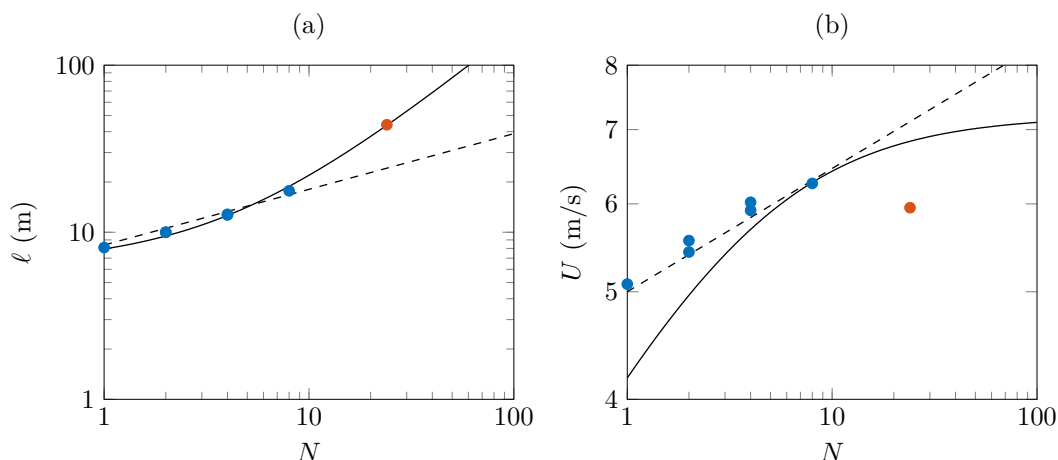

Figure 5.5: (a) Length ℓ of rowing boats depending on the number of rowers N in logarithmic scale. The red dot corresponds to the *Stämpfli Express* (see Fig. 5.6(a)). The black line is a fit of the data including the red dot, $\ell = 1.5(N + 4.1)$, and the dashed line corresponds to the scaling law $\ell \sim N^{1/3}$ from McMahon's model (see Table 2.1 for the characteristics of rowing boats). (b) Mean hull velocity U as a function of the number of oarsmen N in logarithmic scale with the data for the *Stämpfli Express* in red. The black line corresponds to Eq. (5.7) and is the evolution expected when considering that the length ℓ is linear with N. The dashed line corresponds to the scaling law $U \sim N^{1/9}$.

Actually, what is expected and observed when considering the different existing types of man-powered watercraft is the transition in the disposition of the rowers from the line in the case of rowing boats (see Fig. 5.6(a)) to the surface (two lines of rowers), for example for *Dragon* boats (see Fig. 5.6(b)) and even to the volume with the trireme (see Fig. 5.6(c)), a vessel used in the antiquity which had three rows of oars on each side. Classic rowing boats have up to 8 rowers, while a *Dragon* boat has 20 rowers and a trireme about 180. However, among all these boats the fastest is the *eight* rowing boat. This is most likely related to the increase of the total drag, and especially the wave drag, when the disposition of the rowers on the boat transitions from the line to the surface or the volume.
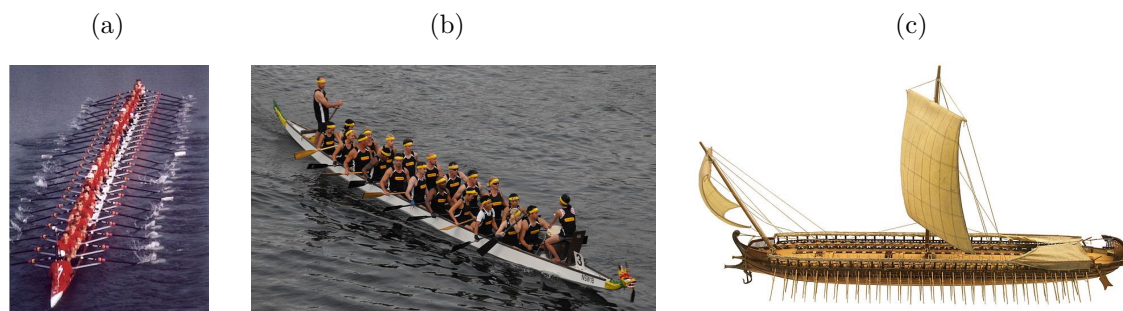
Figure 5.6: (a) Picture of the *Stämpfli Express*, a rowing boat with 24 rowers measuring 44 m (source: [101]). (b) Picture of a *Dragon* boat, a racing boat with 22 persons on board among which 20 rowers (source: [9]). (c) Wood model of a Greek trireme, a boat used in the antiquity which derives its name from its three rows of oars (source: [3]).

5.5 Appendix: Characteristics of sprint canoes and sprint kayaks

Fig. 5.7(a) shows the evolution of the aspect ratio α of both sprint canoes and sprint kayaks. Although the aspect ratios for sprint canoes are rather constant whatever the number of rowers N ($\alpha \simeq 16$), for sprint kayaks, the aspect ratio α increases a lot from $N = 1$ to $N = 4$. So the first assumption of McMahon's model is respected for sprint canoes but not for sprint kayaks. In Fig. 5.7(b), the evolution of the boat mass m_{boat} with the number of rowers N is represented. One can see here that m_{boat} is not exactly proportional to N for both sprint canoes and sprint kayaks.
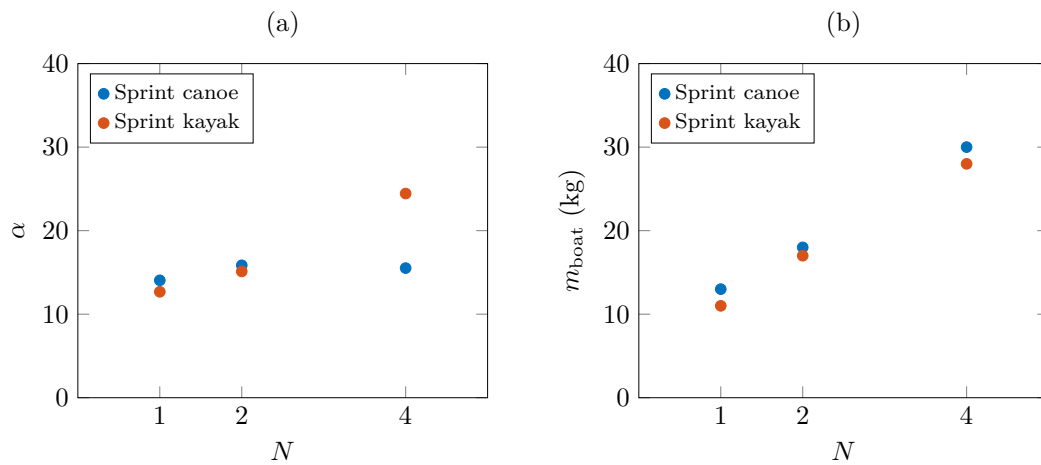
Figure 5.7: (a) Length-to-width aspect ratio α of sprint canoes and sprint kayaks as a function of the number of oarsmen N (see Table 5.1). (b) Boat mass m_{boat} as a function of the number of rowers N.

Table 5.1 gives the characteristics of current sprint canoes and sprint kayaks.

Boat Abbreviation	ℓ (m)	w (cm)	m_{boat} (kg)	U (m/s)
C1	5.2	37	13	4.45
C2	6.5	41	18	4.80
C4	9	58	30	5.24
K1	5.2	41	11	4.95
K2	6.5	43	17	5.35
K4	11	45	28	6

Table 5.1: Characteristics of current sprint canoes (C1, C2, C4) and sprint kayaks (K1, K2, K4). The geometry characteristics and mass are for boats from *Nelo* supplier [91]. The boat speed U given in the table is the world record speed in each category on a distance of 1000 m.

<div style="border:1px solid #1a3c6e; border-radius:8px;">

Take home message of Chapter 5

1. The scaling law for the velocity of a rowing shell $U \sim N^{1/9}$, derived by McMahon, works quite well for a number of rowers ranging from 1 to 8.

2. We extend this model taking into account the optimisation of the rowing shells depending on their number of rowers. The scaling law of McMahon remains valid and we find an explanation for the increase of the length-to-width aspect ratio with the number of rowers.

3. Finally, McMahon's model is criticised in the regard of an additional constraint on the length of the boat not taken into account until now. Indeed, in rowing, a minimal spacing is needed between consecutive rowers. This changes the prediction of McMahon and gives a velocity that saturates as the number of rowers further increases.

</div>

5

5

6

A QUESTION OF SYNCHRONISATION

Synchronisation in rowing seems like a crucial condition for those who aim at winning top-level rowing races. However, in nature, one can observe animals with many legs, such as krill, swimming in a desynchronised manner. From a physicist point of view, desynchronised rowing also seems like a great idea because, at high Reynolds number, the desynchronised gait has one big advantage over the synchronised one: it reduces the fluctuations of speed and thus the drag on the body. In this study, we have built a scale model of a rowing boat to deal with the question of the effect of synchronisation on the boat performance. The results of our model boat are compared to the predictions of a simplified theoretical model.

Synchronisation is also crucial in synchronised swimming.

Contents

This work has been done with Romain Labbé, Michael Benzaquen and Christophe Clanet.

6.1 Introduction

We discuss the effect of the synchronisation between rowers on the speed of a rowing boat. This question is treated by combining an experimental model of a rowing boat and a simplified theoretical model.

6.1.1 Effect of velocity fluctuations

In rowing competitions, the boat moves with large fluctuations of speed, as already discussed in Sect. 2.2 (see Fig. 2.7). They are up to 30% of the mean velocity. At first order, let us model the velocity profile of a rowing boat as a sinusoidal function of time:

$$U = \langle U \rangle + \Delta U \cos(2\pi f t) \ , \tag{6.1}$$

where $\langle U \rangle$ is the mean velocity, ΔU is the amplitude of the fluctuations around the mean velocity and f is the stroke frequency. Assuming, as in McMahon's model (see Sect. 5.2), that the dissipation of the power $\mathcal{P}$ produced by the rowers only comes from skin friction, one has: $\mathcal{P} \sim \rho S_{\mathrm{h}} U^3$ (with S_{h} the hull wetted surface). So the mean power dissipated over one rowing cycle is written:

$$\langle \mathcal{P} \rangle \sim \rho S_{\mathrm{h}} \langle U^3 \rangle = \rho S_{\mathrm{h}} \langle U \rangle^3 \left[1 + \frac{3}{2} \left(\frac{\Delta U}{\langle U \rangle} \right)^2 \right] \ . \tag{6.2}$$

Thus, compared to a motion at constant velocity, the relative increase of the mean dissipated power is $3/2(\Delta U/\langle U \rangle)^2$, which for $\Delta U/\langle U \rangle \simeq 30\%$ gives a 13% increase of the dissipated power. Besides, the velocity fluctuations are also expected to increase the wave resistance and to give rise to added mass force. Reducing these fluctuations in rowing then appears to be crucial to avoid energy losses.

6.1.2 Synchronisation in nature

One way of reducing the velocity fluctuations can be found by looking at animal locomotion: desynchronising the motion of the appendages during the propulsion is often observed and is indeed a way to achieve a constant velocity.
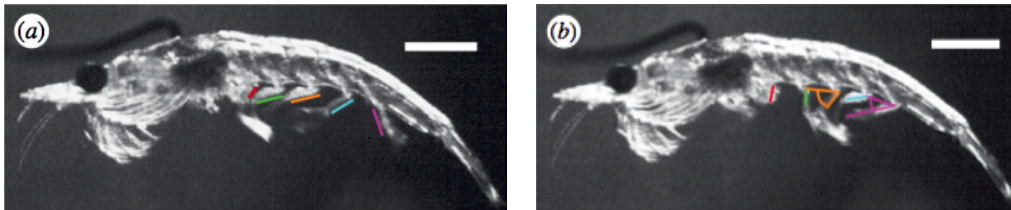
Figure 6.1: Side-view pictures of a krill at two different times during its swimming cycle. The proximal segments of the krill's appendages are highlighted with different coloured lines. The white bar is 5 mm long. Pictures reprinted from [102].

For instance, shrimps and krills swim thanks to five pairs of legs that are activated in a desynchronised way, known as *metachronal* (see Fig. 6.1). This kinematics was shown to lead to the highest average body velocity for a given mean work [102].

Fishing spiders and salticid spiders also display unsynchronised swimming at the surface of water. For example, Fig. 6.2 shows time-lapse pictures of the rowing stroke of a salticid

spider. From the analysis of these pictures, we find that the two pairs of legs that are involved in the propulsion have a phase-shift of about 125°.
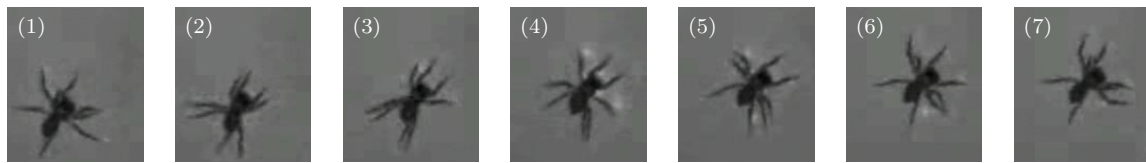
Figure 6.2: Time-lapse pictures of a salticid spider moving at the water surface in a rowing-like stroke. Pictures extracted from a video by Suter [103]. The time between two images is about 0.3 s.

6.1.3 Previous studies

The aim of reducing the velocity fluctuations in rowing led to the invention of sliding riggers in 1877: instead of having a sliding seat with fixed riggers (see Fig. 2.2(a)), this boat had a fixed seat and sliding riggers (see Fig. 6.3). This new concept significantly improved the boat speed. However, it was banned by the International Rowing Federation in 1983, as it was considered more costly than conventional rowing [1].
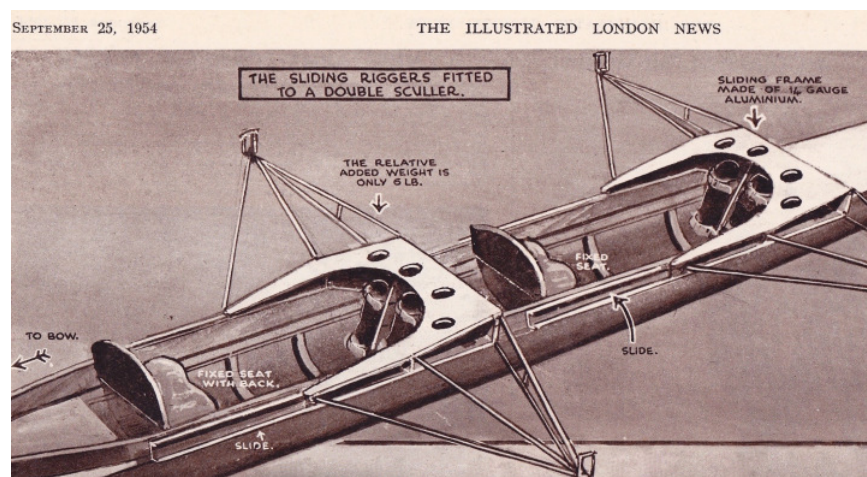
Figure 6.3: Drawing of a double scull with fixed seats and sliding riggers found in the "Illustrated London News" of 25 September 1954.

Phase-shifted rowing has already been considered in the past. This technique was indeed tested, in 1929, on the Thames by the *London Rowing Club* (see the video in [104]). But this trial and others which were conducted in England during the early 1930s lead to inconclusive results and to the question of "whether the trifling gain is worth the loss of all the rhythm, apart from neutralising the genius of strokeship[1]" [105]. At the 1981 and 1982 world championships, the Soviet women's *coxed four* crew placed the coxswain in between the two pairs so that they could row in antiphase. However, the crew ended up rowing in synchrony the day of the race. Despite all these full-scale trials and more recent studies both theoretical [66] or experimental with ergometers [106], it is still unclear whether the very peculiar syncopated technique is more or less efficient than the conventional synchronised rowing.

---

[1]Strokeship means the art of row strokes, *i.e.* the art of rowing with a particular stroke.

6.2 Description of our rowing boat model

To study the influence of oarsmen synchronisation on the boat speed, we built a remote rowing boat at the scale 1/10 with eight rowing robots. In our model boat, to ensure a straight trajectory, each rower has two oars. This kind of rowing boat is called an *octuple scull*.[2] Real *octuple sculls* exist but are not found in rowing competitions. They have the same characteristics as *eight* rowing boats: they are approximately 20 meters long and weigh 100 kg. Our model boat (see Fig. 6.4(a)) is thus 2 meters long with a hull, made of glass fiber, that has the same shape as an *eight* rowing boat [107]. We made 8 independent rowing robots that are controlled separately (see Fig. 6.4(b)). Each robot is made up of a servomotor in a carriage which moves back and forth thanks to a pulley attached with a cable to two fixed points on the boat. In the carriage, a bar with two stable positions simulates the rower hands. When the bar is down, the blades are out of water and when the bar is up, the blades are in the water. Thus, with this system, the whole rowing cycle can be described in a similar way as in real rowing. The speed of our robotic rowers and the phase difference between them, denoted ϕ, is controlled with an Arduino board.

Figure 6.4: (a) Picture of our 2-meter long robotic rowing boat at the *Ecole polytechnique* swimming pool. (b) Zoom on one robotic rower. The blades are attached to a bar that can move up and down as the "rower" moves back and forth, thus mimicking the real rowing cycle.

In Table 6.1 (see Sect. 6.8), the main parameters of our model boat and of a real *eight* rowing boat are given. The effect of the motion of the rowers on the boat can be tested with our model boat. Indeed, even if the ratio of the total moving mass to the total mass of the boat $8m_{\mathrm{r}}/M$ (with m_{r} the mass of a rower) is smaller for our model boat than for real boats, it is still significant ($8m_{\mathrm{r}}/M \simeq 0.4$). Concerning the flow regime, the Reynolds number, Froude number and Weber number are much smaller for our model boat than for real boats. However, the Reynolds number for our model boat ($\mathrm{Re} \simeq 5 \cdot 10^5$) is close to the critical Reynolds number $\mathrm{Re_{cr}}$ (see Sect. 1.4), so that we expect the flow around the hull to be turbulent in a similar way as for real boats. The difference in the Froude number is not so important because, for real rowing boats, the wave drag is negligible compared to the skin friction (see Sect. 2.5). As for the Weber number, in both cases, it is much larger than 1, so that capillary effects are negligible. Thus, our robotic rowing boat is expected to model real rowing boats with a similar rowing movement, the displacement of the rowers on the boat and a similar flow regime, the main difference with real rowing being that, in our model boat, the kinematics is prescribed, while in reality it is the power injected by the rowers.

---

[2]An *octuple scull* (eight rowers with two oars each is different from an *eight* rowing boat where each rower has one oar.

6.3   Experimental results

We performed measurements of the speed of our model rowing boat at the *Ecole polytechnique* swimming pool, changing the phase difference ϕ between consecutive rowers. In the synchronous configuration ($\phi = 0°$), we observe that our boat moves with an instantaneous velocity profile (see Fig. 6.5) similar to the one obtained for real rowing races (see Fig. 2.7). The velocity increases during the power stroke (between the red and green vertical lines) thanks to the propulsion of blades, then continues to increase at the beginning of the recovery stroke and finally decreases at the end of the recovery stroke because of the motion of the rowers on the boat and the hydrodynamic friction on the hull. The similarity of the velocity profiles proves that our model boat displays the same physical features as real rowing boats. At a pace of one stroke per second, our boat moves at a mean speed close to 0.35 m/s. That is almost 0.2 boat length per rowing cycle (to be compared with around 0.45 boat length per rowing cycle in real races), with about 12% speed fluctuations (to be compared with 20 to 30% speed variations in real rowing).
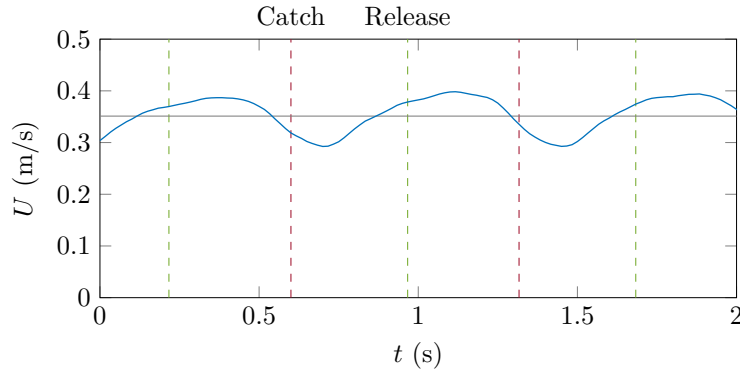
Figure 6.5: Instantaneous velocity of our model rowing boat as a function of time for about three strokes, in the synchronised configuration ($\phi = 0°$) for $f \simeq 1.3$ Hz. The vertical red dashed lines indicate the time of the catch and the vertical green dashed lines the time of the release. The mean speed $\langle U \rangle$ is indicated with a gray horizontal line. This velocity profile is obtained from image analysis.

Changing the phase difference ϕ from 0° to 360°, we observe that desynchronising the rowers indeed reduces the fluctuations of the boat speed, as illustrated in Fig. 6.6(a). They are for instance decreased up to only 2% of the mean speed for $\phi = 45°$. Yet, the at-first surprising and puzzling outcome of these experiments is that the mean speed of the boat is maximal in the synchronised configuration by about 8% (see Fig. 6.6(b)). Our main result is thus in contradiction with our initial intuition: reducing velocity fluctuations does not increase the mean velocity. This can be explained as follows: before we did not take into account that when synchronised rowers return together to the stern of the boat during the recovery stroke, they pull the hull beneath them, accelerating the boat. Thus, there is an additional inertial boost that is lost when the rowers are desynchronised. Also the efficiency of the blade propulsion might be smaller in the desynchronised configurations than in the synchronised one.
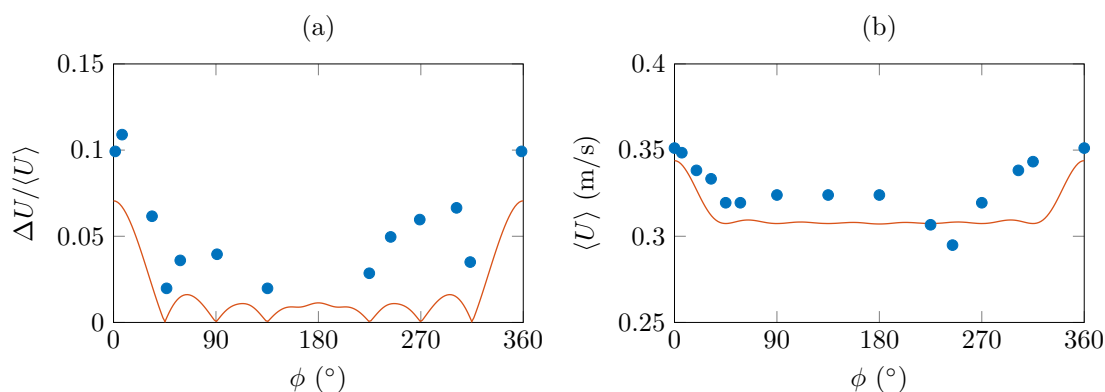
Figure 6.6: (a) Speed fluctuations $\Delta U/\langle U \rangle$ as a function of the phase-shift between consecutive rowers ϕ from the experiment (blue dots) and the numerical model (orange line). (b) Mean boat velocity $\langle U \rangle$ depending on ϕ from the experiment (blue dots) and the numerical model (orange line) (see Sect. 6.4).

6.4   Theoretical framework

To understand these experimental results, we built a simplified theoretical model of rowing. For the sake of simplicity, let us consider a sweep rowing boat (a boat where each rower has one oar) with N rowers (see Fig. 6.7). For a sculling boat (a boat where each rower has two oars), such as in the experiments, the same model holds provided that the total force on the blades is multiplied by the factor 2.
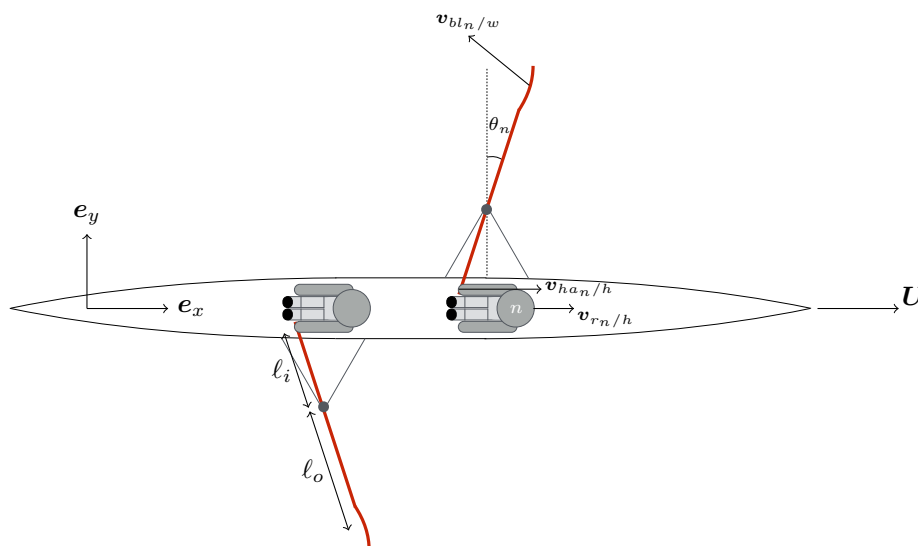
Figure 6.7: Schematics of a sweep rowing boat (each rower has one oar) with $N = 2$ rowers, where $\boldsymbol{U}$ is the velocity of the boat in the reference frame of the water, $\boldsymbol{v}_{bl_n/w}$ the velocity of the blade n with respect to the water, $\boldsymbol{v}_{r_n/h}$ the velocity of the rower n in the reference frame of the boat and $\boldsymbol{v}_{ha_n/h}$ the velocity of the hands of rower n in the reference frame of the boat.

To derive a model equation for the motion of the boat, we write the momentum conservation

for the system {boat + rowers + oars}:

$$\frac{\mathrm{d}\boldsymbol{P}}{\mathrm{d}t} = \boldsymbol{F}_{w/bl} + \boldsymbol{R} \ , \tag{6.3}$$

where $\boldsymbol{P}$ is the momentum of the whole system, $\boldsymbol{F}_{w/bl}$ is the force resulting from the propulsion with the N blades and $\boldsymbol{R}$ is the total drag force exerted by the fluid on the hull. We define $\boldsymbol{U}$ the velocity of the boat with respect to the water and $\boldsymbol{v}_{r_n/h}$ the velocity of the center of mass of the rower n in the reference frame of the boat (see Fig. 6.7). We then have:

$$\boldsymbol{P} = M\boldsymbol{U} + m_{\mathrm{r}} \sum_{n=1}^{N} \boldsymbol{v}_{r_n/h} \ , \tag{6.4}$$

where m_{r} is the mass of a rower and $M = m_{\mathrm{boat}} + N \times m_{\mathrm{r}}$ is the total mass of the system. Note that we assume the mass of the oars to be negligible.[3]

The drag exerted on the hull is modelled by $\boldsymbol{R} = -1/2\rho S_{\mathrm{h}} C_{\mathrm{h}} U^2 \boldsymbol{e}_x$, as given by Eq. (2.1). For a real rowing boat, we take $C_{\mathrm{h}} = 2.5 \cdot 10^{-3}$ (see Sect. 2.5) and, for our model boat, we found experimentally $C_{\mathrm{h}} \simeq 0.04$ (see Sect. 6.8).

Fluid forces on the blades.

In order to write the total force on the blades at any time during the rowing cycle, we introduce the function $H_n(t)$ such that $H_n(t) = 1$ during the power stroke of the rower n (blade n inside the water) and $H_n(t) = 0$ during the recovery stroke of the rower n (blade n outside the water). The force $\boldsymbol{F}_{w/bl}$ is then written:

$$\boldsymbol{F}_{w/bl} = \sum_{n=1}^{N} H_n(t) \boldsymbol{F}_{w/bl_n} \ , \tag{6.5}$$

where $\boldsymbol{F}_{w/bl_n}$ is the force exerted by the water on blade n. The typical speed of the blades with respect to the water is about 5 m/s and a blade measures about 0.5 m $\times$0.25 m (see Table 2.2 in Chap. 2). So the typical Reynolds number for the flow around the blades is Re $\simeq 10^6$. We thus consider three force components acting on the blades, so that the force exerted on blade n is written:

$$\boldsymbol{F}_{w/bl_n} = \boldsymbol{F}_{D_n} + \boldsymbol{F}_{L_n} + \boldsymbol{F}_{A_n} \ , \tag{6.6}$$

where $\boldsymbol{F}_{D_n}$ is the drag, $\boldsymbol{F}_{L_n}$ the lift and $\boldsymbol{F}_{A_n}$ the added mass force. Firstly, the drag force on blade n reads:

$$\boldsymbol{F}_{D_n} = -\frac{1}{2}\rho S_{bl} C_D(\Phi_n) v_{bl_n/w}^2 \boldsymbol{t} \ , \tag{6.7}$$

where S_{bl} is the surface of the blade, C_D its drag coefficient, which depends on the blade angle of attack Φ_n (see Fig. 6.8(a)), $v_{bl_n/w} = |\boldsymbol{v}_{bl_n/w}|$ and $\boldsymbol{t}$ is the unit vector collinear to the blade velocity $\boldsymbol{v}_{bl_n/w}$. Secondly, the lift force is written:

$$\boldsymbol{F}_{L_n} = \frac{1}{2}\rho S_{bl} C_L(\Phi_n) v_{bl_n/w}^2 \boldsymbol{n} \ , \tag{6.8}$$

where C_L is the lift coefficient of the blade[4] and $\boldsymbol{n}$ is the unit vector normal to the blade

---

[3]Oars typically weigh about 1.5 - 2 kg.
[4]C_L can be positive or negative depending on the angle of attack (see Fig. 6.8 (c)).

velocity $\boldsymbol{v}_{bl_n/w}$. The coefficients C_D and C_L were determined experimentally by [55] for a *Macon* blade and a *Big* blade depending on their angle of attack (see Fig. 6.8(b) and (c)).
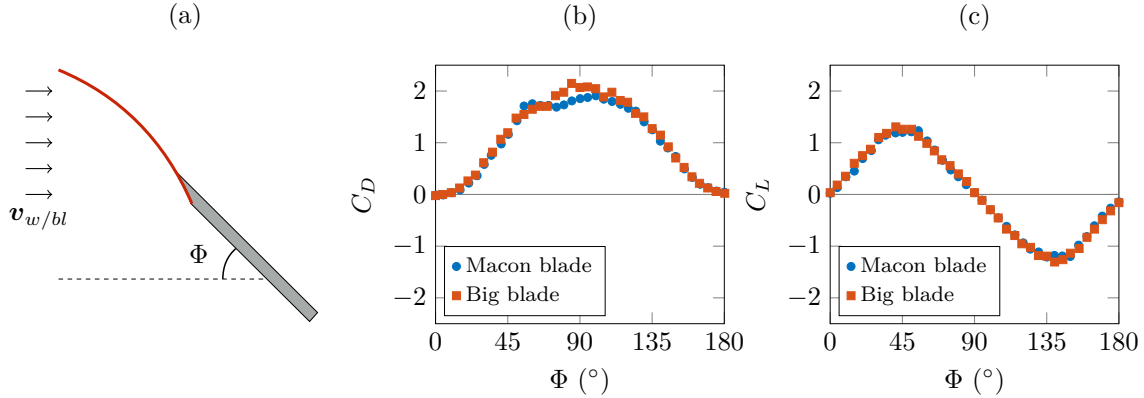

Figure 6.8: (a) Schematics of a blade in a uniform flow at speed $\boldsymbol{v}_{w/bl} = -\boldsymbol{v}_{bl/w}$. The angle of attack is denoted Φ. (b) Drag coefficient C_D and (c) lift coefficient C_L as a function of the angle of attack Φ for a *Macon* blade and a *Big* blade (see Fig. 2.3(a) and (b)). For an angle of attack of 90°, that is for a flow normal to the blade, we recover $C_L \simeq 0$ and $C_D \simeq 2$. Data taken from [55].

Thirdly, the added mass force reads:

$$\boldsymbol{F}_{A_n} = -m_a \frac{\mathrm{d}\boldsymbol{v}_{bl_n/w}}{\mathrm{d}t} \ , \tag{6.9}$$

with m_a the added mass of the blade (see Sect. 1.7.1). The added mass is estimated as $m_a \simeq \pi \rho w_b \ell_b^2 / 4$ with w_b the width of the blade and ℓ_b the length of the blade (see Fig. 2.3(b)). Thus, for real blades, $m_a \simeq 30$ kg and for the blades in our model boat, $m_a \simeq 26$ g.

The speed of the blade n in the reference frame of the hull $\boldsymbol{v}_{bl_n/h}$ is related to the speed of the hands of the rower n denoted $\boldsymbol{v}_{ha_n/h}$ and the angle θ_n (angle between the oar axis and the y axis, see Fig. 6.7) through the kinematic relation:

$$\boldsymbol{v}_{bl_n/h} = -\frac{\ell_o}{\ell_i} \boldsymbol{v}_{ha_n/h} = -\ell_o \dot{\theta}_n \left[\cos(\theta_n) \, \boldsymbol{e}_x + \sin(\theta_n) \, \boldsymbol{e}_y \right] \ . \tag{6.10}$$

Now the speed of the blade in the reference frame of the water reads:

$$\boldsymbol{v}_{bl_n/w} = \left[U - \ell_o \dot{\theta}_n \cos(\theta_n) \right] \boldsymbol{e}_x - \ell_o \dot{\theta}_n \sin(\theta_n) \boldsymbol{e}_y \ . \tag{6.11}$$

Finally, the resulting force exerted by the fluid on the blade n, $\boldsymbol{F}_{w/bl_n}$, projected on the vector $\boldsymbol{e}_x$, reads:

$$F_{w/bl_n} = -\frac{1}{2} \rho S_{bl} C_D v_{bl_n/w} U \left[1 - \eta \frac{v_{ha_n/h}}{U} \cos(\theta_n) - \eta \frac{C_L}{C_D} \frac{v_{ha_n/h}}{U} \sin(\theta_n) \right]$$
$$- m_a \frac{\mathrm{d}U}{\mathrm{d}t} + m_a \eta \frac{\mathrm{d}}{\mathrm{d}t} \left[v_{ha_n/h} \cos(\theta_n) \right] \ , \tag{6.12}$$

with $\eta = \ell_o / \ell_i$ the ratio between the outboard and the inboard oar lengths.

From here, we make two crude assumptions. Firstly, we suppose that $\theta \simeq 0$, this is as if the blades were moving parallel to the direction of motion of the boat, which kills the lift contribution to the total force. Secondly, we consider that the velocity of the rower's hands

and the velocity of the center of mass of the rower are equal, that is: $v_{ha_n/h} = v_{r_n/h}$. These two assumptions are quite far from reality, given the observations made in Chap. 2 (see Sect. 2.3 for the first assumption, which shows the importance of lift in the propulsion of top-level rowing boats and see Sect. 2.4 for the second assumption, in particular Fig. 2.14). However, these two assumptions greatly simplify the expression of the force on the blade:

$$F_{w/bl_n} = \frac{1}{2}\rho S_{bl} C_D |\eta v_{r_n/h} - U| \left[\eta v_{r_n/h} - U\right] - m_a \frac{dU}{dt} + m_a \eta \frac{dv_{r_n/h}}{dt} \ . \tag{6.13}$$

In the following, we use $C_D \simeq 2$, which is the value found experimentally for an angle of attack $\Phi = 90°$ (see Fig. 6.8(b)).

Dynamical equation.

Combining the momentum conservation in Eq. (6.3) with Eqs. (6.4), (2.1) and (6.5), the equation governing the velocity of the boat U reads:

$$\left(M + m_a \sum_{n=1}^{N} H_n(t)\right) \frac{dU}{dt} = -\frac{1}{2}\rho S_h C_h U^2 + \frac{1}{2}\rho S_{bl} C_D \sum_{n=1}^{N} H_n(t)|\eta v_{r_n/h} - U|(\eta v_{r_n/h} - U)$$
$$+ \sum_{n=1}^{N} (m_a \eta H_n(t) - m_r) \frac{dv_{r_n/h}}{dt} \ . \tag{6.14}$$

We take as a characteristic time $T = 1/f$ the period of the rowing cycle and as a characteristic velocity $U^\star = 2Mf/(\rho S_h C_h)$. Writing $U = \hat{U} U^\star$ and $t = \hat{t} T$, the equation of evolution for the dimensionless hull velocity $\hat{U}$ reads:

$$\left(1 + \frac{m_a}{M} \sum_{n=1}^{N} H_n(t)\right) \frac{d\hat{U}}{d\hat{t}} = -\hat{U}^2 + \frac{S_{bl} C_D}{S_h C_h} \sum_{n=1}^{N} H_n(t)|\eta \hat{v}_{r_n/h} - \hat{U}|(\eta \hat{v}_{r_n/h} - \hat{U})$$
$$+ \sum_{n=1}^{N} \frac{m_a \eta H_n(t) - m_r}{M} \frac{d\hat{v}_{r_n/h}}{d\hat{t}} \ . \tag{6.15}$$

Power estimation.

We further define p_n, the instantaneous power injected by the rower n, which is written:

$$p_n = \eta H_n(t) F_{w/bl_n}(t) \times v_{r_n/h}(t) \ , \tag{6.16}$$

with F_{w/bl_n} given in Eq. (6.13). Thus, the total mean power for N rowers $\mathcal{P}_N$ reads:

$$\mathcal{P}_N = \sum_{n=1}^{N} \langle p_n(t) \rangle \ . \tag{6.17}$$

6.5   First model: imposed kinematics

As a first model of rowing, we consider the problem at imposed kinematics, that is we impose the velocity of each rower $v_{r_n/h}$ and consequently the stroke frequency f. Eq. (6.15) is solved taking $v_{r_n/h} = \pi \Delta x f \sin(2\pi f t + (n-1)\phi)$, or in dimensionless form:

$$\hat{v}_{r_n/h} = \pi \Delta x f / U^\star \sin(2\pi \hat{t} + (n-1)\phi) \ , \tag{6.18}$$

with ϕ the phase difference between consecutive rowers and Δx the characteristic distance of the rower's motion on the boat. Following the definition of $H_n(t)$, we consider that $H_n(t) = 1$ if $v_{r_n/h} > 0$ and $H_n(t) = 0$ otherwise.

6.5.1 Prediction for our model boat

Our model rowing boat was operated at a stroke frequency $f \simeq 1.3$ Hz with $\Delta x \simeq 3$ cm. The different parameters needed for the theoretical model are given in Table 6.1. To capture the "steady" dynamics, Eq. (6.15) is solved numerically using an explicit Runge-Kutta method and enforcing the periodic boundary condition: $\hat{U}(\hat{t} = 0) = \hat{U}(\hat{t} = 1)$. The comparison between the experimental results and the numerical ones for the mean velocity and fluctuations of our robotic rowing boat is shown in Fig. 6.6(a) and (b). The numerical results are in good agreement with the experimental data. In particular, with the numerics, we recover that the maximal boat velocity is obtained in the synchronised configuration, even if it is the configuration with the highest speed fluctuations. Note that the evolution of the mean speed $\langle U \rangle$ and the speed fluctuations $\Delta U/\langle U \rangle$ with the phase difference ϕ is symmetric about $\phi = 180°$, which is not what we observed experimentally. This may be due to the hydrodynamic interactions between the blades in the experiments, which depend on the phase difference and are not taken into account in our theoretical model. One can also notice that the smallest fluctuations of the boat speed are obtained for multiples of $45°$ (except for $0°$ and $180°$).

6.5.2 Prediction for a real rowing boat

We now solve the same equation (Eq. (6.15)) in the "steady" (or periodic) regime with the parameters of a real *eight* rowing boat (see Table 6.1). In particular, we take $f = 0.65$ Hz and $\Delta x = 1.3$ m, which are close to the real values in competitions.
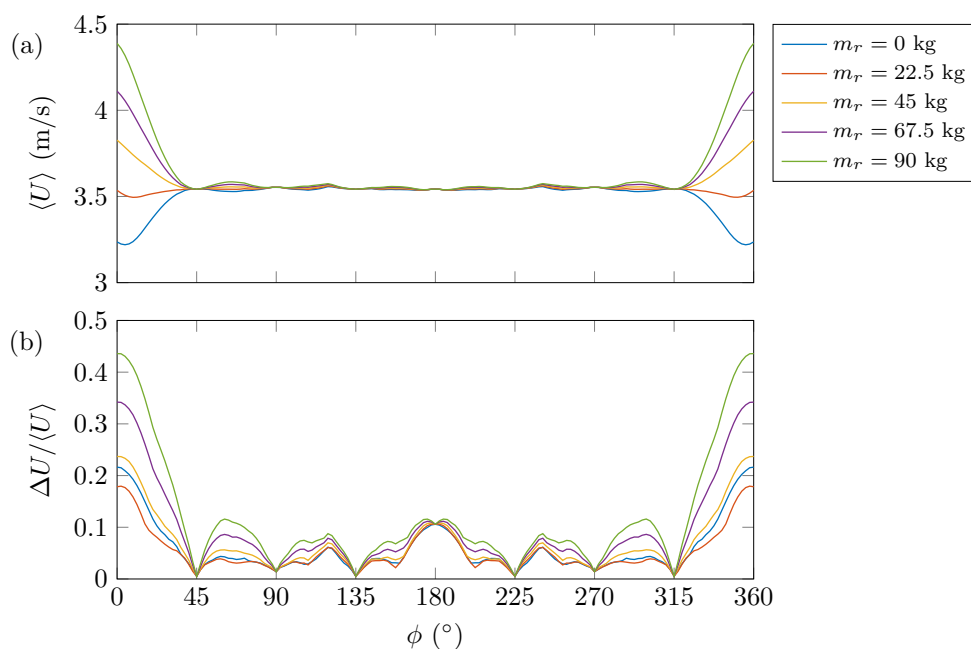

Figure 6.9: (a) Mean hull velocity $\langle U \rangle$ and (b) fluctuations of velocity $\Delta U/\langle U \rangle$, as a function of the phase difference ϕ predicted by our theoretical model at imposed kinematics for five different values of the rower's mass m_r.

The evolution of the mean hull velocity $\langle U \rangle$ and velocity fluctuations $\Delta U / \langle U \rangle$ with the phase difference ϕ is presented in Fig. 6.9 with the mass m_r of each rower ranging from 0 to 90 kg. The curves $\langle U \rangle$ and $\Delta U / \langle U \rangle$ obtained for $m_r = 90$ kg, which is approximately the right value for heavyweight rowing crews, show qualitatively the same evolution with ϕ as the one obtained for our model boat (see Fig. 6.6). For a given mass m_r, we observe that the mean hull velocity $\langle U \rangle$ remains nearly constant over the range $45° < \phi < 315°$. Furthermore, as the rower's mass m_r increases, the mean velocity $\langle U \rangle$ for $\phi = 0°$ increases, while for $45° < \phi < 315°$ it keeps almost the same value. For $m_r = 0$ kg (no moving mass on the boat), then the mean hull velocity for $\phi = 0°$ is smaller than in the desynchronised configurations. On the contrary, for $m_r = 90$ kg, the maximum of $\langle U \rangle$ is reached for $\phi = 0°$.

We thus find the same result for real rowing boats than for our model boat: at imposed kinematics and for a sufficiently large rower's mass (typically for $m_r > 22.5$ kg), the fastest boat is the synchronised one. This model gives a second interesting result: when the mass moving on the boat is small, then it is better to be desynchronised. However, this model at imposed kinematics is not very realistic! In reality, given the physiology constraint, one should rather consider that rowers inject a constant power.

6.6 Second model: imposed power

We consider the same problem but this time at imposed power instead of imposed kinematics. We solve Eq. (6.14) for a real rowing boat in the "steady" regime, now enforcing that the total mean power $\mathcal{P}_N$ given in Eq. (6.17) is a constant. We take $\mathcal{P}_N / N = 500$ W, which is a typical order of magnitude for the mean power injected by a rower during a competition [50, 84]. In this model, the stroke frequency f is a result of the computation and is not imposed a priori. Fig. 6.10 shows the evolution of the mean hull velocity, the velocity fluctuations and the stroke frequency f with the phase difference ϕ. We first observe that the velocity fluctuations $\Delta U / \langle U \rangle$ are the same as in the model at imposed kinematics. This is expected as, in this new model, the only difference with the model at imposed kinematics is that the stroke frequency is free, which do not affect the value of the ratio $\Delta U / \langle U \rangle$.

To keep the total mean power $\mathcal{P}_N$ constant, the stroke frequency f changes with the phase difference between rowers. Its value remains however close to the one imposed in the previous model, which was $f = 0.65$ Hz. For $45° < \phi < 315°$, the stroke frequency is almost independent of the rower's mass m_r, while for ϕ around $0°$, f decreases with m_r. This means that the force exerted by the rowers on the oars becomes larger as m_r increases, allowing f to decrease to maintain a constant injected power.

If we now look at the evolution of the mean velocity $\langle U \rangle$ with ϕ, we first observe, as for the stroke frequency f, that for $45° < \phi < 315°$ the rower's mass m_r has no influence on the mean hull velocity, while for $\phi = 0°$, $\langle U \rangle$ increases with m_r. It is also interesting to notice the position of the local maxima between $0°$ and $180°$ sorted by order of magnitude: $0°$, $360/2 = 180°$, $360/3 = 120°$, $360/4 = 90°$, etc. Local maxima for $\langle U \rangle$ are thus reached when groups of synchronised rowers can be formed (for example, for $\phi = 180°$, there are two groups of four synchronised rowers). Eventually, contrary to the model at imposed kinematics, we now find that, whatever the rower's mass m_r, the fastest boat is always the one with synchronised rowers ($\phi = 0°$).
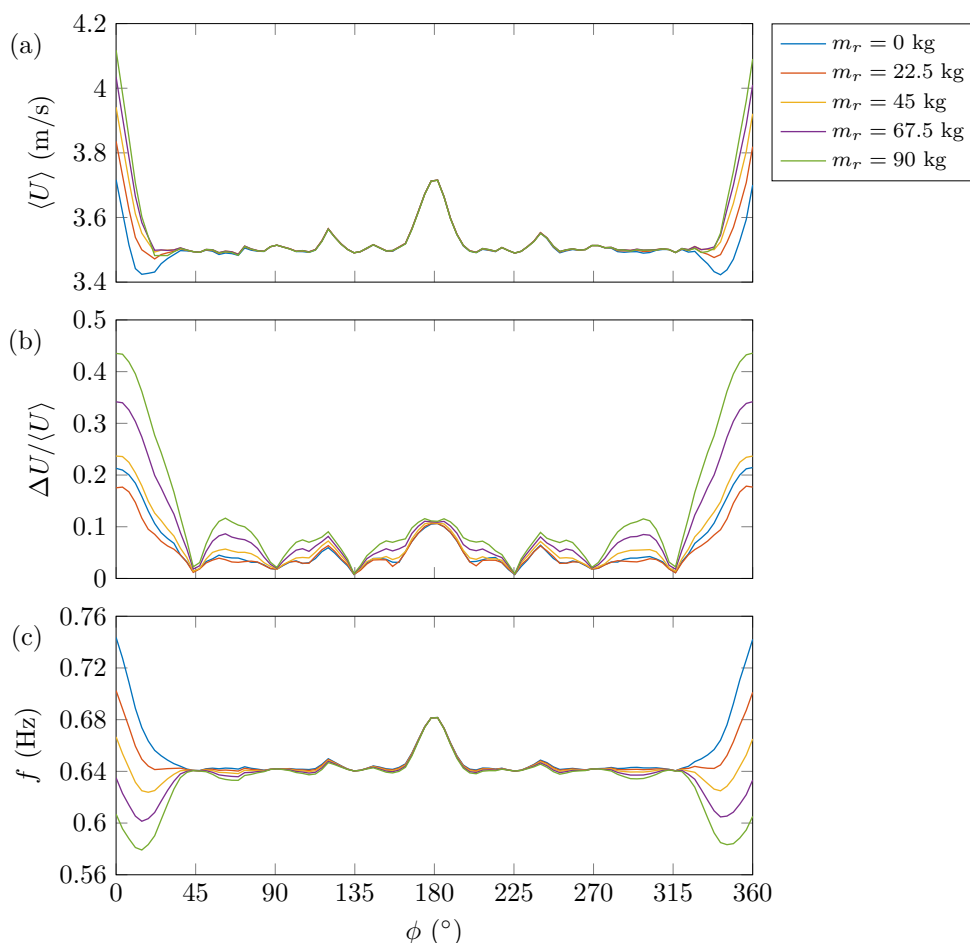
Figure 6.10: (a) Mean hull velocity $\langle U \rangle$, (b) fluctuations of velocity $\Delta U / \langle U \rangle$ and (c) stroke frequency f, as a function of the phase difference ϕ predicted by our theoretical model at imposed power for five different values of the rower's mass.

6.7   Discussion

Our conclusion is a bit disappointing as it will not change the way rowers are currently rowing: we find both numerically and experimentally that the fastest boat is the synchronised one.

From the theoretical model at imposed power (the most realistic one from a physiological perspective), we see that the mass moving on the boat, which is equal to Nm_{r}, plays an important part in the story. Indeed, for $\phi = 0°$ (synchronised configuration), the higher the rower's mass, the fastest the boat. On the opposite, in the desynchronised configurations, the rower's mass has almost no effect on the mean boat velocity. To understand this, one should remember that the velocity of the hull is maximum during the recovery stroke (see Fig. 2.7(a)) because of the simultaneous motion of the rowers towards the stern of the boat. This effect increases with the mass of the rowers but it is lost when the rowers are desynchronised.

Our result contradicts the one from Brearley *et al.* who found that an *eight* rowing boat with two groups of four synchronised rowers (corresponding to $\phi = 180°$) would go faster than the synchronised boat [66]. The discrepancy with our model is related to the efficiency of the blade propulsion (developed in Appendix A). If the propulsive efficiency was the same

for all phase differences, then the model at imposed force and kinematics derived by [66] would apply and give the result expected in the first place when we first considered the drag on the hull (see Subsect. 6.1.1). However, imposing both the force and the kinematics at the same time is impossible as they are related by Eq. (6.12) or Eq. (6.13). In Appendix A, we show that, when imposing the force applied by the rower on the blade, then one can compute the stroke frequency f. Our model at imposed power imply that the propulsion is less efficient in the desynchronised configuration than in the synchronised one, which explains the changes in the stroke frequency and in the resulting mean hull velocity.

We should now mention the limitations of our theoretical model. For the models at imposed kinematics and imposed power, the order of magnitude for the mean hull velocity is about 2 times smaller than the one for rowing boats in competitions. This is surely related to the crude assumptions made earlier in the model, in particular the first one which removed the contribution from the lift to the force on the blade. Taking lift into account in the model would obviously affect our results but is not expected to change the observed tendencies. As for the second assumption, according to Fig. 2.14, the velocity of the rower's hands is about twice the velocity of the rower's center of mass, which could slightly reduce the effect of the moving mass. Eventually, in our model at imposed power, we do not take into account the recovery stroke in the power estimation. The power injected by the rowers during this part of the stroke is indeed neglected compared to the one injected during the power stroke, which seems a reasonable hypothesis.

6.8 Appendix: Parameters of our model boat

To estimate the hull drag coefficient C_h of our model boat, we conducted the same experiment as the one described in Sect. 2.5 for a real boat (see also Fig. 2.15). The instantaneous hull velocity during a deceleration phase is measured (see Fig. 6.11) and fitted using Eq. (2.3). This fit yields $U_0 \simeq 0.21$ m/s and $\tau \simeq 3.7$ s, which, with $M \simeq 2$ kg and $S_h \simeq 0.13$ m^2, gives $C_h \simeq 0.04$.
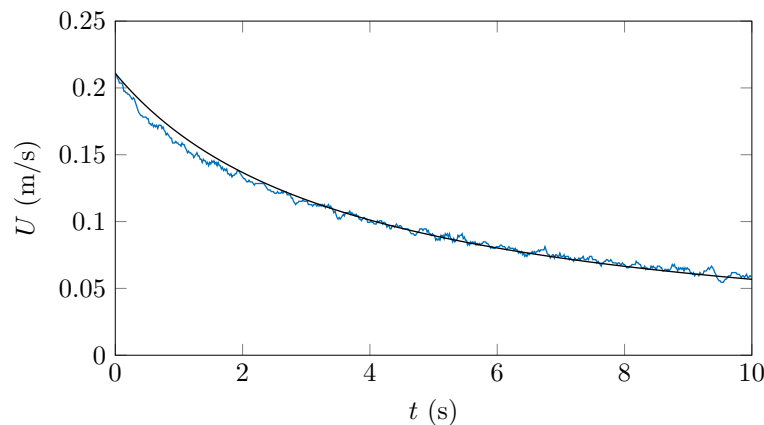
Figure 6.11: Instantaneous speed of our model rowing boat, as a function of time during a deceleration phase (blue curve). The black line is a fit of the experimental curve using Eq. (2.3) with $U_0 \simeq 0.21$ m/s and $\tau \simeq 3.7$ s.

The parameters of our model boat are listed in Table. 6.1 together with the parameters for an *eight* rowing boat for comparison.

Parameter	Model boat	Real boat
ℓ (m)	2	20
w (m)	0.06	0.55
m_{boat} (kg)	1.35	97
m_{r} (kg)	0.1	90
M (kg)	2.15	820
$8m_{\text{r}}/M$	0.4	0.9
S_{h} (m^2)	0.13	13
C_{h}	0.04	0.0025
ℓ_b (cm)	4	45
w_b (cm)	2	21.5
S_{bl} (m^2)	$8 \cdot 10^{-4}$	0.1
C_D	2	2
m_{a} (kg)	0.026	30
η	5	2.2
Re	$5 \cdot 10^5$	10^8
Fr	0.07	0.4
We	2500	$7 \cdot 10^6$

Table 6.1: Typical values of the relevant parameters for our model boat and for an *eight* rowing boat. The last three parameters are dimensionless parameters characterising the flow around the hull. The Weber number We compares the inertia of the fluid to its surface tension.

Take home message of Chapter 6

1. Synchronisation in rowing is responsible for large fluctuations of speed, which in turn increase the energy lost by friction on the hull compared with a motion at constant speed.

2. To study the effect of the synchronisation of rowers on a rowing boat, we built a robotic rowing boat at the scale 1/10 with eight robotic rowers controlled separately. We observed that the boat was going faster in the synchronised configuration.

3. We made a simplified theoretical model of rowing and considered two different hypotheses: imposed kinematics and imposed power, among which the most realistic one physiologically is imposed power. The model with this hypothesis also predicts that the fastest boat is the synchronised one.

4. We explain this result by highlighting two key ingredients: the propulsive efficiency, which decreases when the rowers are desynchronised and the mass of the rowers, which does not affect much the mean hull velocity in the desynchronised cases but significantly increases the mean velocity in the synchronised one.

6

6

7

Shape effects in fin propulsion

Propulsion in water or at its surface can also be achieved with flexible plates, called fins, which were inspired by fish swimming. In this experimental and theoretical study, we look at the effect of geometry and elasticity on the propulsive performance of simple rectangular flexible fins subjected to a heaving forcing. The optimal design of a rectangular fin is mostly dictated by its resonant frequency.

Picture of the tail of a Humpback whale. Source: [9].

Contents

7.1 Position of the problem

The locomotion of animals in water has been widely studied over the past years [108, 109, 110, 111, 112]. In particular, the propulsion of fishes and mammals has been divided into two main categories: the anguilliform and carangiform modes of propulsion [108]. Slender fishes such as eels (see Fig. 7.1(a)) belong to the anguilliform group. In this undulatory mode of propulsion, the whole body is involved in the propulsion. The carangiform group gathers larger and faster fishes, such as salmons (see Fig. 7.1(b)) or sharks, for which only the posterior part of the body participates in the propulsion.
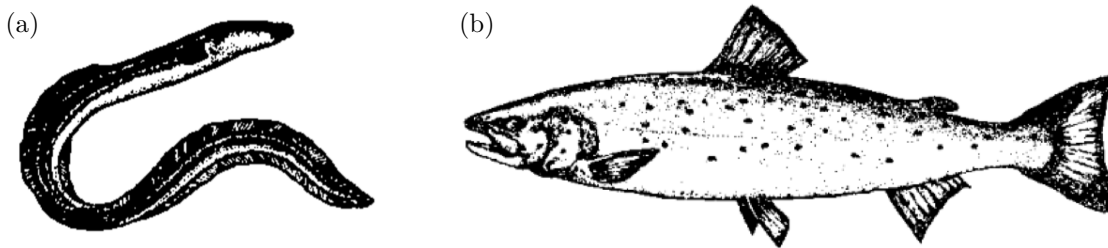

Figure 7.1: (a) Common eel *Anguilla vulgaris* and (b) a salmon *Salmo salar*. Pictures reprinted from [108].

The carangiform propulsion relies on the flexibility of the appendages involved, which is thought to enhance swimming efficiency [113, 114]. To get insight in the propulsive mechanisms at stake, a number of studies modeled this propulsion theoretically [115, 116, 117, 118], numerically [119] or experimentally [113, 114, 120, 121, 122] with pitching and heaving flexible foils and sheets. Most studies indicate that the highest propulsive efficiencies are attained for forcing frequencies close to the resonant frequencies of the fin [113, 120].

Inspired by fish swimming, fins (also called flippers) were designed for human swimming. Their invention is actually fairly recent. The French lieutenant commander Louis de Corlieu (1888 – 1967) designed the first fin model during the 1920s (see Fig. 7.2(a)) and patented it in 1933 [123]. It then took about 30 years, until the 1950s, for this invention to be adopted and to become a usual accessory in swimming pools (see Fig. 7.2(b)). With the development of new materials (plastic or carbon fiber), the monofin (see Fig. 7.2(c)) started to be used in the early 1970s and allowed to beat all fin-swimming world records. Today's world records are 13.85 s in apnea with a monofin (on the 50 m distance) and 15 s at the surface [125]. This makes an 8% difference, which is related to the appearance of wave drag at the water

Figure 7.2: (a) Replica of the first fin model designed by Louis de Corlieu in the 1920s (source: [124]). (b) Picture of one of the current fin models. (c) Picture of one of the current monofin models.

surface (see Sect. 1.6). These records can be compared with the world record in freestyle on 50 m, which is 20.9 s, corresponding to a 40% difference with the monofin record at the surface.

Over the years, the shape of fins has become very complex. Today they have holes and grooves and are made of materials with well-controlled mechanical properties to maximise their propulsive efficiency. Here, we model the fin as a simple rectangular flexible plate, similarly to previous studies, and study the effect of the dimensions of the fin on its propulsion.

7.2 Experimental set-up

We use the experimental set-up presented in Fig. 7.3 and inspired by [126, 127]. Two identical flexible plates are attached at the extremities of a rod on either side. This rod has its center linked to a vertical shaft which is set in translation by an electromagnetic linear actuator and is free to rotate about its axis. When the system oscillates vertically, it spontaneously starts rotating, so that it can be seen as an experimental model of swimming with fins. The advantage of the cylindrical geometry is that the motion is unrestricted in the horizontal direction. However, the drawback is that, at high speeds, the fins move in a fluid disturbed by the preceding fin. We focus on rectangular fins of length L, width b and thickness e (see Fig. 7.3).
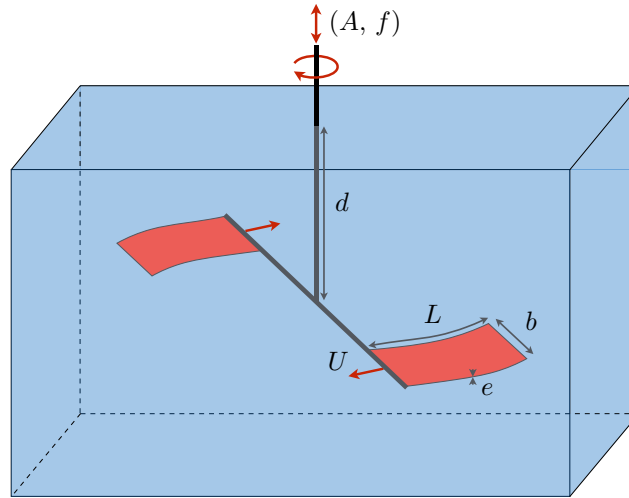
Figure 7.3: Schematic of the experimental set-up. Two identical fins made of a rectangular flexible plate of length L, width b, thickness e ($e \ll b < L$) and Young's modulus $E \simeq 2$ GPa are attached to a rod, itself connected to a vertical shaft. The whole system is forced to oscillate at the frequency f with the amplitude A. The fins are immersed in a water tank of typical size 1 m at a distance d from the water surface.

With this set-up, we measure, on the one hand, the fin speed U and, on the other hand, the propulsive force F while preventing the rotation of the system (*i.e.* $U = 0$). We observe that the speed U is related to the force F through the simple force balance $F \sim U^2$ (see Sect. 7.6), which means that the measured force F is close to the propulsive force when the system is free to rotate. Therefore, in the following, we focus on the characterisation of the propulsive force. The experiment is conducted for different forcing amplitudes, denoted A, and forcing frequencies, denoted f, as well as different geometries of the plate.

7.3 Experimental results

We first present the response of a rectangular plate to an oscillatory forcing. Then, the effect of the shape of the fin is discussed. Finally, we study the effect of the distance of the fin to the water surface, denoted d.

7.3.1 Rectangular plate response to a forcing

Here, we study the effect of the forcing frequency f and amplitude A on the response of a rectangular fin of length $L = 8.5$ cm, width $b = 5$ cm and thickness $e = 1$ mm. When forced to oscillate, we observe that the plate deforms. We define A_q the amplitude of oscillation of the trailing edge. Fig. 7.4 shows the area swept by the fin when looking at it from the side. For low frequencies ($f \leq 3$ Hz), the shape of this area remains nearly rectangular meaning that the plate does not deform much ($A_q \simeq A$). On the contrary, for larger frequencies, the shape of the swept area changes a lot. In particular, the amplitude A_q is maximum for $f = 6$ Hz, which corresponds to the first resonant frequency of the fin, denoted f_1. We also notice the appearance of a node for $f = 9$ Hz, which corresponds to the appearance of the second beam mode (see Fig. 7.9 in Subsect. 7.4.1).
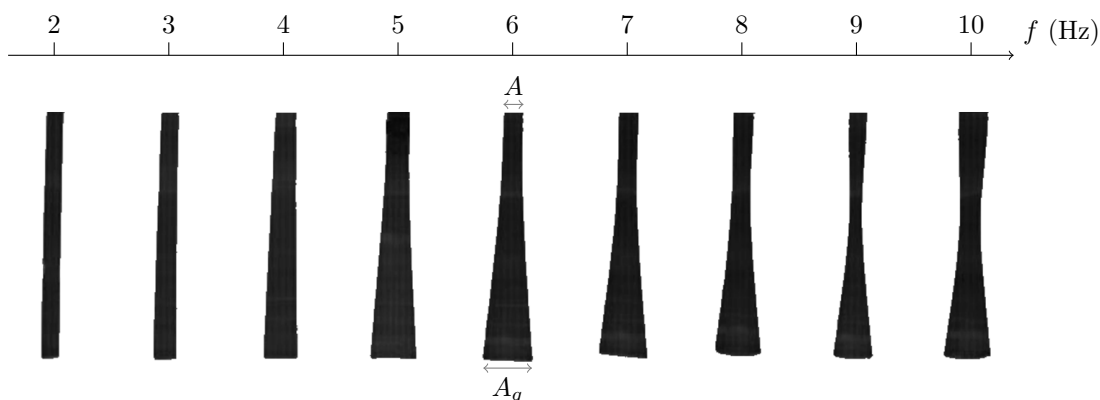
Figure 7.4: Pictures of the area swept by the fin for $A = 5$ mm and increasing forcing frequencies. For each picture, the leading edge is at the top and the trailing edge at the bottom. The width of the swept area corresponds at the top to the forcing amplitude A and at the bottom to the trailing edge amplitude A_q. The pictures are obtained by superposition of images over a few cycles.

To be more quantitative and similarly to previous studies [114], from side-view videos of the plate motion, we measured the amplitude at the leading edge A and at the trailing edge A_q, as well as the phase difference between the leading edge and the trailing edge motions, denoted ψ. Fig. 7.5(a) shows that the ratio A_q/A is indeed maximum for $f = f_1 \simeq 6$ Hz for the three different values of the forcing amplitude A. We further observe that, close to the resonant frequency, the ratio A_q/A becomes lower as A becomes larger, which results from non-linearities in the equation of deformation of the plate. The same tendency is observed in [114]. As for the phase difference ψ, we observe that it increases with the forcing frequency f, while it does not depend much on the forcing amplitude A (see Fig. 7.5(b)). At low frequencies, ψ is close to 0: the leading edge and the trailing edge are in phase. In this case, the time needed for the waves to propagate from the leading edge to the trailing edge is much smaller than the period of the forcing. This is not the case anymore when the

(a)

(b)
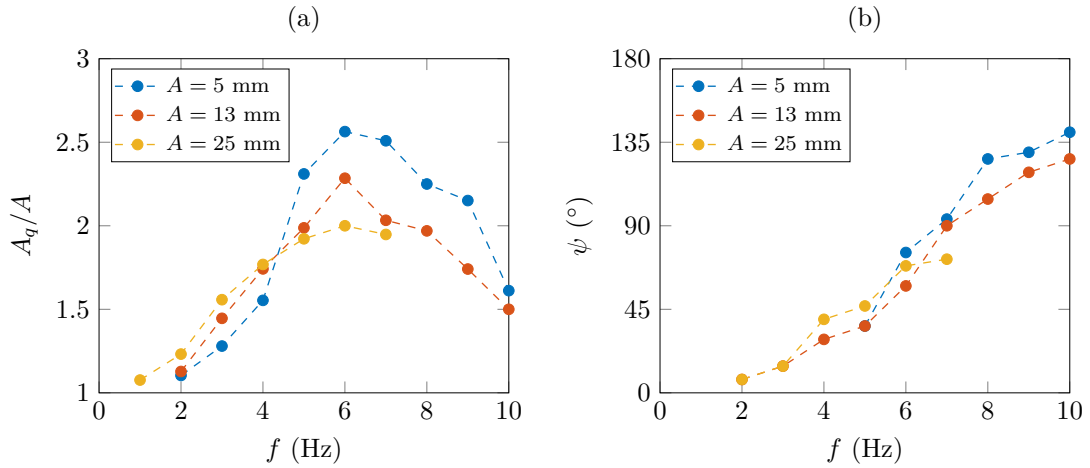
Figure 7.5: (a) Ratio of the trailing edge amplitude to the leading edge amplitude A_q/A and (b) phase difference ψ between the trailing edge and the leading edge, as a function of the forcing frequency f for three different forcing amplitudes A.

frequency is increased and gets closer to the first resonant frequency f_1, which qualitatively explains the increase of the phase difference ψ.

We measured the propulsive force F for different forcing frequencies and forcing amplitudes. The evolution of F with the forcing frequency f is similar to what was observed by Quinn *et al.* for plates of different bending stiffnesses [113]. In particular, one can see that the resonant frequency f_1 delimits two regimes (see Fig. 7.6(a) for $A = 13$ mm). This is even more visible in logarithmic scale (see Fig. 7.6(b)), with the slope of the curve $F(f)$ before the resonance being larger than the one after the resonance. In the following, we characterise the regime before the resonance, that is for $f < f_1$. Two different cases should then be considered: small deformations of the plate for $A \ll L$ and large deformations for $A \sim L$. In the case of small deformations ($A \ll L = 85$ mm), we observe that, $F \sim A^2 f^4$, while for

(a)

(b)
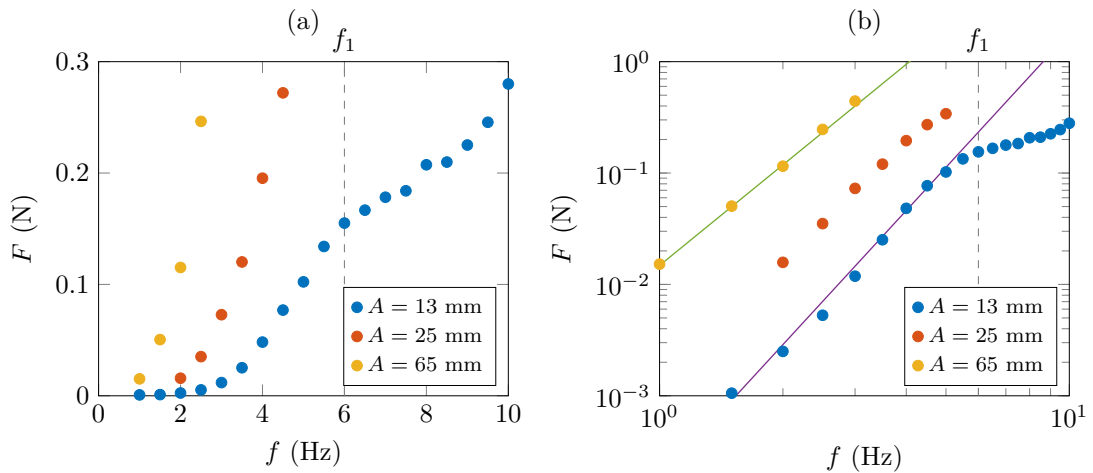
Figure 7.6: Propulsive force as a function of the forcing frequency for three different values of the forcing amplitude in (a) linear scale and (b) logarithmic scale. The resonant frequency f_1 is indicated by a vertical dashed line. In (b), the violet line is a fit of the data for $A = 13$ mm and $f < f_1 \simeq 6$ Hz ($F = 1.8 \cdot 10^{-4} f^4$); and the green line is a fit of the data for $A = 65$ mm ($F = 1.5 \cdot 10^{-2} f^3$).

large deformations we find $F \sim A^2 f^3$ (see Fig. 7.6). The scaling for small deformations is in agreement with the scaling analysis presented in Subsect. 7.4.2.

7.3.2 Shape effects

Fig. 7.7(a) illustrates the typical evolution of the propulsive force F with the forcing frequency for plates of different lengths. As previously observed in Fig. 7.6(a), we see that, at the resonant frequency f_1, the evolution of F with the forcing frequency changes. We denote $F_1 = F(f_1)$ the propulsive force reached at the resonant frequency. The length of the plate L has a significant effect on both the resonant frequency f_1 and the value of F_1: an increase in the length of the plate L decreases F_1, as well as the resonant frequency f_1. We find that the force at the resonance F_1 is inversely proportional to L^4.
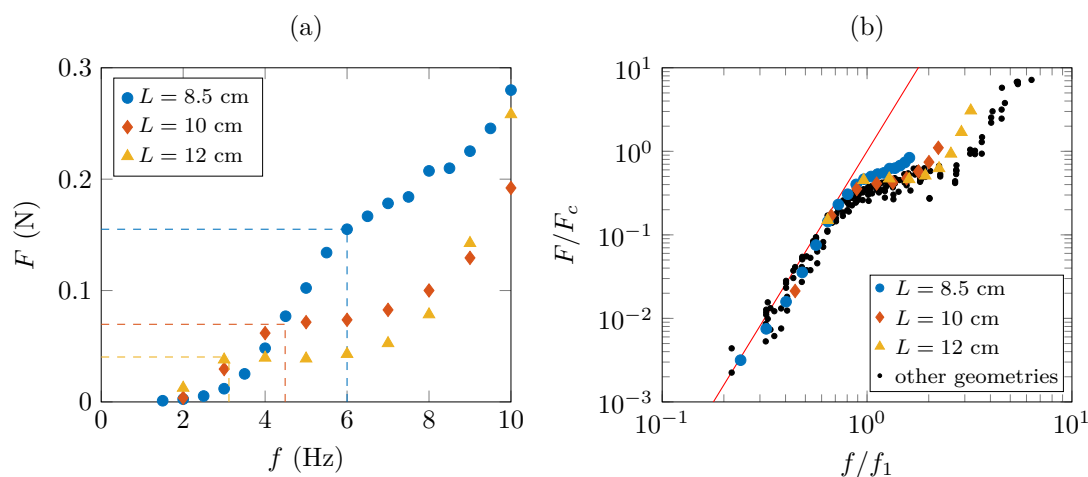
Figure 7.7: (a) Propulsive force F as a function of the forcing frequency f for three fins of different length L but same width ($b = 5$ cm) and same thickness ($e = 1$ mm), with $A = 13$ mm. For the three data sets, the position of the resonant frequency f_1 of the plate is highlighted by a vertical dashed line and the corresponding value of the propulsive force F_1 is indicated by a horizontal dashed line. (b) Propulsive force rescaled by the characteristic force $F_c = Ee^3bA^2/L^4$ as a function of the frequency rescaled by the resonant frequency f_1 for the three data sets plotted in (a) and for plates of varying length, width and thickness. The red line represents the function $f(x) = x^4$.

Considering plates of different length L, width b and thickness e, we find that the resonant frequency f_1 scales as the characteristic frequency $f_c = \sqrt{Ee^3/(12\rho L^4 b)}$, with E the Young's modulus of the plate (see Fig. 7.10 in Sect. 7.4.1). Then, we obtain that the force at the resonance F_1 depends linearly on the width b and scales as e^3. Finally, in the limit of small deformations, we get: $F_1 \sim F_c = Ee^3bA^2/L^4$, which is consistent with the scaling analysis in Subsect. 7.4.2. Fig. 7.7(b) shows the evolution of the force F rescaled by the characteristic force F_c with the forcing frequency f rescaled by the resonant frequency f_1 for plates of different length, width and thickness. All the data collapse for $f/f_1 \lesssim 1$ proving the validity of both scales.

7.3.3 Free-surface effect

Now, for the same fin as in Sect. 7.3.1 ($L = 8.5$ cm, $b = 5$ cm and $e = 1$ mm), we change its distance to the air-water interface, denoted d, and study how this affects the propulsive

force F and the fin velocity U. When getting closer to the water surface the propulsive force and fin velocity are expected to decrease to zero when $d = 0$. This is what can be observed in Fig. 7.8(a) and (b), where F and U are plotted as a function of the ratio d/b. One can see that the distance from which the free-surface starts to play a role is of the order of magnitude of the fin width b. We further notice that the distance of influence of the free-surface is smaller for the propulsive force than for the fin velocity. This difference can be explained by the appearance of wave drag, which increases significantly the total drag force on the fin (see Sect. 1.6).
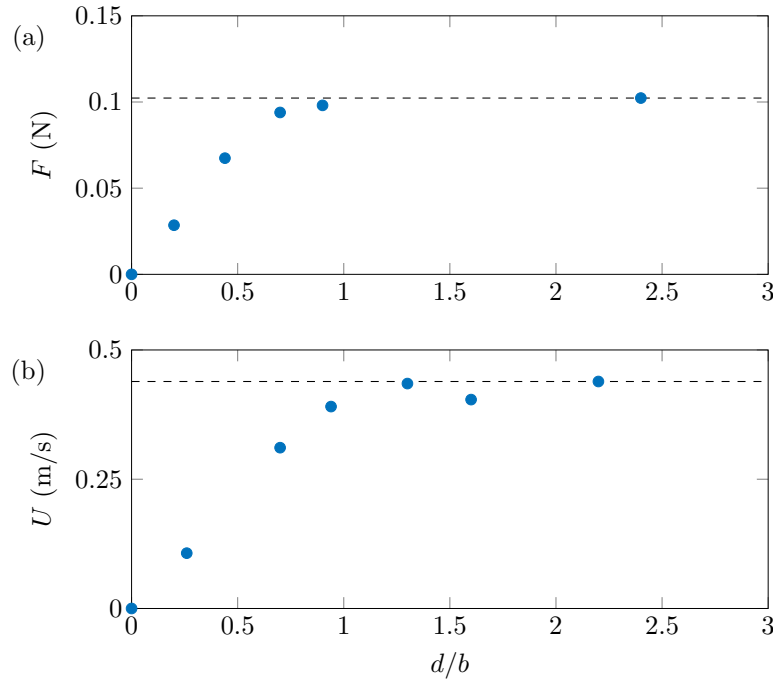
Figure 7.8: (a) Propulsive force F and (b) fin velocity U, as a function of the distance to the free-surface d rescaled by the width of the fin b (for $f = 5$ Hz, $A = 13$ mm). The black dashed line in each plot indicates the value reached far from the free-surface.

Eventually, this part highlights that the free-surface has a strong effect on the propulsion with fins when the distance from the free-surface becomes smaller than the width of the fin. This is one of the reason why the world records in fin-swimming on the 50 m distance are by 8% smaller at the surface than in apnea.

7.4 Theoretical model

Here we focus on the deformation of a rectangular fin deep underwater, subjected to a heaving motion at the leading edge. As observed in the experiments, this forcing produces an horizontal motion of the fin at the speed U. One can define two Reynolds numbers: along the vertical $\mathrm{Re}_v = \rho A f L / \mu$ and along the horizontal $\mathrm{Re}_h = \rho U L / \mu$. Taking $A = 10$ mm, $f = 5$ Hz, $L = 10$ cm and $U = 0.5$ m/s as typical values in the experiments, one finds $\mathrm{Re}_v \simeq 5\,000$ and $\mathrm{Re}_h \simeq 50\,000$. The flow around the fin is thus at high Reynolds number in both cases. The typical aspect ratio b/L is of the order of 0.5. This corresponds to the upper limit of validity of the slender-body theory developed by Lighthill [115], which will still be

used in the following. We will further assume that the boundary layer remains attached to the fin and that the deformation of the fin is small (compared to its length L).

7.4.1 Equation of deformation of the fin

General expression and boundary conditions.

Let $z(x, t)$ be the vertical position of an element of the plate of surface $b \times e$ in x at time t. With the approximation of small slope (or equivalently small deformation of the fin $|\partial z / \partial x| \ll 1$), the Newton's second law applied to an element of the fin of length $ds \simeq dx$ and projected onto the vertical axis leads to the Euler-Bernoulli equation [128]:

$$\rho_s eb \frac{\partial^2 z}{\partial t^2} + EI \frac{\partial^4 z}{\partial x^4} = f_{F/S} \,, \tag{7.1}$$

where ρ_s is the density of the fin, $I = be^3/12$ is the second moment of area and $f_{F/S}$ is the force per unit length exerted by the fluid on the fin.

The boundary conditions correspond to a sinusoidal forcing imposed in $x = 0$ and no force and torque at the end of the fin (in $x = L$). Thus, one has:

$$z(x = 0, t) = \frac{A}{2} \sin(2\pi f t) \,, \tag{7.2a}$$

$$\frac{\partial z}{\partial x}(x = 0, t) = 0 \,, \tag{7.2b}$$

$$\frac{\partial^2 z}{\partial x^2}(x = L, t) = 0 \,, \tag{7.2c}$$

$$\frac{\partial^3 z}{\partial x^3}(x = L, t) = 0 \,. \tag{7.2d}$$

The complicated task is now to model the force exerted by the fluid on the fin $f_{F/S}$.

Model for $f_{F/S}$ and equation of deformation of the plate.

Similarly to [129], we model the force exerted by the fluid on the fin $f_{F/S}$ as the sum of added mass force and pressure drag, so that:

$$f_{F/S} = -m_a \left(\frac{\partial^2 z}{\partial t^2} + 2U \frac{\partial^2 z}{\partial t \partial x} + U^2 \frac{\partial^2 z}{\partial x^2} \right) - \frac{1}{2} \rho b C_D \frac{\partial z}{\partial t} \left| \frac{\partial z}{\partial t} \right| \,, \tag{7.3}$$

where m_a is the added mass per unit length, U the horizontal speed of the plate and C_D the drag coefficient of the plate. The added mass is written: $m_a = \rho b^2 C_a$ with C_a the added mass coefficient ($C_a \simeq \pi/4$ for a plate, see Sect. 1.7.1).

Now given that $\rho_s eb \ll m_a = \rho b^2 C_a$ (because $\rho_s \sim \rho$, $C_a \sim 1$ and $e \ll b$), the equation of deformation of the plate is written:

$$\rho b^2 C_a \left(\frac{\partial^2 z}{\partial t^2} + 2U \frac{\partial^2 z}{\partial t \partial x} + U^2 \frac{\partial^2 z}{\partial x^2} \right) + EI \frac{\partial^4 z}{\partial x^4} + \frac{1}{2} \rho b C_D \frac{\partial z}{\partial t} \left| \frac{\partial z}{\partial t} \right| = 0 \,. \tag{7.4}$$

Taking L as the characteristic length, $\tau = L^2 \sqrt{\rho b^2 C_a/(EI)}$ as the characteristic time and $c = L/\tau$ as the characteristic speed, we define the following dimensionless variables: $\hat{x} = x/L$, $\hat{z} = z/L$, $\hat{t} = t/\tau$, $\hat{U} = U/c$, $\hat{A} = A/L$, $\hat{f} = f\tau$ and $\gamma = C_D L/(2C_a b)$. The dimensionless beam equation is written:

$$\frac{\partial^2 \hat{z}}{\partial \hat{t}^2} + 2\hat{U} \frac{\partial^2 \hat{z}}{\partial \hat{t} \partial \hat{x}} + \hat{U}^2 \frac{\partial^2 \hat{z}}{\partial \hat{x}^2} + \frac{\partial^4 \hat{z}}{\partial \hat{x}^4} + \gamma \frac{\partial \hat{z}}{\partial \hat{t}} \left| \frac{\partial \hat{z}}{\partial \hat{t}} \right| = 0 \,, \tag{7.5}$$

with the boundary conditions:

$$\hat{z}(\hat{x} = 0, \hat{t}) \;=\; \frac{\hat{A}}{2}\sin(2\pi \hat{f}\hat{t})\,, \tag{7.6a}$$

$$\frac{\partial \hat{z}}{\partial \hat{x}}(\hat{x} = 0, \hat{t}) \;=\; 0\,, \tag{7.6b}$$

$$\frac{\partial^2 \hat{z}}{\partial \hat{x}^2}(\hat{x} = 1, \hat{t}) \;=\; 0\,, \tag{7.6c}$$

$$\frac{\partial^3 \hat{z}}{\partial \hat{x}^3}(\hat{x} = 1, \hat{t}) \;=\; 0\,. \tag{7.6d}$$

Solving method: projection onto modes of the free beam.

We follow the method developed by Paraz *et al.* [118]. Let us consider the equation of a free plate (corresponding to taking $\hat{U} = 0$ and $\gamma = 0$ in Eq. (7.5)):

$$\frac{\partial^2 \hat{z}}{\partial \hat{t}^2} + \frac{\partial^4 \hat{z}}{\partial \hat{x}^4} = 0\,, \tag{7.7}$$

with the boundary conditions that the plate is embedded in $\hat{x} = 0$ and free in $\hat{x} = 1$:

$$\hat{z}(\hat{x} = 0, \hat{t}) \;=\; 0\,, \tag{7.8a}$$

$$\frac{\partial \hat{z}}{\partial \hat{x}}(\hat{x} = 0, \hat{t}) \;=\; 0\,, \tag{7.8b}$$

$$\frac{\partial^2 \hat{z}}{\partial \hat{x}^2}(\hat{x} = 1, \hat{t}) \;=\; 0\,, \tag{7.8c}$$

$$\frac{\partial^3 \hat{z}}{\partial \hat{x}^3}(\hat{x} = 1, \hat{t}) \;=\; 0\,. \tag{7.8d}$$

A solution of this equation is of the form $\hat{z}(\hat{x}, \hat{t}) = K\hat{z}_i(\hat{x})e^{ik_i^2 \hat{t}}$ with K a constant and:

$$\hat{z}_i(\hat{x}) = \cos(k_i\hat{x}) - \cosh(k_i\hat{x}) + \frac{\sin k_i - \sinh k_i}{\cos k_i + \cosh k_i}(\sin(k_i\hat{x}) - \sinh(k_i\hat{x}))\,, \tag{7.9}$$

where k_i is the solution of the equation: $\cos(k_i)\cosh(k_i) = -1$. One finds for the first three modes: $k_1 \simeq 1.875$, $k_2 \simeq 4.694$ and $k_3 \simeq 7.855$.
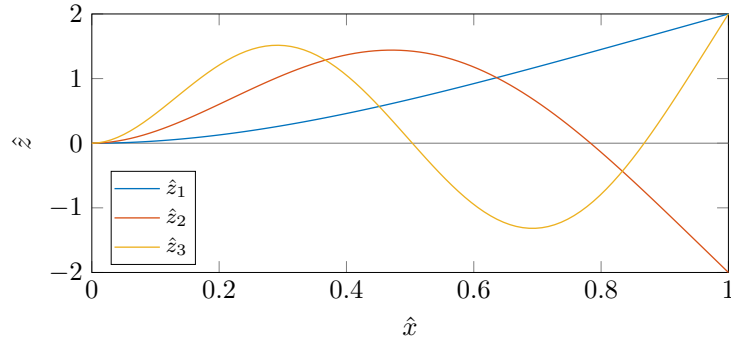

Figure 7.9: Plot of the first three modes $\hat{z}_i(\hat{x})$ of an embedded-free beam (see Eq. (7.7)).

As can be seen in Fig. 7.9, the nth mode crosses the horizontal axis $n-1$ times, so that the beam is more and more deformed as the number of the mode increases. Moreover, it is clear that a higher mode corresponds to a higher resonant frequency. This study is restricted to

quite low frequencies (f small compared to $k_3^2/(2\pi\tau)$), so the solution of Eq. (7.5) can be approximated by a linear combination of the first three beam modes:

$$\hat{z}(\hat{x}, \hat{t}) \simeq \left(\hat{A} + a_1 \hat{z}_1(\hat{x}) + a_2 \hat{z}_2(\hat{x}) + a_3 \hat{z}_3(\hat{x}) \right) e^{2i\pi \hat{f}\hat{t}} \ . \tag{7.10}$$

Such a decomposition is also found in [113] to analyse the deformation of flexible panels in experiments. The forcing parameters $\hat{A}$ and $\hat{f}$ are imposed and the coefficients (a_1, a_2, a_3) are obtained numerically after injecting this form of solution in Eq. (7.5) and projecting the obtained equation on each mode $\hat{z}_i$ with the scalar product $\langle f|g \rangle = \int_0^1 f(\hat{x})g(\hat{x}) \, d\hat{x}$. Compared with linearisation methods [129], this method has the advantage to better take into account the non-linear term.

First resonant frequency.

The characteristic time τ is related to the first resonant frequency through the dispersion relation: $k_1^2 = 2\pi f_1 \tau$. This gives:

$$f_1 = \frac{k_1^2}{2\pi\sqrt{C_a}} f_c \ , \tag{7.11}$$

where $f_c = \sqrt{C_a}/\tau = \sqrt{Ee^3/(12\rho L^4 b)}$.
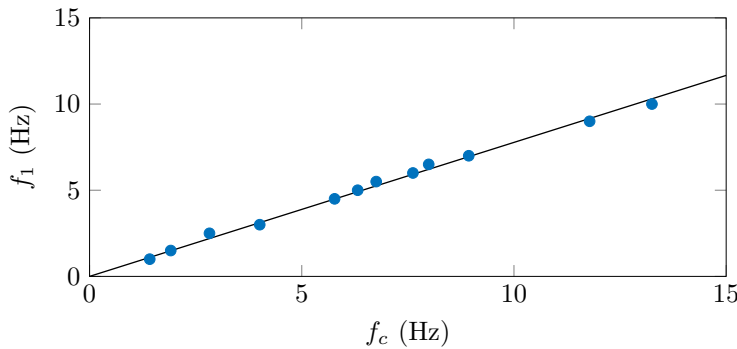
Figure 7.10: First resonant frequency f_1 as a function of the characteristic frequency $f_c = \sqrt{Ee^3/(12\rho L^4 b)}$. The black line is a fit of the experimental data: $f_1 = 0.78 \, f_c$.

The first resonant frequency f_1 was measured experimentally for plates of various geometries and the relation $f_1 \simeq 0.78 \, f_c$ is found (see Fig. 7.10). This gives $C_a \simeq 0.51$, which represents about 35% difference with the expected value $\pi/4$. This might be related to the separation of the boundary layer around the plate.

7.4.2 Expression of the propulsive force

Lighthill expression.

Lighthill developed a theory to predict the mean propulsive force F on a slender body depending on its deformation [115]. Assuming the flow around the fin to be potential and to remain attached, this theory gives, in the limit of small slopes $|\partial z/\partial x| \ll 1$, the following expression for the mean propulsive force:

$$F = \kappa f^2 A_q^2 \ , \tag{7.12}$$

where $\kappa = \pi^2 \rho b^2 C_{\mathrm{a}}/4$.

Scaling analysis.

As seen in Subsect. 7.4.1, the force exerted by the fluid on the fin is the sum of added mass force and pressure drag. In scaling analysis, the added mass force is written: $F_{\mathrm{a}} \sim \rho b^2 L A f^2$ where $\rho b^2 L$ is the scaling of the added mass and $A f^2$ the scaling of the acceleration of the fluid. Similarly, the pressure drag is written: $F_{\mathrm{f}} \sim \rho b L A^2 f^2$ with $A f$ the scaling of the plate velocity. From these scalings, we see that the added mass dominates when $A < b$, which is in the regime of small deformations. Then, in the following, we only consider the added mass force, which is consistent with the expression of the propulsive force derived by Lighthill (see Eq. (7.12)) [115]. The propulsive force is then the projection of F_{a} on the horizontal direction. This is: $F \sim (L/r) F_{\mathrm{a}}$, with r the radius of curvature of the fin. r is obtained from the balance between the torque induced by F_{a} and the bending torque of the plate:

$$F_{\mathrm{a}} L \sim \frac{EI}{r} \ . \tag{7.13}$$

Finally, using the expression of F_{a}, one gets:

$$F \sim \frac{\rho^2 A^2 f^4 L^4 b^3}{E e^3} \ . \tag{7.14}$$

The combination between this scaling and the expression derived from Lighthill (see Eq. (7.12)) gives: $A_q/A \sim f$. In comparison with the results shown in Fig. 7.5(a), this can only be valid before the resonance ($f < f_1$).

Furthermore, the first resonant frequency scales as $f_1 \sim \sqrt{E e^3/(\rho L^4 b)}$ (see Eq. (7.11)). Injecting the scaling of f_1 inside Eq. (7.14), one finds that the propulsive force at the resonance F_1 reads:

$$F_1 \sim F_c = \frac{E e^3 b A^2}{L^4} \sim \rho b^2 A^2 f_1^2 \ . \tag{7.15}$$

This scaling is in fairly good agreement with the experimental data as all the data points for different plate geometries collapse for $f/f_1 < 1$ when the rescaled force F/F_c is plotted as a function of the rescaled frequency f/f_1 (see Fig. 7.7 (b)).

7.5 Comparison and discussion

To predict the propulsive force, we now solve numerically the dynamical equation for the fin using the method presented in Subsect. 7.4.1. Then, we compute the amplitude at the trailing edge A_q, which is eventually injected inside the expression of the propulsive force from Lighthill (see Eq. (7.12)). The dynamical equation for a plate of length $L = 8.5$ cm, width $b = 5$ cm and thickness $e = 1$ mm for a given forcing amplitude ($A = 13$ mm) and increasing forcing frequencies is solved taking $C_{\mathrm{a}} = 0.51$, as estimated experimentally (see Fig. 7.10), and using C_D as a fitting parameter. With $C_D = 3.4$, we obtain a good agreement with the experimental data for the ratio A_q/A depending on the frequency f (see Fig. 7.11(a)). As for the phase difference ψ between the leading edge and the trailing edge, the theoretical model gives qualitatively the good evolution with the forcing frequency but predicts slightly larger values of ψ than the one measured experimentally (see Fig. 7.11(b)).

(a)

(b)
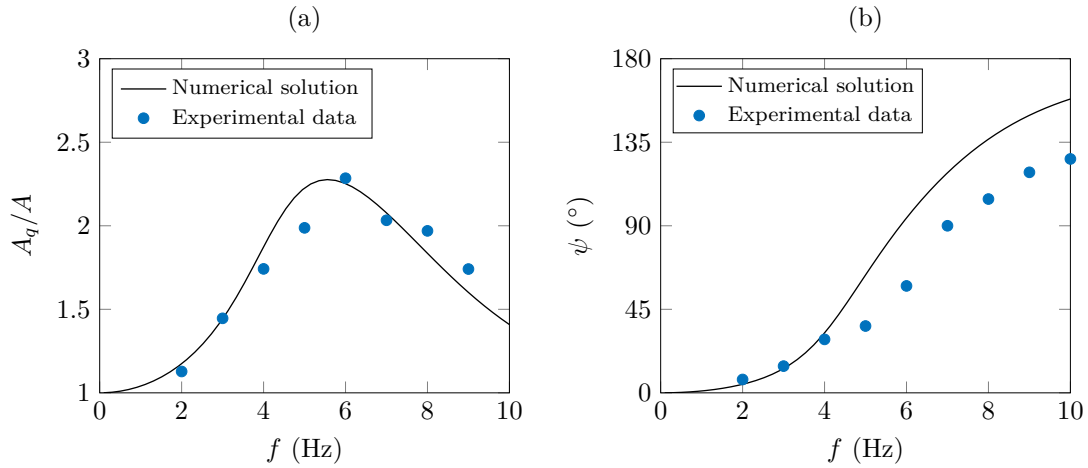
Figure 7.11: (a) Ratio of the trailing edge amplitude to the leading edge amplitude A_q/A and (b) phase difference ψ between the trailing edge and the leading edge, as a function of the forcing frequency f given by the theoretical model (black line) together with experimental data (blue dots). The plate has a length $L = 8.5$ cm, width $b = 5$ cm, thickness $e = 1$ mm and is forced at the amplitude $A = 13$ mm.

Injecting the computed value of A_q in Eq. (7.12), we can now compare the theoretical prediction for the propulsive force F and the experimental data. Taking $F = \delta \kappa f^2 A_q^2$ with δ a new fitting parameter, we find a good agreement between the theoretical model and the experimental data until the resonant frequency $f_1 \simeq 6$ Hz with $\delta = 1.6$ (see Fig. 7.12). After the resonance the higher beam modes start to play a role, which can explain the discrepancy between our model and the experimental data.
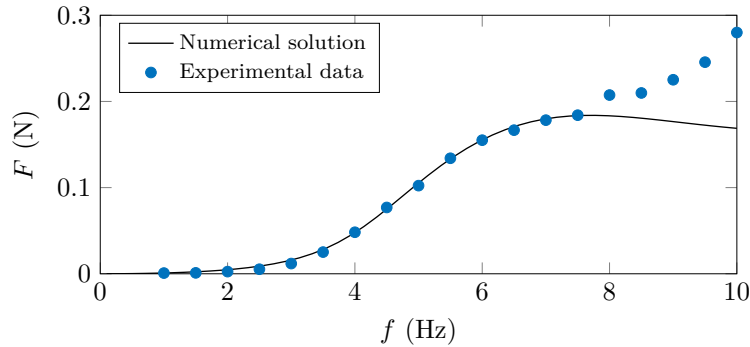
Figure 7.12: Propulsive force F as a function of the forcing frequency f given by the theoretical model (black line) and obtained experimentally (blue dots). The plate has a length $L = 8.5$ cm, width $b = 5$ cm, thickness $e = 1$ mm and is forced at the amplitude $A = 13$ mm.

Eq. (7.15) indicates that in order to maximise the force at the resonance F_1, one should have the largest Young's modulus E, thickness e and width b, and the smallest length L. This is in favor of monofins and rigid fins. As the force at the resonance scales as $F_1 \sim \rho b^2 A^2 f_1^2$, then to have the highest propulsive force, the width of the fin and the forcing amplitude should be as large as possible. Also the parameters of the fin should be adjusted so that the resonant frequency of the fin is as close as possible to the forcing frequency. The conclusions made from this simple scaling analysis must be taken carefully as they are only valid in the regime of small deformations of the fin. They remain however coherent

with previous studies [113, 118, 120]. This work aimed at maximising the propulsive force. However, maximising fin efficiency is often more realistic [113], especially if combined with physiological considerations (such as Hill's relation [130, 131]).

7.6   Appendix: Relation between speed and propulsive force

For the plate of length $L = 8.5$ cm, width $b = 5$ cm and thickness $e = 1$ mm, we measured, on the one hand, the propulsive force at zero velocity F for different forcing amplitudes and frequencies and, on the other hand, the horizontal fin velocity U for the same set of forcing parameters. Fig. 7.13 shows that the propulsive force F and the speed U are related through a power law of the form : $F \sim U^2$. Writing that the propulsive force F is balanced by a resistive force $\sim 1/2\rho b L C_d U^2$, one gets: $C_d \simeq 0.24$. This fairly large value indicates that the resistive force is a sum of skin drag and pressure drag.
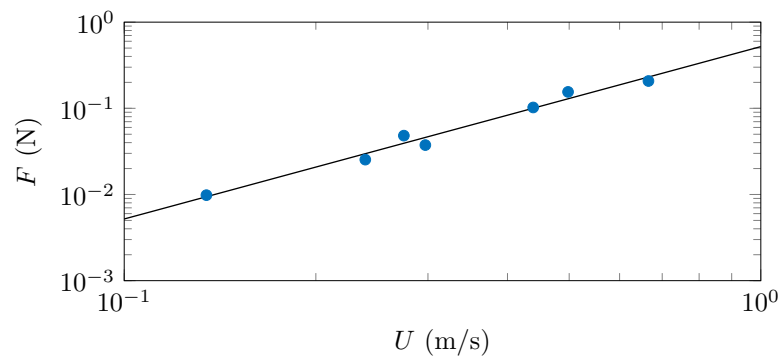
Figure 7.13: Propulsive force F as a function of the resulting fin velocity U in logarithmic scale. The black line is a fit of the experimental data : $F = 0.52U^2$.

Take home message of Chapter 7

1. To model fin-swimming, we consider simple rectangular flexible plates forced to oscillate vertically at the leading edge. The resulting deformation of the plate leads to a propulsion in the horizontal plane. The effects of the forcing parameters and the dimensions of the fin on its propulsion are characterised.

2. A theoretical model with a scaling analysis are then derived to account for the experimental results, especially the deformation of the fin (see Fig. 7.14) and its propulsive force.
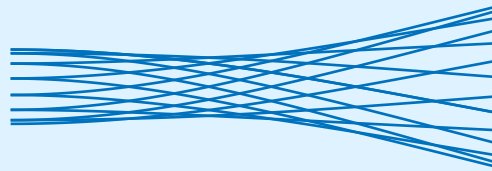
Figure 7.14: Superposition of the positions of the fin at different instants obtained from the theoretical model at the first resonant frequency of the fin.

3. These experimental and theoretical results provide a simple way of estimating the dimensions of a rectangular flexible plate leading to the highest propulsive force for a given forcing. The crucial parameter in the design of optimal rectangular fins appears to be the resonant frequency.

7

Conclusion and future research

In this thesis, we firstly studied the question of the optimisation of ship hulls with a simple theoretical and experimental approach and secondly the question of propulsion in rowing and swimming with fins.

The optimisation of ship hulls is a fairly old subject. However, given the difficulty to properly model the wave drag, the infiniteness of the search space and the number of constraints, it is an extremely complex problem, which still has unanswered questions. Here, we focused on the minimisation of the total drag on the hull at fixed power and immersed volume, by that avoiding all the other constraints, such as stability or manoeuvrability, which are more or less important depending on the boat category.

In Chap. 3, we looked at the simpler problem of the optimal aspect ratios for ship hulls. Considering a simplified geometry, we use a minimal theoretical approach to account for the different drag components. On the one hand, the components of pressure drag and wave drag decrease with increasing aspect ratios, indicating that slender hulls are better. On the other hand, the component of skin drag is minimal for rather small aspect ratios and thus favours bulky hulls. As a result, a compromise is needed and was found to depend on the imposed power. For small imposed power, corresponding to small Froude number, the wave drag is negligible and the optimisation with only skin drag and pressure drag leads to rather bulky hulls. For high propulsive power, corresponding to $\mathrm{Fr} \gg 0.5$, the wave drag is also negligible and the optimal hulls are again rather bulky. Whereas, for intermediate power, that is for Fr around 0.5, the wave drag is important and the optimisation leads to rather slender hulls. Interestingly, these observations are in agreement with the data found for existing hulls. In particular, rowing boats, which typically operate around $\mathrm{Fr} = 0.5$, have the highest length-to-width aspect ratios, close to the predicted optimum. Discrepancies with our results for other boat categories probably come from the importance of other constraints in their design such as stability. For future work, our optimisation framework could be adapted with more complex and realistic hull shapes to give more accurate results. Furthermore, the stability constraint could be added to the optimisation procedure.

In Chap. 4, we then studied the effect of the bow-stern asymmetry of ship hulls. We observed that rowing boats are almost perfectly symmetric, while sprint canoes and sprint kayaks are slightly asymmetric. This work was also motivated by the idea that, at the bow, hulls should be pointed to minimise the wave drag and, at the stern, they should also be pointed to avoid separation of the boundary layer. Yet, as the physical mechanisms at the bow and at the stern are different, the optimal hull shape is not necessarily symmetric. From a theoretical point of view, the current models for the wave drag are not able to account for the asymmetry as they predict the same value for the wave drag for an asymmetric boat moving forward or backward, which is obviously not the case. We conducted both experiments and numerical simulations. We found that asymmetry can indeed decrease the total drag and that the optimal hull should be more pointed at the front than at the rear. Future work is needed on the numerical simulations to match with the experiments and confirm these first results. Also studying further the pressure distribution along the hull (see Appendix B) could be another step in the direction of building a theoretical model of wave drag that can include asymmetry.

This work on optimal shapes at the water surface can be extended in two main directions. Firstly, it is of great interest to consider the effect of the unsteady motion of the boat on the total drag and especially on the wave drag. Indeed, as discussed in Sect. 2.2, in rowing races, the boat does not move at constant speed but with quite large fluctuations of speed. The same observation also holds for sprint canoes. Havelock considered the case of a cylinder

immersed in water near the free-surface and impulsively started from rest [132]. He found theoretically that the wave drag coefficient C_w reaches its steady value with oscillations of decreasing amplitude (see Fig. 7.15). The instantaneous wave drag coefficient on an object moving with velocity fluctuations is then expected to oscillate, which in turn increases the time-averaged wave drag, as found in [68] and [69]. The optimisation of hull shapes in this context is obviously of interest for the design of increasingly fast racing shells. Following the study in Chap. 4, it is also likely that the optimal asymmetry would be different for a motion at constant speed and for an unsteady motion.
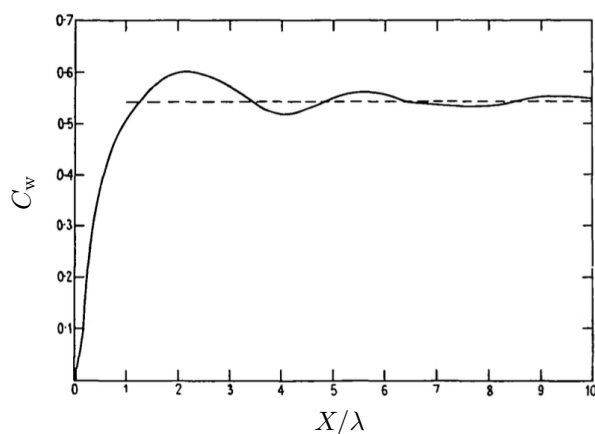
Figure 7.15: Wave drag coefficient C_w as a function of the dimensionless travelled distance X/λ (where λ is the wave length), for a cylinder close to the water surface started impulsively from rest. The dashed line indicates the value of the wave drag coefficient in the steady regime. Adapted from [132].

Secondly, the two questions of optimal aspect-ratios and optimal asymmetry can be extended to the capillary-gravity regime, so as to better understand animal locomotion at the air-water interface. Indeed, animals moving at the water surface either aim at maximising drag forces between their appendages and the water surface to propel themselves or aim at reducing their total drag. In this regime, wave resistance, which is due to the generation of capillary-gravity waves, plays an important role [46, 133].

(a) (b)
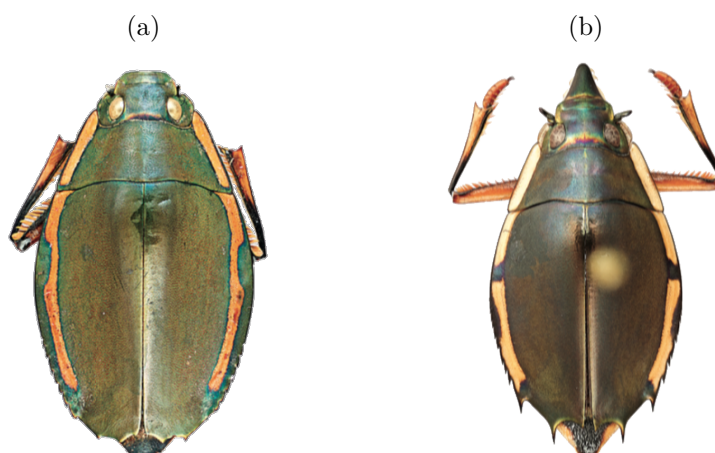
Figure 7.16: Pictures of two whirligig beetles found in South Asia: (a) the *Porrorhynchus landaisi*, and (b) the *Porrorhynchus marginatus* (reprinted from [134]).

Let us quickly mention whirligig beetles, which are water beetles known for swimming

rapidly in circles at the water surface [133, 135]. Within this family, the shape of these insects can be very different. Some of them, like the *Porrorhynchus landaisi* (see Fig. 7.16(a)), have an elliptical shape when seen from above, while others, such as the *Porrorhynchus marginatus* (see Fig. 7.16(b)), are very asymmetric [134]. From the top-view pictures of these two whirligig beetles, we obtain similar length-to-width aspect ratios ($\alpha = \ell/w \simeq 2$) but very different values for the asymmetry parameter ϵ defined in Eq. (4.1) (see Table 7.1). In particular, the shape of the *Porrorhynchus marginatus* with its pointed front and its rather bulky rear with small spikes seems to be dictated by drag minimisation. Experiments and numerical simulations could be used to address the question of optimal asymmetry in the capillary-gravity regime and determine if the shapes of whirligig beetles are optimal in this regard.

Name	α	ϵ
Porrorhynchus landaisi	1.8	-0.036
Porrorhynchus marginatus	2	-0.097

Table 7.1: Values of the asymmetry parameter ϵ for the two whirligig beetles shown in Fig. 7.16.

The propulsion in rowing and fin-swimming was considered in a second part.

In Chap. 5, we looked at the effect of the number of rowers on the mean speed of a rowing boat. McMahon suggested a model based on the assumption of geometric similarity of the rowing shells [62]. It predicts that the mean boat velocity slowly increases with the number of rowers following a power law of power 1/9. This model compares well with the world record speeds in different rowing categories and is fairly robust, as when we relaxed two main assumptions of the model, the power law was still valid. A limitation of the model for a large number of rowers was also presented.

In Chap. 6, we then considered the question of the synchronisation between rowers. Synchronisation is at the origin of velocity fluctuations, which increase the total drag force compared to a motion at constant speed. However, with a robotic rowing boat at the scale 1/10, we showed that, even though the fluctuations of speed are reduced when desynchronising the rowers, the mean speed remains higher in the synchronised configuration. This experimental result was validated with a simplified theoretical model of rowing and we identified two main reasons for this at-first surprising result: the rower's motion on the boat and the blade efficiency.

The rowing propulsion and the notion of blade efficiency is further discussed in Appendix A. For future work, the mechanism of rowing propulsion could be studied more precisely by characterising the different drag components acting on the blade: inertial drag, lift and added mass. The difficulty of this task comes firstly from the water surface since the added mass at the water surface would surely be different from the one far from the free-surface; and secondly from the complex dynamics of the blade motion in water due to the simultaneous motion of the boat.

Finally, we studied the propulsion in fin-swimming, which is also an unsteady mode of propulsion in water. An experimental set-up consisting of simple rectangular flexible plates forced to oscillate vertically was used as a model of fin-swimming. Varying the forcing frequency, we found that the resonant frequency of the system expresses the balance between a distributed added mass force and a restoring bending moment. Measuring the propulsive force for different forcing amplitudes and frequencies and for different geometries of the plate, we were able to derive the scaling for the propulsive force at the resonance. A theoretical model was derived to account for the experimental results, in particular the deformation

of the fin and its propulsive force. For future work, the propulsion of other geometries of fins could be considered such as triangular shapes to model swimming with a monofin and flapping flight or streamlined shapes to study luna-tail propulsion.

APPENDICES

A

OPTIMISATION OF OARS

In each rowing sport, the oars have their very own characteristics most of the time selected through a long time experience. Here we address experimentally and theoretically the problem of rowing efficiency in rowing sports as function of row lengths and blade sizes. In contrast with previous studies which consider imposed kinematics, we set an imposed force framework which is closer to physiological constraints. We find that optimal row lengths depend on sport and sportsmen strength.

Picture of Alexis Guerinot and Augustin Mouterde, winner crew of the lightweight coxless pair category at the 2016 world championships in Rotterdam. Photo credits: Daniel Blin, FFA.

Contents

This work has been done with Romain Labbé, Michael Benzaquen and Christophe Clanet. The reader is also referred to the thesis of Romain Labbé for details on this study.

A.1   Position of the problem

Most sports require different equipment for different weight categories and genders. However in rowing sports [83, 84], row characteristics are surprisingly quite constant in each discipline regardless of athletes strength and gender. In *sculling*, the row size ranges from 287 to 291 cm [43, 136]. For sweep boats, the row size reads 371 to 376 cm [43, 136]. Through rowing history, the tendency was to reduce row lengths (by almost 25% since 1850, see Fig. A.1(a) and (b)). This evolution is also related to an increase in the blade area and the shift to asymmetric blades.
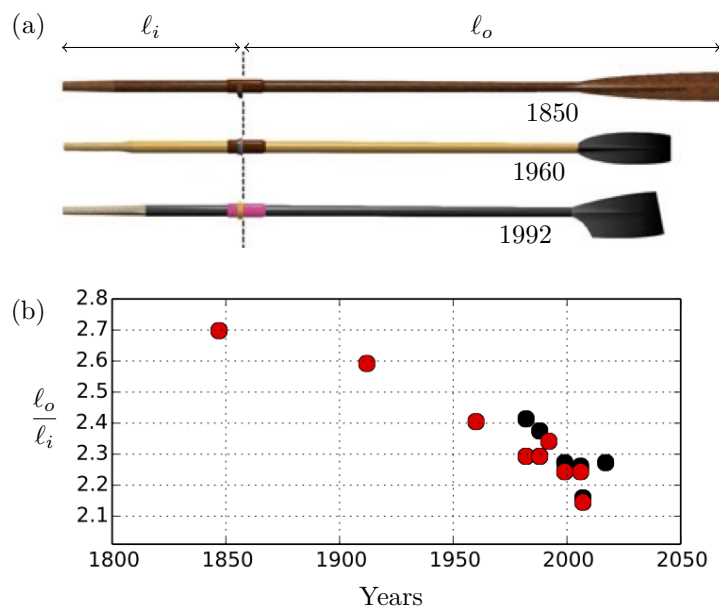

Figure A.1: (a) Picture of three different sweep oars (taken from [137]). The first oar dates back to 1850, the second one to 1960, and the last one to 1992. (b) Historical evolution of the row aspect ratio $\eta = \ell_o/\ell_i$ for sculling oars in black and sweep oars in red. Note that the inboard length ℓ_i remained quite constant through time such that η can be seen as the dimensionless row length. The oldest data points were obtained from race photographs, while the more recent ones come from [138] or were provided by the French athlete Thomas Baroukh.

During the propulsive stroke, typical force profiles exerted by the blade on the water were measured by Valery Klesnev [50]. The maximal force exerted at the handle is found around 700 N. More interestingly, as described by the coaches, a good rowing stroke corresponds to a force profile as constant as possible. The whole study is conducted in this limit. Volker Nolte [138] performed an empirical study of the effects of row length on a dataset of rowing races. He reported that "shorter oars are more effective". However, Laschowski *et al.* [139] studied experimentally the effect of oar-shaft stiffness and length with elite athletes. They showed that changes in stiffness and length of the oar led to small differences in the measured boat acceleration but these differences remained of the same order of magnitude as inter-stroke fluctuations. Caplan *et al.* [65], Leroyer *et al.* [140], and Hémon [141] took interest in the effects of row blade shapes by comparing real oars and highlighted the complexity of addressing such a problem. A number of authors [56, 142, 143, 144, 145, 146, 147] addressed the problem of rowing efficiency and optimal rowing movement from the biomechanical perspective. In particular, Kleshnev *et al.* [50, 148] performed an intensive experimental study on propulsive efficiency varying oar travel, handle force, stroke rate and many other

parameters. Here we present a minimal and self-consistent analysis of the effects of row length and blade size on rowing performance, with a particular focus on rowing boat (fixed rowlock). We first decouple the physics from its physiological counterpart. In contrast with the majority of fluid-structure interaction studies (see for instance Chap. 6), we address the problem with imposed force instead of imposed kinematics. We propose a simple theoretical model that is compared to experiments made on a homemade rowing robot.

A.2   Experimental study

In order to understand the effect of the ratio $\eta = \ell_o/\ell_i$ on the boat speed under the assumption of constant force, we designed and manufactured a robot rowing boat with imposed propulsive force (see Fig. A.2(a)). Using a homemade wooden mold based on a real rowing shell [107] at the scale 1/10 (the same as in Sect. 6.2), we built a glass fiber rowing boat with 4 robot rowers with one oar each. Constant force during the propulsive phase was ensured through a pulley-mass system. Each row was linked to a pulley centered at its rowlock. A suspended mass $m = 80\,\mathrm{g}$ was connected to the pulley through a string (see Fig. A.2(b)) by that setting the row in motion at constant force $F_\mathrm{r} = mg$ (if we neglect frictional losses in all connections). The angular travel of the row was fixed to $\theta_0 = 90$ degrees. The recovery phase and the blade flips were ensured by two servomotors and position sensors connected to an Arduino$^{\mathrm{TM}}$ board. Four polystyrene floats were added to ensure stability.
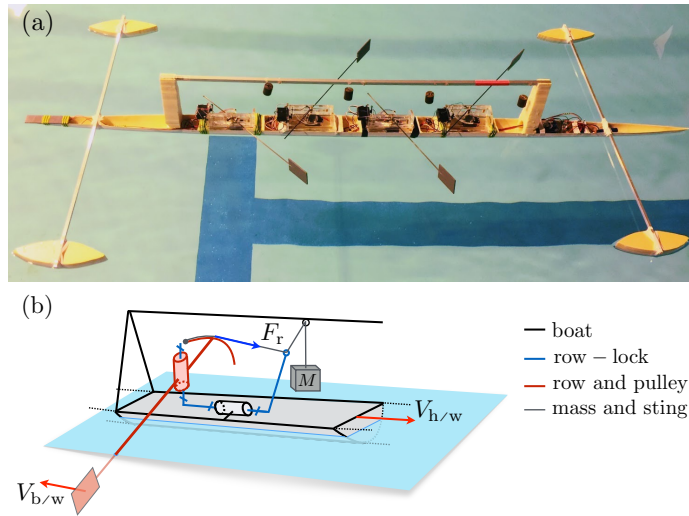
Figure A.2: (a) Picture of the $2\,\mathrm{m}$ long model rowing boat with 4 robot rowers at constant force. (b) Sketch of the mechanism of one robot rower. The row and pulley (red) rotate with respect to the rowlock (blue), itself in rotation with respect to the hull (black) to ensure lifting/dropping of the row between the propulsive and recovery phases. A suspended mass/string system (gray) ensures row motion at constant force during the propulsive phase. The recovery phase and the blade flips were ensured by two servomotors and position sensors connected to an Arduino$^{\mathrm{TM}}$ board (not shown for clarity).

The experiments were performed at the *Ecole polytechnique* swimming pool. Setting the recovery phase time to a constant value $T^{(\mathrm{r})} = 1.3\,\mathrm{s}$, we filmed the model boat rowing over a $25\,\mathrm{m}$ distance for four different row lengths, with corresponding aspect ratios spanning from $\eta = 5$ to $\eta = 8$. As one can see in Fig. A.3(a), when starting from rest, the speed of

the hull increases for about 8 seconds (corresponding to about three strokes) until reaching a "steady" regime where the average speed is constant. The time of the propulsive stroke in the "steady" regime, denoted $T_\infty^{(p)}$, was recorded for each stroke using the position sensors mentioned above and averaged for each race. The experiments show that, when increasing the ratio η, the average hull velocity $\langle U \rangle$ decreases (black dots in Fig. A.3(b)), coherent with an increase in the propulsive stroke duration $T_\infty^{(p)}$ (see Fig. A.3(c)). This observation agrees quite well with the historical evolution of the ratio η for real oars, as η decreased over the years with boats going faster and faster.
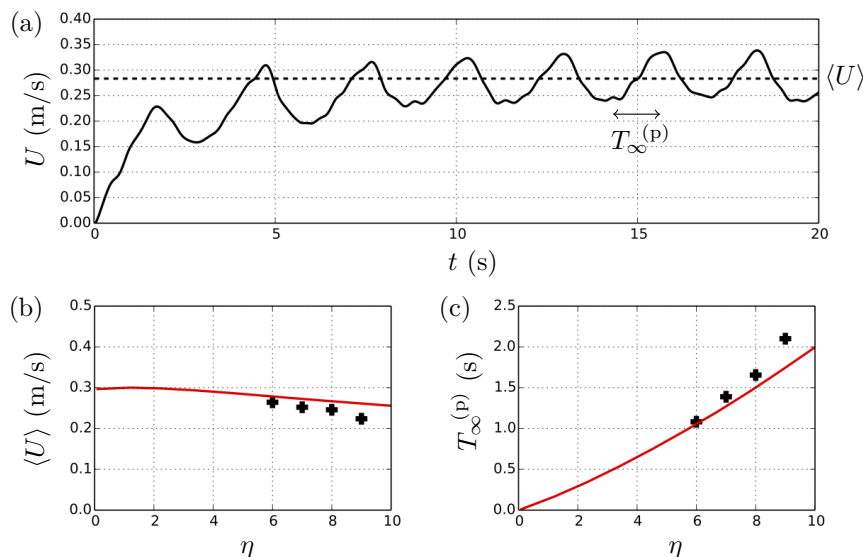
Figure A.3: (a) Instantaneous velocity of the hull starting from rest as a function of time for $\eta = 7$. The mean velocity $\langle U \rangle$ reached after about three strokes is indicated with an horizontal dashed line. The time of the power stroke is denoted $T_\infty^{(p)}$. (b) Mean boat velocity $\langle U \rangle$ as a function of the row aspect ratio η. (c) Propulsive stroke duration $T_\infty^{(p)}$ as function of the ratio η. The red line in (b) and (c) is the prediction from the numerical model (see Sect. A.3).

A.3 Theoretical model

To account for these experimental results, we derive a simple theoretical model of rowing, similar to the one in Sect. 6.4, but here with imposed force instead of imposed kinematics.

A.3.1 Single oar dynamics

Following the same steps as in Sect. 6.4, the total force exerted on a blade is written (see Eq. (6.13)):

$$F_{w/bl} = -\frac{1}{2}\rho S_{bl}C_D|v_{bl/w}|v_{bl/w} - \rho \mathcal{V}C_a \frac{\mathrm{d}v_{bl/w}}{\mathrm{d}t} \ . \tag{A.1}$$

where $v_{bl/w}$ is the velocity of the blade with respect to the water, $S_{bl} = \ell_b w_b$ is the surface of the blade, C_D and C_a are the drag and added mass coefficients, and $\mathcal{V} = \pi w_b \ell_b^2/4$ is the volume of the cylinder of diameter ℓ_b and height w_b. The force $F_{w/bl}$ exerted by the water

on the blade must match that of the rower F_r through a torque conservation relation at the rowlock (assuming the oar tubes to be rigid and of negligible mass). That is:

$$\frac{1}{2}\rho S_{bl} C_D |v_{bl/w}|v_{bl/w} + \rho \mathcal{V} C_a \frac{\mathrm{d}v_{bl/w}}{\mathrm{d}t} = -\frac{1}{\eta}F_r \ . \tag{A.2}$$

Eq. (A.2) can be solved numerically for any force profile $F_r(t)$, such that one can determine the exact blade velocity $v_{bl/w}$. To go one step further, we can work out the stroke duration $T^{(\mathrm{p})}$. The travel of the oar handle (held by the rower hands) is given by $\Lambda = \theta_0 \ell_i$ where Λ is the stroke length and $\theta_0 \simeq 90$ degrees. The stroke duration $T^{(\mathrm{p})}$ then solves:

$$\int_0^{T^{(\mathrm{p})}} v_{r/h} \mathrm{d}t = \Lambda \ , \tag{A.3}$$

where $v_{r/h}$ is the velocity of the rower's hands.

In the following we choose to work on a simple and analytically solvable case by assuming a constant imposed force. Although previous studies show evidence of slightly time-dependent force profiles [142, 143], we here wish to extract the general physics and scaling arguments of rowing mechanics with minimal ingredients, for which a constant force seems appropriate. Furthermore this hypothesis is in contrast with most fluid-structure interaction studies where imposed kinematics seems to be the golden rule. This point of view is actually quite natural from a physiological point of view.

A.3.2 Ship propulsion at constant force

The additional equation needed to close the problem results from the force balance on the hull. This is $F_{w/h} = NF_r/\eta$, with N the number of blades. We here assume that the drag force on the hull is dominated by skin friction (see Sect. 2.5) and we do not take into account the motion of the rowers on the boat, contrary to the model in Sect. 6.4. According to Newton's second law, one obtains in this limit:

$$M\frac{\mathrm{d}U}{\mathrm{d}t} + \frac{1}{2}\rho S_h C_h |U|U = \frac{NF_r}{\eta} \ , \tag{A.4}$$

where M is the mass of the boat, U the velocity of the hull with respect to water, S_h the wetted surface of the hull and C_h its skin drag coefficient. To non-dimensionalise the problem, we introduce the velocity scale $U_c = \sqrt{2NF_c/(\rho S_h C_h)}$ and the time scale $\tau_c = M\sqrt{2/(\rho N F_c S_h C_h)}$, with F_c a characteristic force and we write $U = \tilde{U}U_c$, $t = \tilde{t}\tau_c$ and $F = \tilde{F}F_c$. The natural characteristic length of the problem is $L_c = U_c\tau_c$. The dimensionless equation governing the boat velocity then reads:

$$\frac{\mathrm{d}\tilde{U}}{\mathrm{d}\tilde{t}} + |\tilde{U}|\tilde{U} = \frac{1}{\eta}\tilde{F}_r \ . \tag{A.5}$$

With this set of characteristic parameters, the dimensionless equation governing the dynamics of the oar (Eq. (A.2)) is written:

$$\beta|\tilde{v}_{bl/w}|\tilde{v}_{bl/w} + \gamma\frac{\mathrm{d}\tilde{v}_{bl/w}}{\mathrm{d}\tilde{t}} = -\frac{1}{\eta}\tilde{F}_r \ , \tag{A.6}$$

where $\beta = NS_{bl}C_D/(S_h C_h)$ denotes the ratio between the blades' pressure drag and the hull skin drag and $\gamma = N\rho\mathcal{V}C_a/M$ is the ratio between the blades' added mass and the

boat mass. In the following, we consider self-similar blades (ratio w_b/ℓ_b constant), so that $\gamma \sim \beta^{3/2}$, by that reducing the number of dimensionless parameters.

Each rowing cycle k is made of two phases: (i) the propulsive phase at constant force with duration $T_k^{(\mathrm{p})}$ for which we set $\tilde{F}_\mathrm{r} = 1$ in Eq. (A.5) and (ii) the recovery phase with duration $T_k^{(\mathrm{r})}$ for which $\tilde{F}_\mathrm{r} = 0$. The overall cycle period reads $T_k = T_k^{(\mathrm{p})} + T_k^{(\mathrm{r})}$. We restrict to a constant and prescribed duration for the recovery phase $T_k^{(\mathrm{r})} = T^{(\mathrm{r})}$. Eq. (A.5) and Eq. (A.6) can be solved analytically for each rowing cycle k with the power stroke duration $T_k^{(\mathrm{p})}$ of the kth propulsive phase satisfying:

$$\int_{t_k}^{t_k+T_k^{(\mathrm{p})}} v_{bl/h}\mathrm{d}t = \int_{t_k}^{t_k+T_k^{(\mathrm{p})}} \left(v_{bl/w} - U\right)\mathrm{d}t = -\alpha\Lambda \ . \tag{A.7}$$

After a transient regime, a "steady" regime is reached: the average hull velocity over one cycle and the stroke duration converge towards constant values, respectively denoted $\langle U \rangle$ and $T_\infty^{(\mathrm{p})}$, as observed experimentally (see Fig. A.3(a)).

A.3.3 Propulsive efficiency

We define the *anchoring* $\mathcal{A}$ of the blade, as the ratio of the distance travelled by the hull during the propulsive phase $\Lambda_\mathrm{h}(\eta)$ and the travel of the blade in the reference frame of the boat $\eta\Lambda$:

$$\mathcal{A} = \frac{\Lambda_\mathrm{h}}{\eta\Lambda} \ , \quad \text{with} \ \Lambda_\mathrm{h}(\eta) = \int_0^{T_\infty^{(\mathrm{p})}} U\mathrm{d}t \ . \tag{A.8}$$

The anchoring can be seen as the blade efficiency. Indeed, if $\mathcal{A} = 1$, the blade does not move with respect to the water and all the rower's energy is transferred to the boat. In contrast, if $\mathcal{A} = 0$ the boat does not move and the blades slip in the water.

Interestingly the anchoring has an energetic interpretation. The propulsive energy provided by the rower $E_\mathrm{r} = \Lambda F_\mathrm{r}$ is dissipated by both the hull $E_\mathrm{h} = \Lambda_\mathrm{h} F_\mathrm{r}/\eta$ and the blades E_bl, such that $E_\mathrm{r} = E_\mathrm{h} + E_\mathrm{bl}$. Equation (A.8) yields:

$$\mathcal{A} = \frac{E_\mathrm{h}}{E_\mathrm{r}} \ , \tag{A.9}$$

that is: the anchoring $\mathcal{A} \in [0,1]$ quantifies the efficiency of the energy transfer between the rower and the boat [50, 148]. For $\mathcal{A} \to 0$ all of the rower's energy is dissipated by the blade with almost no propulsion of the boat, while for $\mathcal{A} \to 1$ the rower's energy is efficiently transferred to the boat (in this case $\Lambda_\mathrm{h}(\eta) \approx \eta\Lambda$ as if the blade was planted in a solid medium).

A.4 Discussion

Our theoretical model is first tested with the parameters of our robotic rowing boat. The predictions of the model for the mean hull velocity and the stroke duration in the "steady" regime are compared to the experimental results in Fig. A.3(b) and (c). In particular, as in the experiments, the mean hull velocity is found to decrease with increasing row aspect ratios η, which is in favour of shorter oars [138]. The small discrepancies can be the results of two different effects. First, our model does not account for the dynamic inclination of $F_{bl/w}$

with respect to the direction of motion of the boat, by that overestimating the propulsive force. Second, our robotic rowing boat suffered from an abrupt slow down at the end of the propulsive phase (see Fig. A.3(a)) due to both (*i*) the rows hitting the mechanical stop before being lifted out of the water, and (*ii*) the deceleration of the masses increasing the drag on the hull.
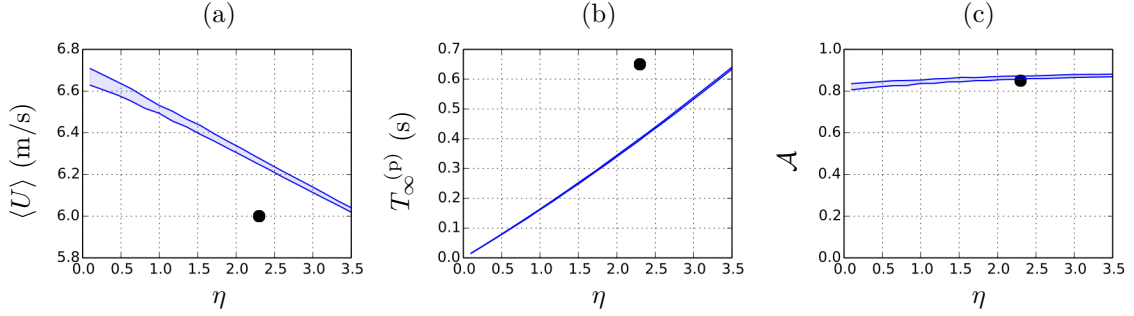

Figure A.4: (a) Mean boat velocity as function of the oar aspect ratio η. (b) Propulsive stroke duration as function of η. (c) Anchoring (or equivalently energy transfer efficiency, see Eq. (A.8)) as function of η. The blue curves were obtained numerically for β between 90 and 120. Empirical data for a *coxless four* rowing boat are indicated with a black dot.

Now, let us focus on the case of a *coxless four* rowing boat. We consider that each rower deploys a force $F_{\mathrm{r}} = 700\,\mathrm{N}$ [50]. The mean boat velocity, the stroke duration and the anchoring computed from our model in this specific case are presented in Fig. A.4. For real sweeping oars, $\alpha \simeq 2.2$ and $\beta \simeq 100$. The real mean velocity (Fig. A.4(a)) is smaller than the theoretical one. This is related to the assumptions of our model: in particular we did not take into account the motion of the rowers on the boat and the drag on the hull might be underestimated. As one can see in Fig. A.4(c), the estimated anchoring for a *coxless four* rowing boat [148] compares well with the theoretical anchoring predictions: $\mathcal{A}$ is close to 80%. The stroke duration is also off compared to the theory (Fig. A.4(b)). Physiology imposes a limit to our model: the mechanical optima identified here are not always attainable by the athletes [130, 131, 149]. In particular, the rowers are not able to hold the pace and row at too high frequencies (or equivalently too small stroke durations). A given rower should thus choose the smallest possible rows corresponding to the minimal stroke duration he is able to achieve while deploying a maximal force.

Eventually, other physiological and practical aspects can be important when it comes to the choice of the row length. With smaller rows, the rower would have to raise more the hands during the recovery stroke. The techniques for the catch (or blade entry in water) and the release (blade going out of water) would also need to be changed to adapt to the new oars.

A

B

PRESSURE DISTRIBUTION ALONG A HULL

In this chapter, we study experimentally and numerically the pressure distribution along the surface of a hull. In particular, we aim at characterising the effect of both the free-surface and the asymmetry of the hull on this distribution. With the experiments, we were not able to measure precisely enough the pressure along a given hull in water. The numerical results show interesting tendencies for the pressure distributions depending on the Froude number and the asymmetry.
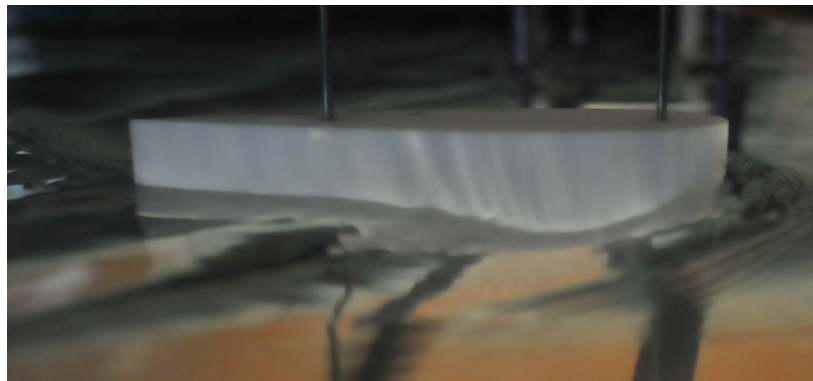
Hull with a NACA profile towed at the water surface.

Contents

This work has been done with Vedant Kumar, Louis Richard, Nguyen Thanh-Vinh (University of Tokyo, Japan).

B.1 Experimental study

The point of this study is to measure the pressure distribution along a hull experimentally to see how it depends on the direction of motion of the hull (see Chap. 4). The pressure distribution past an airfoil profile is first measured in air and is then measured in water near the air-water interface.

B.1.1 Pressure distribution past an airfoil in air

The pressure at the surface of a symmetric NACA airfoil profile is measured in a wind tunnel. For this purpose, small holes were made at a given cross-section of the hull (see the picture of the airfoil in Fig. B.1(a)). Their position along the airfoil profile is made clearer in Fig. B.1(b). These holes are connected through tubes to pressure sensors.
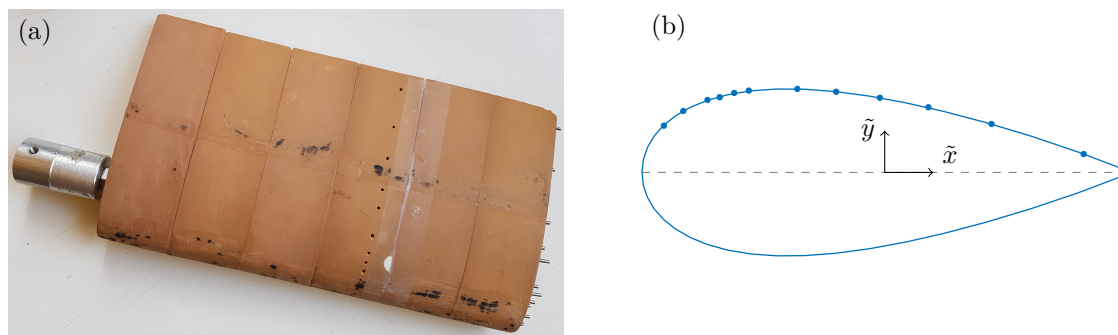
Figure B.1: (a) Picture of the model airfoil with which the pressure distribution is measured. Small holes were made along the airfoil profile at a given height and can be seen on the picture. They are connected with tubes to pressure sensors. (b) Schematics of the airfoil with the position of the 12 points of measurements (dots on the airfoil profile).

We performed the measurements for three different flow velocities $U \in \{11.7, 14, 16.2\}$ m/s and the presented results are averaged over five measurements. In Fig. B.2, the pressure coefficient $c_p = (p - p_\infty)/(\rho U^2)$, where p_∞ is the pressure at infinity (see Sect. 1.5), is plotted as a function of the coordinate $\tilde{x}$ along the hull for three different Reynolds numbers and
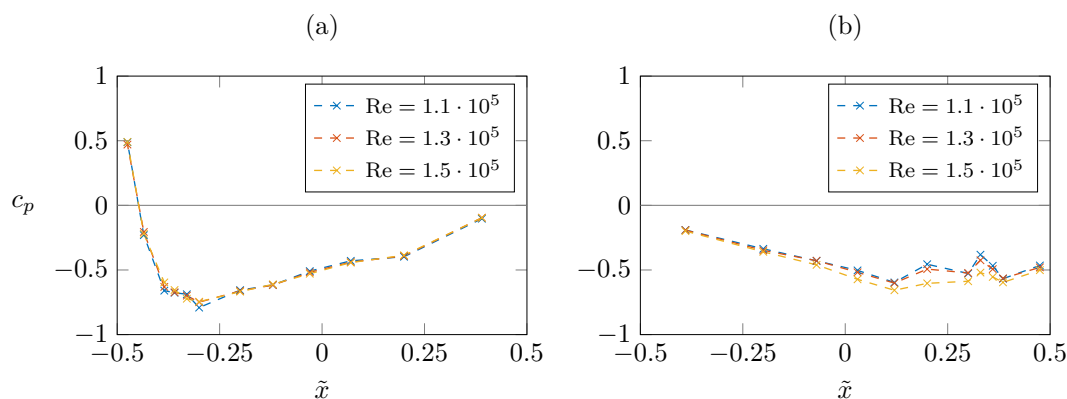
Figure B.2: Pressure coefficient c_p as a function of the position $\tilde{x}$ along the airfoil for three different Reynolds numbers for (a) $\epsilon > 0$ and for (b) $\epsilon < 0$ (see Fig. 4.4 and Eq. (4.1)). In both cases, the position $\tilde{x} = -0.5$ corresponds to the leading edge of the airfoil.

two cases. One first notices that the pressure distributions $c_p(\tilde{x})$, either for $\epsilon > 0$ or $\epsilon < 0$, do not depend much on the Reynolds number (the range of Reynolds number being however quite small). Secondly, when one compares the results for $\epsilon > 0$ and $\epsilon < 0$, one can observe that the pressure distribution is very different. In particular, the pressure coefficient for $\epsilon < 0$ plateaus for $\tilde{x} \in [0, -0.5]$, which might be related to the formation of a recirculation bubble in this region.

B.1.2 Pressure distribution past an airfoil near the air-water interface

This work was done at the University of Tokyo in the laboratory of Shimoyama under the supervision of Nguyen Thanh-Vinh. Its aim is to measure the pressure distribution along an airfoil profile near the water surface to observe the difference with the case where the airfoil is fully immersed in a fluid as measured experimentally in the previous section.

B.1.2.1 Description of the experimental set-up

The laboratory of Shimoyama at the University of Tokyo is specialised in developing micro-sensors based on MEMS technology (Micro Electro Mechanical Systems). In particular, they have designed sensors, made of micro cantilevers that can deform under small loads and whose deformation can be measured through a change in the resistance of the cantilevers. These sensors are used in particular for air pressure measurements.

The challenge here was to adapt these sensors to make measurements in water. This has been done following the schematics in Fig. B.3.
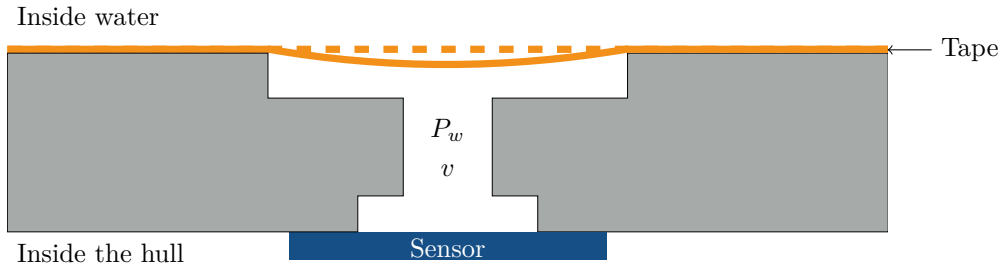
Figure B.3: Schematics of the principle of the pressure measurements performed. A hole is made through the hull. Tape is sticked on the external side of the hull in contact with water and one of the sensors shown in Fig. B.4 is attached on the inner side. This set-up creates a closed chamber in which the pressure changes due to changes in the water pressure P_w through the deformation of the tape.

A series of holes were made in the hull at a given distance from the bottom of the hull. They were covered with tape on the external side of the hull, which is in contact with water, and the micro-sensors for air pressure measurements were sticked inside the hull at the other end of the hole. We thus created a closed chamber in which the pressure changes with the water pressure, through the deformation of the tape which reduces the volume of the chamber. The first sensors that we tried are shown in Fig. B.4(a) and were the initial sensors developed in the lab for air pressure measurements [150]. These sensors were very sensitive but could only measure pressure changes and not the absolute pressure. This is for this reason that we adapted the design of these sensors and created new sensors (see Fig. B.4(b)) that have a cap filled with glycerol to prevent air leakage and thus measure the absolute pressure inside the chamber.

(a) (b)

Figure B.4: Pictures of (a) the first sensors used in this study and (b) the final sensors.

The shape of the hull used here is also a NACA airfoil profile. It was modeled in 3d using a CAD software (see Fig. B.5(a)) and made using a 3d printer. The hull is equipped with ten sensors (see Fig. B.5(b)), which are connected to a board and an amplification circuit. The acquisition of the signal is made using a numerical oscilloscope. Fig. B.5(c) shows the picture of the whole set-up with the 2m-long water tank and the towing system.

(a) (b) (c)
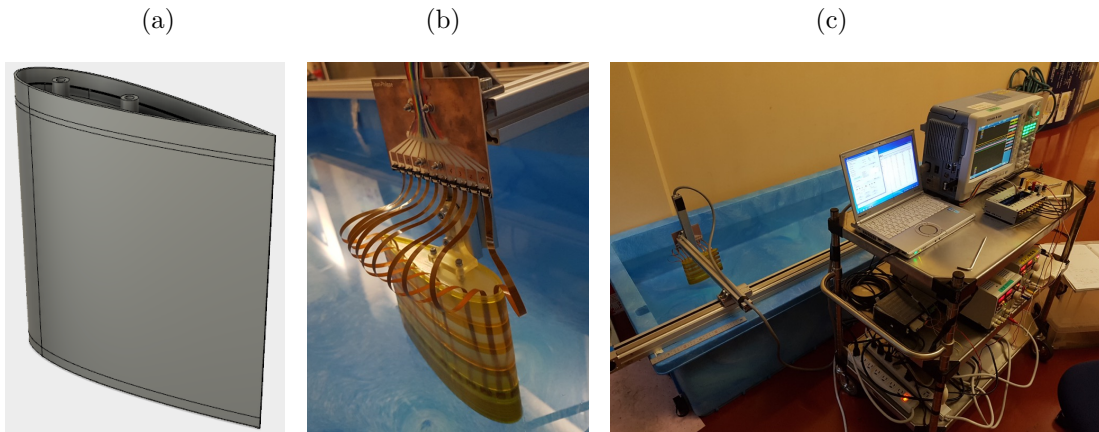
Figure B.5: (a) 3d model of the NACA hull used here. (b) Picture of the hull equipped with 10 sensors. (c) Picture of the whole set-up with the towing tank, the hull equipped with the sensors and the acquisition devices.

B.1.2.2 Experimental results

The experiment was quite difficult to conduct because of the fragility of the sensors. The results shown in Fig. B.6 were obtained with one set of sensors. Experiments were carried out for different immersions of the hull d/D (ranging from 0.17 to 0.43), for different velocities ($U \in \{0.6, 0.75\}$ m/s) and the two directions of motion. Fig. B.6(a) and (b) show the pressure coefficient c_p depending on the coordinate $\tilde{x}$ for different immersions d/D and the two directions of motion. For both cases, in the first half of the plot ($\tilde{x} < 0$), the pressure coefficient is higher for the smallest immersion $d/D = 0.17$. The pressure distributions in both directions look similar but are quantitatively very different as emphasised in Fig. B.6(c), where the pressure distribution for the two directions are plotted together for $d/D = 0.17$. In Fig. B.6(d), the pressure distribution $c_p(\tilde{x})$ for two different velocities, corresponding to
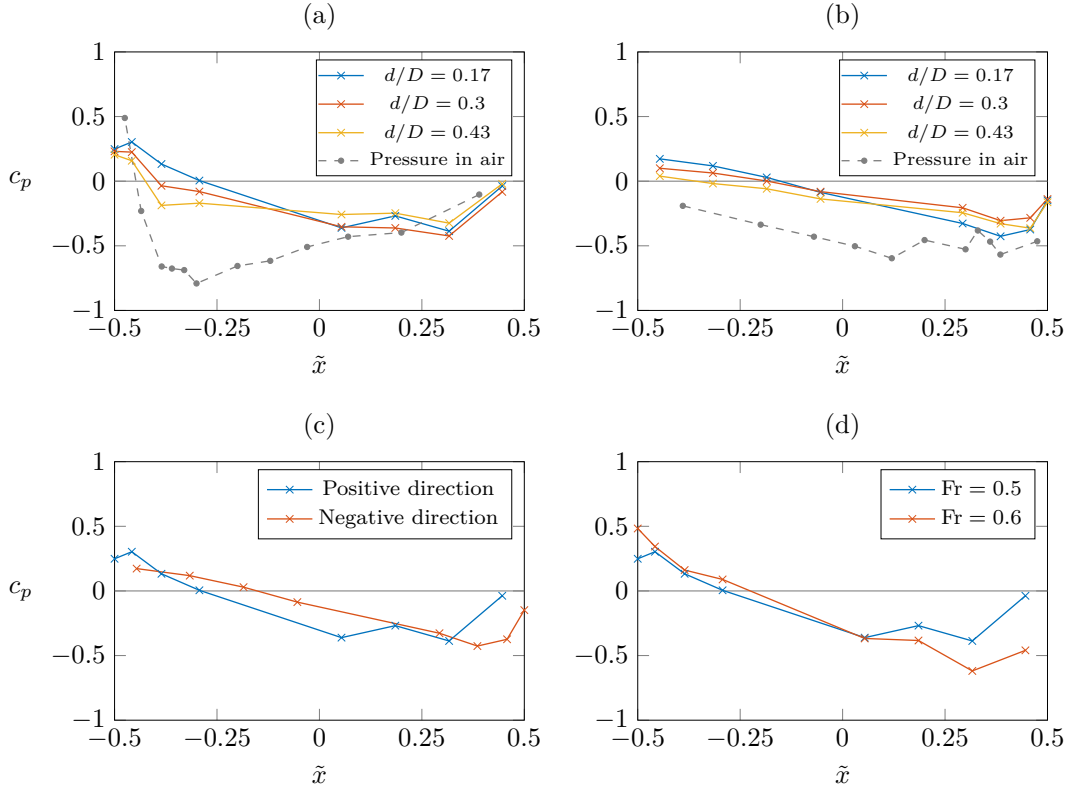
Figure B.6: Pressure coefficient c_p depending on the coordinate $\tilde{x}$, (a) for the hull moving with the rounded part first ($\epsilon > 0$) and for different immersions d/D ; (b) for the hull moving in the other direction ($\epsilon < 0$) and for different immersions d/D ; (c) for the hull moving in both directions for $d/D = 0.17$; and (d) for the hull moving with the rounded part first for two different Froude numbers, for $d/D = 0.17$. In the same way as in Fig. B.2, the position $\tilde{x} = -0.5$ in each plot corresponds to the leading edge of the airfoil. For subplots (a) and (b), the pressure distribution obtained for the airfoil profile in air is plotted for comparison.

Fr $\in \{0.5, 0.6\}$ look qualitatively similar. If we now compare these results with the one obtained from the experiments in the wind tunnel (see previous section and Fig. B.6(a) and (b)), the pressure distributions are very different. This might primarily be due to the presence of the water surface and the creation of wave by the moving hull. However, we must mention that the bad accuracy of the sensors can not be eliminated as a possible source of errors in the data points.

B.2 Theoretical study

This work was done by Vedant Kumar (student from Indian Institute of Technology (BHU) Varanasi, India). The idea here is to try to determine how the pressure along a given hull can be predicted.

B.2.1 Pressure distribution from the numerical simulations

From the numerical simulations performed in Sect. 4.4, we also obtained the pressure distribution along the different hulls and for the different sets of parameters. Fig. B.7(a) shows

the pressure distribution $c_p(\tilde{x})$ at a fixed depth ($\ell\tilde{z}/D = -0.36$) for the symmetric hull and $d/D = 0.75$, for three different Froude numbers.
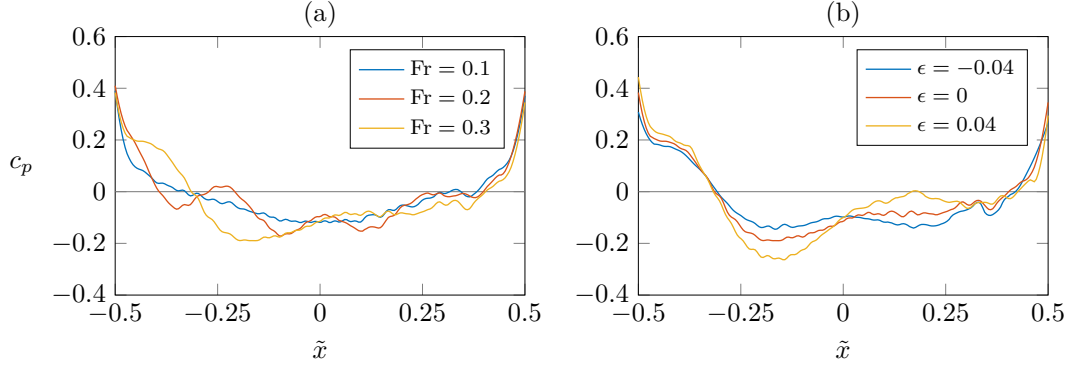

Figure B.7: (a) Pressure coefficient c_p obtained numerically as a function of the coordinate $\tilde{x}$ for the symmetric hull (hull 1), for three different values of the Froude number, for $d/D = 0.75$ and at the depth $\ell\tilde{z}/D = -0.36$. (b) Pressure coefficient c_p obtained numerically as a function of the coordinate $\tilde{x}$ for three different values of the asymmetry parameter ϵ, for Fr = 0.3, $d/D = 0.75$ and at the depth $\ell\tilde{z}/D = -0.36$.

It can be noticed that the curves for Fr = 0.2 and Fr = 0.3 oscillate around a mean curve close to the curve for Fr = 0.1. These oscillations, particularly visible for Fr = 0.2 are the signatures of the waves created by the moving hull. Indeed, the wavelength of the waves produced by the hull depends on the Froude number as given in Eq. (1.19). If we denote the dimensionless wavelength $\tilde{\lambda} = \lambda/\ell$, one has: $\tilde{\lambda} = 2\pi\text{Fr}^2$. Then, for Fr $\in \{0.1, 0.2, 0.3\}$, $\tilde{\lambda} \in \{0.06, 0.25, 0.565\}$. The second local maximum in the pressure distribution for Fr = 0.2 is situated around $\tilde{x} = -0.25$ in fairly good agreement with the value of the dimensionless wavelength $\tilde{\lambda} = 0.25$.
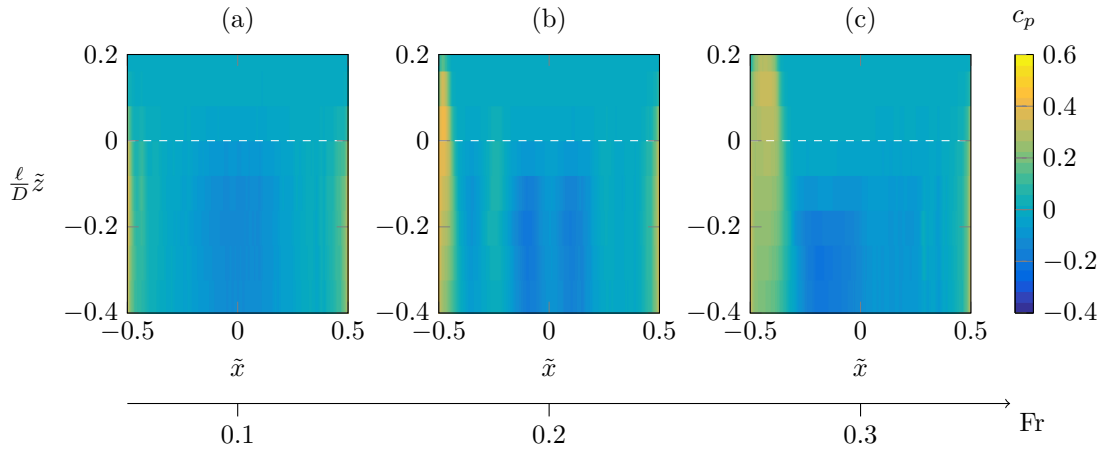
Figure B.8: Image plot of the pressure coefficient c_p as a function of the coordinates $\tilde{x}$ and $\ell\tilde{z}/D$ for the symmetric hull (hull 1) and for (a) Fr = 0.1, (b) Fr = 0.2 and (c) Fr = 0.3, for $d/D = 0.75$.

These signatures of the waves can also be seen in Fig. B.8, where the pressure coefficient is represented as a function of the two coordinates $\tilde{x}$ and $\ell\tilde{z}/D$. On these image plots, one clearly see the wave created at the bow with the appearance of a positive pressure coefficient above the initial level of water near $\tilde{x} = -0.5$. In Fig. B.7(b), the pressure coefficient $c_p(\tilde{x})$

is represented for three different values of the asymmetry parameter ϵ. The curve for $\epsilon = 0$ is situated in between the two curves for $\epsilon = 0.04$ and $\epsilon = -0.04$ and the amplitude of the curve is maximum for $\epsilon = 0.04$, which coincides with the idea that asymmetric hulls with $\epsilon > 0$ (moving with the bulky part first) create more waves than symmetric hulls or the asymmetric hulls with $\epsilon < 0$ (moving with the pointed part first).

B.2.2 Fit with Fourier series

The pressure distributions along the different hulls $c_p(\tilde{x})$ at a given depth $\tilde{z}$ are fitted with Fourier series, that is with the function:

$$y = b_0 + \sum_{n=1}^{N} b_n \sin\left[n\pi(\tilde{x} + 0.5)\right] \;, \tag{B.1}$$

with $N = 8$. The resulting coefficients b_n of the fitting of the pressure distributions shown in Fig. B.7 with Fourier series are plotted in Fig. B.9.
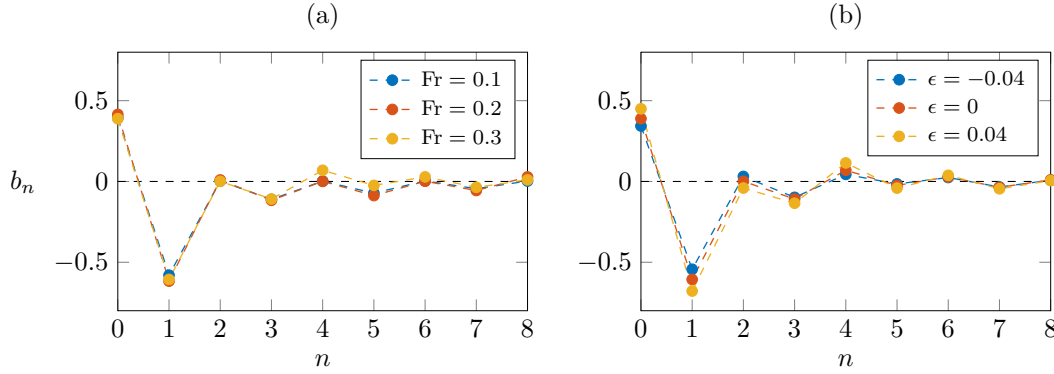
Figure B.9: Coefficients b_n of the fit of the pressure distributions in Fig. B.7 (a) for the symmetric hull (hull 1) and three different Froude numbers and (b) for Fr = 0.3 and three different values of the asymmetry parameter ϵ. For both plots, the immersion is $d/D = 0.75$ and the pressure distribution is taken at the depth $\ell\tilde{z}/D = -0.36$.
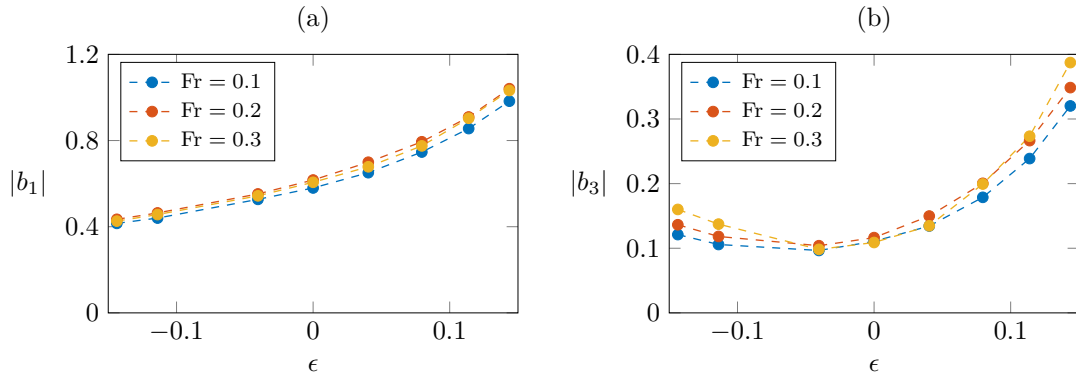
Figure B.10: Evolution of the absolute value of the coefficients (a) b_1 and (b) b_3 with the asymmetry parameter ϵ for three different Froude numbers. The immersion is $d/D = 0.75$ and the pressure distribution is taken at the depth $\ell\tilde{z}/D = -0.36$.

In Fig. B.9(a), the coefficients for three different Froude numbers are compared. The coeffi-

cients b_n are quite close together whatever the Froude number Fr. In Fig. B.9(b), the effect of the asymmetry is made quite clear: the coefficients seem to be increasing functions of the asymmetry parameter ϵ. In both plots, b_1 is the coefficient with the largest magnitude and the other coefficients decay as n increases. It can also be mentioned that the coefficients corresponding to even frequencies are close to zero.

Since b_1 and b_3 are considerably larger than the higher frequency coefficients, we plot their variation with the asymmetry parameter in Fig. B.10. These plots show that b_1 is indeed an increasing function of ϵ on the available range, while b_3 has a minimum around $\epsilon = -0.04$.

Another possibility could be to perturb the pressure distribution of a given hull fully immersed in a fluid with a function that accounts for the presence of the free-surface and the formation of waves. The pressure coefficient $c_p(\text{Fr} = 0.1)$ is expected to be close to the pressure coefficient when the hull is fully immersed in a fluid. Fig. B.11 thus presents the subtracted pressure coefficient $c_p - c_p(\text{Fr} = 0.1)$ as a function of the coordinate $\tilde{x}$ for the symmetric hull at a given depth for $\text{Fr} = 0.2$ and $\text{Fr} = 0.3$. Periodic oscillations of decreasing amplitude along the ship hull are clearly visible on this figure and their wavelengths is close to the wavelength of the waves created by the hull at the surface: $\lambda/\ell \simeq 0.25$ for $\text{Fr} = 0.2$ and $\lambda/\ell \simeq 0.56$ for $\text{Fr} = 0.3$ (see Eq. 1.19). As a result, the function to be used to perturb the pressure distribution for the fully immersed hull should be an oscillatory function of wavelength $2\pi\text{Fr}^2$ and decreasing amplitude.
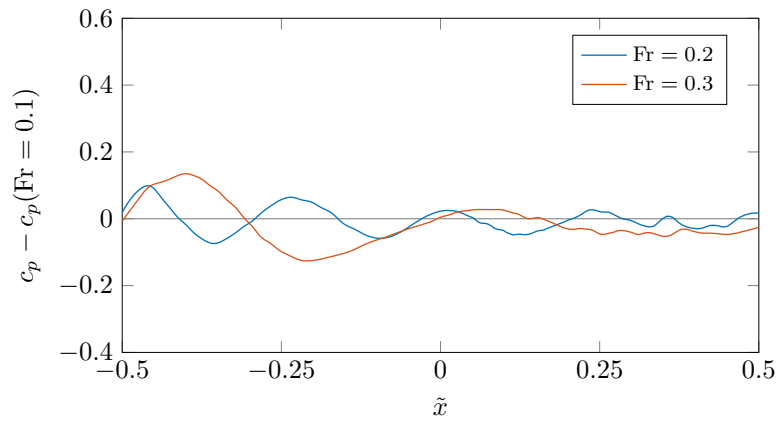
Figure B.11: Subtracted pressure coefficient $c_p - c_p(\text{Fr} = 0.1)$ as a function of the coordinate $\tilde{x}$ for the symmetric hull (hull 1), for $\text{Fr} = 0.2$ and $\text{Fr} = 0.3$, for $d/D = 0.75$ and at the depth $\ell\tilde{z}/D = -0.36$.

C
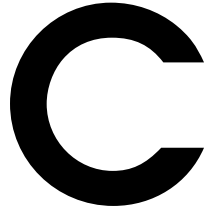
ARTICLES

The articles published during my thesis can be found below. The first one is about the optimal aspect ratios of ship hulls and corresponds to Chap. 3. It was published in the journal Physical Review Fluids *in July 2018. The second one deals with the original subject of the popsicle-stick cobra wave, which I worked on at the beginning of my thesis. It was published in the journal* Physical Review Letters *in August 2017. Finally, the short article about our experimental study of synchronisation in rowing (see Chap. 6), published in the journal* Physics Today *in June 2017, is reprinted here with its Japanese version (reproduced with the permission of the American Institute of Physics).*

Contents

Thin or bulky: optimal aspect ratios for ship hulls

Jean-Philippe Boucher[1], Romain Labbé[1], Christophe Clanet[1] and Michael Benzaquen[1*]

[1]LadHyX, UMR 7646 du CNRS, École polytechnique, 91128 Palaiseau Cedex, France

(Dated: June 22, 2018)

Empirical data reveals a broad variety of hull shapes among the different ship categories. We present a minimal theoretical approach to address the problem of ship hull optimisation. We show that optimal hull aspect ratios result – at given load and propulsive power – from a subtle balance between wave drag, pressure drag and skin friction. Slender hulls are more favourable in terms of wave drag and pressure drag, while bulky hulls have a smaller wetted surface for a given immersed volume, by that reducing skin friction. We confront our theoretical results to real data and discuss discrepancies in the light of hull designer constraints, such as stability or manoeuvrability.

PACS numbers: 47.85.lb, 47.35.Bb, 45.10.Db

I. INTRODUCTION

The long-lived subject of ship hull design is with no doubt one of infinite complexity. Constraints may significantly vary from one ship class to another. When designing a sailing boat (see Fig. 1(a)), stability and manoeuvrability are of paramount importance [1–4]. Liners and warships must be able to carry a maximal charge and resist rough sea conditions. Ferrys and cruising ships (see Fig. 1(b)) must be sea-kindly such that passengers don't get sea-sick. All ship hulls share however one crucial constraint: they must suffer the weakest drag possible in order to minimise the required energy to propel themselves, or similarly maximise their velocity for a given propulsive power. Of particular interest is the case of rowing boats (see Fig. 1(c)) [5, 6], sprint canoes and sprint kayaks as they do not really have other constraints than the latter. Indeed manoeuvrability is not relevant as they usually only have to go along straight lines, stability is at its edge and they only need to carry the athletes, usually on very calm waters.

In Fig. 2, the length to width aspect ratio (ℓ/w) of different kinds of bodies moving at the water surface is plotted against their Froude number (see Table I for details). The Froude number is defined as $\mathrm{Fr} = U/\sqrt{g\ell}$ with U the hull velocity, g the acceleration of gravity and ℓ the length of the hull (see Fig. 1(c)). As one can see, different ship categories tend to gather into clusters. These groups display very different aspect ratios, from 2-3 to about 30, even in the same Froude number regime. The highest aspect ratios are reached for rowing boats ($\ell/w \approx 30$, $\mathrm{Fr} \approx 0.5$). The majority of ships stand on the left hand side of the plot ($\mathrm{Fr} \lesssim 0.7$). For $\mathrm{Fr} \gtrsim 0.7$, most hulls can no longer be considered as *displacement* hulls (weight balanced by buoyancy) but rather as *planing* hulls (weight balanced by hydrodynamic lift) and thus

have a much smaller immersed volume [4]. Here we wonder how all these shapes compare to the optimal aspect ratios in terms of drag.

For a fully immersed body moving at large Reynolds numbers, the drag (also called *profile drag*) is the sum of two contributions [2, 4, 7]: (*i*) the skin-friction drag, which comes from the frictional forces exerted by the fluid along the surface of the body (dominant for a streamlined body, such as a plate parallel to the flow), and (*ii*) the pressure drag, which results from the separation of the flow and the creation of vortices (dominant for a bluff body such as a sphere) [7]. One additional force arises when moving at the air-water interface: the *wave resistance* or *wave drag* [8–10]. This force results from the generation of surface waves which

FIG. 1: Pictures of (a) a 44-footer sailing boat: length-to-width aspect ratio 3 and typical Froude number 0.6, (b) the *Queen Mary 2* liner: length-to-width aspect ratio 8.4 and typical Froude number 0.26, and (c) a coxless quadruple scull rowing boat: length to width aspect ratio 31 and typical Froude number 0.54. See Table I for details and characteristics of other boats.

*Corresponding author: michael.benzaquen@polytechnique.edu
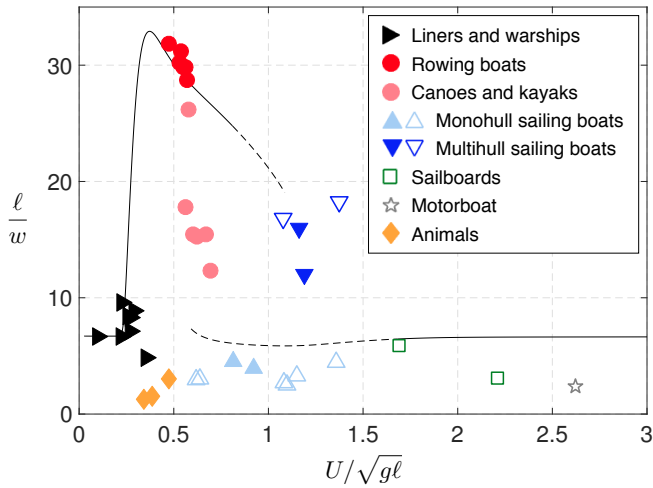
FIG. 2: Length to width aspect ratio ℓ/w as a function of Froude number $U/\sqrt{g\ell}$ for different kinds of bodies moving at the water surface (see Table I for details). Solid symbols represent displacement hulls, whereas open symbols indicate planing hulls. The aspect ratio for multihulls is computed for each hull independently. The black line corresponds to the optimal aspect ratio, see Sect. III. Solid lines indicate global optima, while dashed lines signify local optima.
α $\mathcal{F}$

continuously remove energy to infinity. Thereby it is interesting to notice that many animals have air or water as a natural habitat but only a few (e.g. ducks, muskrats or sea otters) actually spend most of their time at the water surface [11, 12].

As one can expect, a number of technological advances have been developed over the years, such as bulbous bows intended to reduce wave drag through destructive interference [3, 13, 14]. There exists an extended literature of numerical and experimental studies dedicated to the optimisation of ship hulls. Quite surprisingly some of them only consider wave drag in the optimisation setup (see e.g. [15–17]). Others consider both the skin drag and the wave drag [14, 18, 19]. Very few consider the pressure drag [20] as most studies address slender streamlined bodies for which the boundary layer does not separate, leading to a negligible pressure drag. The complexity of addressing analytically this optimisation problem comes from the infiniteness of the search space. Indeed without any geometrical constraints, the functions defining the hull geometry can be anything, and computing the corresponding drag can become an impossible task.

Here we present a minimal approach to address the question of optimal hull aspect ratios in presence of skin drag, pressure drag and wave drag. Let us stress that we do not claim for our results to be quantitative but rather present qualitative ideas and general trends on the very complex matter of ship hull optimisation. We first consider a model hull shape with a minimum number of

parameters and derive the expression of the total drag coefficient. Then we perform the shape optimisation at given propulsive power and load. Finally we confront our results to the empirical data and discuss concordances and discrepancies.

II. WAVE AND PROFILE DRAG

In order to account in a minimal way for the wide variety of hull shapes, we restrict to two-dimensional hulls (namely hulls with a constant horizontal cross-section, see Fig. 3). Following the generic parametrisation of hull shapes with respect to the central plane [8, 21–23], we let $y = f(x)\mathbb{1}_{z\in[-d,0]}$ the compact support hull boundary. We define the length ℓ, width w and draft d and introduce the dimensionless coordinates through $x = \tilde{x}\ell$, $y = \tilde{y}\ell$ and $z = \tilde{z}\ell$ as well as $f(x) = \tilde{f}(\tilde{x})w$ [36]. We further define the aspect ratios $\alpha = \ell/w$ and $\beta = \ell/d$.

There exist two main theoretical models to estimate the wave resistance, both assuming that the fluid is incompressible, inviscid, irrotational and infinitely deep. Havelock suggested to replace the moving body by a moving pressure disturbance [9, 10]. This first model allows to compute the far-field wave pattern as well as the wave resistance [17, 24, 25] but is too simple to account for the exact shape of the hull and especially to study the effect of the draft. The second model was developed by Michell for slender bodies [8, 21, 26]: the linearised potential flow problem with a distribution of sources on the centerplane of the hull is solved to get the expression of the wave resistance. The advantage of the latter is that it gives a very practical formula in the sense that it only takes as inputs the parametric shape of the hull and its velocity, with no need of inferring the corresponding pressure distribution. Using Michell's approach, we compute the wave drag $R_{\mathrm{w}} = \rho\Omega^{2/3}U^2 C_{\mathrm{w}}$ where ρ is the water density and $\Omega = \ell w d$ [37]. The wave drag coefficient C_{w} writes (see Appendix A):

$$C_{\mathrm{w}}(\mathrm{Fr}, \alpha, \beta) = \frac{4\beta^{2/3}}{\pi\alpha^{4/3}\mathrm{Fr}^4}\, G_{\tilde{f}}(\mathrm{Fr}, \beta)\,, \qquad (1)$$
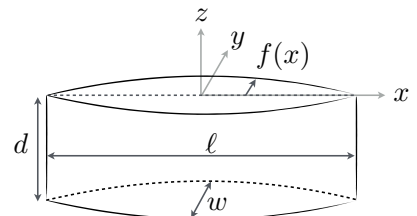

FIG. 3: Schematics of the simplified hull geometry considered in this study. The hull of length ℓ, width w and draft d has a constant horizontal cross-section, which is defined by $y = f(x)\mathbb{1}_{z\in[-d,0]}$. Note that only the part of the hull immersed in the water is represented.

where we have defined:

$$G_{\tilde{f}}(\mathrm{Fr}, \beta) = \int_{1}^{+\infty} \frac{|I_{\tilde{f}}(\lambda, \mathrm{Fr}, \beta)|^2}{\sqrt{\lambda^2 - 1}} \, \mathrm{d}\lambda$$

$$I_{\tilde{f}}(\lambda, \mathrm{Fr}, \beta) = \left(1 - e^{-\lambda^2/(\beta \mathrm{Fr}^2)}\right) \int_{-\frac{1}{2}}^{\frac{1}{2}} \tilde{f}(\tilde{x}) e^{i\lambda \tilde{x}/\mathrm{Fr}^2} \, \mathrm{d}\tilde{x} \quad . (2)$$

To compute the wave-drag we consider a Gaussian hull profile:

$$\tilde{f}(\tilde{x}) = \frac{1}{2} \exp[-(4\tilde{x})^2] \quad . \tag{3}$$

This particular kind of profile allows to analytically compute the wave resistance coefficient. The choice of this profile in comparison with more realistic profiles has no qualitative impact on our main results (see Appendix A).

The profile drag R_{p} is the sum of the skin drag R_{s} which scales with the wetted surface, and the pressure drag (or form drag) R_{f} which scales with the main cross-section. Given the typical Reynolds numbers for ships (ranging from 10^7 to 10^9), both the skin and pressure contributions scale with U^2 and the profile drag can be written as $R_{\mathrm{p}} = R_{\mathrm{s}} + R_{\mathrm{f}} = \rho \Omega^{2/3} U^2 C_{\mathrm{p}}$ with (see Appendix B):

$$C_{\mathrm{p}}(\alpha, \beta) = \frac{C_{\mathrm{d}}(\alpha)\beta^{2/3}}{\alpha^{1/3}} \left[a_{\tilde{f}} + \frac{\alpha}{\beta} b_{\tilde{f}}(\alpha) \right] \quad , \tag{4}$$

where $C_{\mathrm{d}}(\alpha)$ is the profile drag coefficient of the hull, and where:

$$a_{\tilde{f}} = \int_{-\frac{1}{2}}^{\frac{1}{2}} \tilde{f}(\tilde{x}) \, \mathrm{d}\tilde{x} \tag{5a}$$

$$b_{\tilde{f}}(\alpha) = \int_{-\frac{1}{2}}^{\frac{1}{2}} [1 + \tilde{f}'(\tilde{x})^2/\alpha^2]^{1/2} \, \mathrm{d}\tilde{x} \quad . \tag{5b}$$

The evolution of the profile drag coefficient C_{d} with α was empirically derived for streamlined bodies [7]: $C_{\mathrm{d}}(\alpha) = C_{\mathrm{f}}(1 + 2/\alpha + 60/\alpha^4)$ with C_{f} the skin drag coefficient for a plate. The term $(1 + 2/\alpha)$ refers to the skin friction, while the term $60/\alpha^4$ corresponds to the pressure drag [38]. In the considered regimes, the skin drag coefficient is only weakly dependent on the Reynolds number [7] (see Appendix B). We thus consider here a constant skin drag coefficient $C_{\mathrm{f}} = 0.002$, corresponding to a Reynolds number $\mathrm{Re} \simeq 10^8$.

The total drag force on the hull reads $R = R_{\mathrm{w}} + R_{\mathrm{p}} = \rho \Omega^{2/3} U^2 C$ where $C(\alpha, \beta, \mathrm{Fr}) =$

$$\frac{\beta^{2/3}}{\alpha^{4/3}} \left\{ \frac{4}{\pi \mathrm{Fr}^4} G_{\tilde{f}}(\mathrm{Fr}, \beta) + C_{\mathrm{d}}(\alpha)\alpha \left[a_{\tilde{f}} + \frac{\alpha}{\beta} b_{\tilde{f}}(\alpha) \right] \right\} \quad . \tag{6}$$

Within the present framework and choice of dimensionless parameters, the total drag coefficient is thus completely determined by the three dimensionless variables α, β and Fr, together with the function $\tilde{f}$. Let us stress that this expression of the total drag coefficient is only expected to be accurate for slender hulls, as required in Michell's model [21, 26, 27].

III. OPTIMAL HULLS

We now seek the optimal hull shapes, that is the choice of parameters that minimises the total drag for a given load (equivalently immersed volume through Archimedes principle) and given propulsive power – consistent with operational conditions. Before engaging in any calculations, let us stress that the optimal aspect ratios will naturally result from a subtle balance between skin drag, pressure drag and wave drag. Indeed, on the one hand reducing skin drag amounts to minimising the wetted surface which corresponds to rather bulky hulls [39], while on the other hand reducing wave drag or pressure drag pushes towards rather slender hulls. Figure 4 displays the contour plots of C_{p} and C_{w} as function of (α, β) [40]. One notices that for sufficiently large α and β the gradients $\boldsymbol{\nabla} C_{\mathrm{p}}$ and $\boldsymbol{\nabla} C_{\mathrm{w}}$ roughly point in opposite directions.

To close the problem we define the imposed propulsive power $\mathcal{P} = RU$. Using $U = \mathrm{Fr}[\alpha\beta\Omega g^3]^{1/6}$ one obtains:

$$\mathrm{Fr}^3 \sqrt{\alpha\beta} C(\alpha, \beta, \mathrm{Fr}) = \Pi \quad , \tag{7}$$

where $C(\alpha, \beta, \mathrm{Fr})$ is given by Eq. (6), and where we have defined the rescaled and dimensionless power:

$$\Pi = \frac{\mathcal{P}}{\rho g^{3/2} \Omega^{7/6}} \quad . \tag{8}$$

Minimising the total drag coefficient C as given by Eq. (6) with respect to α, β and Fr, under the constraint given by setting the dimensionless power Π in Eq. (7), yields the optimal set of parameters $(\alpha^\star, \beta^\star, \mathrm{Fr}^\star)$ for the optimal hull geometry at given load (equivalently Ω) and given propulsive power $\mathcal{P}$.

This optimisation is performed numerically using an interior-point algorithm [28, 29]. The optimal parameters and the resulting total drag coefficient
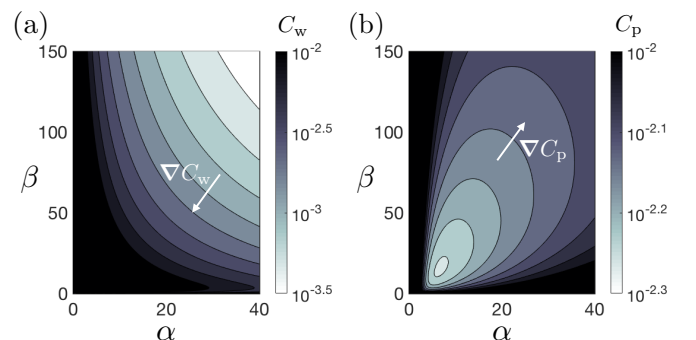

FIG. 4: Contour plots of (a) the wave drag coefficient C_{w} and (b) the profile drag coefficient C_{p} as a function of the aspect ratios α and β. For the wave drag coefficient, we set $\mathrm{Fr} = 0.5$. In both plots, black regions correspond to $C_{\mathrm{p/w}} \geq 10^{-2}$ and arrows indicate the direction of the gradient.

$C^\star = C(\alpha^\star, \beta^\star, \mathrm{Fr}^\star)$ as function of dimensionless power Π, are presented in Fig. 5, together with the empirical data points for comparison. Interestingly the optimisation yields two separate solutions (see orange and green branches) corresponding to two local optima. For $\Pi \leq \Pi_c$ (resp. $\Pi \geq \Pi_c$) with $\Pi_c \approx 0.2$, the orange (resp. green) branch constitutes the global optimum, consistent with a lower total drag coefficient $C^\star$ (see Fig. 5(d)). As one can see on Figs. 5(a) and (b) the optimal aspect ratios $\alpha^\star$ and $\beta^\star$ show very similar evolutions with Π. On the one hand, both of them are maximal around $\Pi_{\max} \approx 0.03$ corresponding to $\mathrm{Fr}_{\max} \approx 0.4$, that is the maximum wave drag regime (see Fig. 6 in Appendix A). This is consistent with the idea that thin and shallow hulls are favourable in terms of wave drag as illustrated in Fig. 4(a). On the other hand, for $\Pi \ll \Pi_{\max}$ or $\Pi \gg \Pi_{\max}$ the wave drag becomes negligible compared to the profile drag, and one recovers the optimal aspect ratios in the absence of wave drag: $\alpha^\star \simeq 7$ and $\beta^\star \simeq 10$. Figure 5(c) shows that the optimal Froude number $\mathrm{Fr}^\star$ increases with Π. Like for $\alpha^\star$ and $\beta^\star$, there is a shift of value from $\mathrm{Fr}^\star \approx 0.8$ to $\mathrm{Fr}^\star \approx 1.7$, for $\Pi = \Pi_c$, which indicates that in this setting $0.8 < \mathrm{Fr} < 1.7$ is never a suitable choice. This shift is also made visible in Fig. 2 where the optimal aspect ratio $\alpha^\star$ is plotted against the Froude number. These results obviously depend on the Reynolds number but only weakly. Let us stress that, while for the optimal geometries ($\alpha^\star$, $\beta^\star$) the profile drag is always the dominant force regardless of the Froude number, our study shows that it is crucial to consider the wave drag in the optimisation.

IV. DISCUSSION

Our work provides a self-consistent framework to understand and discuss the design of existing boats. Figure 5 confronts the real data with the calculated optimal geometries. As one can see, while some ship categories are found in a rather good agreement with the theoretical predictions (such as liners and warships), others are very far from the computed optima (such as monohull sailing boats). Discrepancies with empirical data might primarily come from other constraints on the design of the boat which can prevail on the minimisation of the drag, such as stability, manoeuvrability, resistance to rough seas or seakindliness as mentioned in the introduction. They could also come from the assumptions of our model. In particular, a steady motion is considered here, while for rowing boats and sprint canoes, high fluctuations of speed are encountered (about 20% of the mean velocity) and are expected to affect the total drag, notably through added mass.

The data for rowing boats, canoes and kayaks are found in good agreement with the optimal Froude number $\mathrm{Fr}^\star(\Pi)$. For rowing shells, while the aspect
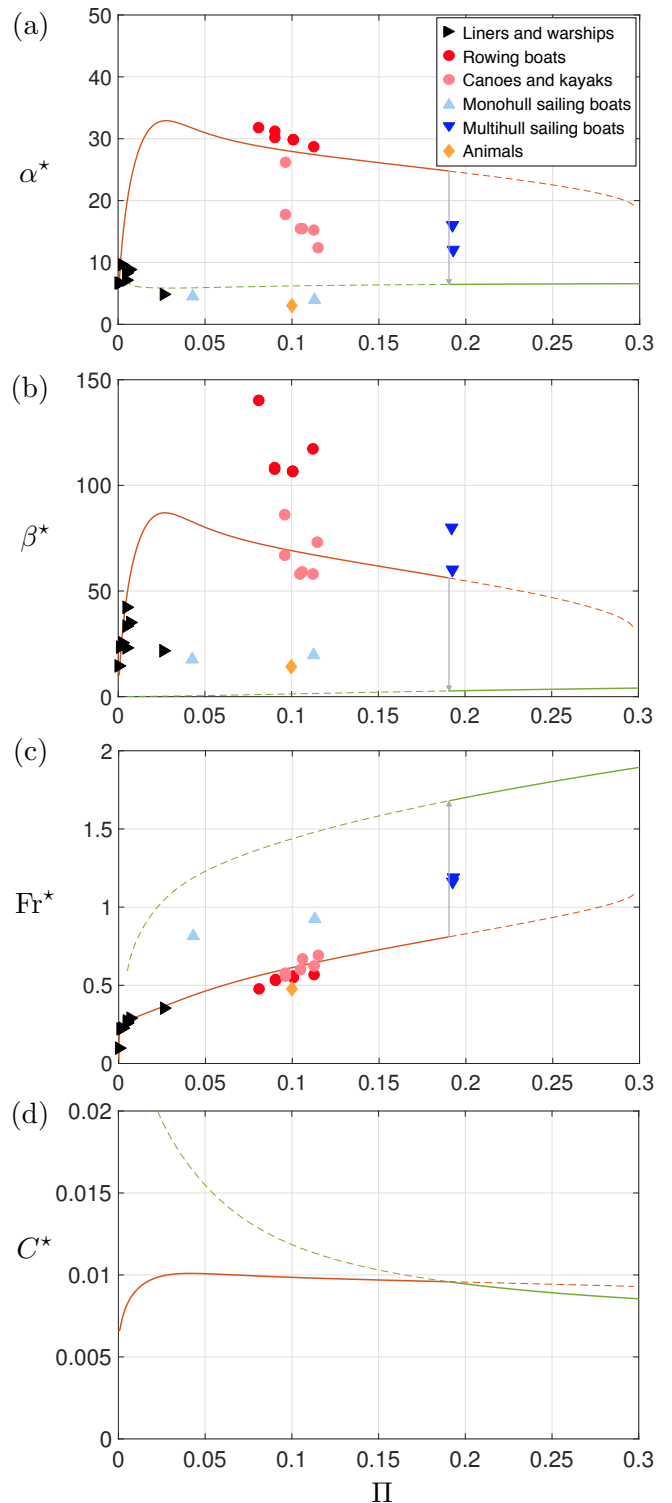
FIG. 5: (a) Optimal aspect ratio $\alpha^\star$, (b) optimal aspect ratio $\beta^\star$, (c) optimal Froude number $\mathrm{Fr}^\star$, and (d) corresponding value of the total drag coefficient $C^\star = C(\alpha^\star, \beta^\star, \mathrm{Fr}^\star)$, as a function of the dimensionless power Π. The curves in orange and green represent the two optimal branches. Solid/dashed lines indicate global/local optima.

ratios α are found quite close to the optimal value, the aspect ratios β lie well above the optimal curve. This indicates that rowing shells could be shorter or have a larger draft. This discrepancy might be related to the need for sufficient spacing between rowers (long shells) and/or for stability (small draft). For sprint canoes and kayaks, the competition rules from the *International Canoe Federation* [30] impose maximal lengths for the boats [41] which could explain their relatively low aspect ratio α compared to the optimal one. As for their aspect ratio β, contrary to rowing boats, it is found in good agreement with the optimal results.

For the monohull sailing boats, the significant difference between real data and the computed optima surely comes from the need for stability (see Appendix C). The stability of a boat mostly depends on the position of its center of gravity (which should be as low as possible) with respect to the position of the metacentre [2, 4] (which should in turn be as high as possible). Imposing that the metacenter be above the center of gravity yields a simple criterion for static stability [42]. This is w/d should be larger than a certain value depending on mass distribution and effective density of the hull, which constitutes an additional constraint that could be easily taken into account in the optimisation problem. In the simple geometry considered here and assuming a homogeneous body of density ρ_s the latter criterion writes: $w/d = \beta/\alpha > \psi(\rho_s/\rho)$ where $\psi(u) \approx 3\sqrt{1/u - 1}$ with $u \in [0,1]$. For real boats, the critical value of w/d is highly affected by the presence of a keel, intended to lower the position of the center of gravity. In short, stability favours wide and shallow ships. This explains why most real data points lie below the optimal curve $\alpha^\star(\Pi)$ in Fig. 5(a) but above the curve $\beta^\star(\Pi)$ in Fig. 5(b). Stability is all the more important for sailing boats where the action of the wind on the sail contributes with a significant destabilising torque. Interestingly, this matter is overcome for multihull sailing boats, in which both stability and optimal aspect ratios can be achieved by setting the appropriate effective beam, namely the distance between hulls [31]. This allows higher hull aspect ratios, closer to the optimal curves in Fig. 5.

As displayed in Fig. 5(c), we predict a shift in the Froude number for $\Pi \approx 0.2$ which indicates that boats should not operate in the range of Froude numbers Fr $\in [0.8, 1.7]$. However, when the Froude number is above Fr ≈ 0.7, the hulls start riding their own bow wave: they are planing. Their weight is then mostly balanced by hydrodynamic lift rather than static buoyancy [4, 7]. As planing is highly dependent on the hull geometry and would require to consider tilted hulls, we do not expect our model to hold in this regime. Some changes though allow to understand the basic principles. Planing drastically reduces the immersed volume of the hull which in turn reduces both the wave drag and the profile drag. The effect on the immersed volume can be taken into account by adding the hydrodynamic lift in the momentum balance along the vertical direction (see [43]).

Our study provides the guidelines of a general method for hull-shape optimisation. It does not aim at presenting quantitative results on optimal aspect ratios, in particular due to the simplified geometry we consider and the limitations of Michell's theory for the wave drag estimation [21, 26, 27]. Our method can be applied in a more quantitative way for each class of boat by considering more realistic hull geometries. Future work should be devoted to applying this method to the category of rowing boats, sprint canoes and sprint kayaks as these particular boats mostly require to experience the least drag, with no or little concern on stability and other constraints.

Acknowledgments

[1] Kenneth John Rawson. *Basic ship theory*, volume 1. Butterworth-Heinemann, 2001.

[2] Fabio Fossati. *Aero-hydrodynamics and the performance of sailing yachts: the science behind sailing yachts and their design*. A&C Black, 2009.

[3] L. Larsson, H.C. Raven, and J.R. Paulling. *Ship Resistance and Flow*. Principles of naval architecture. Society of Naval Architects and Marine Engineers, 2010.

[4] Rolf Eliasson, Lars Larsson, and Michal Orych. *Principles of yacht design*. A&C Black, 2014.

[5] John McArthur. *High performance rowing*. Crowood Press, 1997.

[6] Volker Nolte. *Rowing faster*. Human Kinetics 1, 2005.

[7] Sighard F Hoerner. *Fluid-dynamic drag: practical information on aerodynamic drag and hydrodynamic resistance*. Hoerner Fluid Dynamics, 1965.

[8] John Henry Michell. XI. The wave-resistance of a ship. *The London, Edinburgh, and Dublin Philosophical Magazine and Journal of Science*, 45(272):106–123, 1898.

[9] Thomas Henry Havelock. Wave resistance: some cases of three-dimensional fluid motion. *Proceedings of the Royal Society of London. Series A, Containing Papers of a Mathematical and Physical Character*, 95(670):354–365, 1919.

[10] Thomas Henry Havelock. The theory of wave resistance. *Proceedings of the Royal Society of London. Series A, Containing Papers of a Mathematical and Physical Character*, 138(835):339–348, 1932.

[11] Frank E Fish. Influence of hydrodynamic-design and propulsive mode on mammalian swimming energetics.

Australian Journal of Zoology, 42(1):79–101, 1994.

[12] William T Gough, Stacy C Farina, and Frank E Fish. Aquatic burst locomotion by hydroplaning and paddling in common eiders (Somateria mollissima). *Journal of Experimental Biology*, 218(11):1632–1638, 2015.

[13] Scott W McCue and Lawrence K Forbes. Bow and stern flows with constant vorticity. *Journal of Fluid Mechanics*, 399:277–300, 1999.

[14] Scott Percival, Dane Hendrix, and Francis Noblesse. Hydrodynamic optimization of ship hull forms. *Applied Ocean Research*, 23(6):337–355, 2001.

[15] Chi-Chao Hsiung. Optimal ship forms for minimum wave resistance. *J. Ship Research*, 25(2), 1981.

[16] Bao-ji Zhang, Ma Kun, and Zhuo-shang Ji. The optimization of the hull form with the minimum wave making resistance based on rankine source method. *Journal of Hydrodynamics, Ser. B*, 21(2):277–284, 2009.

[17] Michael Benzaquen, Alexandre Darmon, and Elie Raphaël. Wake pattern and wave resistance for anisotropic moving disturbances. *Physics of Fluids*, 26(9):092106, 2014.

[18] Chi-Chao Hsiung and Dong Shenyan. Optimal ship forms for minimum total resistance. *Journal of ship research*, 28(3):163–172, 1984.

[19] Julien Dambrine, Morgan Pierre, and Germain Rousseaux. A theoretical and numerical determination of optimal ship forms based on Michell's wave resistance. *ESAIM: Control, Optimisation and Calculus of Variations*, 22(1):88–111, 2016.

[20] Emilio F Campana, Daniele Peri, Yusuke Tahara, and Frederick Stern. Shape optimization in ship hydrodynamics using computational fluid dynamics. *Computer methods in applied mechanics and engineering*, 196(1):634–651, 2006.

[21] Ernest O Tuck. The wave resistance formula of JH Michell (1898) and its significance to recent research in ship hydrodynamics. *The ANZIAM Journal*, 30(4):365–377, 1989.

[22] Takao Inui. *Wave-making resistance of ships*. Society of Naval Architects and Marine Engineers, 1962.

[23] John V Wehausen. The wave resistance of ships. *Advances in applied mechanics*, 13:93–245, 1973.

[24] Elie Raphaël and Pierre-Gilles De Gennes. Capillary gravity waves caused by a moving disturbance: wave resistance. *Physical Review E*, 53(4):3448, 1996.

[25] Alexandre Darmon, Michael Benzaquen, and Elie Raphaël. Kelvin wake pattern at large Froude numbers. *Journal of Fluid Mechanics*, 738, 2014.

[26] A Sh Gotman. Study of Michell's integral and influence of viscosity and ship hull form on wave resistance. *Oceanic Engineering International*, 6(2):74–115, 2002.

[27] Finn Christian Michelsen. Wave resistance solution of Michell's integral for polynomial ship forms. 1960.

[28] Richard H Byrd, Jean Charles Gilbert, and Jorge Nocedal. A trust region method based on interior point techniques for nonlinear programming. *Mathematical Programming*, 89(1):149–185, 2000.

[29] Richard H Byrd, Mary E Hribar, and Jorge Nocedal. An interior point algorithm for large-scale nonlinear programming. *SIAM Journal on Optimization*, 9(4):877–900, 1999.

[30] International Canoe Federation. Canoe sprint competition rules. www.canoeicf.com/rules, 2017.

[31] Pierre Yves Belly. *250 réponses aux questions d'un marin curieux*. Le gerfaut, 2004.

[32] Ernest O Tuck. Wave resistance of thin ships and catamarans. *Applied Mathematics Report T8701*, 1987.

[33] RB Chapman. Hydrodynamic drag of semisubmerged ships. *Journal of Basic Engineering*, 94(4):879–884, 1972.

[34] Milton Abramowitz and Irene A Stegun. *Handbook of mathematical functions: with formulas, graphs, and mathematical tables*. Courier Corporation, 1964.

[35] JB Hadler. Coefficients for international towing tank conference 1957 model-ship correlation line. Technical report, David Taylor Model Basin Washington DC, 1958.

[36] In dimensionless coordinates, the hull boundary $y = f(x)$ with $x \in [-\ell/2, \ell/2]$ becomes $\tilde{y} = y/\ell = (w/\ell)\tilde{f}(\tilde{x})$ with $\tilde{x} \in [-1/2, 1/2]$.

[37] The immersed volume Ω_{i} is related to Ω through $\Omega_{\mathrm{i}} = 2a_{\tilde{f}}\Omega$ (see Eq. (5a)).

[38] This empirical expansion is expected to hold for $\alpha \gtrsim 2$ (see [7]).

[39] With no constraint on the geometry of the hull, the shape minimising the wetted surface is a spherical cap.

[40] Note that in order to avoid oscillations due to the sharp edges of the hull, the integral over x in Eq. (2) was actually computed over $\mathbb{R}$ (see Appendix A). We checked that doing so had negligible effect on the results.

[41] The maximal lengths for canoes and kayaks are the same for C1 and K1 (5.2 m), C2 and K2 (6.5 m) but not for C4 (9 m) and K4 (11 m) (see also Table I).

[42] Note that for real hull design one should also address dynamic stability [1], but the latter falls beyond the scope of our study.

[43] Vertical momentum balance writes $Mg \simeq \rho\Omega_{\mathrm{i}}g + \frac{1}{2}\rho C_L \ell w \sin(2\theta)U^2$ where M is the mass of the boat, Ω_{i} is the immersed volume, and $\theta(\mathrm{Fr})$ is the Froude-dependent angle of the hull with respect to the horizontal direction of motion [4, 7]. This leads to an immersed volume which depends on the Froude number through: $\Omega \simeq (M/\rho)/[1 + 0.5C_L\beta\sin(2\theta)\mathrm{Fr}^2]$. For low Froude number, $\theta(\mathrm{Fr}) \simeq 0$ and the volume is that imposed by static equilibrium, while for larger Fr number $\theta > 0$ and the volume Ω is decreased. Note that foil devices also contribute to decreasing the immersed volume, by increasing the lift.

Appendix

A. Wave drag coefficient

Here we derive the wave drag coefficient and discuss its behaviour for parabolic and Gaussian hull shapes. According to [8, 21], the wave drag in Michell's theory writes:

$$R_{\mathrm{w}}(f) = \frac{4\rho U^2}{\pi \ell^4 \mathrm{Fr}^4} \int_1^{+\infty} \frac{|\mathcal{I}_f(\lambda, \mathrm{Fr})|^2}{\sqrt{\lambda^2 - 1}} \, \mathrm{d}\lambda \,, \qquad (9)$$

where:

$$\mathcal{I}_f(\lambda, \mathrm{Fr}) = \frac{\lambda^2}{\mathrm{Fr}^2} \int_{-d}^{0} \mathrm{d}z \int_{-\frac{\ell}{2}}^{\frac{\ell}{2}} f(x) e^{\lambda^2 z/(\ell \mathrm{Fr}^2)} e^{i\lambda x/(\ell \mathrm{Fr}^2)} \, \mathrm{d}x \,. \qquad (10)$$
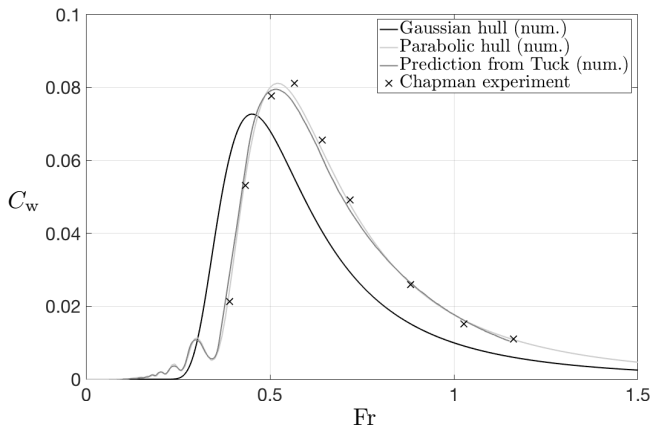
FIG. 6: Wave-drag coefficient $C_{\rm w}$ as function of the Froude number Fr for a Gaussian hull and a parabolic hull for $\alpha = 6.7$ and $\beta = 2.3$. These results are compared to the theoretical curve from Tuck [32] and experimental data points from Chapman (black crosses) [33].

Taking $\Omega^{1/3} = (\ell w d)^{1/3}$ as a characteristic length, we define the wave drag coefficient through the equation $R_{\rm w} = \rho \Omega^{2/3} U^2 C_{\rm w}$. Then using the dimensionless coordinates $\tilde{x}$, $\tilde{y}$, $\tilde{z}$ and the dimensionless parameters Fr, α, β, and integrating over $\tilde{z}$, we obtain the expression of the wave drag coefficient $C_{\rm w}$ given in Eqs. (1)-(2) with $I_{\tilde{f}} = \mathcal{I}_f/(\ell^2 w) = \mathcal{I}_f/(\Omega\beta)$. The wave-drag coefficient compares quite well with previous numerical and experimental works [32, 33] as shown in Fig. 6. This plot shows that the wave drag coefficient has the same qualitative evolution with the Froude number for a Gaussian hull and a parabolic hull. The main differences between the two are the presence of humps and hollows at low Froude number for the parabolic profile and a slight translation of the peak of wave resistance. For a Gaussian hull, one can approximate analytically the integrals in Eq. (10) by integrating x over $\mathbb{R}$. One obtains (see Eq. (2)):

$$G_{\rm gauss}({\rm Fr}, \beta) = \frac{\pi}{64} J\left(\frac{1}{32{\rm Fr}^4}\right) - \frac{\pi}{32} J\left(\frac{1}{32{\rm Fr}^4} + \frac{1}{\beta{\rm Fr}^2}\right)$$
$$+ \frac{\pi}{64} J\left(\frac{1}{32{\rm Fr}^4} + \frac{2}{\beta{\rm Fr}^2}\right), \quad (11)$$

where:

$$J(u) = \int_1^{+\infty} \frac{e^{-u\lambda^2}}{\sqrt{\lambda^2-1}}\, {\rm d}\lambda = \frac{1}{2}e^{-u/2}\mathcal{K}_0(u/2), \quad (12)$$

with $\mathcal{K}_0(u)$ the modified Bessel function of the second kind of order zero [34].

B. Profile drag coefficient

Here we discuss the derivation of the profile drag coefficient. The profile drag is commonly written $R_{\rm p} = (1/2)\rho S C_{\rm d} U^2$ where S is the wetted surface and $C_{\rm d}$ the profile drag coefficient of the hull. Here, the wetted surface can be decomposed in two contributions $S = S_{\rm b} + \mathcal{L}d$ where $S_{\rm b} = 2w\ell \int_{-1/2}^{1/2} \tilde{f}(\tilde{x})\, {\rm d}\tilde{x}$ is the surface of the bottom horizontal cross section of the hull and $\mathcal{L} = 2\ell \int_{-1/2}^{1/2} [1 + \tilde{f}'(\tilde{x})^2/\alpha^2]^{1/2}\, {\rm d}\tilde{x}$ is the perimeter of the hull. This leads to the expression of the coefficient $C_{\rm p}$ given in Eq. (4). As mentioned in the main text, $C_{\rm d}$ depends on the geometry through an empirical relation $C_{\rm d}(\alpha) = C_{\rm f}(1 + 2/\alpha + 60/\alpha^4)$ where the skin drag coefficient $C_{\rm f}$ weakly depends on the Reynolds number [7]. In the turbulent regime (Re $> 5.10^5$) one has the empirical law $C_{\rm f}({\rm Re}) \simeq 0.075/(\log({\rm Re}) - 2)^2$ [35].

C. Static stability criterion

Here we explicit the derivation of the stability criterion for the model hull presented in Fig. 3. Consider a homogenous body of density $\rho_s < \rho$ standing at the air-water interface (see Fig. 7). We define the center of gravity G, the center of buoyancy B, and the metacenter M [2, 4] as the point of intersection of the line passing through B and G and the vertical line through the new centre of buoyancy B' created when the body is displaced (see Fig. 7(b)). As mentioned in the main text, the stability criterion reads $\overline{\rm GM} > 0$, or equivalently $\overline{\rm BM} > \overline{\rm BG}$. On the one hand, the so-called metacentric height BM can be computed for small inclination angles through the longitudinal moment of inertia of the body $\mathscr{I} = (8c_{\tilde{f}})w^3\ell/12$ with $c_{\tilde{f}} = \int_{-1/2}^{1/2} [\tilde{f}(\tilde{x})]^3\, {\rm d}\tilde{x}$ and the immersed volume $\Omega_{\rm i} = 2a_{\tilde{f}}\Omega$ as:

$$\mathrm{BM} = \frac{\mathscr{I}}{\Omega_{\rm i}} = \frac{z}{3} \frac{c_{\tilde{f}}}{d_{\tilde{f}}} \frac{w^2}{f(x)}. \quad (13)$$

On the other hand, one has $\mathrm{BG} = (h - d)/2$ where h is the total height of the hull. We then use the static equilibrium $\rho_s\Omega_{\rm tot} = \rho\Omega_{\rm i}$, where $\Omega_{\rm tot} = 2a_{\tilde{f}}w\ell h$ is the total volume of the body, to eliminate h. This finally
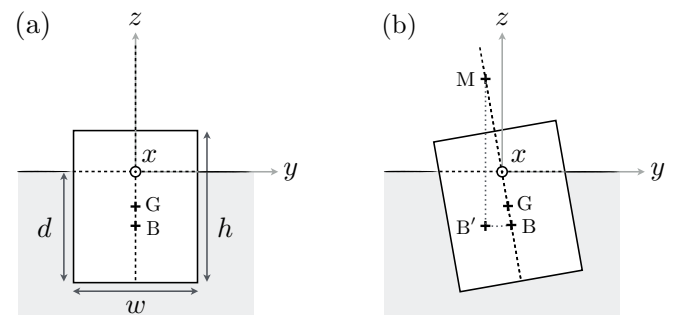
FIG. 7: Cross-section of the model hull (see Fig. 3) in (a) vertical position and (b) slightly inclined position.

yields the criterion $w/d > \psi(\rho_s/\rho)$ with:

$$\psi(u) = \sqrt{\frac{3a_{\tilde{f}}}{2c_{\tilde{f}}}\left(\frac{1}{u} - 1\right)}, \quad u \in [0,1] \tag{14}$$

where ψ is a decreasing function of u. For neutrally buoyant bodies, $\psi(1) = 0$, all configurations are stable as B and G coincide. While for bodies floating well above the level of water, $\lim_{u \to 0} \psi(u) = +\infty$, wide and shallow hulls are required to ensure stability. In the specific model case of Fig. 3, one has $a_{\tilde{f}} \approx 0.33$, $c_{\tilde{f}} \approx 0.057$ and thus $\psi(u) \approx 3\sqrt{1/u - 1}$. Taking this stability criterion into account in the optimisation procedure would reduce the search space and thus constraint the optimum curves to $\beta/\alpha > \psi(\rho_s/\rho)$.

D. Empirical data

Category	Boat Name	Length ℓ (m)	Width w (m)	Draft (*) d (m)	Mass M (kg)	Speed U (m/s)	Power (*) P (kW)
Liner	Titanic	269.0	28.00	10.50	52300000	11.70	33833.0
Liner	Queen Mary 2	345.0	41.00	8.10	76000000	14.90	115473.0
Liner	Seawise Giant	458.0	68.90	31.20	650000000	6.60	37300.0
Liner	Emma Maersk	373.0	56.00	15.80	218000000	13.40	88000.0
Liner	Abeille Bourbon	80.0	16.50	3.70	3200000	9.95	16000.0
Liner	France	300.0	33.70	8.50	57000000	15.80	117680.0
Warship	Charles de Gaulle	261.5	31.50	7.80	42500000	13.80	61046.0
Warship	Yamato	263.0	36.90	11.40	73000000	13.80	110325.0
Rowing boat	Single Scull	8.1	0.28	0.07	104	5.08	0.4
Rowing boat	Double Scull	10.0	0.34	0.09	207	5.56	0.8
Rowing boat	Coxless Pair	10.0	0.34	0.09	207	5.43	0.8
Rowing boat	Quadruple Scull	12.8	0.41	0.12	412	6.02	1.6
Rowing boat	Coxless Four	12.7	0.42	0.12	412	5.92	1.6
Rowing boat	Coxed Eight	17.7	0.56	0.13	820	6.26	3.2
Canoe	C1	5.2	0.34	0.09	104	4.45	0.4
Canoe	C2	6.5	0.42	0.11	200	4.80	0.8
Canoe	C4	8.9	0.50	0.13	390	5.24	1.6
Kayak	K1	5.2	0.42	0.07	102	4.95	0.4
Kayak	K2	6.5	0.42	0.11	198	5.35	0.8
Kayak	K4	11.0	0.42	0.13	390	6.00	1.6
Sailing boat Monohull	Finn (p)	4.5	1.51	0.12	240	4.10	4.0
Sailing boat Monohull	505 (p)	5.0	1.88	0.15	300	7.60	18.9
Sailing boat Monohull	Laser (p)	4.2	1.39	0.10	130	4.10	2.7
Sailing boat Monohull	Dragon	8.9	1.96	0.50	1000	7.60	16.5
Sailing boat Monohull	Star	6.9	1.74	0.35	671	7.60	18.5
Sailing boat Monohull	IMOCA 60 (p)	18.0	5.46	0.50	9000	15.30	843.4
Sailing boat Monohull	18ft Skiff (p)	8.9	2.00	0.24	420	12.70	85.2
Sailing boat Monohull	49er (p)	4.9	1.93	0.20	275	7.60	25.9
Sailing boat Multihull	Nacra 450 (p)	4.6	0.25	0.12	330	9.20	20.7
Sailing boat Multihull	Hobie Cat 16 (p)	5.0	0.30	0.12	330	7.60	20.1
Sailing boat Multihull	Macif	30.0	2.50	0.50	14000	20.40	1218.3
Sailing boat Multihull	Banque populaire V	40.0	2.50	0.50	14000	23.00	1701.1
Sailing boat Multihull	Groupama 3	31.5	2.40	0.50	19000	18.50	1407.3
Sailboard	Mistral One Design (p)	3.7	0.63	0.05	85	10.20	6.9
Sailboard	RS:X (p)	2.9	0.93	0.05	85	11.70	10.2
Motorboat	Zodiac (p)	4.7	2.00	0.11	700	17.80	180.0
Animal	Swan	0.5	0.40	0.08	10	0.76	N.A.
Animal	Duck	0.3	0.20	0.13	5	0.66	N.A.
Animal	Human	1.8	0.60	0.13	90	2.00	0.3

TABLE I: Characteristics of bodies moving at the water surface. The planing hulls are indicated with (p) in the column Boat Name. N.A. stands for *Not Available*. (*) For all hulls (including planing hulls for which this estimation might be too rough), the draft is estimated using the mass of the boat and the relation $M/\rho \simeq 2a_{\bar{f}}\ell wd$ (with $a_{\bar{f}} = 0.33$). The power is estimated through diverse methods depending on the category of the boat. For liners and warships, the propulsive power can easily be found in the specification documents. For rowing boats, canoes and kayaks, we consider that the power per oarsman is 400 W. For sailing boats and sailboards, we use the sail area of the boat to derive its propulsive power (with a typical wind of 10 m/s). Note that for multihull sailing boats, the indicated dimensions correspond to one of the hulls.

P H Y S I C A L   R E V I E W   L E T T E R S

ↄ

Popsicle-Stick Cobra Wave

Jean-Philippe Boucher,[1] Christophe Clanet,[1] David Quéré,[2] and Frédéric Chevy[3]
[1]*LadHyX, UMR 7646 du CNRS, École Polytechnique, 91128 Palaiseau Cedex, France*
[2]*PMMH, UMR 7636 du CNRS, ESPCI, 75005 Paris, France*
[3]*Laboratoire Kastler Brossel, ENS-PSL Research University, CNRS,
UPMC, Collège de France, 24, rue Lhomond, 75005 Paris, France*

The cobra wave is a popular physical phenomenon arising from the explosion of a metastable grillage made of popsicle sticks. The sticks are expelled from the mesh by releasing the elastic energy stored during the weaving of the structure. Here we analyze both experimentally and theoretically the propagation of the wave front depending on the properties of the sticks and the pattern of the mesh. We show that its velocity and its shape are directly related to the recoil imparted to the structure by the expelled sticks. Finally, we show that the cobra wave can only exist for a narrow range of parameters constrained by gravity and rupture of the sticks.

The physics of metastable states is a classical topic of statistical physics [1,2]. A well-known route to relax towards equilibrium is via a nonlinear front that propagates with a constant speed, such as in viral spread [3,4], biochemical reactions [5], or combustion [6,7]. In mechanics, the domino race provides an example of such a process for a nonconnected network [8,9]. For entangled structures, the question of the optimization of the strength of grillages has been addressed [10,11] especially because of its role in construction [12], but their stability remains an open question. The same type of question also arises in biological systems, such as in the microtubule catastrophe [13,14]. Microtubules are assemblies of GDP tubulin arranged in a tubular shape ending with a cap of GTP tubulin. The loss of this cap triggers a rapid depolymerization driven by the release of the stored mechanical strain [15–17]. Here we study a macroscopic version of such a system, namely, the so-called "popsicle-stick cobra wave" [18], obtained by releasing a mesh of sticks woven according to Fig. 1(b).

To generate a cobra wave, the whole structure is loaded by the geometrically constrained bending of the individual sticks and is held together by the red and blue sticks at the end of the mesh [see Fig. 1(b)]. When one of them is removed, the structure unravels by expelling one by one the freed sticks. Because of the asymmetry of the weaving and the presence of the ground, two very different dynamics occur depending on which stick was initially removed. When the red stick is taken away first, the sticks are expelled upwards and by reaction they pin down the rest of the mesh to the ground (see movie Inverse-Cobra-Wave in the Supplemental Material [19]). The outcome is dramatically different when the blue stick is removed. In this case, the sticks are expelled downwards and they raise the whole structure as presented in Fig. 2(a) (see also the movie Cobra-Wave provided in Ref. [19]). After a few hundreds of ms, the shape of the wave reaches a steady state

[Fig. 2(b)], and propagates at a few meters per second. Both the shape and the velocity remain the same until the wave front reaches the end of the grillage [Fig. 2(c)]. In this Letter, we combine experimental and theoretical approaches to characterize the velocity and the shape of the cobra wave in the steady state.

Since the lifting force raising the lattice originates from the recoil imparted by the expelled sticks, the global dynamics of the wave is set by the ejection rate γ and the momentum transferred during the expulsion Mv, where M is the mass of a stick and v the velocity of a stick right after expulsion. The time γ^{-1} taken by a stick to exit the mesh is given by L/v, where L is the length of the stick [Fig. 1(a)]. Taking E the Young's modulus, w the width, and e the thickness of individual sticks [Fig. 1(a)], v can be estimated from the balance between the kinetic energy Mv^2
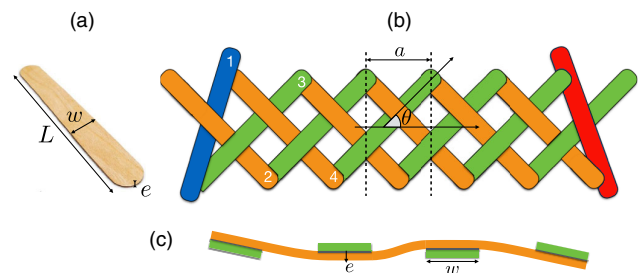

FIG. 1.   (a) Picture of a wooden stick with its characteristic parameters: length L, width w, thickness e, mass M, density ρ and Young's modulus E. (b) Schematics of the lattice with definition of the angle θ of the lattice and the spatial period a of the pattern. The blue and red sticks are the sticks that end the lattice. The construction of the lattice starts with the blue stick, then the sticks are added one after the other according to the numbering for the first four sticks. (c) Schematic side view of a stick deformed in the mesh.
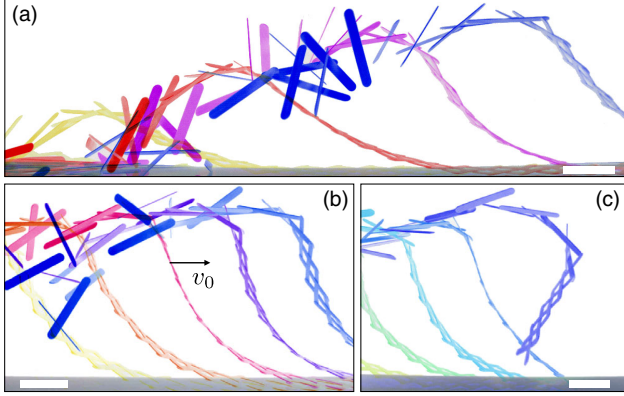
FIG. 2.   Time-lapse photographs of the cobra wave obtained with sticks of type 1 (see the Supplemental Material [19]) for $\theta = 45°$, from videos taken at 1000 fps with a Photron-Fastcam high-speed camera. The different colors represent the wave at different instants. (a) At the beginning ($\Delta t = 100$ ms between two consecutive images); (b) during the stationary phase ($\Delta t = 70$ ms), with $v_0 \simeq 2.2$ m/s the velocity of the wave front; (c) at the end ($\Delta t = 70$ ms). Scale bars are 10 cm long.

of a stick after ejection and the bending energy $E_{el} \sim Ewe^5/L^3$ stored in each stick blocked by the lattice [this expression is obtained by noting that the curvature of a stick imposed by its neighbors is $\Gamma \sim e/L^2$, see Fig. 1(c)].

From the previous scaling analysis, we readily deduce the velocity v_0 of the wave front. Indeed, since the sticks are expelled one by one, we have $v_0 = a\gamma/2$, where a is the spatial period of the pattern [Fig. 1(b)]. Noting that, up to a geometric factor depending on the angle θ, we have $a \propto L$, both v and v_0 scale as

$$v \sim v_0 = b(\theta)\sqrt{\frac{E}{\rho}}\left(\frac{e}{L}\right)^2, \qquad (1)$$

where ρ is the mass density of a stick and $b(\theta)$ is a scaling factor that depends on the geometry of the mesh. With $c = \sqrt{E/\rho}$ the speed of sound in the material, we find that $v_0 \propto c(e/L)^2$. In Fig. 3, we confirm experimentally this scaling for six kinds of wooden sticks (the values of the mechanical and geometric parameters of the different stick models are given in Ref. [19]) and we observe that indeed $v \propto v_0$. As expected, the speed does not depend on the width of the sticks and increases quadratically with the ratio e/L. In Fig. 3(i), one can see that the speed of the cobra decreases with the angle of the lattice θ. This trend can be easily understood qualitatively by noting that the velocity of the wave is proportional to the spatial periodicity $a = L \cos\theta/3$.

We now focus on the shape of the wave. The height of the cobra can be understood quantitatively within a generalized version of Euler's elastica theory, where the mesh profile results from a competition between elasticity,
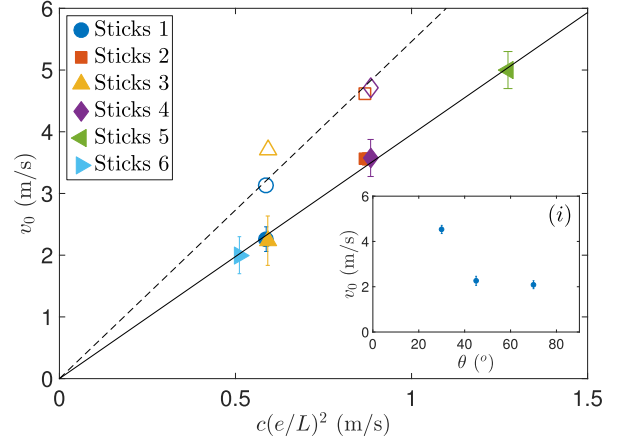

FIG. 3.   Speed of the wave front v_0 (solid dots) and speed of the expelled sticks v (open dots) as a function of a characteristic speed $c(e/L)^2$ for $\theta = 45°$ and six different kinds of sticks (see the Supplemental Material [19]). The black line corresponds to the fit $v_0 = 3.95c(e/L)^2$ and the dashed line to the fit $v = 5.46c(e/L)^2$. (i) Speed of the cobra wave v_0 as a function of the angle of the lattice θ for sticks of type 1.

gravity, and recoil imparted by the expelled sticks [20]. We treat the mesh as a linear continuous medium characterized by a flexion modulus $\bar{K}$ [19] and we describe the expulsion of the sticks by a force F_0 and a torque C_0 exerted at the free end of the grillage. We further assume that the friction between sticks prevents the deformation of the lattice, allowing us to describe the mesh as an inextensible linear medium described by a profile $r(s,t)$, where s is the curvilinear abscissa (Fig. 4), the local force $F(s,t)$ and torque $C(s,t)$ are given by

$$F = -\bar{K}\partial_s^3 r, \qquad C = \bar{K}\partial_s r \times \partial_s^2 r. \qquad (2)$$

In the steady state, the shape of the cobra is constant and moves at the velocity v_0. We therefore have $r(s,t) = r(s' = s - v_0 t)$ and writing Newton's law for an infinitesimally small element of the mesh leads to the following dynamical equation,

$$\mu v_0^2 \partial_{s'}^2 r = \mu g - \bar{K}\partial_{s'}^4 r + \partial_{s'}(T\tau) + R, \qquad (3)$$

where $\mu = 2M/a$ is the linear mass density of the cobra, T the longitudinal tension, τ the tangent unit vector, and R the ground reaction. We assume that the contact with the ground occurs for $s' \leq 0$, so that $z(s' \leq 0) = 0$ and $R(s' \geq 0) = 0$, and s_{max} is the total mesh length rising above the ground. Projecting Eq. (3) on the tangent and normal directions, these equations can be recast into a closed equation for the curvature $\Gamma = |\partial_s^2 r|$,

$$\frac{1}{2}\left(\frac{d^3\Gamma^2}{d\alpha^3} + \frac{d\Gamma^2}{d\alpha}\right) = \frac{\mu g}{\bar{K}}\left(\frac{2\sin\alpha}{\Gamma} + \frac{\cos\alpha}{\Gamma^2}\frac{d\Gamma}{d\alpha}\right), \qquad (4)$$
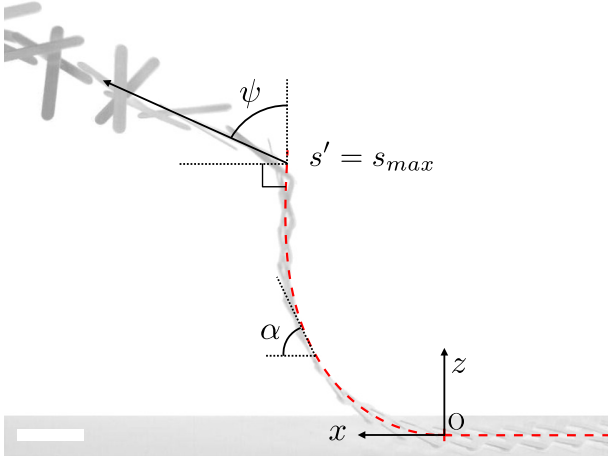
FIG. 4. Experimental cobra profile for sticks of type 2. The steady profile (red dashed line) is described theoretically by a parametric curve $\boldsymbol{r}(s')$, where s' is the curvilinear abscissa. α is the angle between the mesh and the horizontal axis, and ψ the angle between the velocity of the expelled sticks and the tangent vector in $s' = s_{\max}$. The scale bar is 10 cm long.

where α is the local angle between the mesh and the horizontal axis.

This equation is of third order in α and thus requires three boundary conditions to be solved. We obtain these conditions by writing the stress at the free end $\alpha_{\max} = \alpha(s_{\max})$ of the mesh, namely,

$$C_0 = \bar{K}\Gamma, \tag{5}$$

$$F_\parallel = T + \bar{K}\Gamma^2, \tag{6}$$

$$F_\perp = -\frac{K}{2}\frac{d\Gamma^2}{d\alpha}, \tag{7}$$

where $F_\parallel = \boldsymbol{F}_0 \cdot \boldsymbol{\tau}$ and $F_\perp = \boldsymbol{F}_0 \cdot \boldsymbol{n}$ and the right-hand side terms are taken at $\alpha = \alpha_{\max}$. A fourth condition is required by the fact that, contrary to the elastica problem where the length of the beam is fixed, we must here determine self-consistently the mesh length rising above the ground. To close the system, we, therefore, impose the usual mobile contact-point condition $\Gamma(\alpha = 0) = 0$ that assumes that there is no adhesion energy between the mesh and the ground [21].

On the one hand, the forces can be calculated from the momentum transfer between the lattice and the expelled sticks and we have $F_\perp = \mu v_0 v \sin\psi$ and $F_\parallel = \mu v_0(v_0 - v\cos\psi)$.

On the other hand, the torque exerted at the free end of the cobra can be neglected. Indeed, assuming that all the elastic energy $E_{\rm el}$ is converted into rotational energy of the sticks $E_{\rm rot} = \frac{1}{2}I\omega^2$ with I the moment of inertia of a stick and ω its angular velocity, the angular momentum of an expelled stick is $\mathcal{L} = I\omega = \sqrt{2IE_{\rm el}}$. Since the torque is

$C = (d\mathcal{L}/dt) \sim \gamma\mathcal{L}$, we get the upper bound $C_{\max} \sim \gamma\sqrt{2IE_{\rm el}}$. In Eq. (6), the torque is compared to $\bar{K}\Gamma$. Using Eq. (5), we can eliminate Γ and we see that the relative importance of the torque and the force is driven by the dimensionless number

$$\frac{C^2}{\bar{K}F} \simeq \frac{\gamma^2 I(Ke^2/L^3)}{K\gamma M v_0} \simeq \left(\frac{e}{L}\right)^2 \ll 1,$$

where $K \sim \bar{K}$ is the flexion modulus of a single stick [19] and we have used the fact that $v \sim v_0 \sim \gamma L$ and $I \sim ML^2$. We thus see that for thin sticks, the torque does not affect much of the shape of the cobra.

Equation (4) can be solved numerically in the general case using the shooting method and the height of the cobra can be obtained from

$$H = \int_0^{\alpha_{\max}} \frac{\sin\alpha}{\Gamma(\alpha)} d\alpha. \tag{8}$$

The analysis of Eqs. (4)–(9) shows that H follows the general scaling

$$H = \sqrt{\frac{\bar{K}}{\mu v_0 v}} h_\psi(\Lambda), \quad \text{with} \quad \Lambda = g\sqrt{\frac{\bar{K}}{\mu v_0^3 v^3}}.$$

When gravity can be neglected, Eq. (4) can be solved analytically and yields $\Gamma = \Gamma_0\sqrt{\cos(\psi - \alpha) - \cos(\psi)}$ with $\Gamma_0 = \sqrt{2\mu v v_0/\bar{K}}$. We then obtain $\alpha_{\max} = 2\psi$ and the dimensionless height can be expressed in terms of the elliptic integrals $\mathcal{E}$ and $\mathcal{K}$ [22] with

$$h_\psi(0) = 2\sin(\psi)\{2\mathcal{E}[\sin(\psi/2)] - \mathcal{K}[\sin(\psi/2)]\}. \tag{9}$$

For large values of Λ, gravity becomes dominant and the cobra does not rise as high. In this regime, $\alpha_{\max} \to 0$ and we can therefore neglect the lower order derivatives in each sides of Eq. (4) leading to the simplified expression

$$\frac{d^3\Gamma^2}{d\alpha^3} = \frac{2\mu g}{\bar{K}\Gamma^2}\frac{d\Gamma}{d\alpha}. \tag{10}$$

This equation can be solved analytically leading to an asymptotic behaviour $h_\psi \simeq 2\sin^4\psi/3\Lambda^3$.

The asymptotic behaviors obtained in both the weak and strong gravity regimes can be understood by a straightforward argument. We note first that Eqs. (7) and (8) lead to the following scalings:

$$F_\perp \simeq \bar{K}\frac{\Gamma_0^2}{\alpha_{\max}}, \qquad H \simeq \frac{\alpha_{\max}^2}{\Gamma_0}. \tag{11}$$

We can then distinguish two regimes. For small g, the height is saturated and $\alpha_{\max} \simeq 1$, hence, $\Gamma_0 \simeq \sqrt{F_\perp/\bar{K}}$ and
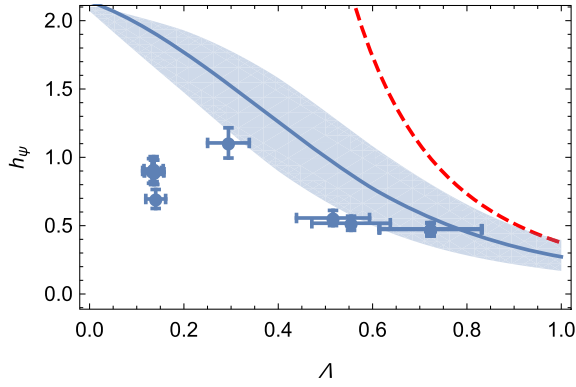
FIG. 5. Dimensionless height h_ψ as a function of the dimensionless number $\Lambda = g\sqrt{\bar{K}/(\mu v_0^3 v^3)}$ which compares gravity and elasticity, for the six different kinds of sticks (see the Supplemental Material [19]). The solid line corresponds to the prediction of Eqs. (4)–(9) for $\psi = 60°$. The shaded band corresponds to the observed 10° variations of the ejection angle. The red dashed line represents the large Λ expansion $h_\psi \simeq 2\sin^4\psi/3\Lambda^3$ for $\psi = 60°$.

$H \simeq \Gamma_0^{-1} \simeq \sqrt{\bar{K}/F_\perp}$. The scaling for H yields the condition $h_\psi \simeq 1$ for weak gravity. Using Eq. (1), we can express v_0 and $F_\perp$ with K, e, and L. We then obtain a simple scaling for $H \simeq L^2/e$, which does not depend any more on the elasticity of the mesh. This purely geometric scaling stems from the fact that, when gravity is negligible, stick elasticity provides both the thrusting and restoring forces responsible for the shape of the mesh.

For heavy sticks, the lattice is almost horizontal and the value of α_{max} is set by the balance between $F_\perp$ and the weight. The length of the cobra being $s_{max} \simeq \alpha_{max}/\Gamma_0$, we have thus the additional condition

$$F_\perp \simeq \frac{\mu g \alpha_{max}}{\Gamma_0}. \tag{12}$$

Combining Eqs. (11) and (12) yields the condition $\alpha_{max} \simeq \Lambda^{-2}$ and $h_\psi \simeq 1/\Lambda^3$. The transition between the two regimes occurs for $\Lambda \simeq 1$.

We now compare the previous model to our measurements. We measured the velocity v and the angle ψ at which the sticks are expelled. We observe that for almost all stick models, ψ varies between 50° and 70°. In Fig. 5, we compare our measurements to the predicted value $h_{\psi=60°}$ without any adjustable parameter (note in particular that the effective flexion modulus of the mesh is measured independently as described in Ref. [19]). Except in the weak-gravity regime, we observe a relatively good agreement between experiment and theory. We attribute the saturation of the height of the cobra wave for small Λ to the strong curvature of the mesh (in this regime the radius of curvature is only a few times larger than stick length), leading to a breakdown of the underlying assumptions of the theoretical
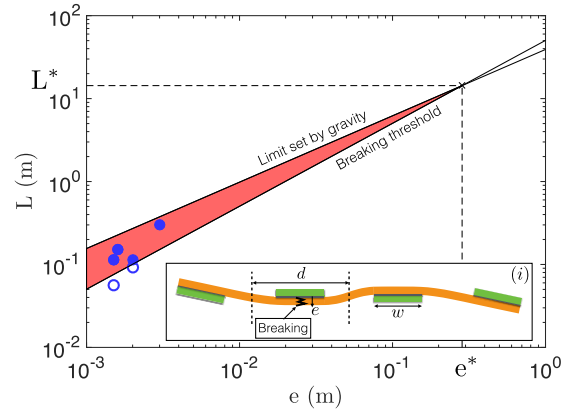

FIG. 6. Set of parameters (e, L) for which a cobra stick wave can be observed (red region). This region is limited by two conditions given in Eqs. (13) and (15): the limit set by gravity $L_{max} = (36Ee^4/\rho g)^{1/5}$ and the breaking limit $L_{min} = 1.5 \times 3\sqrt{E/\sigma^*}e$. Solid blue dots: sets of parameters for which the cobra-stick wave is observed. Open blue dots: sets of parameters for which the cobra-stick wave could not be observed (the sticks are too small and therefore break). (i) Schematics of the shape of a stick in the lattice with the most probable breaking region.

model. For instance, the validity of the continuum approximation for the description of the mesh, or the linear approximation for the bending energy. Friction can also play a larger role, and the strong deformation can weaken the structure, preventing it from reaching its predicted height.

Finally, we discuss the condition of existence of the cobra wave. The first requirement is that the curvature energy stored in a single stick ($E_{el} = 18Ewe^5/L^3$) should overcome the gravitational energy ($E_g = \rho gweL^2/2$). This leads to an upper bound for the length L of the sticks:

$$L < L_{max} = \left(\frac{36Ee^4}{\rho g}\right)^{1/5}. \tag{13}$$

However, the length L of the sticks cannot be too small because if so it becomes impossible to build the lattice: the sticks either break or slide over each other destroying the lattice. The breaking condition is derived from a simple scaling law for the bending stress in a beam that sets an upper limit for the curvature of a stick in the lattice [Fig. 6(i)],

$$\mathcal{C} \sim \frac{e}{d^2} < \frac{\sigma^*}{Ee}, \tag{14}$$

where the length $d = (L - w)/3$ is defined in Fig. 6(i) and σ^* is the bending stress at rupture of the material. We then get a lower bound for the length L of the sticks

$$L > L_{min} \sim 3\sqrt{\frac{E}{\sigma^*}}e + w. \tag{15}$$

For wooden sticks, these two conditions set the boundaries of the cobra-wave region of existence. The phase diagram (e, L) is plotted in Fig. 6 with the region of existence of the cobra stick wave in red, assuming the width w to be negligible compared to the length L of the sticks.

In conclusion, we have shown that the shape of the popsicle-stick cobra wave was the result of a competition between the thrust provided by the expulsion of the sticks and the elastic and gravitational restoring forces. Depending on the relative importance of gravity, we identified two asymptotic regimes. In particular, for negligible gravity, the cobra rises at a height which is solely set by the weaving pattern and the dimensions of single sticks. Finally, we showed that the Cobra wave can only exist in a narrow region of the parameter space bounded by gravity and rupture of the sticks.

[1] L. D. Landau and E. M. Lifshitz, *Statistical Physics*, Vol. 5 (Pergamon Press, New York, 1980).

[2] J. S. Langer, Statistical theory of decay of metastable states, Ann. Phys. (N.Y.) **54**, 258 (1969).

[3] R. A. Fisher, The wave of advance of advantageous genes, Ann. Hum. Genet. **7**, 355 (1937).

[4] A. Kolmogoroff, I. Petrovsky, and N. Piscounoff, Study of the diffusion equation with growth of the quantity of matter and its application to a biological problem, Moscow Univ. Math. Bull. **1**, 1 (1937).

[5] J. D. Murray, *Mathematical Biology* (Springer, New York, 2000).

[6] Ya. B. Zeldovich, G. I. Barenblatt, V. B. Librovich, and G. M. Makhviladze, *The Mathematical Theory of Combustion and Explosions* (Consultants Bureau, New York, 1985).

[7] P. Clavin and G. Searby, *Combustion Waves and Fronts in Flows* (Cambridge University Press, Cambridge, England, 2016).

[8] W. J. Stronge, The domino effect: A wave of destabilizing collisions in a periodic array, Proc. R. Soc. A **409**, 199 (1987).

[9] W. J. Stronge and D. Shu, The domino effect: Successive destabilization by cooperative neighbours, Proc. R. Soc. A **418**, 155 (1988).

[10] G. I. N. Rozvany, Grillages of maximum strength and maximum stiffness, Int. J. Mech. Sci. **14**, 651 (1972).

[11] T. Tarnai, Duality between plane trusses and grillages, Int. J. Solids Struct. **25**, 1395 (1989).

[12] P. M. Stylianidis, D. A. Nethercot, B. A. Izzuddin, and A. Y. Elghazouli, Robustness assessment of frame structures using simplified beam and grillage models, Engineering structures **115**, 78 (2016).

[13] I. M. Cheeseman and A. Desai, Molecular architecture of the kinetochore–microtubule interface, Nat. Rev. Mol. Cell Biol. **9**, 33 (2008).

[14] A. Desai and T. Mitchison, Microtubule polymerization dynamics, Annu. Rev. Cell Dev. Biol. **13**, 83 (1997).

[15] T. Mitchison and M. Kirschner, Dynamic instability of microtubule growth, Nature (London) **312**, 237 (1984).

[16] T. Mitchison and M. Kirschner, Microtubule assembly nucleated by isolated centrosomes, Nature (London) **312**, 232 (1984).

[17] H. Bowne-Anderson, A. Hibbel, and J. Howard, Regulation of microtubule, growth and catastrophe: Unifying theory and experiment, Trends Cell Biol. **25**, 769 (2015).

[18] https://en.wikipedia.org/wiki/Stick_bomb.

[19] See Supplemental Material at http://link.aps.org/supplemental/10.1103/PhysRevLett.119.084301 containing two movies describing the dynamics of the mesh, as well as the physical parameters of the sticks used in our study and the experimental characterization of the effective modulus of the mesh.

[20] B. Audoly and Y. Pomeau, *Elasticity and Geometry: From Hair Curls to the Non-Linear Response of Shells* (Oxford University Press, New York, 2010).

[21] R. Burridge and J. B. Keller, Peeling, slipping and cracking—some one-dimensional free-boundary problems in mechanics, SIAM Rev. **20**, 31 (1978).

[22] M. Abramowitz and I. A. Stegun, *Handbook of Mathematical Functions: With Formulas, Graphs, and Mathematical Tables* (Courier Corporation, 1964).

Supplementary materials

I. CHARACTERISTICS OF THE STICKS

We obtained the Young's modulus E of our wooden sticks through measurements of the load on a force sensor for given deflections of the sticks and we found $E \simeq 15\,\mathrm{GPa}$. The bending stress at rupture of the sticks $\sigma^* \simeq 120\,\mathrm{MPa}$ was estimated experimentally through a three-point flexural test.

Sticks	L (mm)	w (mm)	e (mm)	M (g)
1	150	18.0	1.6	2.64
2	114	14.3	1.5	1.45
3	150	9.0	1.6	1.30
4	114	7.0	1.5	0.70
5	113	9.0	2.0	1.23
6	150	17.0	1.5	2.45
7	56	7.0	1.5	0.25
8	93	9.0	2.0	1.02

TABLE I: Geometrical and mechanical properties of the wooden sticks used in this study. Sticks 7 and 8 are sticks for which the cobrastick wave was not observed.

II. ELASTIC MODULUS OF THE MESH

The elastic properties of the mesh are described by a bending energy

$$E_{\mathrm{el}} = \frac{\bar{K}}{2} \int \Gamma(s)^2 \, \mathrm{d}s, \qquad (1)$$

where Γ is the local curvature of the mesh and $\bar{K}$ the effective bending modulus. $\bar{K}$ is determined experimentally by measuring the load on a force sensor for given deflections of the mesh. In Fig. 1, we plot the measured value $\bar{K}$ normalized by the bending modulus of a single stick $K = EI_\perp$ (where $I_\perp = we^3/12$ is the second moment of area) as a function of the weaving angle θ. For $\theta = \pi/4$, we find in particular $\bar{K} \simeq 0.7K$. Assuming that the sticks are simply wrapped with an angle θ on a cylinder of radius Γ^{-1}, one obtains $\bar{K} = 3K \cos(\theta)^3$. This scaling is close to the fitted behaviour $\bar{K}/K = k_0 \cos(\theta)^3$, with $k_0 = 2.2$. The discrepancy with the expected value $k_0 = 3$ may come from the torsion of the sticks in the mesh or from the fact that even in the absence of macroscopic bending of the mesh, individual sticks are already bent by the weaving of the mesh.
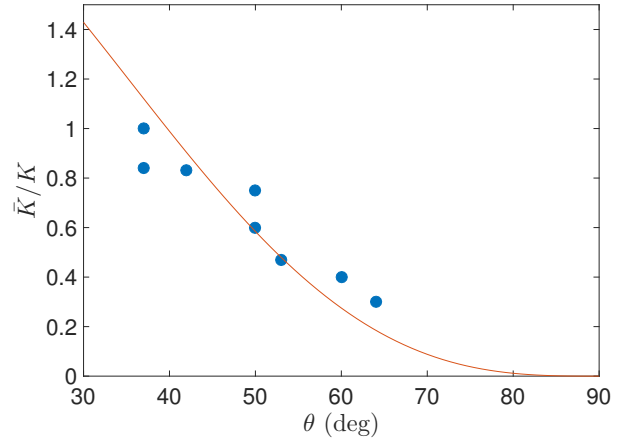

FIG. 1: Normalized bending modulus of the mesh $\bar{K}/K$ as a function of the weaving angle θ obtained experimentally by measuring the force on a load cell for imposed deflections of the mesh. Solid line: fit of the data using the theoretical function $\bar{K}/K = k_0 \cos(\theta)^3$ with $k_0 = 2.2$, close to the expected value $k_0 = 3$ derived from a purely geometric argument.

QUICK STUDY

Jean-Philippe Boucher and **Romain Labbé** are PhD students in fluid mechanics at the laboratory of hydrodynamics (LadHyX) at the École Polytechnique in Paris. **Christophe Clanet** is a CNRS research director at LadHyX.

Row bots

Jean-Philippe Boucher, Romain Labbé, and Christophe Clanet

By dipping their oars into the water asynchronously, a rowing crew can reduce the friction on their racing shell. Experiments with robots determine whether that trick increases the boat's speed.

Rowing is a challenging sport, and not just for athletes. It mixes physiology, mechanics, and fluid dynamics, so from a physicist's perspective, the sport is much more complex than the elegant movement of a rowing shell might suggest.

Many scientists have tried to work out the details of rowing propulsion, often with a view to improving the performance of rowing crews. For example, in a 1971 *Science* paper (volume 173, page 349), Thomas McMahon showed that the speed of a racing boat scales as the number of rowers to the power 1/9. In our research, we have taken a closer look at the boat speed within one rowing cycle. In a single stroke, a propulsive phase is followed by a gliding phase. As the figure shows, for racing boats, the variation in speed during the stroke is typically around 20% of the mean speed of 5 m/s or so. Such a variation is a consequence of the synchronized rowing of the crew, a technique that seems to be essential for success in top-level rowing competitions. Consider, however, that for a boat moving through water, larger fluctuations about the boat's average speed imply increased friction on the hull. As a consequence, the mean power dissipated due to fluid friction for speed variations typical of a racing boat is about 5% higher than it would be if the boat could somehow be propelled steadily at the same mean speed.

Desynchronizing the rowers can reduce speed variations. Nature employs an out-of-sync propulsion strategy in, for example, shrimp-like krill that swim with the so-called metachronal movement of five pairs of legs that are activated in a desynchronized way. Indeed, a 2010 study by Silas Alben and colleagues published in the *Journal of the Royal Society Interface* (volume 7, page 1545) showed that the krill's metachronal kinematics leads to the highest average body velocity for a given amount of work. Some fishing spiders also display unsynchronized swimming at the surface of water. Given that in rowing competitions, 2 km races are often won by less than a boat length, it's worth considering the possible advantage of unsynchronized rowing.

Row, rOw, roW your boat

Phase-shifted rowing had been tried as early as 1929, by the London Rowing Club; you can see a video of the effort at www.youtube.com/watch?v=zQ6fxsmo3V8. But the London club's exercise and others conducted in the UK during the early 1930s led to indecisive results. As one reporter for the *Sydney Morning Herald* mused on 11 October 1933, the experiments raised the question of "whether the trifling gain is worth the loss of all the rhythm, apart from neutralising the genius of strokeship." At the 1981 and 1982 World Rowing Championships, the Soviet women's coxed four crew placed the coxswain (the person who steers the boat) between the two pairs so that they could row perfectly out of phase. However, on race days the crew chose to row in synchrony. Despite the full-scale trials and other studies, out-of-phase techniques never have convincingly been shown to be more or less efficient than conventional synchronized rowing.

To perform a systematic study of the influence of rower synchronization on boat speed, we built a boat at 1/10 scale with eight robotic rowers. A real racing boat with eight rowers, known as a coxed eight, has a length of about 20 m and weighs about 100 kg. Our 2-m-long model, shown in panel c of the figure, has a fiberglass hull with the same shape as on a real coxed eight. The mass ratio of robot rower to model boat is the same as for human rowers and racing boats, and we designed the mechanics of the robotic rowing to be as human as possible. With the help of a device called an Arduino board, we were able to control the stroke speed and synchronization of our robot rowers.

Which strategy is best?

We measured the speed of our rowing boat at the swimming pool of the École Polytechnique and explored how it changed as we varied the phase difference ϕ between consecutive rowers. Panel d of the figure shows the results for two of our trials, which you can view in the supplemental videos available online. In the synchronous configuration, $\phi = 0°$, the velocity profile of our boat is similar to the one obtained from videos of real rowing races (as in figure panel b). The speed increases during the power stroke, from a black vertical line to a red one in the figure plots, due to the propulsion given by the oar blades. During the recovery stroke, from red line to black line, the speed decreases, partly due to the hydrodynamic friction on the hull. The similarity of the velocity profiles proves that our model boat does a good job of imitating real rowing boats.

At a pace of one stroke per second, our boat moves at a mean speed close to 0.36 m/s, almost 0.2 boat length per rowing cycle. By means of comparison, real race boats travel roughly 0.45 boat length per rowing cycle in competitions. As with real boats, our model displayed large variations around its average speed—approximately 12% of the mean.
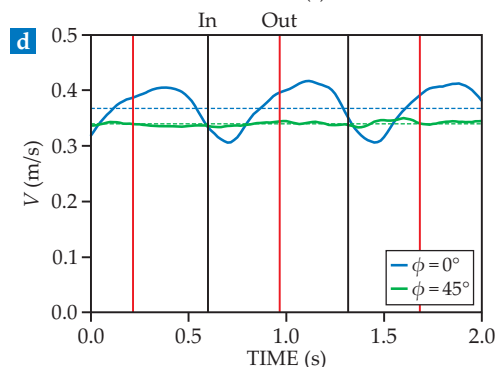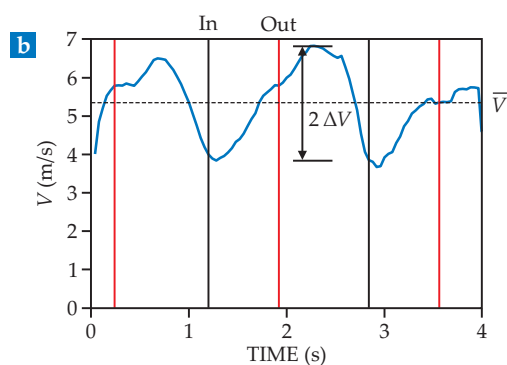
ROWING IN AND OUT OF SYNC. Great Britain holds a slim lead over Australia **(a)** halfway toward its victory in the men's four rowing final at the London 2012 Olympics. **(b)** The velocity V of the British boat was determined from a video of the race. The black vertical lines in the plot indicate the times at which the blades enter the water, and the red vertical lines indicate the times at which the blades are lifted out. The mean speed of the boat $\overline{V}$, about 5.3 m/s, fluctuates by about 20%, as indicated by ΔV. **(c)** Robots row a 2-m-long boat at the École Polytechnique swimming pool. **(d)** The robots were able to row synchronously ($\phi = 0°$) or asynchronously; in the out-of-sync trial plotted, each robot is 45° out of phase with its neighbor. As we expected, relative fluctuations were reduced for asynchronous rowing, but we were surprised to learn that the mean speed (indicated by dashed lines) was also reduced.

For phase-shifted rowers, we show $\phi = 45°$ in the figure panel and supplemental video. The bots row one after the other to propel the boat, and when the last rower on the boat finishes its power stroke, the first one starts anew. In this case the instantaneous velocity profile displays much less speed variation than in the synchronized case: about 2% of the approximately 0.34 m/s mean speed. The diminished fluctuations were expected, but we were surprised and initially puzzled that the mean speed of our boat was also reduced—by about 5%. We repeated our experiments for many phase differences spanning the range 0°–360°. Although the quantitative values varied, we found that compared with synchronized rowing, desynchronized rowing always decreases both the relative fluctuations and the mean speed.

Another propulsive mechanism

Our main result thus contradicts our initial intuition that reducing velocity fluctuations would increase the mean velocity. So, luckily for rowing athletes who have trained to row synchronously, we can confirm the commonly accepted wisdom that rowing together maximizes speed.

In our initial thinking, we failed to take into account that the rowers are not stationary. Indeed, if you return to the velocity profiles in figure panels b and d, you'll see that the speed in the synchronized configuration keeps increasing at the beginning of the recovery stroke—that is, after the oars have been lifted from the water, as indicated by the red lines. If the velocity keeps increasing when the oars are out of the water, there must be an additional propulsive force that does not depend on oars. In fact, the force results from the motion of the rowers on the boat. When the rowers return together to the stern of the boat during the recovery stroke, they pull the hull beneath them and accelerate the boat. Since the crew of a coxed eight weighs several times what the boat does, the rowers generate a significant force. When they are desynchronized, that inertial boost is reduced.

For krill, whose tiny churning legs are always underwater, there is no such inertial boost effect. They do better with desynchronized propulsion.

Additional resources

▶ B. Sanderson, W. Martindale, "Towards optimizing rowing technique," *Med. Sci. Sports Exerc.* **18**, 454 (1986).
▶ A. Baudouin, D. Hawkins, "A biomechanical review of factors affecting rowing performance," *Br. J. Sports Med.* **36**, 396 (2002).
▶ A. J. de Brouwer, H. J. de Poel, M. J. Hofmijster, "Don't rock the boat: How antiphase crew coordination affects rowing," *PLOS One* **8**, e54996 (2013).
▶ V. Kleshnev, *The Biomechanics of Rowing*, Crowood Press (2016). **PT**

漕艇ロボット，ロウボット

ジャン＝フィリップ・ブーシェ，ロマン・ラッベ，クリストフ・クラネ

漕手たちがオールを水中に入れるタイミングをずらすことで，ボートに作用する摩擦力を減らすことができる。この試みでボートの速度を上げることができるかをロボットを使った実験によって検証する。

漕艇はスポーツとして興味深いが，それは競技者にとってだけではない。漕艇は生理学，力学，流体力学が混在した問題であり，物理学者の視点からみれば，ボートのエレガントな動きからは想像もつかないほど複雑な運動といえる。

オールをこぐことによる推進のメカニズムを明らかにしようと，多くの科学者たちが試みてきた。その多くは漕手のパフォーマンス向上を目的としたものである。たとえば1971年にScience誌（173巻349ページ）に掲載されたマクマホン（Thomas McMahon）の論文では，競艇用ボートの速度は漕手の人数の1/9乗に比例するとしている。私たちは今回，1サイクルのこぐ動きのなかでのボートの速度の変化に着目した。ひとこぎのなかで，ボートは推進状態からグライディング状態（慣性で進む状態）に入る。〈図1〉に示すように競

勝井辰博　訳

Row bots

Jean-Philippe Boucher, Romain Labbé and Christophe Clanet

Jean-Philippe Boucher and Romain Labbé are PhD students in fluid mechanics at the laboratory of hydrodynamics（LadHyX）at the École Polytechnique in Paris. Christophe Clanet is a CNRS research director at LadHyX.

技用ボートの場合，ひとこぎのあいだのボートの速度変化は平均速度5 m/sに対して20%程度である。このような変動は漕手のこぐ動きが同期した結果であり，トップレベルの競技で勝ち抜くためには，このテクニックが必須だといわれている。しかし考えてみると，ボートが水中を進むとき平均速度が大きく変動すると，より大きな摩擦力が船体に作用すると考えられる。結果として漕手のパワーは，ボートの速度変動にともなう摩擦抵抗の増加によって分散してしまう。典型的な競技ボートの場合，仮に同じ速度で一定の推進力で進むときに比べて，約5%大きな力が必要となる。

漕手の動きを同期させないことによって，ボートの速度の変動は抑えることができる。自然界では非同期の推進法を採用している例もある。たとえばオキアミは5組の足を使って，非同期のメタクロナル（metachronal）運動とよばれる方法で泳いでいる。2010年にJournal of the Royal Society Interface誌（7巻1545ページ）に掲載されたアルベン（Silas Alben）たちの論文では，オキアミはメタクロナル運動によって，一定の仕事量に対してもっとも速い体の移動が可能になることが示されている。ウオツリハシリグモのなかには，水面を移動するさいに非同期の泳ぎ方をするものもいる。漕艇の競技では2 kmのレースでもボートの長さ以内の差で勝敗が決まることがあるから，非同期のこぎ方の優位性を検証することには意義がある。

ボートをこごう

位相をずらした（タイミングをずらした）こぎ方は，すでに1929年ロンドンローイングクラブによって試みられている。この様子についてはユーチューブ https://www.youtube.com/watch?v=zQ6fxsmo3V8 で動画を視聴できる。しかしこのロンドンクラブの試みや1930年代初頭に英国で行われた同様の試みも，決定的な成功は収められなかった。1933年10月11日付のSydney Morning Herald紙は，以下のように報じた。「この実験によってわかったことは，『わずかな利益のために，才能ある漕手の技術を台なしにするだけでなく，すべてのリズムを崩す価値はあるのか』ということである」。1981年と1982年の世界漕艇選手権で，女子かじ付きフォア（coxed four，4人の漕手とコックスが同乗する競技）のソビエトチームはコックス（ボートを操る人）を漕手2人ずつのペアのあいだに配置した。そのため彼らは完全に非同期でこぐことができたが，レース当日は同期してこぐことを選択した。フルスケールでの試験やさまざまな研究が行われたにもかかわらず，従来型の同期するこぎ方よりも非同期のこぎ方が優れているかいないかについて，説得力ある説明はいまだなされていない。

漕手が非同期でオールをこぐとき，ボートの速度に与える影響を体系的に研究することを目的として，私たちは8体の漕手ロボットを搭載した1/10スケールのボートを製作した。漕手が8人のボート競技はかじ付きエイト（coxed eight，漕手8人の競技でコックスも同乗する）とよばれ，長さ20 m，重量は100 kgのボートを使用する。今回使用した〈図1c〉の長さ2 mのボート模型はグラスファイバー製で，かじ付きエイトと船の形状は同じである。ボート模型とロボット漕手の質量比は，レース
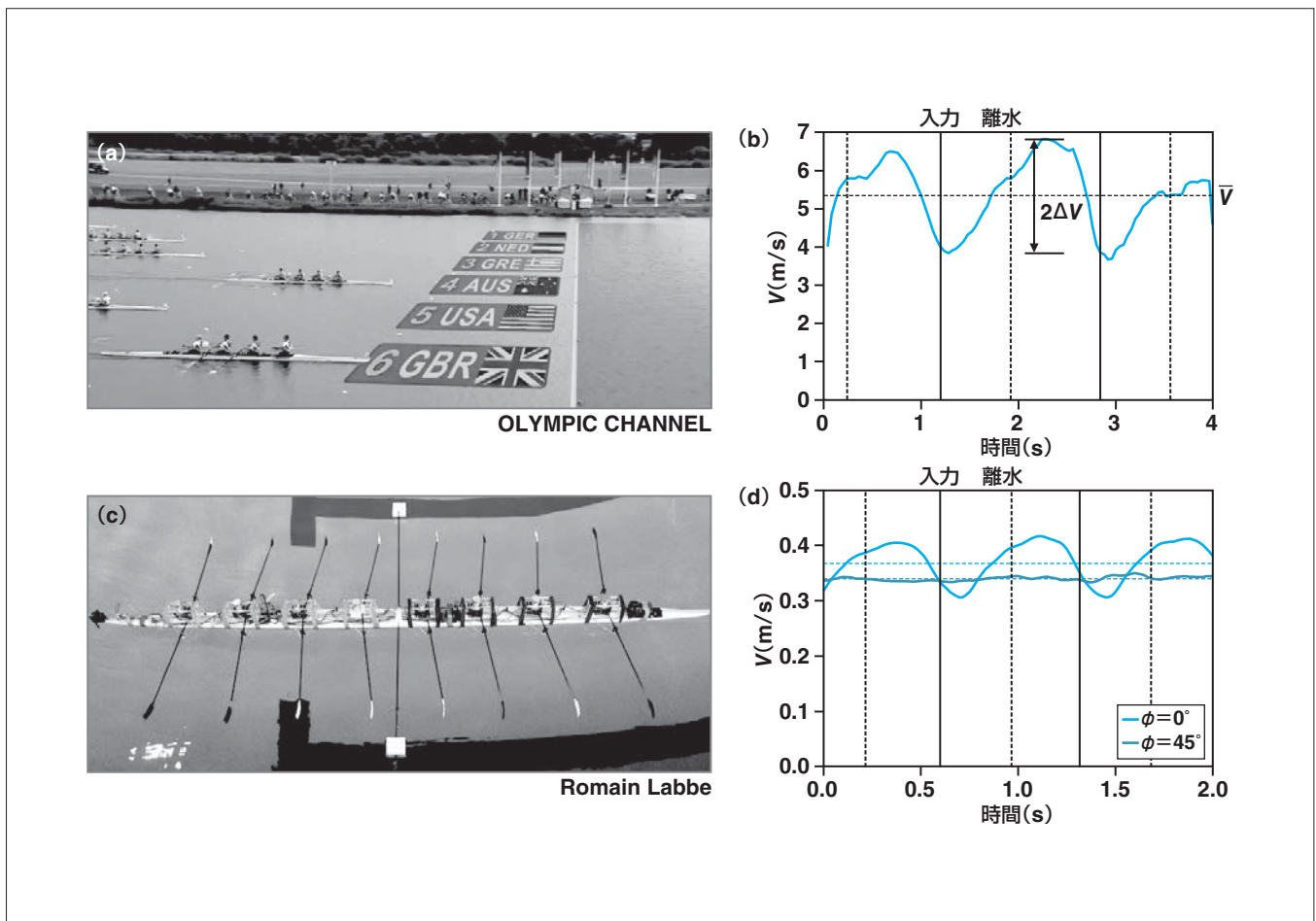
〈図1〉同期および非同期のこぎ方
英国チームがオーストラリアチームに対して僅差を守り切る。(a)2012年ロンドンオリンピックでの男子フォア決勝の終盤。(b)英国チームのボートの速度Vを，レースの動画から計測したもの。図中の縦の実線はオールが水中に入った時間，縦の破線はオールがもち上げられた時間を表す。ボートの平均速度は約5.3 m/s，図中にΔVで示した変動は平均値の約20％である。(c)エコールポリテクニークの水泳プールでロボット漕手が2 mのボート模型をこぐ様子。(d)ロボット漕手は同期（$\phi＝0$），または非同期でボートをこぐことができる。非同期の実験ではそれぞれの漕手ロボットは隣りに対して45°の位相差でこいでいる。期待したとおり，非同期のこぎ方ではボートの速度変動は減少した。しかし水平の破線で示した平均速度も，非同期のときは減少してしまうという結果に驚いた。

用ボートと人間の漕手と同じである。またロボット漕手の動きの機構は，人間の動きとできるかぎり同一にしてある。アルドゥイーノボード（Arduino board）とよばれる装置を使用することにより，漕手ボットのこぐ速度や同期を制御できるようになっている。

どちらの戦略がベストか？

私たちはエコールポリテクニークの水泳プールでロボット漕手ボートの速さを計測し，それぞれの漕手のこぐタイミングの位相差ϕをさまざまに変化させて，それがボートの速さに与える影響を調査した。〈図1d〉はそのうちの2種類の結果を示している。これらについては補足の動画をPhysics Today

のオンライン版でみることができる。同期状態でのこぎ方（つまり$\phi＝0$）では，模型ボートの速度の時間変化は〈図1b〉に示す，実際のレースでのボートの動画から得られる結果と同様になる。ボートの速度はオールのブレードによる推進力が作用しているあいだ，すなわちパワーストロークのあいだは増加する。これは図中の縦の実線から縦の破線までのあいだにあたる。リカバリーストローク，すなわちオールを空中に浮かせて後方にもどす，破線から実線までのあいだは速度が減少する。これは部分的には，ボートに作用する流体摩擦力に起因する。速度の変化の様子は，実際のボートもロボット漕手による模型ボートもよく似ており，模

型ボートは実際をよく模擬できていると判断できる。

1秒あたり1回こぐペースでは，模型ボートは平均で0.36 m/s程度の速度で動く。これは1こぎあたりボートの長さの約20％前進することになる。実際の競技時のレースボートと比較すると，こちらは1こぎあたりボート長さの45％程度進む。実際のボートと同様に，私たちの模型ボートも平均速度を中心に大きな時間変動を示す。その大きさはおおむね平均の12％程度である。

同期しないこぎ方をする場合，位相差ϕが45°のときの結果を〈図1〉と補足の動画で示す。このとき漕手ロボットは順々にボートを推進させ，最後の漕
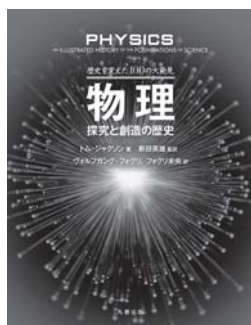
古代ギリシアの哲学から、2016年に報告された重力波の観測まで、物理学史に残る100の大発見を豊富な図版とともにビジュアルに紹介。発見の意義だけでなく、それに至る過程や、偉人たちの興味深いエピソードも多数掲載。

手がパワーストロークを終えたとき，先頭の漕手が次のパワーストロークに入る。この場合，ボートの速さは同期してこぐ場合に比べて変動が小さく，およそ0.34 m/sの平均速度に対して2％の変動にとどまる。速度変動の減少は期待どおりであったが，平均速度も5％減少してしまうという結果には驚き，また当初は困惑した。非同期の実験はさまざまな位相差（0°〜360°）でくり返し行った。しかし程度の差こそあれ，非同期の場合の平均速度と速度変動量は，同期したときと比較してつねに下回っていた。

別の推進メカニズム

このように私たちの実験結果は，速度変動を抑えれば，平均速度は上昇するはずだという，当初の直感を覆すものとなった。したがって，こぎ方を同期させるトレーニングを行ってきた漕艇競技者にとっては幸運なことに，同時にこぐことはボートの速度を最大化させるという一般常識を，この研究が裏づけることになった。

　私たちの当初の考えでは，漕手は動かずにこぎ続けるわけではないということを考慮していなかった。実際〈図1b, d〉をもう一度みてみるとわかるように，同期状態での速度はリカバリーストローク開始時，すなわちオールが水面からもち上げられた後（図中の縦の破線が示す位置）も増加していることがわかる。もしオールが水中にないときも速度が増加し続けているなら，オールに依存しない別の推進力が働いているはずである。実際，この力はボート上の漕手の運動に起因している。漕手がリカバリーストローク中に同時に後方にもどるとき，彼らは自分

たちの下にある船体を引っぱり，ボートを加速させている。かじ付きエイトのクルーの重量は船体重量の数倍なので，漕手の動きは有意な力を発生させる。非同期のこぎ方の場合，この慣性力が減少してしまう。

　オキアミの場合，小さくて激しく動く足がつねに水中にあるため，このような大きな慣性力の効果がなく，非同期運動による推進が功を奏するのである。

参考文献
1) B. Sanderson and W. Martindale: "Towards optimizing rowing technique," Med. Sci. Sports Exerc. **18**, 454（1986）.
2) A. Baudouin and D. Hawkins: "A biomechanical review of factors affecting rowing performance," Br. J. Sports Med. **36**, 396（2001）.
3) A. J. de Brouwer, H. J. de Poel and M. J. Hofmijster: "Don't rock the boat: How antiphase crew coordination affects rowing," PLOS One **8**, e54996（2013）.
4) V. Kleshnev: *The Biomechanics of Rowing*（Crowood Press, 2016）.

Bibliography

[1] Niels H Secher and Stefanos Volianitis. *Handbook of sports medicine and science, rowing.* John Wiley & Sons, 2009.

[2] Lionel Casson. *Ships and seamanship in the ancient world.* JHU Press, 1995.

[3] `https://en.wikipedia.org/wiki/Trireme`. Accessed: 2018-08-21.

[4] Luigi Tursini. Leonardo da Vinci and the problems of the navigation and naval design. *Trasactions del INA*, 95:97–102, 1953.

[5] Lars Larsson and Hoyte Raven. *Ship resistance and flow.* Society of Naval Architects and Marine Engineers, 2010.

[6] Johan Jong. Standvastigheid & verwachting: a historical and philosophical inquiry into standardization and innovation in design and production of the VOC retourschip during the 18th century. Master's thesis, University of Twente, 2010.

[7] John Henry Michell. XI. The wave-resistance of a ship. *The London, Edinburgh, and Dublin Philosophical Magazine and Journal of Science*, 45(272):106–123, 1898.

[8] Thomas Henry Havelock. The theory of wave resistance. *Proceedings of the Royal Society of London. Series A, Containing Papers of a Mathematical and Physical Character*, 138(835):339–348, 1932.

[9] `https://www.wikipedia.org/`. Accessed: 2018-08-21.

[10] Sighard F Hoerner. *Fluid-dynamic drag: practical information on aerodynamic drag and hydrodynamic resistance.* Hoerner Fluid Dynamics, 1965.

[11] `https://en.wikipedia.org/wiki/Seawise_Giant`. Accessed: 2018-08-21.

[12] `https://www.youtube.com/watch?v=-Pr4T5ClWEw`. Accessed: 2018-08-21.

[13] `https://en.wikipedia.org/wiki/Rowing_(sport)`. Accessed: 2018-08-21.

[14] Pijush K Kundu and Ira M Cohen. Fluid mechanics. *Academic, Calif*, 1990.

[15] Milton Van Dyke and Milton Van Dyke. An album of fluid motion. 1982.

[16] `https://www.nuclear-power.net/nuclear-engineering/fluid-dynamics/boundary-layer/velocity-boundary-layer-thermal-boundary-layer/`. Accessed: 2018-08-21.

[17] Hermann Schlichting and Klaus Gersten. *Boundary-layer theory.* Springer, 2016.

[18] JB Hadler. Coefficients for international towing tank conference 1957 model-ship correlation line. Technical report, David Taylor Model Basin Washington DC, 1958.

[19] Fabio Fossati. *Aero-hydrodynamics and the performance of sailing yachts: the science behind sailing yachts and their design.* A&C Black, 2009.

[20] Rolf Eliasson, Lars Larsson, and Michal Orych. *Principles of yacht design.* A&C Black, 2014.

[21] George Keith Batchelor. *An introduction to fluid dynamics.* Cambridge university press, 2000.

bib

[22] Elmar Achenbach. Influence of surface roughness on the cross-flow around a circular cylinder. *Journal of fluid mechanics*, 46(2):321–335, 1971.

[23] Elie Raphaël and Pierre-Gilles De Gennes. Capillary gravity waves caused by a moving disturbance: wave resistance. *Physical Review E*, 53(4):3448, 1996.

[24] William Thomson. On ship waves. *Proceedings of the Institution of Mechanical Engineers*, 38(1):409–434, 1887.

[25] Thomas Henry Havelock. Wave resistance: some cases of three-dimensional fluid motion. *Proceedings of the Royal Society of London. Series A, Containing Papers of a Mathematical and Physical Character*, 95(670):354–365, 1919.

[26] `https://wikiwaves.org/Ship_Kelvin_Wake`. Accessed: 2018-08-21.

[27] John Nicholas Newman. *Marine hydrodynamics*. MIT press, 2018.

[28] Ernest O Tuck. The wave resistance formula of JH Michell (1898) and its significance to recent research in ship hydrodynamics. *The ANZIAM Journal*, 30(4):365–377, 1989.

[29] Takao Inui. *Wave-making resistance of ships*. Society of Naval Architects and Marine Engineers, 1962.

[30] John V Wehausen. The wave resistance of ships. *Advances in applied mechanics*, 13:93–245, 1973.

[31] RB Chapman. Hydrodynamic drag of semisubmerged ships. *Journal of Basic Engineering*, 94(4):879–884, 1972.

[32] Ernest O Tuck. Wave resistance of thin ships and catamarans. *Applied Mathematics Report T8701*, 1987.

[33] A Sh Gotman. Study of Michell's integral and influence of viscosity and ship hull form on wave resistance. *Oceanic Engineering International*, 6(2):74–115, 2002.

[34] Michael Benzaquen, Alexandre Darmon, and Elie Raphaël. Wake pattern and wave resistance for anisotropic moving disturbances. *Physics of Fluids*, 26(9):092106, 2014.

[35] Alexandre Darmon, Michael Benzaquen, and Elie Raphaël. Kelvin wake pattern at large Froude numbers. *Journal of Fluid Mechanics*, 738, 2014.

[36] Pierre Lecointre. An analysis of wave-making resistance and wave interference of di-hull systems using wave height measurements. Master's thesis, University of California, Berkeley, 2015.

[37] John V Wehausen and Edmund V Laitone. Surface waves. In *Fluid Dynamics/Strömungsmechanik*, pages 446–778. Springer, 1960.

[38] Richard W Johnson. *Handbook of fluid dynamics*. CRC Press, 2016.

[39] Fuat Odar and Wallis S Hamilton. Forces on a sphere accelerating in a viscous fluid. *Journal of Fluid Mechanics*, 18(2):302–314, 1964.

[40] Lev D Landau and Evgeny M Lifshitz. *Course of theoretical physics. vol. 6: Fluid mechanics*. London, 1959.

[41] `https://www.youtube.com/watch?v=4CU8gYYkwSw`. Accessed: 2018-08-21.

[42] `http://www.filippiboats.com/eng`. Accessed: 2018-10-11.

bib

[43] Concept2. `https://www.concept2.com/oars`. Accessed: 2018-10-11.

[44] Marco Polin, Idan Tuval, Knut Drescher, Jerry P Gollub, and Raymond E Goldstein. Chlamydomonas swims with two "gears" in a eukaryotic version of run-and-tumble locomotion. *Science*, 325(5939):487–490, 2009.

[45] Kirsty Y Wan, Kyriacos C Leptos, and Raymond E Goldstein. Lag, lock, sync, slip: the many 'phases' of coupled flagella. *Journal of the Royal Society Interface*, 11(94):20131160, 2014.

[46] Thomas Steinmann, Maxence Arutkin, Précillia Cochard, Elie Raphaël, Jérôme Casas, and Michael Benzaquen. Unsteady wave pattern generation by water striders. *Journal of Fluid Mechanics*, 848:370–387, 2018.

[47] David L Hu, Brian Chan, and John WM Bush. The hydrodynamics of water strider locomotion. *Nature*, 424(6949):663, 2003.

[48] Robert B Suter, Oren Rosenberg, Sandra Loeb, Horatio Wildman, and John H Long. Locomotion on the water surface: propulsive mechanisms of the fisher spider. *Journal of Experimental Biology*, 200(19):2523–2538, 1997.

[49] Robert B Suter and Horatio Wildman. Locomotion on the water surface: hydrodynamic constraints on rowing velocity require a gait change. *Journal of Experimental Biology*, 202(20):2771–2785, 1999.

[50] Valery Kleshnev. *Biomechnanics of rowing*. The Crowood Press, 2016.

[51] `http://www.worldrowing.com/`. Accessed: 2018-10-11.

[52] Chris R Abbiss and Paul B Laursen. Describing and understanding pacing strategies during athletic competition. *Sports Medicine*, 38(3):239–252, 2008.

[53] Amandine Aftalion and J Frederic Bonnans. Optimization of running strategies based on anaerobic energy and variations of velocity. *SIAM Journal on Applied Mathematics*, 74(5):1615–1636, 2014.

[54] Nick Caplan, Anna Coppel, and Trevor Gardner. A review of propulsive mechanisms in rowing. *Proceedings of the Institution of Mechanical Engineers, Part P: Journal of Sports Engineering and Technology*, 224(1):1–8, 2010.

[55] Nicholas Caplan and Trevor N Gardner. A fluid dynamic investigation of the Big Blade and Macon oar blade designs in rowing propulsion. *Journal of sports sciences*, 25(6):643–650, 2007.

[56] Vladimir M Zatsiorsky and Nikolai Yakunin. Mechanics and biomechanics of rowing: a review. *International journal of sport biomechanics*, 7(3):229–281, 1991.

[57] David Cabrera, Andy Ruina, and V Kleshnev. A simple 1+ dimensional model of rowing mimics observed forces and motions. *Human movement science*, 25(2):192–220, 2006.

[58] S Serveto, S Barré, JM Kobus, and JP Mariot. A three-dimensional model of the boat-oars-rower system using ADAMS and LifeMOD commercial software. *Proceedings of the Institution of Mechanical Engineers, Part P: Journal of Sports Engineering and Technology*, 224(1):75–88, 2010.

[59] Joseph Hamill and Kathleen M Knutzen. *Biomechanical basis of human movement*. Lippincott Williams & Wilkins, 2006.

bib

[60] Stanley Plagenhoef, F Gaynor Evans, and Thomas Abdelnour. Anatomical data for analyzing human motion. *Research quarterly for exercise and sport*, 54(2):169–178, 1983.

[61] John Garrett Pascoe Williams and JF Wellicome. *Rowing: a Scientific Approach: A Symposium.* AS Barnes, 1967.

[62] Thomas A McMahon. Rowing: a similarity analysis. *Science*, 173(3994):349–351, 1971.

[63] Brian Sanderson and Walter Martindale. Towards optimizing rowing technique. *Medicine and science in sports and exercise*, 18(4):454–468, 1986.

[64] Luca Formaggia, Edie Miglio, Andrea Mola, and Antonio Montano. A model for the dynamics of rowing boats. *International journal for numerical methods in fluids*, 61(2):119–143, 2009.

[65] Nicholas Caplan and Trevor Gardner. A mathematical model of the oar blade–water interaction in rowing. *Journal of sports sciences*, 25(9):1025–1034, 2007.

[66] Maurice N Brearley, Neville J de Mestre, and Donald R Watson. Modelling the rowing stroke in racing shells. *The Mathematical Gazette*, 82(495):389–404, 1998.

[67] Olympic Channel. `https://www.youtube.com/watch?v=DniKM5SKe6c`, 2012. Accessed: 2018-08-21.

[68] Alexander Day, Ian Campbell, David Clelland, Lawrence J Doctors, and Jakub Cichowicz. Realistic evaluation of hull performance for rowing shells, canoes, and kayaks in unsteady flow. *Journal of sports sciences*, 29(10):1059–1069, 2011.

[69] Yoann Robert. *Simulation numérique et modélisation d'écoulements tridimensionnels instationnaires à surface libre. Application au système bateau-avirons-rameur.* PhD thesis, Ecole Centrale Nantes, 2017.

[70] `https://thames.me.uk/s00231a.htm`. Accessed: 2018-08-21.

[71] Kenneth John Rawson. *Basic ship theory*, volume 1. Butterworth-Heinemann, 2001.

[72] `https://en.wikipedia.org/wiki/Bulbous_bow`. Accessed: 2018-08-21.

[73] Scott W McCue and Lawrence K Forbes. Bow and stern flows with constant vorticity. *Journal of Fluid Mechanics*, 399:277–300, 1999.

[74] Scott Percival, Dane Hendrix, and Francis Noblesse. Hydrodynamic optimization of ship hull forms. *Applied Ocean Research*, 23(6):337–355, 2001.

[75] Chi-Chao Hsiung. Optimal ship forms for minimum wave resistance. *J. Ship Research*, 25(2), 1981.

[76] Bao-ji Zhang, Ma Kun, and Zhuo-shang Ji. The optimization of the hull form with the minimum wave making resistance based on Rankine source method. *Journal of Hydrodynamics, Ser. B*, 21(2):277–284, 2009.

[77] Chi-Chao Hsiung and Dong Shenyan. Optimal ship forms for minimum total resistance. *Journal of ship research*, 28(3):163–172, 1984.

[78] Julien Dambrine, Morgan Pierre, and Germain Rousseaux. A theoretical and numerical determination of optimal ship forms based on Michell's wave resistance. *ESAIM: Control, Optimisation and Calculus of Variations*, 22(1):88–111, 2016.

bib

[79] Emilio F Campana, Daniele Peri, Yusuke Tahara, and Frederick Stern. Shape optimization in ship hydrodynamics using computational fluid dynamics. *Computer methods in applied mechanics and engineering*, 196(1):634–651, 2006.

[80] Milton Abramowitz and Irene A Stegun. *Handbook of mathematical functions: with formulas, graphs, and mathematical tables.* Courier Corporation, 1964.

[81] Richard H Byrd, Mary E Hribar, and Jorge Nocedal. An interior point algorithm for large-scale nonlinear programming. *SIAM Journal on Optimization*, 9(4):877–900, 1999.

[82] Richard H Byrd, Jean Charles Gilbert, and Jorge Nocedal. A trust region method based on interior point techniques for nonlinear programming. *Mathematical Programming*, 89(1):149–185, 2000.

[83] John McArthur. *High performance rowing.* Crowood Press, 1997.

[84] Volker Nolte. *Rowing faster.* Human Kinetics 1, 2005.

[85] International Canoe Federation. Canoe sprint competition rules. `https://www.canoeicf.com/rules`, 2017. Accessed: 2018-10-11.

[86] Pierre Yves Belly. *250 réponses aux questions d'un marin curieux.* Le gerfaut, 2004.

[87] Finn Christian Michelsen. *Wave resistance solution of Michell's integral for polynomial ship forms.* PhD thesis, University of Michigan, 1960.

[88] Jianchun Huan and Vijay Modi. Design of minimum drag bodies in incompressible laminar flow. *Inverse Problems in Engineering*, 3(4):233–260, 1996.

[89] Bijan Mohammadi and Olivier Pironneau. Shape optimization in fluid mechanics. *Annu. Rev. Fluid Mech.*, 36:255–279, 2004.

[90] Lloyd Steven Sieden. *Buckminster Fuller's universe.* Perseus Pub., 1989.

[91] `http://www.nelo.eu/find-a-boat/?mod=flatwater`. Accessed: 2018-10-11.

[92] `https://www.mathcurve.com/courbes2d.gb/oeuf/oeuf.shtml`. Accessed: 2018-10-11.

[93] Stéphane Popinet. Gerris: a tree-based adaptive solver for the incompressible Euler equations in complex geometries. *Journal of Computational Physics*, 190(2):572–600, 2003.

[94] Stéphane Popinet. An accurate adaptive solver for surface-tension-driven interfacial flows. *Journal of Computational Physics*, 228(16):5838–5866, 2009.

[95] Maximilien Ringelmann. Recherches sur les moteurs animés: Essais des boeufs de travail [Research on animate sources of power: Tests of oxen]. *Annales de l'Institut National Agronomique, 2e série*, 6:243–279, 1907.

[96] Maximilien Ringelmann. Recherches sur les moteurs animés: Travail de l'homme [Research on animate sources of power: The work of man]. *Annales de l'Institut National Agronomique, 2e série*, 12:1–40, 1913.

[97] `https://en.wikipedia.org/wiki/1912_Summer_Olympics`. Accessed: 2018-10-11.

[98] David A Kravitz and Barbara Martin. Ringelmann rediscovered: The original article. *Journal of Personality and Social Psychology*, 1986.

bib

[99] Alan G Ingham, George Levinger, James Graves, and Vaughn Peckham. The Ringelmann effect: Studies of group size and group performance. *Journal of experimental social psychology*, 10(4):371–384, 1974.

[100] Sulisay Phonekeo, Tanvi Dave, Matthew Kern, Scott V Franklin, and David L Hu. Ant aggregations self-heal to compensate for the Ringelmann effect. *Soft matter*, 12(18):4214–4220, 2016.

[101] http://archive.usrowing.org/news/details/2015/09/14/the-st%C3%A4mpfli-express-is-coming-to-a-city-near-you. Accessed: 2018-10-11.

[102] Silas Alben, Kevin Spears, Stephen Garth, David Murphy, and Jeannette Yen. Coordination of multiple appendages in drag-based swimming. *Journal of The Royal Society Interface*, 2010.

[103] Robert B Suter, Gail Stratton, and Patricia R Miller. Water surface locomotion by spiders: distinct gaits in diverse families. *Journal of Arachnology*, pages 428–432, 2003.

[104] British Pathé. https://www.youtube.com/watch?v=zQ6fxsmo3V8, 1929. Accessed: 2017-01-19.

[105] Syncopated rowing. *The Sydney Morning Herald*, 1933.

[106] Anouk J de Brouwer, Harjo J de Poel, and Mathijs J Hofmijster. Don't rock the boat: how antiphase crew coordination affects rowing. *PloS one*, 8(1):e54996, 2013.

[107] Michael Vespoli, Bruce Nelson, and Carl Scragg. Eight man rowing shell, December 12 1995. US Patent 5,474,008.

[108] Michael J Lighthill. Hydromechanics of aquatic animal propulsion. *Annual review of fluid mechanics*, 1(1):413–446, 1969.

[109] Michael J Lighthill. *Mathematical biofluiddynamics*. SIAM, 1975.

[110] Stephen Childress. *Mechanics of swimming and flying*, volume 2. Cambridge University Press, 1981.

[111] Frank E Fish. Influence of hydrodynamic-design and propulsive mode on mammalian swimming energetics. *Australian Journal of Zoology*, 42(1):79–101, 1994.

[112] Michael S Triantafyllou, GS Triantafyllou, and DKP Yue. Hydrodynamics of fishlike swimming. *Annual review of fluid mechanics*, 32(1):33–53, 2000.

[113] Daniel B Quinn, George V Lauder, and Alexander J Smits. Scaling the propulsive performance of heaving flexible panels. *Journal of fluid mechanics*, 738:250–267, 2014.

[114] Florine Paraz, Christophe Eloy, and Lionel Schouveiler. Experimental study of the response of a flexible plate to a harmonic forcing in a flow. *Comptes Rendus Mécanique*, 342(9):532–538, 2014.

[115] Michael J Lighthill. Note on the swimming of slender fish. *Journal of fluid Mechanics*, 9(2):305–317, 1960.

[116] T Yao-Tsu Wu. Swimming of a waving plate. *Journal of Fluid Mechanics*, 10(3):321–344, 1961.

bib

[117] T Yao-Tsu Wu. Hydromechanics of swimming propulsion. Part 1. Swimming of a two-dimensional flexible plate at variable forward speeds in an inviscid fluid. *Journal of Fluid Mechanics*, 46(2):337–355, 1971.

[118] Florine Paraz, Lionel Schouveiler, and Christophe Eloy. Thrust generation by a heaving flexible foil: Resonance, nonlinearities, and optimality. *Physics of Fluids*, 28(1):011903, 2016.

[119] Peter Derek Yeh and Alexander Alexeev. Effect of aspect ratio in free-swimming plunging flexible plates. *Computers & Fluids*, 124:220–225, 2016.

[120] Silas Alben, Charles Witt, T Vernon Baker, Erik Anderson, and George V Lauder. Dynamics of freely swimming flexible foils. *Physics of Fluids*, 24(5):051901, 2012.

[121] Peter A Dewey, Birgitt M Boschitsch, Keith W Moored, Howard A Stone, and Alexander J Smits. Scaling laws for the thrust production of flexible pitching panels. *Journal of Fluid Mechanics*, 732:29–46, 2013.

[122] Veronica Raspa, Sophie Ramananarivo, Benjamin Thiria, and Ramiro Godoy-Diana. Vortex-induced drag and the role of aspect ratio in undulatory swimmers. *Physics of Fluids*, 26(4):041701, 2014.

[123] Alain Perrier. *250 Réponses aux questions du plongeur curieux*. Le gerfaut, 2008.

[124] `http://museedumas.fr/pages/georges_serenon/`. Accessed: 2018-10-11.

[125] `https://en.wikipedia.org/wiki/List_of_world_records_in_finswimming`. Accessed: 2018-08-21.

[126] Nicolas Vandenberghe, Jun Zhang, and Stephen Childress. Symmetry breaking leads to forward flapping flight. *Journal of Fluid Mechanics*, 506:147–155, 2004.

[127] Nicolas Vandenberghe, Stephen Childress, and Jun Zhang. On unidirectional flight of a free flapping wing. *Physics of Fluids*, 18(1):014102, 2006.

[128] James M Gere and Stephen P Timoshenko. Mechanics of materials. *Cole, Pacific Grove, CA*, pages 815–39, 2001.

[129] Sophie Ramananarivo, Ramiro Godoy-Diana, and Benjamin Thiria. Propagating waves in bounded elastic media: Transition from standing waves to anguilliform kinematics. *EPL (Europhysics Letters)*, 105(5):54003, 2014.

[130] Archibald Vivian Hill. The heat of shortening and the dynamic constants of muscle. *Proc. R. Soc. Lond. B*, 126(843):136–195, 1938.

[131] DR Wilkie. The relation between force and velocity in human muscle. *The Journal of physiology*, 110(3-4):249–280, 1949.

[132] Thomas Henry Havelock. The wave resistance of a cylinder started from rest. *The Quarterly Journal of Mechanics and Applied Mathematics*, 2(3):325–334, 1949.

[133] Alexei D Chepelianskii, Frédéric Chevy, and Elie Raphael. Capillary-gravity waves generated by a slow moving object. *Physical review letters*, 100(7):074504, 2008.

[134] Grey T Gustafson and Kelly B Miller. Revision of the Southeast Asian Whirligig Beetle Genus Porrorhynchus Laporte, 1835 (Coleoptera: Gyrinidae: Gyrininae: Dineutini). *The Coleopterists Bulletin*, 70(4):675–714, 2016.

bib

[135] Jonathan Voise and Jérôme Casas. The management of fluid and wave resistances by whirligig beetles. *Journal of The Royal Society Interface*, 7(43):343–352, 2010.

[136] Thor S Nilson, Ted Daigneault, and Matt Smith. *The FISA Coaching Development Programme Course.* FISA, 1987.

[137] Oar (sport rowing). `https://en.wikipedia.org/wiki/Oar_(sport_rowing)`. Accessed: 2018-10-11.

[138] Volker Nolte. Shorter oars are more effective. *Journal of applied biomechanics*, 25(1):1–8, 2009.

[139] Brock Laschowski, Volker Nolte, Michael Adamovsky, and Ryan Alexander. The effects of oar-shaft stiffness and length on rowing biomechanics. *Proceedings of the Institution of Mechanical Engineers, Part P: Journal of Sports Engineering and Technology*, 229(4):239–247, 2015.

[140] Alban Leroyer, Sophie Barré, Jean-Michel Kobus, and Michel Visonneau. Experimental and numerical investigations of the flow around an oar blade. *Journal of marine science and technology*, 13(1):1–15, 2008.

[141] Pascal Hémon. Hydrodynamic characteristics of sea kayak traditional paddles. *Sports Engineering*, pages 1–9, 2017.

[142] Alexandre Baudouin and David Hawkins. A biomechanical review of factors affecting rowing performance. *British journal of sports medicine*, 36(6):396–402, 2002.

[143] Alexandre Baudouin and David Hawkins. Investigation of biomechanical factors affecting rowing performance. *Journal of biomechanics*, 37(7):969–976, 2004.

[144] Richard M Smith and Constanze Loschner. Biomechanics feedback for rowing. *Journal of Sports Sciences*, 20(10):783–791, 2002.

[145] Floren Colloud, Pascal Bahuaud, Nathalie Doriot, Stéphane Champely, and Laurence Chèze. Fixed versus free-floating stretcher mechanism in rowing ergometers: mechanical aspects. *Journal of sports sciences*, 24(05):479–493, 2006.

[146] Robert C Sprague IV, James C Martin, Christopher J Davidson, and Roger P Farrar. Force-velocity and power-velocity relationships during maximal short-term rowing ergometry. *Medicine & Science in Sports & Exercise*, 39(2):358–364, 2007.

[147] Bruce Elliott, Andrew Lyttle, and Olivia Birkett. Rowing: The RowPerfect Ergometer: a training aid for on-water single scull rowing. *Sports Biomechanics*, 1(2):123–134, 2002.

[148] Valery Kleshnev. Propulsive efficiency of rowing. In *ISBS-Conference Proceedings Archive*, volume 1, 1999.

[149] C Cohen, B Darbois Texier, G Laffaye, L Auvray, and C Clanet. Weightlifting and the actomyosin cycle. *Proc. R. Soc. A*, 471(2184):20150473, 2015.

[150] Hidetoshi Takahashi, Kiyoshi Matsumoto, and Isao Shimoyama. Differential pressure measurement of an insect wing using a mems sensor. In *Complex Medical Engineering (CME), 2012 ICME International Conference on*, pages 349–352. IEEE, 2012.

bib

Titre : Problèmes d'optimisation à la surface de l'eau

Des coques de bateaux à la propulsion par rame

Mots clés : Propulsion, Vagues, Aviron, Optimisation, Trainée.

Résumé : Plusieurs problèmes d'optimisation — dans l'eau ou à l'interface avec l'air — sont abordés, allant de l'optimisation de la forme des coques de bateaux à celle de la propulsion en aviron et dans la nage avec palmes. Des approches théorique, expérimentale et numérique sont combinées. Nous développons d'abord une approche théorique minimale afin de déterminer, à volume immergé et puissance donnés, les rapports d'aspect optimaux des coques de bateau, qui sont discutés et comparés aux rapports d'aspect de bateaux réels. L'effet de l'asymétrie avant-arrière des coques est ensuite discuté. Dans une deuxième partie, nous étudions la propulsion en aviron et dans la nage avec palme. Dans le cas de l'aviron, nous réexaminons la question de la synchronisation des rameurs sur le bateau à l'aide d'un modèle réduit de bateau robotisé et cherchons quelle est la synchronisation qui permet à l'équipage d'aller le plus vite. Enfin, nous analysons l'effet de la géométrie des palmes pour trouver les stratégies de nage optimales.

Title : Optimisation problems at the air-water interface.

From ship hulls to rowing propulsion

Keywords : Propulsion, Waves, Rowing, Optimisation, Drag.

Abstract : We consider a few optimisation problems — in water and at its surface — ranging from drag minimisation on ship hulls to propulsion efficiency in rowing and swimming with fins. We use theoretical, experimental and numerical methods. In a first part, we focus on the question of optimal hull shapes. We develop a minimal theoretical approach to determine, at given load and propulsive power, the optimal aspect ratios of ship hulls, which are discussed and confronted to empirical data. Then, the effect of the fore-aft hull asymmetry is addressed. In a second part, we study the question of propulsion in rowing and swimming with fins. In particular, the long-standing question of whether rowers should be synchronised or not is brought up to date with a scaled rowing robot. Finally, we analyse the optimal shape of fins in order to find optimal swimming strategies.